THE UNIVERSITY OF SHEFFIELD

DEPARTMENT OF CIVIL AND STRUCTURAL ENGINEERING

PROPERTIES OF CONCRETE SUBJECTED TO EXPLOSIVELY GENERATED IMPACT AND IMPULSE LOADING

by

BERNARD ARCHER, B.Eng.(SHEFFIELD), C.Eng., M.I.C.E., M.I.H.T.

A thesis presented to the University
of Sheffield for the degree of Doctor
of Philosophy

SEPTEMBER 1985

To the memory of my dear mother

SUMMARY

The use of models to simulate full scale structural effects has long been attempted and various types of models have been developed. One type, the replica model, in which prototype materials are used was selected for this study. Much interest has been shown in the past on damage prediction based on extrapolation of the results from small explosive charge tests. In this study, scale model concrete ground slabs have been subjected to high rates of loading using explosively propelled copper and aluminium projectiles impacting on the concrete to air surface and explosive devices buried in the soil beneath the concrete slab. The copper or aluminium projectile was produced from a truncated cone of metal in direct contact with a shaped charge of RDX/TNT explosive. The subsurface charge was uncased PE4 plastic explosive inserted into a hole through the slab and into the soil. In many tests the hole was produced by the metal jet impact without any modification. Other scaled concrete targets have also been tested using explosively propelled projectiles. Transient results from the tests have been collected using high speed photography, electrical resistance strain gauges, crack velocity detection devices and a projectile velocity measurement system. Other measurements of post test damage have utilised stereoscopic photography, coloured particles of soil in the foundations of the concrete slabs and a scanning electron microscope. Concretes of various strengths and densities have been used but all conformed to a scaled down specification for pavement quality concrete. Explosive charges were similarly scaled in size from prototype devices. Some additional experimental work has been carried out to obtain fundamental data on the explosive charges and on 'perspex', metal and concrete blocks for calculation

and comparison purposes. Comparisons are also made with work of a related nature undertaken at larger scales.

ACKNOWLEDGEMENTS

This research was carried out in the Department of Civil and Structural Engineering of the University of Sheffield, for which the author expresses his gratitude to Professor Hanna for the use of the facilities.

The author would like to thank the Procurement Executive, Ministry of Defence for the granting of the research contract, on which this thesis is based, Dr R J Lynch, Dr A R Sinden, Dr I Cullis and Mr A V Bowden of the Royal Armament Research and Development Establishment, Sevenoaks, for arranging the contract and their advice throughout.

The author is indebted to Dr A J Watson and Dr W F Anderson for their supervision and assistance during the research programme and to the academic staff of the department who contributed ideas and constructive criticism.

The support of the technical staff was much appreciated especially Mr N P Hodgson, contract technician, whose help in fabrication and testing was invaluable. In addition, the work of Mr A Hindle and Mr P Trick with the high speed photography, Mr A Shelton with the electron microscopy, Mr D Thompson with the stereoplotting and Miss J Stacey with the typing is much appreciated.

It is not possible to list all the people who contributed to this work so my thanks and apologies are extended to all those not mentioned.

Finally I should like to express my gratitude to my family for their unswerving support during my research.

WARNING

The information given in this thesis on the use of explosives should not be treated as exhaustive. Due regard must be paid to standing instructions and procedures particularly where explosives are fabricated or modified and where it is necessary to use live instrumentation circuits in the proximity of charges and firing circuits.

LIST OF CONTENTS

			Page
SUMMARY			i
ACKNOWLEDGEMENTS			ii
WARNING			iv
LIST OF CONTENTS			v
LIST OF TABLES			x
LIST OF FIGURES			xiii
LIST OF PLATES			xix
LIST OF SYMBOLS			xx
GLOSSARY OF TERMS USED			xxviii
CHAPTER 1		INTRODUCTION	1
CHAPTER 2		LITERATURE SURVEY OF EXPLOSIVES AND THEIR USE AGAINST CONCRETE AND SOIL	4
	2.1	PRINCIPLES OF SHAPED CHARGES	4
	2.2	SHAPED CHARGE JET PENETRATION THEORIES	7
	2.2.1	Penetration of a Semi-Infinite Medium by a Shaped Charge Jet	8
	2.2.2	The Volume-Energy Theory of Shaped Charge Jet Penetration	12
	2.2.3	The Hydrodynamic Theory of Shaped Charge Jet Penetration	14
	2.3	SHAPED CHARGE JET IMPACT ON CONCRETE	21
	2.4	BEARING CAPACITY OF CONCRETE BLOCKS	24
	2.5	EXPLOSIVE CRATERING IN SOIL	25
	2.5.1	The Scaling of Crater Dimensions	26
	2.5.2	Cratering by Explosives as a Cavity Expansion Effect	30
	2.5.3	Cratering of Soils by Buried Explosives as an Energy-Density Problem	32
	2.5.4	Summary of Soil Cratering by Explosives and Instrumentation Used by Previous Workers	36
	2.6	CRATERING OF AIRFIELD PAVEMENTS	36
	2.7	STRESS WAVES	38
	2.7.1	Elastic Waves in an Infinite Medium	39
	2.7.2	Reflection and Refraction of Waves at Interfaces	41
	2.7.3	Plastic Waves	42
	2.7.4	Waves in Elastic Rods	44
	2.7.5	Attenuation of Waves	45
	2.8	MODELLING TECHNIQUES FOR EXPLOSION TESTING	46
	2.8.1	The Scaling of Shaped Charges	46
	2.8.2	Scaling Explosive Blast Effects on Concrete Models	47
	2.8.3	Limitations and Assumptions in Replica Scaling	49

Page

CHAPTER 3		THE SELECTION AND TESTING OF MATERIALS FOR USE IN THE CONSTRUCTION OF TEST SPECIMENS	72
	3.1	REQUIREMENTS AND GENERAL DETAILS OF THE MODELS USED IN THIS STUDY	72
	3.2	AGGREGATES USED IN THE MODELS	73
	3.3	CONCRETES USED IN THE MODELS	73
	3.4	REINFORCEMENT USED IN MODEL SLABS	76
	3.5	JOINTS AND SEPARATION LAYERS USED WITH MODEL GROUND SLABS	77
	3.6	SOILS USED AS FOUNDATIONS TO MODEL GROUND SLABS	77
CHAPTER 4		THE CONSTRUCTION OF INSTRUMENTATION AND TEST SPECIMENS	98
	4.1	INSTRUMENTATION WORK PRIOR TO THE CONSTRUCTION OF TEST SPECIMENS	98
	4.1.1	Soil Pressure Gauge	98
	4.1.2	Coloured Sand Technique for Soil Movement Detection	100
	4.1.3	'Plasticine' Blocks for Soil Particle Movement Detection	101
	4.1.4	Shaped Charge Jet Penetration Detection Gauge	101
	4.1.5	Electrical Resistance Strain Gauges for Burial in Concrete	102
	4.1.6	Graphite Rod Spall Detection Gauge	104
	4.2	CONSTRUCTION OF THE TEST SPECIMENS	104
	4.2.1	Construction of Scale Model Concrete Ground Slabs	105
	4.2.2	Construction of Concrete Block Test Specimens	114
	4.2.3	Construction of Other Test Specimens	115
	4.3	CONSTRUCTION OF EXPLOSIVE CHARGES AND CHARGE HOLDERS	117
	4.3.1	Shaped Charges	117
	4.3.2	Subsurface Charges	117
	4.4	INSTRUMENTATION OF TEST SPECIMENS AFTER CONSTRUCTION	118
	4.4.1	Conducting Silver Paint Crack Detector	118
	4.4.2	Shaped Charge Jet Velocity Detector	119
	4.4.3	Explosion Blast Detector	119
	4.4.4	Displacement Gauge	120
	4.5	TECHNIQUES ABANDONED OR IMPROVED	121
	4.5.1	Coloured Sand Column Technique for Measuring Soil Particle Movement When Used With Shaped Charges	121
	4.5.2	Electrical Resistance Strain Gauges as Crack Detectors	121
	4.5.3	RACAL Timers	122
	4.5.4	Resistance Circuit for Shaped Charge Jet Detector	122

			Page
CHAPTER 5		EXPERIMENTAL PROCEDURES AND THE MEASUREMENT OF DAMAGE PARAMETERS	170
	5.1	EXPERIMENTAL PROCEDURES	170
	5.1.1	Pre-test Electrical Instrumentation Checking Procedure	170
	5.1.2	Shaped Charge Jet Impact Test Procedure	171
	5.1.3	Subsurface Explosive Charge Test Procedure	173
	5.1.4	Post Test Procedures	175
	5.2	POST TEST INVESTIGATION TECHNIQUES FOR THE DETERMINATION OF DAMAGE PARAMETERS	176
	5.2.1	Paint Wash Technique to Determine the Extent of Surface Cracking	176
	5.2.2	Physical Measurements and Still Photography	176
	5.2.3	Stereoscopic Photography of Craters	176
	5.2.4	Sawing and Coring of Test Specimens by Diamond Tipped Tools for Electron Microscope Inspection and Crushing Strength Tests	177
	5.2.5	Soil Property Tests	178
	5.2.6	Investigations of Craters in Soil Foundations by Wax and Cement Castings	178
CHAPTER 6		EXPERIMENTAL RESULTS FROM THE SHAPED CHARGE TEST PROGRAMME	216
	6.1	INTRODUCTION	216
	6.2	SHAPED CHARGE JET VELOCITY MEASUREMENTS	216
	6.3	SHAPED CHARGE JET PENETRATION RATE MEASUREMENTS	218
	6.4	STRESS PULSES IN CONCRETE DUE TO SHAPED CHARGE JET IMPACTS	218
	6.4.1	Radial Compression Pulse	219
	6.4.2	Circumferential Tensile Pulse	220
	6.4.3	Vertical Compression Pulse	221
	6.5	CRACK AND SPALL MEASUREMENT	222
	6.5.1	Cracking	222
	6.5.2	Spalling	224
	6.6	OVERALL CRACKING OF CONCRETE TEST SPECIMENS	226
	6.6.1	Influence of the Size of Test Specimens	226
	6.6.2	Influence of Different Aggregates	228
	6.6.3	Influence of the Cement Content of the Mix	229
	6.6.4	Influence of the Shaped Charge Parameters	230
	6.7	SHAPED CHARGE HOLE DIAMETER AND PENETRATION DEPTH	230
	6.7.1	Influence of the Type of Aggregate	231
	6.7.2	Influence of the Shaped Charge Parameters	232
	6.7.3	Influence of Charge Standoff and the Obliquity of the Jet Impact	234
	6.7.4	Influence of the Soil Foundation	235
	6.8	TEST SPECIMEN MOVEMENT UNDER IMPACT	235
	6.9	LIMITATIONS OF THE TEST PROGRAMME	236

Page

CHAPTER 7		EXPERIMENTAL RESULTS FROM SUBSURFACE CHARGE EXPLOSION TESTS IN SOILS OVERLAIN BY GROUND SLABS	281
	7.1	THE INFLUENCE ON CRATERING OF GROUND SLABS OVERLYING SOIL SUBJECTED TO SUBSURFACE EXPLOSIONS	281
	7.2	INFLUENCE OF THE SOIL TYPE AND CONDITION ON CRATERING	282
	7.3	THE INFLUENCE ON CRATERING OF REINFORCEMENT IN GROUND SLABS	283
	7.4	THE INFLUENCE ON CRATERING OF DAMAGED CONCRETE GROUND SLABS	284
	7.5	MOVEMENT OF SLABS AND STRESS PULSE INVESTIGATION IN THE SOIL	284
	7.6	COMPARISONS BETWEEN CRATERS AT 1/5 SCALE AND AT OTHER SCALES	285
	7.7	LIMITATIONS	286
CHAPTER 8		CALCULATIONS	301
	8.1	INTRODUCTION	301
	8.2	SHAPED CHARGE JET PENETRATION	301
	8.2.1	Assumptions	301
	8.2.2	Calculation of Projectile Parameters	302
	8.2.3	Comparison with Penetration of the Copper Jet into Mild Steel	306
	8.2.4	Comparison with Penetration of the Copper Jet into 'Plasticine'	306
	8.2.5	Comparison with Penetration of the Copper Jet into Concrete	307
	8.2.6	Calculation of the Copper Jet Length from Geometry Considerations	307
	8.2.7	Calculation of the Jet Length from Target and Jet Density Considerations	309
	8.3	PENETRATION FORMULAE APPLIED TO CONCRETE	309
	8.4	CALCULATION OF THE PRESSURE GENERATED ON THE SPECIMEN DURING IMPACT OF A HIGH VELOCITY COPPER JET	310
CHAPTER 9		GENERAL DISCUSSION, CONCLUSIONS, LIMITATIONS AND RECOMMENDATIONS FOR FUTURE WORK	313
	9.1	GENERAL DISCUSSION	313
	9.1.1	Shaped Charge Jet Impact on Concrete	313
	9.1.2	Local Damage to Concrete Caused by Shaped Charge Jet Impact	313
	9.1.3	Gross Damage Caused to Test Specimens by Shaped Charge Jet Impact	317
	9.1.4	Other Observations of Shaped Charge Jet Impact Damage to Concrete Specimens	319
	9.2	SUBSURFACE EXPLOSIVE SHOCK TESTS	320
	9.3	LIMITATIONS	323

Page

9.4	CONCLUSIONS	325
9.4.1	Shaped Charge Jet Impact on Concrete	325
9.4.2	Subsurface Blast Loading of Concrete	327
9.5	SUGGESTIONS FOR FUTURE WORK	328
REFERENCES		339
APPENDIX 1	EQUIPMENT AND MATERIALS SUPPLIERS	350
APPENDIX 2	RULES FOR USING SHAPED CHARGES AND OTHER EXPLOSIVES	355
APPENDIX 3	COMPUTER PROGRAM AND CALCULATIONS FOR STEREOCOMPARATOR DATA	361

LIST OF TABLES

2.1 List of Parameters for Modelling Shaped Charge Jet Impact.

2.2 Projectile Impact Pi Terms.

2.3 Replica Model Scale Factors.

2.4 Summary of Ideal Scale Factors.

3.1 Requirements for Aggregates.

3.2 Grading Limits for Aggregates.

3.3 Requirements for Concrete.

3.4 Requirements for Joint and Separation Layers.

3.5 Properties of Aggregates.

3.6 Zone 2 Sand Grading.

3.7 Grading of Aggregates.

3.8 Concrete Mix Details.

3.9 Constants for Apparatus.

3.10 Casting Details and Compaction Times for Concrete Trial Mixes.

3.11 Cement Properties.

3.12 Typical Strength Test Results for Concrete Trial Mixes.

3.13 Computed Values of the Dynamic Modulus of Elasticity of Concrete.

3.14 Properties of the Clay Used in Experiments.

4.1 List of Test Specimens and Instrumentation Details for Shaped Charge Tests on Slabs.

4.2 List of Test Specimens and Instrumentation Details for Shaped Charge Tests on Concrete Blocks.

4.3 List of Test Specimens and Instrumentation for Shaped Charge Tests on Other Materials.

4.4 List of Test Specimens and Instrumentation for Subsurface Charge Tests on Concrete Slabs.

4.5 List of Abbreviations Used in tables 4.1 to 4.4.

4.6 Properties of Pavement Materials.

4.7 Properties of Concrete Block Materials.

4.8 Soil Foundation Properties

4.9 Principal Dimensions of Main Test Specimens.

4.10 Principal Dimensions of Minor Test Specimens.

4.11 Compaction Details for Materials Used in Test Specimens.

4.12 Details of Shaped Charges.

4.13 Details of Explosives.

5.1 High Speed Camera Delay Data.

5.2 Measurement of Cracking and Local Damage by 43g Copper Lined Shaped Charge Jet Impacts on Concrete Slabs.

5.3 Measurements of Cracking and Local Damage by 43g Aluminium Lined Shaped Charge Jet Impacts on Concrete Slabs.

5.4 Measurements of Cracking and Local Damage by 43g Copper Lined Shaped Charge Jet Impacts on Concrete Blocks.

5.5 Measurements of Cracking and Local Damage by Modified Copper Lined Shaped Charge Jets on Concrete Blocks.

5.6 Measurements of Cracking and Local Damage by 43g Aluminium Lined Shaped Charge Jet Impacts on Concrete Blocks.

5.7 Measurements of 43g Copper Lined Shaped Charge Jet Impact Holes in Concrete Slabs.

5.8 Measurements of 43g Aluminium Lined Shaped Charge Jet Impact Holes in Concrete Slabs.

5.9 Measurements of 43g Copper Lined Shaped Charge Jet Impact Holes in Concrete Blocks.

5.10 Measurements of Modified Copper Lined Shaped Charge Jet Impact Holes in Concrete Blocks.

5.11 Measurements of 43g Aluminium Lined Shaped Charge Jet Impact Holes in Concrete Blocks.

5.12 Summary of Results from Impact Experiments on Non Cementitious Specimens.

5.13 Summary of Crater Data from Impulse Experiments.

5.14 Summary of Concrete Slab Cracks from Impulse Experiments.

6.1 Summary of Shaped Charge Jet Impact Tests.

6.2 Shaped Charge Jet Flight Time and Velocity Data.

6.3 Shaped Charge Jet Impact Penetration Data.

6.4 Stress Pulse Data from Shaped Charge Jet Impact Tests. (Radial Compression)

6.5 Stress Pulse Data from Shaped Charge Jet Impact Tests. (Circumferential Tension)

6.6 Stress Pulse Data from Shaped Charge Jet Impact Tests. (Vertical Compression)

6.7 Concrete Cracking Times from Shaped Charge Jet Impact Tests.

6.8 Speed of Cracks Formed by Shaped Charge Jet Impacts.

6.9 Spalling Data from Shaped Charge Jet Impacts.

6.10 Normalised Crack Lengths of Specimens Subjected to a Shaped Charge Jet Impact.

6.11 Reduction in Shaped Charge Jet Penetration in Concrete by Steel Plates.

6.12 Data from Oblique Impacts of 43g Shaped Charge Jets on Concrete.

6.13 Statistical Data from 43g Shaped Charge Jet Impacts on Mild Steel.

6.14 Statistical Data from 43g Shaped Charge Jet Impacts on Concrete Specimens.

7.1 Subsurface Explosive Charge Effects.

7.2 Subsurface Crater Data.

8.1 Predictions of Copper Lined Shaped Charge Jet Impact Parameters from Equation 8.10.

8.2 Predictions of Aluminium Lined Shaped Charge Jet Impact Parameters from Equation 8.10.

8.3 Predicted Shaped Charge Jet Penetration from Equation 2.14.

LIST OF FIGURES

2.1 Cross Sectional View of a Shaped Charge.

2.2 Collapse of a Shaped Charge Liner. (After Johnson 1972)

2.3 Formation of a Shaped Charge Jet. (After Cousins 1968)

2.4 Velocity Diagrams for the Formation of a Shaped Charge Jet. (After Johnson 1972)

2.5 Direction and Velocity of the Material Flow During the Formation of a Shaped Charge Jet. (After Johnson 1972)

2.6 The Length of a Shaped Charge Jet - Geometry Considerations. (After Johnson 1972)

2.7 Penetration of a Semi-Infinite Medium by a Shaped Charge Jet. (After Johnson 1972)

2.8 Idealised Penetration - Standoff Relationship for Shaped Charge Jet Impact. (After Johnson 1972)

2.9 Actual Penetration - Standoff Relationship for Shaped Charge Jet Impact. (After Johnson 1972)

2.10 Bearing Capacity of Rock Under Point Loading. (After Chen 1969)

2.11 Crater and Camouflet Nomenclature.

2.12 Apparent and True Crater Nomenclature.

2.13 The Mechanism of Cratering for Deep Buried Explosive Charges.

2.14 The Mechanism of Cratering for Explosive Charges at Moderate Depth.

2.15 Stress - Strain Diagrams for Material Behaviour at Different Loading Rates.

2.16 Crater Formation Derived from Fastax Camera Pictures and Coloured Sand Column Technique. (After Townsend 1961)

2.17 Craters Produced by Explosive Charges Buried Under Pavements. (After Kvammen 1973)

2.18 Stresses Acting on a Small Element.

2.19 Reflected Stress Waves at an Interface.

2.20 Reflection of Irrotational Waves at a Solid/Air Interface.

2.21 Reflection of an Irrotational Wave or a Vertically Polarised Transverse Wave.

2.22 Reflection and Refraction of a Horizontally Polarised Transverse Wave.

2.23 Plastic Impact Strain Distributed in a Rod.

3.1 Cross Section of a Full Scale Concrete Pavement. (Joint Details)

3.2 Cross Section of a Model Concrete Pavement.

3.3 Grading Limits for Pavement Quality Concrete Aggregates. (Full Scale)

3.4 Grading Limits for Dry Lean Mix Concrete Aggregates. (Full Scale)

3.5 Stress - Strain Curves for 12 and 16 Gauge Mild Steel Wire Used as Scale Reinforcement in Concrete Slabs.

3.6 Dry Density Versus Moisture Content for Zone 2 Sand.

3.7 Dry Density Versus Moisture Content for Naylor's Fireclay.

3.8 Dry Density Versus Undrained Triaxial Shear Strength for Naylor's Fireclay.

3.9 Moisture Content Versus Undrained Triaxial Shear Strength for Naylor's Fireclay.

4.1 Soil Pressure Gauge Details.

4.2 Calibration Graph for the Soil Pressure Gauge.

4.3 Wheatstone Bridge Circuit for Electical Resistance Strain Gauges.

4.4 'Plasticine' Block No.1 Details.

4.5 'Plasticine' Block No.2 Details.

4.6 'Plasticine' Block No.3 Details. (Test M19)

4.7 Cross Section of a Shaped Charge Jet Detector Gauge.

4.8 Circuit Diagram for a Shaped Charge Jet Detector Gauge.

4.9 Calibration Graph for Electrical Resistance Strain Gauges Fixed to Small Concrete Blocks.

4.10 Circuit Diagram for Graphite Rod Spall Detectors.

4.11 Cross Section of a Typical Test Bay Showing Explosive Charge Location and Construction Details.

4.12 California Bearing Ratio Test Arrangements.

4.13 Guide Frame for Making Holes for Coloured Sand Columns in Soils.

4.14 Experimental Details for a ⅓ Scale Test Specimen.

4.15 Details of the Turnbuckle for Tensioning Holding Wires for Reinforcement Mesh in Concrete Slabs.

4.16 Orientations of Electrical Resistance Strain Gauges Buried in Concrete Test Specimens.

4.17 Locations of Graphite Rod Spall Detectors Buried in Concrete Test Specimens.

4.18 Copper Block No.1 (M16) Details.

4.19 Copper Block No.2 (M17) Details.

4.20 Cross Section of Block B26 with Buried 'Perspex' Plate.

4.21 Concrete Plate Stack Details. (Test M18)

4.22 Concrete Plate Stack Embedded in Slab S28.

4.23 43g 34mm dia. Shaped Charge.

4.24 298g 56mm dia. Shaped Charge.

4.25 Cross Section of a Typical Shaped Charge and Jet Detector Holder.

4.26 Details of Buried Explosive Charges.

4.27 Typical Locations of Crack Detectors on Concrete Slabs.

4.28 Typical Locations of Crack Detectors on Concrete Blocks.

4.29 Circuit Diagram for Conducting Silver Paint Crack. Detectors.

4.30 Location and Details of an Explosion Blast Detection Gauge.

4.31 Circuit Diagram for an Explosion Blast Detector Gauge.

4.32 Cross Section of a Potentiometric Linear Variable Displacement Transducer Showing Basic Details.

4.33 Circuit Diagram for a Potentiometric Linear Variable Displacement Transducer.

4.34 Experimental Details for using the Barr and Stroud High Speed Camera.

4.35 Resistance Circuit Diagram for Shaped Charge Jet Detectors.

5.1 Explosive Charge Firing Circuit Diagram.

5.2 Diagrammatic Circuit for all Test Equipment Used with the Barr and Stroud High Speed Camera.

5.3 Oscilloscope Trace of the Output from a Potentiometric Linear Variable Displacement Transducer.

5.4 Oscilloscope Trace of the Output from Two Electrical Resistance Strain Gauges.

5.5 Oscilloscope Trace of the Output from a Jet or Blast Detector Gauge.

5.6 Oscilloscope Trace of the Output from Electrically Conducting Silver Paint Crack Detectors and Graphite Rod Spall Detectors.

5.7 Location of Stereoscope Cameras Over a Test Specimen.

5.8 Cross Sections at 6mm Intervals of a Shaped Charge Jet Hole in Concrete from Stereoscope Photography.

5.9 Crushing Strength Versus Distance from Impact for 25mm dia. Concrete Cores from a Slab Impacted by a 43g Shaped Charge Jet.

5.10 Idealised Shaped Charge Jet Hole in a Concrete Slab for Measurement Purposes.

6.1 Jet Flight Time Versus Distance Travelled for 43g and 298g Shaped Charges.

6.2 Penetration Distance Versus Time for 43g Shaped Charges.

6.3 Penetration Velocity Versus Distance Penetrated for 43g Shaped Charge Jets.

6.4 Directions of Stress Pulses Generated by Shaped Charge Jet Impact.

6.5 Distance Penetrated Versus Time for 43g and 298g Shaped Charge Jets in Concretes.

6.6 Types of Spalling in Concrete Due to Shaped Charge Impacts.

6.7 Cracks in a 380mm Sand/Gravel Concrete Cube. (43g Shaped Charge Jet Impact)

6.8 Cracks in a 760mm Sand/Gravel Concrete Cube. (298g Shaped Charge Jet Impact)

6.9 Cracks in Concrete Slabs. (43g Shaped Charge Jet Impacts)

6.10 Cracks in a 500mm Concrete Slab Impacted by a Shaped Charge Jet.

6.11 Cracks in a Concrete Slab Impacted Off-centre by a Shaped Charge Jet.

6.12 Cracks in a 380mm 'Lytag' Contrete Cube. (43g Shaped Charge Jet Impact)

6.13 Cracks in a 380mm Barytes Concrete Cube. (43g Shaped Charge Jet Impact)

6.14 Cracks in a Sand/Gravel Concrete Slab After 3 Shaped Charge Jet Impacts.

6.15 Cracks in a 'Lytag' Concrete Slab After 3 Shaped Charge Jet Impacts.

6.16 Cracks in a Barytes Concrete Slab After 3 Shaped Charge Jet Impacts.

6.17 Normalised Crack Length Versus Mix Proportions for Sand/Cement Mortar. (380mm Cubes, 43g Jet Impact)

6.18 Cross Section of a Typical Hole Formed in Concrete by a Shaped Charge Jet Impact.

6.19 43g Copper Shaped Charge Impact Hole Diameter Frequency in Concrete.

6.20 43g Copper Shaped Charge Impact Hole Diameter Frequency in Various Concretes.

6.21 43g Aluminium Shaped Charge Impact Hole Diameter Frequency in Concrete.

6.22 43g Copper Shaped Charge Impact Hole Diameter Frequency in Lean Mix Concrete.

6.23 43g Copper Shaped Charge Jet Penetration Depth Frequency in Concrete Slab Tests.

6.24 43g Copper Shaped Charge Jet Penetration Depth Frequency in Concrete Slabs on Sand.

6.25 43g Copper Shaped Charge Jet Penetration Depth Frequency in Concrete Slabs on Clay.

6.26 43g Copper Shaped Charge Jet Penetration Depth Frequency in Concrete Blocks.

6.27 43g Aluminium Shaped Charge Jet Penetration Depth Frequency in Concrete Slabs.

6.28 43g Aluminium Shaped Charge Jet Penetration Depth Frequency in Concrete Blocks.

6.29 Modified Initiatior System for a 43g Copper Lined Shaped Charge.

6.30 Cross Section of a Typical Hole Formed in Sand/Gravel Concrete by a 43g Copper Shaped Charge Jet After Perforating a Steel Plate.

6.31 43g Copper Shaped Charge Impact Hole Diameter and Penetration Depth in Concrete Versus Standoff.

6.32 Cracks in a 380mm Concrete Cube Impacted by a 43g Copper Shaped Charge Jet at 60° to the Horizontal.

6.33 Details of 43g Shaped Charge Jet Impact Holes in 'Plasticine Blocks'.

7.1 Crater Formed in Surchanged Sand by a 16g Subsurface Explosive Charge.

7.2 Crater formed in Crusted Sand by a 16g Subsurface Explosive Charge.

7.3 Crater Formed in Surchanged Clay by a 16g Subsurface Explosive Charge.

7.4 Crater Formed in Crusted Clay by a 16g Subsurface Explosive Charge.

7.5 Crater Formed in 'Wet' Sand by a 16g Subsurface Explosive Charge.

7.6 Cracks Formed in an Unreinforced Sand/Gravel Concrete Slab by a 16g Subsurface Explosive Charge in Clay.

7.7 Cracks in an Unreinforced Sand/Gravel Concrete Slab by a 16g Charge in 'Wet' Sand.

7.8 Cracks in an Unreinforced Sand/Gravel Concrete Slab by a 16g Charge in Sand. ('Damp' or 'Dry' Sand)

7.9 Cracks in a Reinforced Sand/Gravel Concrete Slab by a 16g Charge in Clay.

7.10 Cracks in a Reinforced Sand/Gravel Concrete Slab by a 16g Charge in Sand. ('Damp' or 'Dry' Sand)

7.11 Crater Formed in Clay under a Reinforced Concrete Slab by a 16g Explosive Charge. (Subsurface)

7.12 Crater Formed in Sand under a Reinforced Concrete Slab by a 16g Explosive charge. (Subsurface)

7.13 Crack Formed by a Shaped Charge Jet Impact on a Concrete Slab.

7.14 Location of a Crack Detector on a Concrete Slab Prior to a Subsurface Explosion.

7.15 True Crater Diameter Frequency in Soils. (16g Subsurface Charges)

7.16 True Crater Depth Frequency in Soils. (16g Subsurface Charges)

7.17 True Crater Volume Frequency in Soils. (16g Subsurface Charges)

7.18 Compilation of Typical Craters in Sand and Silty Clay Caused by Subsurface Explosions. (After Kvammen 1973)

9.1 Hole Formed by a 43g Copper Shaped Charge in a Ductile Material. (EN28 Steel)

9.2 Influence of Possible Scouring Action by a Shaped Charge Jet. (After Johnson 1972)

9.3 Horizontal Striations in the Upper Conic Section of a Typical Shaped Charge Hole in Concrete.

9.4 Radial Pressure Explanation for the Formation of the Upper Conic Section of a Shaped Charge Jet Hole in Concrete.

9.5 Forces on a Particle on the Upper Conic Boundary of a Shaped Charge Jet Hole in Concrete.

9.6 Definition of Cracks Formed in Concrete Blocks by Shaped Charge Jet Impacts.

9.7 Definition of Cracks Formed in Concrete Slabs by Shaped Charge Jet Impacts.

9.8 Cracking of Slabs into Segments Under the Action of Shaped Charge Jet Impacts.

9.9 Forces Acting on a Segment of a Slab Under the Action of a Shaped Charge Impact.

LIST OF PLATES

3.1 Concrete Mixer

4.1 Concrete Saw

4.2 Bar and Stroud High Speed Rotating Mirror Camera (Interior View)

4.3 Bar and Stroud Camera Operating Units

5.1 Gould OS4000 Digital Storage Oscilloscope

5.2 Reynolds FS10 EBW Firing System

5.3 A 298g 56mm dia. Shaped Charge in Position on a Concrete Test Specimen

5.4 High Speed Camera Frame of a 43g Shaped Charge Jet in Air (Before Impact)

5.5 Two High Speed Camera Frames of a 43g Shaped Charge Jet Perforating a Jet Detector

5.6 Typical Stereo Camera Frame of Three 43g Shaped Charge Jet Impacts on a Concrete Slab

5.7 Cross Section of a Typical 43g Shaped Charge Jet Hole in a 65mm Thick Concrete Slab

5.8 Scanning Electron Microscope Frame of the Lower Spall Zone of a Shaped Charge Jet Hole in Barytes Aggregate Concrete

5.9 Wax Castings of 43g Shaped Charge Jet Holes in Clay Soil

5.10 Wax Castings of 43g Shaped Charge Jet Holes in Sand Soil

5.11 Coloured Sand Columns in Sand Soil After a 16g Charge Subsurface Explosion

5.12 Coloured Sand Columns in Clay Soil After a 16g Charge Subsurface Explosion

6.1 High Speed Camera Frame of a Shaped Charge Jet Penetrating Copper

6.2 Spalling and Concrete Movement During Shaped Charge Jet Penetration

6.3 Cross Sectional View of a 298g Shaped Charge Impact Hole in a 760mm Concrete Cube

6.4 Cross Sectional View of a 43g Shaped Charge Impact Hole in a 'Plasticine' Block

9.1 Scanning Electron Microscope Picture of a Suspected Aggregate/Cement Bond Failure

9.2 Scanning Electron Microscope Picture of a Crack in an Aggregate Particle

9.3 Scanning Electron Microscope Picture of a Structural Crack in Concrete

9.4 Scanning Electron Microscope Picture of a Concrete/Steel Reinforcement Interface

LIST OF SYMBOLS

A	Unused energy factor
A'	Area of hole produced
A_f	Final cross sectional area of hole
A_o	Area of projectile
A_r	Area of reinforcement
A_r'	Area of reinforcement/unit length
A_s	Area of slab
A_w	Wavelength
a	A constant
a_r	Radius of a rod
a_1 to a_7	Simultaneous equation factors
B	Explosive and soil behaviour factor
C	Deviation from spherical crater factor
C_d	Irrotational wave speed
C_o	Rod wave velocity
C_p	Rod wave velocity at constant strain
$\bar{C}_s$	Average heat capacity/unit volume
C_t	Wave propagation speed
C_u	Specific heat
c	Phase velocity
c_j	Specific heat of jet
c_s	Seismic velocity
c_t	Specific heat of target
c_1	Constant for explosion gaseous products
D	Hole or crater diameter
D_p	Prototype depth

d	Differentiation operator
d_b	Depth of burial of charge
d_f'	A penetration depth
d_f''	A penetration depth
d_j	Diameter of jet
d_m	Model depth
d_o	Diameter of projectile
d_s	Depth of slab
E	Culmulative kinetic energy of jet
E_d	Dynamic elastic modulus
E_x	Recoverable work done in a cycle
e_p	Plastic strain
F	Force
f	Frequency
f_1	A function
f_2	A function
G	Lamé constant
G_1	A constant
g	Gravity constant
g_e	Energy density of shock heating
H	Stored potential energy lost during unloading
h	Jet formation distance
h'	Jet length minus the jet formation distance
h_a	Work of compression
h_c	Work of compression at an impact explosion
h_m	Model standoff
h_t	Test specimen thickness
$\bar{I}$	Moment of inertia

I	Impulse
i	Unit impulse
$\bar{i}$	Scaled impulse
KE	Kinetic energy
k	A constantfor target and jet hardness
k_a	A constant
k_g	Gravity effect factor
L	Length
L_j	Length of jet
L_m	Linear dimension of model
L_p	Linear dimension of prototype
l_n	Logarithms to the base n
l_s	Length of slab
M	Mass
$\bar{M}$	Moment/unit length
M_o	Moment
m	Mass of jet liner Subscript denoting model
m_a	Mass
m_j	Mass of jet
m_s	Mass of slug
n	Dimensionless number
n_j	Heat of fusion of jet
n_o	Heat of fusion
n_t	Heat of fusion of target
P	Jet penetration distance
P'	Penetration distance
P_c	Critical level of shock heating
PE	Potential energy

P_r	Peak explosion pressure
p	Subscript denoting prototype
$\bar{p}_o$	A pressure
p_r	Pressure
p_u	Ultimate cavity pressure
$\bar{p}_u$	Ultimate cavity pressure for deep craters
R	Soil crater radius
R_p	Prototype radius
R_t	Total resistance
R_u	Ultimate cavity radius
R_x	Energy loss due to particle vibration and intergranular friction
r	Radius of the base of the impacted hole Crater radius
r_d	Distance
r_j	Radius of the jet nose
r_m	Model radius
S	Ultimate stress of the target
$\bar{S}$	Radiating shock loss pressure
S_i	Target stress
T	Time
$\bar{T}$	Kinetic energy of target
T_a	Energy required for impact explosion
$\bar{T}_a$	Average energy required for impact explosion
T_i	Explosive loading time
T_r	Explosion rise time
t	Time
U	Velocity of jet impact point
U_D	Detonation wave speed
U_o	Flow velocity at impact explosion

u	Displacement
u_c	Velocity at impact explosion
V	Shock velocity
$\bar{V}$	Shear/unit length
V_a	Crater volume of impact explosion
V_b	Crater or hole volume due to plastic deformation
V_c	Critical impact velocity for impact explosion
V_f	Ultimate crater volume
V_j	Velocity of jet
V_p	Volume of projectile
V_s	Velocity of slug
V_t	Crater or hole volume
V_u	Ultimate cavity volume
V_z	Shear force (In dimensional analysis)
V_σ	Impact velocity for plastic flow
V_o, V_1, V_2	Velocities
v	Displacement
v_t	Crater or hole volume
W	Explosive energy
W_{cm}	Charge mass
W_m	Weight of the model
W_p	Weight of the prototype
w	Displacement
w_a	Length
w_r	Unit resistance
x	A variable
x_a	Distance along the cone axis
x_c	Ratio of densities at the critical level of shock loading

x_d	Ratio of densities (ρ_j/ρ_t)
Y	Static yield strength of target
Z	Depth of burial
Z_c	Critical depth of burial for charge
z	Depth
z_d	Scaled distance
α	Initial angle of jet liner cone
$\bar{\alpha}$	Angle
α_i	A constant
α_1	Leading end of jet angle
β	Angle collapsing jet liner makes with its axis
β'	Angle of obliquity of jet impact
β_a	Compressibility of a material
β_c	A constant
β_o	Initial compressibility of a material
γ	A statistical term for factors influencing λ_F or ρ_j in calculations
Δ	An increment
Δ_d	Density ratio (ρ_j/ρ_t)
Δ_t	Depth ratio Z/Z_c
δ	Deflection
∂	Partial differential operator
ϵ	Strain
ϵ_c	Strain
ϵ_p	Strain associated with normal stress
θ	Temperature
θ_j	Jet temperature
θ_t	Target temperature

λ	Lamé Constant
λ_c	Normalised charge depth
λ_{cc}	Strain energy factor
λ_f	Fragmentation factor
λ_s	Scale factor
π	A constant
π_1 to π_{16}	Buckingham terms
ρ	Density
ρ_j	Density of jet
ρ_j'	Effective density of jet
ρ_p	Density of prototype explosive charge
ρ_m	Density of model explosive charge
ρ_t	Density of the target
ρ_u	Initial density of a material
ρ_1	Projectile density
ρ_2'	A target density
ρ_2''	A target density
σ	Stress
σ_j	Jet stress
σ_o	A stress level
σ_s	Soil stress factor
σ_t	Static yield strength of target
σ_u	Ultimate stress of the jet
τ	Shear stress
τ_c	Culmulative volume of a hole
ν	Poisson's ratio
ϕ	A function
$\bar{\phi}$	Average dynamic yield strength

ϕ_o	A constant
ϕ_v	Dynamic yield strength
ω	Particle velocity
∇	Laplace operator
∇_s	Standoff

GLOSSARY OF TERMS USED

Apparent crater	The visible cavity formed in soil when an explosive charge buried in the soil is detonated.
Aspect ratio	The ratio of the true crater depth to the surface crater radius.
Clay	The naturally occurring material used as the foundation for the test slabs in some experiments.
Concrete	The scaled material modelling the various concretes detailed in the Property Services Agency (1978) specification for airfield works.
Crater	The cavity formed by the action of a subsurface explosive charge.
Depth of burst	The depth from the concrete/air surface to the centre of a buried subsurface charge.
Edge block	The concrete block cast against the edge of a test slab, separated by a joint, to create the effect of an adjacent slab.
Ejecta	Material thrown out of a crater by the explosion.
Fallback	Loose material which falls back into a crater through not having sufficient velocity to be removed from the explosion area.
Firing system	The electrical equipment used to activate the initiator of the explosive charge.

Heave	The vertical displacement of any point of the target due to the action of a subsurface charge.
Hole	The term applied to a burrow formed by a shaped charge jet impact.
Initiator	The device used to activate the main explosive charge often incorrectly defined as a detonator.
Joint	The division between the sides of the slabs and the edge blocks. Normally filled with balsa wood 2mm thick to allow for expansion or contraction of the concrete.
Lean mix	The scaled material modelling lean concrete specified in the Property Services Agency (1978) specification for airfield works.
Maximum radius	The greatest radius of a crater or hole at any depth.
Minimum radius	The smallest radius of a crater or hole at any depth.
Pavement	The combination of concrete and lean mix slabs cast onto a soil foundation.
Pavement quality concrete	The concrete specified in the Property Services Agency (1978) specification for airfield works and modelled in these tests.
Reinforcement	The mild steel wire mesh modelling the steel mesh specified in the Property Services Agency (1978) specification for airfield works.
Sand	The Zone 2 sand used as the soil foundation for some test specimens.

Shaped charge	The RDX/TNT cylindrical explosive device containing a truncated cone liner of copper or aluminium. On initiation it produces a high speed jet of copper or aluminium which acts as a projectile and impacts the specimen.
Shaped Charge Holder	The perspex apparatus used in this study to hold a shaped change at its prescribed angle of incidence and standoff distance from the test specimen.
Slab	The concrete test specimen modelling a full scale concrete slab as specified in the Property Services Agency (1978) specification.
Soil	The sand or clay foundation to a concrete and lean mix pavement.
Subsurface charge	The explosive device buried in the soil at a prescribed distance below the overlying concrete pavement.
True crater	The apparent crater when all fallback has been removed to leave the extent of the crater visible.

CHAPTER 1

INTRODUCTION

In a civilian environment the prime aims when attacking concrete with explosives or projectiles are economic demolition and site clearance. The military requirements are for guaranteed demolition and maximum disruption in the area of the demolished facility. Military explosives were used in this study and may not necessarily be commercially available but there is no technical reason why the results obtained could not be put to use in either military or civilian operations.

In the past work done on the use of explosives to attack concrete has been limited particularly in the measurement, both dynamically and statically, of damage parameters. A major problem in this respect is that the rate of loading, which occurs when a structure is loaded by explosively generated blast pressure or impact loading by a very high velocity projectile, is sufficient to produce inertia forces of the same order as the loading forces. The pressure generated can be so high that the materials' strengths may be considered negligible by comparison. Both the target and the projectile in the case of high velocity impact loading may be considered to act as fluids, that is with extremely low shear strength. The rapid variation of applied force with time and the short overall duration of loading, characteristic of dynamic loading, also present difficulties in studying the response of concrete to explosive shock.

In this study two types of quite separate explosive charges were used against concrete ground slabs. The ground slab was usually first subjected to an impact from a jet of fluid metal generated by a shaped explosive charge. This charge, also known as the Munroe or Neumann Charge, has been used for many years. It was developed for drilling by mining engineers who found that an explosive charge placed on a rock surface was not very efficient at penetrating the surface. It was found that if a cone shaped indentation was made in the face of the charge adjacent to the rock surface, the blast was more concentrated. Futhermore, if the cone shaped indentation was lined by a thin layer of metal, such as copper or aluminium, then this liner would be inverted and formed into a thin needle of fluid metal. This needle would then be propelled at high velocity at the rock face behaving as a fluid because of the pressure, not the temperature. To increase the drilling action of the needle of metal, it was found that the charge needed to be positioned a short distance from the target, this distance being known as "standoff". The action of the shaped charge is therefore the impact of a very high velocity projectile which in this study was a jet of copper or aluminuim.

The second explosive charge used in this investigation was a mass of explosive, usually introduced into a previously formed hole made by a shaped charge. The action of the charge was to cause impulse loading from the resulting pressure of explosion gases as they formed a cavity in the material beneath the slab.

The aims of the project were to study the nature and extent of fracture zones and overall damage resulting from the action of the two charge types on concrete ground slabs and mass concrete blocks. The investigation was conducted using scale model concrete specimens with scaled explosive devices. Chapter 2 reviews work done in the past both on impact loading by shaped charges and impulse loading caused by buried explosives. Various theories and empirical rules for the effects of these explosive devices are reported with an assessment of their usefulness and the limitations of previous work. Information from the literature on stress waves caused by dynamic loading and a review of literature on modelling techniques, their validity and limitations are also given.

In chapter 3 the selection of materials for use in this study is described. Instrumentation and measurement techniques developed for use are detailed in chapter 4 along with the method of construction of test specimens. The experimental procedures and damage investigation methods employed are described in chapter 5.

Chapters 6 and 7 are respectively the results of the shaped charge jet impact tests and the subsurface impulse tests on the concrete ground slabs. Calculations to test the validity of theories reported in chapter 2 and based on the results of this study are given in chapter 8. Chapter 9 presents the conclusions drawn from the test programme.

CHAPTER 2

LITERATURE SURVEY OF EXPLOSIVES AND THEIR USE AGAINST CONCRETE AND SOIL

A survey was made of general and military literature relating to six broad subject areas; principles of shaped charges, projectile penetration, fracture mechanics, soil cratering theories, stress waves and modelling techniques for explosion testing. Only those theories of soil cratering where the soil has an overlying crust such as a pavement should be considered because of the influence of the pavement. However, information was found to be scant particularly on scaling of explosives, so the various empirical scaling rules for buried explosive charges in soils are given. It is also convenient to explain the principles of shaped charges before considering the theories of shaped charge jet penetration.

2.1 PRINCIPLES OF SHAPED CHARGES

Figure 2.1 shows a cross sectional view through a shaped charge. All main details are given and are drawn to scale in order to show their relative sizes. A simplified cross section for the purpose of explaining salient features and the modification made to the metal cone liner by the advancing detonation wave is given in figure 2.2. The initial cone angle α is modified to angle β by the detonation wave, where $\beta > \alpha$. For well designed charges the jet produced can have a velocity of up to 9000 m/s.

The mechanism of liner collapse and jet formation has been determined from high speed radiographs and has been analysed by the method of Birkhoff et al (1948). Figure 2.3 shows the progression from predetonation state to final jet formation of a shaped charge device.

The pressure transmitted to the liner by the explosive is very large by comparison with the liner material's yield strength and hence it can be assumed that the yield strength is negligible. This allows the system to be analysed hydrodynamically assuming the liner metal flow to be similar to non-viscous fluid flow. Nevertheless, the metal is not necessarily in a molten state even when flowing. A further assumption is that the pressure acting on the liner does not influence the length of the liner. Johnson (1972) has outlined the mechanism of particle movements and can be summarised as follows.

In figure 2.4a when the detonation wave reaches P the portion of liner AP has moved to A'P, where A'P = AP. All particles of AP are considered to move with velocity V_o after the passage of the detonation wave. Now if the direction of a particle at P is PN, parallel to A'A, then angle BPN = angle PAA' and angle NPA' = angle PA'A. AP = A'P thus angle PA'A = angle PAA' and angle BPN = angle NPA'. Hence P moves along the bisector of angle BPA' with speed V_o together with any other particle in PM. If in figure 2.4a the current collision point M moves to the right with a speed of V_1, then the velocity diagram of figure 2.4b can be constructed showing V_o and V_2. In figure 2.4b the moving collision point M has been brought to rest by imposing a velocity of V_1 to the left. All particles in PM, previously of velocity V_o, then have a velocity of V_2 along the line PM. Thus at the stationary collision point, two streams of material, one from each side of the liner, collide and form a slug and a jet. Application of the sine rule to the velocity triangle of figure 2.4b gives

$$\frac{V_o}{\sin\beta} = \frac{V_1}{\sin(\frac{\pi}{2} - \frac{(\beta-\alpha)}{2})} = \frac{V_2}{\sin(\frac{\pi}{2} - \frac{(\beta+\alpha)}{2})} \qquad \ldots \ 2.1$$

$$\text{similarly } V_1 = V_o \left(\frac{\cos\frac{(\beta-\alpha)}{2}}{\sin\beta}\right) \qquad \text{... 2.2a}$$

$$V_2 = V_o \left(\frac{\cos\frac{(\beta+\alpha)}{2}}{\sin\beta}\right) \qquad \text{... 2.2b}$$

The speeds of the particles remain unchanged from their pre-collision values in the stationary system. In figure 2.5 both jet and slug speeds are V_2.

In the actual system the speeds of the slug and the jet are $(V_1 - V_2)$ and $(V_1 + V_2)$ rspectively. If the mass of liner material is taken as m per unit length and m_s and m_j are respectively the portions of m going to the slug and jet, then by the linear momentum principle

$$m\, V_2 \cos\beta = m_s\, V_2 - m_j\, V_2 \qquad \text{... 2.3}$$

$$\text{since} \quad m = m_s + m_j \qquad \text{... 2.4}$$

$$\text{then} \quad m_j = \tfrac{1}{2}m\,(1 - \cos\beta) \qquad \text{... 2.5a}$$

$$\text{and} \quad m_s = \tfrac{1}{2}m\,(1 + \cos\beta) \qquad \text{... 2.5b}$$

$$\text{Therefore} \quad \frac{m_j}{m_s} = \frac{1 - \cos\beta}{1 + \cos\beta} = (\tan\frac{\beta}{2})^2 \qquad \text{... 2.6}$$

In figure 2.4a if the detonation wave advances from P to Q (length PB) while a particle moves from P to N,

$$\text{and if} \quad \frac{w_a}{\sin\left(\frac{\pi}{2} - \frac{(\beta-\alpha)}{2}\right)} = \frac{V_o}{\sin(\beta-\alpha)} \qquad \text{... 2.7}$$

$$\text{then} \quad U_D = w_a \cos\alpha = V_o \frac{\cos\left(\frac{\beta-\alpha}{2}\right)}{\sin(\beta-\alpha)} \cos\alpha = \frac{V_o \cos\alpha}{2\sin\frac{(\beta-\alpha)}{2}} \qquad \text{... 2.8}$$

where U_D is the wave speed.

Using equations 2.2 and 2.8

$$V_j = 2U_D \frac{\sin\frac{(\beta-\alpha)}{2}\cos\frac{\alpha}{2}}{\sin\frac{\beta}{2}\cos\alpha} \qquad \ldots 2.9$$

and $$V_s = 2U_D \frac{\sin\frac{(\beta-\alpha)}{2}\sin\frac{\alpha}{2}}{\cos\alpha\ .\ \cos\beta/2} \qquad \ldots 2.10$$

A limiting case of equation 2.9 is that when α tends to zero, the velocity of the jet V_j tends to $2U_D$, hence the jet velocity cannot be greater than twice the forward detonation velocity of the charge.

2.2 SHAPED CHARGE JET PENETRATION THEORIES

In a review of hypervelocity impact theories, into the range of which the velocity of shaped charge jets falls, Roney (1961) found that most theories had a common limitation. This was that each theory was only valid for a single material target, more especially, a metal. Even then, any one theory could not account for every impact velocity. Work done by the Canadian Armament Research and Development Establishment (1961) into impacts on non-homogeneous plastics has revealed different types of damage suggesting a different fracture mechanism for brittle materials.

Several theories have been found which appear to be of use in this study. All have limitations, especially where boundary conditions influence steady state penetration. Of these theories the one which has found most support in the past and on which other theories partially depend, is the hydrodynamic theory. This theory treats both target and impactor as incompressible fluids and assumes that the pressures generated by the impact are so great that materials' strengths can be considered negligible. Before considering this theory in detail it is convenient to review the work of Johnson (1972), Johnson et al (1968) and Feldman (1958).

2.2.1 Penetration of a Semi Infinite Medium by a Shaped Charge Jet

Johnson (1972) has shown that the length, L_j, of a jet which would be produced by a charge shown in figure 2.6 would be given by

$$L_j = h\left(1 + \tan\alpha \tan \frac{(\alpha+\beta)}{2}\right) \qquad \ldots 2.11$$

where h is the jet formation distance and α and β are the angles shown in figure 2.6.

If in figure 2.6 the standoff ∇_s is less than h',where h' is the jet length L_j minus the jet formation distance h, then maximum penetration would not be expected to occur. Maximum penetration should occur when $\nabla_s = h'$ or $h \tan\alpha \cdot \tan \frac{(\beta+\alpha)}{2}$ the least value of which is $h \tan^2\alpha$ since $\beta > \alpha$.

Johnson (1972) also gives an expression relating penetration P, target and projectile densities, ρ_t and ρ_j respectively, projectile length, L_j and projectile speed, V_j from the hydrodynamic model. Figure 2.7 shows an idealised penetration mechanism in which the jet tip is brought to rest by the application of a velocity U equal and opposite to the penetration velocity of the jet.

Following hydrodynamic theory assumptions that the jet and target behave as fluids under the pressures generated, then the pressure p_r, on both sides of the stationary interface must be equal (Bernoulli's Theorem).

$$\text{Hence } p_r = \tfrac{1}{2} \rho_j (V_j - U)^2 = \tfrac{1}{2} \rho_t U^2 \qquad \ldots 2.12$$

where V_j is the velocity of the jet and ρ_j and ρ_t are the jet and target densities respectively.

Assuming instantaneous arrival at steady state and cessation of penetration with the arrival of the end of the jet on the target then total penetration P is:

$$P = U \times \text{penetration time}$$

$$\text{Penetration time} = \frac{L_j}{(V_j - U)}$$

$$\text{thus } P = U . \frac{L_j}{(V_j - U)} \qquad \ldots 2.13$$

$$\text{or using 2.12 } \frac{P}{L_j} = \sqrt{\frac{\rho_j}{\rho_t}} \qquad \ldots 2.14$$

The derivation assumes steady state conditions deep in a target, but since constraints to flow near surfaces are reduced, the prediction of equation 2.14 would give an underestimation.

Figures 2.8 and 2.9 show the influence of standoff variation, ∇_s, which is more complicated than the foregoing simplified penetration treatment. Figure 2.8 is the idealised standoff effect on penetration, while figure 2.9 gives an example of jet penetration.

With conical lined charges the metal of the liner moves more slowly the further its location is from the central axis of the charge. This causes a lengthening of the jet and if the speed is sufficiently high a deeper but smaller diameter cavity may be formed. If speed is low, penetration may decrease.

An extra term, k, may be added to equation 2.12 to allow for the target and projectile hardness under low speed impact.

$$\tfrac{1}{2} \rho_j (V_j - U)^2 = \tfrac{1}{2} \rho_t U^2 + k \qquad \ldots 2.15$$

Similarly equation 2.12 can be modified to account for non coherent jets by the addition of a factor, λ_F, where $\lambda_F = 1$ for a continuous jet (copper, aluminium) or 2 for a fragmented jet (glass).

$$\text{Thus } \tfrac{1}{2} \lambda_F \rho_j (V_j - U)^2 = \tfrac{1}{2} \rho_t U^2 \qquad \ldots 2.16$$

Jets which possess speeds greater than the elastic wave speeds in the materials used are said to possess hypervelocity. Johnson (1972) has described the sequence of events leading up to the formation of a crater from a hypervelocity impact as consisting of three stages.

1. On impact, shock waves propagate in both target and projectile. Pressures generated far exceed material strengths.
2. Target material may be ejected as an annular spray with particle speeds in excess of the impact speed due to the relief wave following the initial compression wave.
3. Mushrooming of the projectile on impact continues during penetration leading to a fluid jet forcing itself into the target. Target material is forced radially away from the impact zone. This expanding crater follows the shock wave which is attennuated and overtaken by the unloading waves from the free surface.

In each of the following analyses, taken from Johnson et al (1968),it is assumed that there are no secondary explosions when the kinetic energy of the projectile is dissipated as heat or vaporisation. Similarly projectiles are considered to possess uniform velocity along their lengths.

If, from equation 2.16, λ_F is assumed to lie between 1 and 2, then a quantity ρ_j' can be introduced. ρ_j' is known as the effective density and is given by

$$\rho_j' = \lambda_F \rho_j \qquad \ldots\ 2.17$$

where ρ_j is the true density of the material of the jet.
Thus if penetration stops when the last part of the jet reaches the target, from 2.14, maximum penetration P' is given by

$$P' = L_j \left(\frac{\rho_j'}{\rho_t}\right)^{\frac{1}{2}} \qquad \ldots\ 2.18$$

In a soft material, residual flow of material may occur due to, in practice, slower moving after parts of the projectile causing further penetration. A factor $[1 - \alpha_1 (\frac{Y}{\rho_j V^2})]$ can be introduced to allow for the finite strength of the target. Y is the yield strength of the target, α_1 is a constant. Residual flow can be accommodated by the inclusion of a second term, r, where r is the radius of the bottom of the crater and assumes that residual penetration is equivalent to the distance which material flowed laterally away from the jet.

Thus penetration P becomes

$$P = P' (1 - \alpha_1 (\frac{Y}{\rho_j V^2})) + r \qquad \ldots 2.19$$

Further modifications can be made by substituting σ_t in equation 2.16 for $\lambda_F \rho_j$ and adding $\gamma \rho_\ell$ where γ is a statistical term to allow for all factors affecting λ_F or ρ_j and ρ_ℓ is the density of projectile particles.

$$\text{Then} \quad \tfrac{1}{2} \gamma \rho_\ell (V_j - U)^2 = \tfrac{1}{2} \rho U^2 + \sigma \qquad \ldots 2.20$$

where σ is the difference between the target yield strength σ_t and the projectile yield strength σ_j.

If a term, k, is added to allow for target strength such that

$$\tfrac{1}{2} \rho_j (V_j - U)^2 = \tfrac{1}{2} \rho U^2 + k \qquad \ldots 2.21$$

k is then defined by the pressure produced by the projectile when the penetration velocity U is 0.

$$\text{That is} \quad k = \tfrac{1}{2} \rho_j V_j^2 \qquad \ldots 2.22$$

Assuming that momentum transferred to the target by the projectile results effectively only in lateral flow of the target then the cross sectional area A' of the hole produced by a projectile of area A_o is given by:

$$A' = \frac{A_o}{\sigma_t} \cdot \tfrac{1}{2} \rho_j (V_j - U)^2 \qquad \ldots 2.23$$

Hence from the penetration P' and area A' the crater volume V_t is given by

$$V_t = P'A' \qquad \ldots 2.24$$

For a single projectile, mass m_j, ($\lambda = 1$) of similar material to the target, the crater volume V_t is

$$V_t = \frac{V_p \rho V_j^2}{8 \sigma_t} = \frac{m_j V_j^2}{8\sigma_t} \qquad \ldots 2.25$$

The ratio of the diameter of the crater D to the projectile diameter d_j is thus

$$D/d_j = V_j \left(\frac{\rho_t}{8\sigma_t}\right)^{1/2} = 0.35\, V_j \sqrt{\frac{\rho_t}{\sigma_t}} \qquad \ldots 2.26$$

A similar result occurs if the kinetic energy of the projectile, $\tfrac{1}{2} \left(\frac{\pi d^2 j}{4}\right) \ell \rho_j V_j^2$, is equated to the plastic work done in expanding a cylindrical cavity in a semi-infinite medium, $\left(\frac{\pi D^2}{4}\right). 4\sigma_t$, where the pressure to achieve the latter is $4\sigma_t$.

2.2.2 The Volume-Energy Theory of Shaped Charge Jet Penetration

Feldman (1958) proposed a volume-energy relation which depended on the assumptions that materials may be regarded as fluids during impact and that material from the impactor and the target flows radially. The following equations were proposed by Feldman (1958) following experiments on layered metal targets. The assumption required by the theory was that the material of the target and jet flows radially from the axis of the jet and in planes perpendicular to the axis of the jet. This is not quite true on the target surface where material forms a conical shaped crater surface.

Now if r = crater radius

τ_c = culmulative volume of hole

P = penetration depth

E = culumulative kinetic energy of jet

then from the second assumption

$$\pi r^2 = \frac{d\tau_c}{dp} = \frac{d\tau_c}{dE} \cdot \frac{dE}{dv} \cdot \frac{dv}{dp} \qquad \ldots 2.27$$

and crater efficiency $\frac{d\tau_c}{dE}$ is given by

$$\frac{d\tau_c}{dE} = \frac{\frac{d\tau_c}{dp}}{\frac{dE}{dv} \cdot \frac{dv}{dp}} \qquad \ldots 2.28$$

where $\frac{d\tau_c}{dp}$ is the cross sectional area of the crater.

Now the first assumption takes the form

$$V_j = \left(\frac{1 + \rho}{\rho}\right) \frac{d\rho}{dr} \qquad \ldots 2.29$$

$\rho = \left(\frac{\rho_j}{\rho_t}\right)^2$ and ρ_t and ρ_j are the target and jet densities respectively.

V_j is jet velocity

T = time

$$\text{Therefore} \quad \frac{dV_j}{dp} = \left(\frac{1 + \rho}{\rho}\right) \cdot \frac{\frac{d^2 \rho}{dt^2}}{\frac{d\rho}{dV_j}} \qquad \ldots 2.30$$

which is the rate of change of jet velocity with respect to the penetration depth.

Finally dE/dv which known as the 'energy-density' function of the jet is calculated by the hydrodynamic theory of shaped charge jet liner collapse. The calculation requires the solution of one of two first order differential equations numerically.

These equations are:

$$\frac{dV_o}{dx_a} = f_1 (V_o, V_j, x_a) \qquad \ldots 2.31$$

and
$$\frac{dV_o}{dx_a} = f_2 (V_o, \beta, x_a) \qquad \ldots 2.32$$

where f_1 and f_2 are functions

V_o is the collapse velocity of the shaped charge liner

x_a is the distance measured along the axis of the cone

β is the angle with which the collapse liner makes with the axis of the liner as it touches the axis

V_j is the jet velocity

The solution of equations 2.31 and 2.32 is not possible with current knowledge. Numerical values for some of the terms in the preceding mathematical explanation are unavailable and much work remains to be done before the volume-energy theory can be put to practical use.

2.2.3 The Hydrodynamic Theory of Shaped Charge Jet Penetration

The hydrodynamic theory of penetration has been described in the literature by Birkhoff et al (1948), Pugh et al (1952) and Eichelberger (1956). Cook (1958) has extended this theory to account for hole volumes in jet and single particle penetration in the region of plastic deformation impacts. At supersonic penetration appreciable target vaporisation caused by impact explosion can be expected. However the velocity to cause this is much greater than the velocity to cause plastic flow. Shaped charges fall into the lower velocity range.

Cook (1958) has shown that by taking the Bernoulli equation 2.12 and including a function $\phi(u, \sigma)$ describing dissipative pressures this gives

$$\tfrac{1}{2}\ \rho_j\ (V_j - U)^2 = \tfrac{1}{2}\ \rho_t\ U^2 + \phi(U, \sigma) \qquad \text{... 2.33}$$

From $P = \dfrac{UL_j}{(V_j - U)}$ and equation 2.33

For $\rho_j \neq \rho_t$

$$U = V_j\ (1 - (\Delta_d + 2\phi\ /\rho_1 V_j^2\ (1 - \Delta_d))^{\frac{1}{2}}/1 - \Delta_d) \qquad \text{... 2.34}$$

where $\Delta_d = \rho_t/\rho_j$ For $\rho_j = \rho_t$

$$U = V_j\ (1 - 2\phi/\rho_j\ V_j^2)/2 \qquad \text{... 2.35}$$

Penetration, P, for $\rho_j \neq \rho_t$ is

$$P = \frac{L_j(1 - (\Delta_d + 2\phi/\rho_j\ V^2\ (1 - \Delta_d))^{\frac{1}{2}})}{(\Delta_d + 2\phi(\rho_j\ V_j^2\ (1 - \Delta_d))^{\frac{1}{2}} - \Delta_d} \qquad \text{... 2.36}$$

or for $\rho_j = \rho_t$

$$P = L_j(1 - 2\phi\ \rho_j\ V^2)/(1 + 2\phi/\rho_j\ V_j^2) \qquad \text{... 2.37}$$

Cook (1959) found that the target may still be subjected to residual dynamic pressure even after the end of the penetration. So long as the flow pressure in the target exceeded the dynamic yield strength of the target, plastic deformation could continue. Only when the velocity of the jet impact point, U, became zero would flow cease.

When considering an infinitely small depth of penetration δP compared to penetration P and since $\dot{U}$ would be greatest at the beginning of residual flow this increment of penetration would give rise to a cylindrical crater expansion. Then the final cylindrical hole, cross sectional area A_f, would be given by

$$dP.\ A_o.\ (\rho_t\ U_o^2\ /2) = dP \int_{A_o}^{A_f} \phi(U, \sigma)\ dA \qquad \text{... 2.38}$$

from conservation of energy,

where U_o is the flow velocity in primary penetration

and A_o is the cross sectional area of the projectile.

For large values of P/A_o then

$$V_f = \int_o^P \int_{A_o}^{A_f} \Phi(U, \sigma)\ dA\ dP/(\rho_t U_o^2/2) \qquad \ldots\ 2.39$$

where V_f is the ultimate crater volume.

Equation 2.38 can be expressed in integral form as $A_o \bar{p}_o = \bar{\Phi} A_f$ where

$\bar{p}_o = \rho_t U_o^2/2$ and $\bar{\Phi}$ is the average dynamic yield

Similarly $V_o \bar{p}_o = \bar{\Phi} \cdot V_f$ ... 2.40

where V_o is the primary hole volume at pressure $\bar{p}_o$

and V_f is the final residual flow volume.

Equation 2.40 may be rewritten since $\bar{\Phi}$ does not depend on the direction of residual flow as

$$V_f = \bar{T}/4\bar{\Phi} \qquad \ldots\ 2.41$$

where $\bar{T} = LA_o\rho_j V_j^2/2$ and is the kinetic energy of the target. Φ and $\bar{\Phi}$ remain to be established.

In previous studies, except that by Eichelberger (1955), ϕ has been treated as negligible in equations 2.33, 2.34 and 2.36. Assuming that ϕ may be neglected in primary penetration, in equation 2.41 Φ is the static strength σ. This is known as the idealised theory and the equations simplify to:

$$\rho_j (V_j - U)^2 = \rho_t U^2 \qquad \ldots\ 2.42$$

$$U = V_j/(1 + \Delta_d^{1/2}) \qquad \ldots\ 2.43$$

$$P = L \Delta_d^{-\frac{1}{2}} \qquad \ldots 2.44$$

$$V_f = \bar{T}/4\sigma \qquad \ldots 2.45$$

where $\Delta_d = \rho_j/\rho_t$.

The idealised theory is limited in application and is expected to break down in the impact explosion region.

Equation 2.45 may be further evaluated by comparing crater diameter with the corresponding elements of jet in different targets. Rewriting equation 2.38 for two materials with, respectively, final hole diameters d_f' and d_f'', densities ρ_2' and ρ_2'' and yield stresses σ' and σ''

$$\text{then} \quad \frac{d_f'}{d_f''} = \frac{(\rho_j^{\frac{1}{2}} + \rho_2''^{\frac{1}{2}})}{(\rho_j^{\frac{1}{2}} + \rho_2'^{\frac{1}{2}})} \cdot \left(\frac{\sigma''}{\sigma'}\right)^{\frac{1}{2}} \qquad \ldots 2.46$$

In the case of $\rho_j = \rho_2$ equation 2.46 reduces to

$$\frac{d_f}{d_o} = V_j\ (\rho_j/8\sigma)^{\frac{1}{2}} \qquad \ldots 2.47$$

where d_f is the hole diameter, d_o is the diameter of the projectile, and σ is the yield stress of the material of the target. In practice it is difficult to give a value to both the jet and hole diameter because of wide variations in the diameters.

Besides the idealised theory, there is the non-idealised theory which assumes the possibility of obtaining (U, Φ) and $\bar{\Phi}$. Assuming that compressibility β_a is defined as

$$\beta_a = -\,d\ \ln V/dp_r \qquad \ldots 2.48$$

then from Cook(1959) $d\beta_a = -\ a\ \beta_a^{\,2}\, dp_r$ $\qquad \ldots 2.49$

where a is a constant.

Hence $\beta_a = \beta_o \sum_{i=0}^{\infty} (-\ a\ \beta_o\ p_r)^i = \beta_o/(1 + a\ \beta_o\ p_r)$ $\qquad \ldots 2.50$

or $p_r = (\beta_o/\beta - 1)/a\,\beta_o$ ... 2.51

and $\beta/\beta_o = (\rho_o/\rho)^a$ ... 2.52

where $a = 2.33 - 0.67/\,\phi_o$ in which ϕ_o is a constant.

The contribution of the work of compression to the dynamic yield strength ϕ_y is:

$$h_a = -\int_0^x V^{-1}\, p_r dV$$

$$= (a\beta_o)^{-1}\,(x^a/a - \ln x_d - a^{-1}) \qquad \text{... 2.53}$$

where $x_d = \rho/\rho_o$ and

h_a is the contribution to ϕ from the compression of the target subjected to pressure p_r and compression ratio ρ_o/ρ.

Cooke (1959) has shown that the resultant temperature rise ΔT by shock heating may be expressed as

$$\Delta T\,/(1 - \rho_o/\rho)^3 = k_a \text{ (approximately)} \qquad \text{... 2.54}$$

k_a is a constant.

The contribution g_e, to ϕ_y from shock heating is given, approximately by

$$g_e = \bar{C}_s \cdot \Delta T$$

$$= \bar{C}_s \cdot k_a\,(x_d - 1)^3/x_d^3 \qquad \text{... 2.55}$$

where $\bar{C}_s$ is the average heat capacity per unit volume and g_e is known as the energy density of shock heating.

The dynamic yield strength ϕ_y is given by

$$\phi_y = h_a + g_e + \sigma \qquad \text{... 2.56}$$

which substituting for h_a, g_e and σ gives

$$\phi_y = (a\beta_o)^{-1}(x_d^a/a - \ln x_d - a^{-1}) + \bar{C}_s k_a(x_d - 1)^3/x_d^3 + \sigma$$

... 2.57

Equation 2.33 and ϕ_y (u, σ) defined by equation 2.57 present the proper form of Bernoulli's equation, when dissipative energies are involved.

Shocks may propagate in a target following impact at sufficient magnitudes to cause the target to explode. Assuming that when the pressure in the shock wave reaches a critical value the target vaporises and explodes then this pressure, P_r can be computed by $P_r = \rho_1 VW$ where ρ_1 is density, V is shock velocity, W is particle velocity. The problem is, however, to physically define V and W during target penetration.

The critical level, P_c, of initial heating by shock and the work of compression is given by

$$P_c = \epsilon_c \rho/M \qquad \text{... 2.58}$$

where ϵ_c = strain, and M = mass,

which neglecting g_e and σ gives

$$P_c = (a\beta_o)^{-1}(x_c^a/a - \ln x_c - a^{-1}) + \bar{C}_s k(x_c - 1)^3/x_c^3 \qquad \text{... 2.59}$$

At impact velocities above the critical level to cause impact explosion, the crater formed may be divided into two distinct sections, one formed by the impact explosion and one formed by plastic deformation.

In the impact explosion section, subscript a, the energy required T_a may be taken to be the energy produced by a high explosive detonated in the same volume as the crater, V_a.

Hence $$T_a = mV_j^2/2 - V_a P_c = V_a \rho_2 U_c^2/2 \qquad \text{... 2.60}$$

where $V_a P_c$ is the energy lost in varporising material and $V_a \rho_2 U_c^2 /_2$ is the energy available for the penetration in the plastic deformation region, subscript b.

The volume of the second part of the crater is thus given by equation 2.41, that is

$$V_b = \bar{T}_a/4\bar{\phi} \qquad \ldots 2.61$$

The volume of the first part of the crater from equation 2.60 is given by:

$$V_a = mv^2/2\ (h_c + \rho_2\ U_c^2\ /_2) = mv^2/2p_c \qquad \ldots 2.62$$

where m is the mass of the projectile and $mV_j^2/2$ is its initial kinetic energy.

Total crater volume $V_t = V_a + V_b$

hence $V_t = V_a(1 + \rho_2\ U_c^2/8\phi)$

$$\simeq V_a\ \rho_2\ U_c^2/8\bar{\phi} \qquad \ldots 2.63$$

Since $\rho_2 U_c^2 >> 8\bar{\phi}$ the impact explosion part of the crater is very small compared to the plastic deformation contribution.

Where the critical velocity exceeds the velocity of the particle but the particle velocity exceeds the velocity required for plastic flow (that is $V_c > V_j > V\sigma$) then

$$\bar{\phi} = h_a + g_e + \bar{S} + \sigma \qquad \ldots 2.64$$

where $\bar{S}$ is a pressure term for radiating shock losses

and h_a and g_e are given by equations 2.53 and 2.55 repectively

The hydrodynamic theory suffers from the same deficiency of practical information as the volume-energy relation. Insufficient data for some of the terms in the equations for shaped charge jet impact on ductile materials means that progress with the solution of impacts on brittle materials is more difficult.

Data obtained from this investigation has been used in some of the formulae from both the hydrodynamic theory and Johnson's (1972) work. These calculations are given in chapter 8 and the relevance of the various theories is discussed in chapter 9.

2.3 SHAPED CHARGE JET IMPACT ON CONCRETE

Reported work on shaped charge impact has mainly been concerned with metallic specimens though some reports have mentioned the use of such charges against brittle materials. The Ministry of Defence has used shaped charges of various sizes in the past against concrete, in particular to determine optimum penetration and efficient charge design.

Sparkes and Hayes (1946) have performed experiments to study shaped charge penetration into concrete. They were concerned with optimising penetration and thus they varied cone material and thickness, charge weight, charge dimensions, standoff and explosive filling. Experiments were scaled such that 5 ounces (142g) of explosive were used and verified with larger 100lbs (45.4kg) charges.

The results of this study gave penetration to be proportional to charge diameter. Optima were obtained for liner dimensions and angles, liner material and charge standoff. It was then found that, using an explosive of detonation velocity greater than 7000 m/s as a filling for an efficiently designed charge, the penetration was about six times the charge diameter.

This work was mainly concerned with developing the design of shaped charges to otpimise certain parameters. It did not attempt to explain the formation of the hole caused by the impact of the jet nor were any measurements made of target parameters such as strength.

Rees and Evans (1946) did endeavour to measure the dynamic response of the target. They performed experiments to compare both fragment and fluid jets against cement-mortar and steel. Cement-mortar specimens were 125mm diameter cylinders of various lengths. The compressive strength was 18 N/mm^2 and the flexural tensile strength 2.6 N/mm^2. It was found that the velocity of shock waves was 3400 m/s and when a shaped charge jet lost sufficient initial velocity then the shock wave preceded it. It was also found that the rate of penetration of jets into cement-mortar decreased linearly with distance penetrated due to the energy gradient from the tip to the base of the jet. No information was given on how the value of the shock wave velocity was found. This lack of information on instrumentation is a common feature of all reported work on the penetration of concrete by shaped charge jets.

Jonas (1954) reviewed shaped charge jet penetration of concrete and reached several conclusions which are also discussed in Chapter 9 along with conclusions drawn from this study. Jonas (1954) found that overall penetration by jets was greater in thinner targets because material spalled off the face of the target opposite from the face under impact. Massive targets in which the concrete was sufficiently thick for stresses to be attenuated to less than the tensile strength of the material were not so easily penetrated. Target material determined the penetration depth, which was fairly predictable for most metals, but not so for concrete where penetration did not seem to be a function of target strength. It was observed that the volume of the hole formed by the jet decreased as the concrete strength increased. It had also been found that, in spite of empirical formulae, target density in metals determined penetration depth but the inclusion of metal reinforcement in concrete did not deflect nor impair the jet, provided the volume of reinforcement was not too great. Generally in metals penetration was reported to be proportional to target density though some non-metallic materials have greater resistance to penetration. Concrete was thought to follow the trend of the non-metallic materials.

Cousins (1969) performed a series of experiments to demonstrate the shaped charge jet impact effect against a number of metallic targets and to test the validity of the hydrodynamic theory of penetration (cf.2.2.2). He concluded that, while the theory was useful for high velocity impact problems, brittle materials such as cast iron, concrete, methyl methacrylate (Perspex) and epoxy resin shattered too much and made the measurement of penetration impossible. He failed to appreciate that, with brittle materials, target size is important. Much of this study is concerned with the fractures caused by shaped charge jet impacts and the influence of target size is discussed in later chapters.

Briggs (1974) derived an empirical formula for the penetration depth of a shaped charge jet into concrete. This formula is only accurate to ± 20% but in dynamic testing this is not unacceptble. It is of the form

$$P = 0.177\ Wcm^{0.43} \qquad \ldots\ 2.65$$

where Wcm is the mass of explosive in kilogrammes when penetration depth, P, is measured in metres.

The formula was derived from the results of experiments carried out on blocks 610mm by 610mm by 50mm stacked thirty deep to produce a target 1500mm thick. The cube crushing strength of the concrete was 52.0 ± 3.4 N/mm^2 at 44 days and the charges varied in weight and standoff, both unspecified. Results from this investigation have proved Briggs' formula to be valid, though limited.

Joachim (1983) studied the use of shaped charges and linear charges for cutting concrete aircraft runway slabs at model scale. However the primary aim was to develop a simple full scale method of effectively and quickly cutting concrete slabs. Thus the work was primarily concerned with the development of a linear shaped charge. For the purposes of this study the main information of interest was the cross sectional diagrams of the holes produced by the charges in the concrete. Joachim also discovered that different scale charges did not quite produce exactly scaled damage parameters in the concrete. This was thought to be because not all the parameters of the charge were scaled in the same ratio. Penetration data varied up to 38% from the predicted value and the results were not verified at full scale in Joachim's work.

Davison (1983) studied the use of aluminium lined shaped charges used against steel and concrete. Flash radiography was used to study the shape of the jet produced by the charge. Cross sectional diagrams of crater shapes in the steel and concrete were produced and these are the main result of interest to this study.

2.4 BEARING CAPACITY OF CONCRETE BLOCKS

Chen and Drucker (1969) proposed that concrete blocks when carrying load over part of their surface, figure 2.10, could be analysed by limit theorems of perfect plasticity. However the tensile strength of concrete is assumed zero and load capability of the block is no greater than the unconfined compressive strength of the material under the loaded area. For this reason, some account must be taken of the tensile strength of the concrete in order to correlate experimental results with predictions.

For each loading type both an upper bound and a lower bound solution can be derived. For three dimensional square and circular punching loads the upper bound solution is found by equating the rate at which work is done by the force on the punch to the rate of internal dissipation of energy. Lower bounds are obtained for the value of the average indentation pressure over an octagonal area of contact.

Chen and Drucker (1969) concluded that concrete is a material of limited deformability in tension and is nearer to a frictional-brittle model than a perfectly plastic model. Nevertheless, there are theoretical and experimental indications that load bearing capacity can be calculated or at least bounded. A limitation on size exists in that when the ratio of unloaded to loaded area is greater than 25:1 crack propagation occurs in large blocks requiring an appropriate fracture mechanism. In this study such a loading state existed and is a function of the target size as stated earlier in section 2.3, in connection with the work of Cousins (1969).

2.5 EXPLOSIVE CRATERING IN SOIL

The second part of this study was concerned with the impulse loading caused by an explosive charge placed in a previously formed hole in a concrete ground slab. The result of such loading is to fracture the concrete slab and to crater the subsoil beneath the slab. Figure 2.11 shows the types of crater which can be formed by buried explosives and also explains some of the terminology used in cratering work. The depth of burial of the charge is the main variable causing the crater differences.

The influence of a ground slab is to affect the cratering as the shear strength of the slab is greater than the shear strength of an equal weight of soil surcharge. In this study scale model ground slabs were used and so scale model explosive charges were required. In the past much work has been done in trying to find empirical rules for predicting soil crater dimensions using dimensional analysis. Most common is the Lampson or Cube Root rule which is based purely on dimensional reasoning and uses the cube root of the ratio of charge masses as the scale factor. Other workers have examined the problem using theories of cavity expansion in soil.

2.5.1 The Scaling of Crater Dimensions

Chabai (1965) concluded that since there were no complete theories for cratering from buried explosives he would try to find a qualitative explanation for empirical scaling rules derived from dimensional analysis. Reference may be made to Chabai's work for the full mathematical treatment of scaling but of more practical importance are the conclusions Chabai made on the use of empirical scaling rules. These are:

1. If gravity effects are not significant then crater dimensions scale by $\sqrt[3]{\text{charge weight}}$.
2. If gravity effects are significant then the $\sqrt[3]{\text{mass gravity}}$ and $\sqrt[4]{\text{energy gravity}}$ rules are used.
3. Without gravity scaling, stress and velocity fields are invariant but with gravity included, only acceleration fields are invariant.
4. For mass or energy scaling without gravity effects velocities are invariant and times are scaled by $\sqrt[3]{\text{charge weight}}$.
5. When gravity is not significant only viscosities or dissipation variables need to be scaled by $\sqrt[3]{\text{charge weight}}$.

6. For energy scaling the explosive charge radius should be scaled by $\sqrt[4]{\text{energy}}$.

In experiments using the same explosives at both scales this rule is violated as the dimension scales as $\sqrt[3]{\text{energy}}$.

7. Moisture content and void ratio are never scaled, they remain constant.

8. Similarity can never be achieved as at least one variable cannot be scaled. Viscosity always violates the rules and this tends to result in larger craters than predicted for larger explosions.

9. Inability to scale shear strength, sonic velocity or atmospheric pressure has a similar effect as the medium's viscosity.

10. If $\sqrt[4]{\ }$ scaling is correct, and if similar experiments are to be conducted at differing scales, then the same explosive cannot be used.

The overall qualitative effect of all violations is to underestimate the crater dimensions for scaled up explosions. The reverse is also true. None of the scaling systems predict accurately large craters. Evaluation of the various rules places more credence on the $\sqrt[4]{\ }$ rule at explosive masses greater than the equivalent of 20000 kg TNT. Cratering with small charges does tend to make gravity significant, but this is inconclusive.

Saxe (1963) reported that any linear dimension, L, in an explosive test may be expressed as $LW^{-1/3}$ where W represents the energy of the charge expressed as an equivalent mass of TNT.

i.e. $L_p/L_m = (W_p/W_m)^{1/3}$ ... 2.66

where p denotes prototype

m denotes model

There exists however a definite charge size effect especially in extrapolations from small scale to very large scale events and in order to overcome the overestimate of crater size a value of 0.3 is thought to be more valid as the power of the charge weight ratio.

Lynch et al (1970) reported that simple scaling rules were insufficient to predict cratering because of gravitational effects on fallback material. Empirical relationships were proposed by Saxe and Del Manzo (1970) in terms of constant charge weight for underground explosions

$$\frac{R_p}{(R_p + d_m)^{\frac{1}{2}}} = \text{constant} \qquad \ldots\ 2.67$$

$$\frac{D_p}{(d_m + D_p)^{\frac{1}{2}}} = \text{constant} \qquad \ldots\ 2.68$$

and for air blasts

$$\frac{d_m}{(d_m + h_m)^{\frac{1}{2}}} = \text{constant} \qquad \ldots\ 2.69$$

where $\frac{d_m}{W^{1/3}}$ = scaled charge depth

$\frac{h_m}{W^{1/3}}$ = scaled standoff

$\frac{R_p}{W^{1/3}}$ = scaled crater radius

$\frac{D_p}{W^{1/3}}$ = scaled crater depth

Westine (1970) considered that only five parameters were required to define the radius of a crater formed by an explosive charge in a soil medium. These were explosive energy, W, depth of burial of the charge, d_b, the crater radius itself, R, a stress parameter for the soil, σ_s, and a factor with dimensions of force divided by length cubed to incorporate gravity effects into the analysis. By application of the Buckingham Pi theorem to these five variables, three non-dimensional variables resulted and are written in the form of equation 2.70 .

$$\frac{R}{d_b} = f\left(\frac{W^{1/3}}{\sigma_s^{1/3} . d_b}, \frac{W^{1/4}}{K^{1/4} . d_b}\right) \quad \ldots 2.70$$

Equation 2.70 defines a three dimensional space. The scaled crater radius defines geometric similarity and the non-dimensional factors are energy ratios.

$W^{1/3}$ and $W^{1/4}$ represent the magnitude of expolosive energy release,

$\sigma_s^{1/3} . d_b$ represents strain energy,

$K^{1/4} . d_b$ represents energy expended in overcoming gravity effects.

Chabai (1965) found that neither $W^{1/3}$ or $W^{1/4}$ were adequate in defining scaled crater radius. For small changes in explosive size $W^{1/3}$ was appropriate while for large variations $W^{1/4}$ was preferred. Statistical analysis on craters in desert alluvium showed that R/d closely equalled $W^{1/3.4}/d_b$.

Equation 2.70 can be thus rewritten as

$$\frac{R}{d_b} = f\left(\frac{W^{1/3}}{\sigma_s^{1/3} . d_b} \cdot \frac{W^{1/4}}{K^{1/4} . d_b}\right) = f\left(\frac{W^{7/12}}{\sigma_s^{1/3} . K^{1/4} . d_b^{1/2}}\right) \quad \ldots 2.71$$

If gravity and constitutive effects are included then

$$\frac{R}{d_b} = f\left(\frac{W^{7/24}}{\sigma_s^{1/6} . K^{1/8} . d}\right) \quad \ldots 2.72$$

where the exponent 7/24 closely resembles Chabai's statistical analysis factor of 1/3.4.

Neither gravitational effects nor constitutive effects can be ignored in considering soil excavation by explosives.

Substituting ρc^2 for σ_s and ρg for k in equation 2.72 where ρ is the soil density, c_s is the seismic velocity and g is the gravity constant

$$\frac{R}{d_b} = f\left(\frac{W^{7/24}}{\rho^{7/24} \cdot g^{1/8} \cdot c_s^{1/3} \cdot d_b}\right) \qquad \ldots\ 2.73$$

The independent parameter in equation 2.73 is insenstive to soil type. Soil density varies so little that it may be taken as constant and seismic velocity has little influence on crater radius.

The various scaling systems described all have limitations which need to be recognised. Provided that these limitations are minimised to suit the specific problem then a useful result can be obtained. In this study cube root scaling with the neglect of gravity and time effects was considered to be the best compromise. Further discussion on scaling will appear in Chapter 4 which is concerned with modelling and in the conclusions of Chapter 9.

2.5.2 Cratering by Explosives as a Cavity Expansion Effect

A second approach to the scaling of craters caused by buried explosives has been described by Vesic (1965). Vesic defined the various components of a crater formed by an explosive charge in soil, fig. 2.12 and considered the problem as one of steadily increasing internal pressure in the soil. Figs. 2.13a to d show the sequence of events occurring if an explosive charge were detonated deep in a soil mass. The detonation pressure would steadily increase the cavity size and at the ultimate cavity pressure there would be large plastic deformation. All explosives have detonation pressures in excess of the ultimate cavity pressure. The expansion of the cavity continually reduces the gas pressure inside until at the cavity's ultimate radius, R_u, at which the gas pressure equals the ultimate cavity pressure p_u, equilibrium exists.

Subsequent events would depend on the nature of the soil medium after dispersal of gaseous by-products of the explosion, for example, the cavity roof may fall in. Figs. 2.14a to 2.14d show a modified sequence of events when an explosive charge is detonated close to a free surface. In this case cavity expansion continues until the overburden is sheared away. The pressure p_r which causes this is usually greater than p_u and due to high kinetic energy and velocity of the gases, soil material is lifted from the crater. A limiting case of this occurs when the explosion is so shallow that a gas sphere has barely time to form. Scouring effects of the gas then predominate and compression of the underlying soil becomes barely significant.

The cratered medium is assumed to behave as a rigid-plastic solid near the cavity and as a linearly deformable isotropic solid further away.

The relationship between ultimate cavity radius R_u to the ultimate cavity pressure p_u can be developed from

$$p_u\ (V_u/W_{cm})^n = c_1 \qquad \ldots\ 2.74$$

where V_u is the ultimate cavity volume

W_{cm} is the explosive mass

n is a dimensionless number

c_1 is a constant for the explosive's gaseous products

For a point charge and spherical cavity equation 2.74 becomes

$$R_u = G_1(W_{cm}^{1/3}/p_u^{1/3n}) \qquad \ldots\ 2.75$$

G_1 is a constant

Ultimate cavity pressure p_u varies with the shear strength and rigidity index of the cratered medium. Equation 2.75 shows that craters scale according to $W^{1/3}$ where p_u is independent of depth. In a deep homogeneous medium p_u increases to $\bar{p}_u$, a finite value as a function of the depth z such that

$$p_u = \bar{p}_u + \beta_c z \qquad \ldots 2.76$$

β_c is a constant.

Asssuming for large explosive charges and deep depths of burial that $\bar{p}_u$ is small compared to $\beta_c z$, then from equation 2.76 and taking z to be proportional to $W^{1/m}$, the crater dimensions scale as

$$1/m = n/(3n + 1) \qquad \ldots 2.77$$

If $3n = 4$ $\quad m = 3.75$ for large yields

If $3n = 8$ $\quad m = 3.37$ $\quad$ n is a dimensionless number

Vesic's observations agreed with these predictions and the ultimate value of m appeared to be 3.4.

Vesic (1972) produced mathematical expressions for cylindrical and spherical cavity expansion together with numerical examples. These cavity expansion theories have been used to study the problem of cratering by explosives and the full mathematical treatment can be found in Vesic's work. They were not suitable for use in this study since numerical data was not complete.

2.5.3 Cratering of Soils by Buried Explosives as an Energy-Density Problem

Livingstone (1960) proposed a theory which attempted to correlate the behaviour of material subjected to an explosion, assuming that such behaviour is dependent on the 'energy density' within the material and that failure depends on the propagation rate of the disturbance caused.

The theory assumes that explosive energy is transferred directly to the cratered medium and the term 'energy density' is a term measuring the ratio of explosion energy to the volume of material which has received transferred energy at any instant. Energy density and loading rate are important but physical properties of the medium are assumed to be less important.

Idealised stress/strain diagrams, fig. 2.15,show the application of the theory to a material under different rates of loading. The areas R_x, represent energy lost to the medium by particle vibration and integranular friction, the latter being also on extension of relaxation processes such as creep and plastic flow. On unloading the strain recovers less rapidly than the stress removal. The areas H, represent stored potential energy lost as heat during unloading. The areas E, beneath the curves represent recoverable work done on the system on completion of the cycle. Elastic rebound or rock burst action following venting and the decrease of explosion cavity pressure determine the amount of energy recoverable.

Fig. 2.15 may also be used to show the effect of a charge in the type of material at a given loading rate. Fig. 2.15a may be applied to brittle materials and fig. 2.15b to slightly ductile materials.

Dynamic loading may be classified into three distinct types depending on the physical properties of the material and the scale of the experiment.

These are

(i) shock type

(ii) shear type

(iii) viscous damping type

Shock type behaviour is a characteristic of brittle solids and is the result of a reflected shock wave from a free surface. The material fails in tension and the failure planes are almost parallel to the free face. Failure begins at the free face and progresses in stages back to the explosion cavity.

Shear type failure is characteristic of plastic materials and is a result of explosion cavity expansion by compaction and plastic deformation resulting in material being displaced towards the free face. The size of the displacement is a function of the pressure and the direction of displacement is radially outwards from the explosion cavity. Shearing failure begins at the explosion cavity and progresses outwards if the material's shear strength is exceeded.

Viscous damping type failure is exhibited by porous and permeable solids and is due partly to the solid's elastic behaviour and partly to the air in the voids. Normally the shock wave rises rapidly to a peak value in a short time and the effect of the porous material is to alter the shape of the shock front in its early stages.

A strain energy equation can be written which describes the relationship amongst the three major variables when fracture begins and all the explosion energy is partitioned to the medium. A single factor λ_{cc} is chosen, termed the strain energy factor, to represent the effect of the explosive on the material. This strain energy equation is written as

$$Z_c = \lambda_{cc} W_{cm}^{1/3} \qquad \ldots 2.78$$

where Z_c is the critical depth of burial of the change, that is where the soil surface shows no tension type failure

W_{cm} is the explosive mass.

The general equation

$$Z = \Delta_r \lambda_{cc} W_{cm}^{1/3} \qquad \ldots 2.79$$

applies where the depth of burial Z is other than Z_c and

Δ_r is the depth ratio Z/Z_c

Equation 2.79 may be written as

$$Z = \Delta_r Z_c \qquad \text{... 2.80}$$

Crater volume, V, is a function of Z so that

$$V = f_1(\Delta_r, Z_c)^3 \qquad \text{... 2.81}$$

Δ_r is a direct measure of energy partitioned to the medium and is related to the medium's energy density.

Variables affecting energy density other than those related to Z_c are

(i) loss or incomplete use of available energy

(ii) variation in explosive or soil medium behaviour

(iii) deviation of the stressed volume from spherical.

The variables affecting energy density can be taken into account separately. Equation 2.81 then becomes

$$V = f_1 (A, B, C) (Z_c)^3 \qquad \text{... 2.82}$$

or $$V = ABC \lambda_{cc}^3 W_{cm} \qquad \text{... 2.83}$$

or $$\frac{V}{W_{cm}} = ABC \lambda_{cc}^3 \qquad \text{... 2.84}$$

where A is the factor for lost or unused available energy (dimensionless)

B is a factor for explosive and soil material behaviour relative to behaviour at optimum depth (dimensionless)

C is the factor for deviation from spherical of the stressed cavity (dimensionless).

V, W_{cm} and λ_{cc} can be measured so A, B and C remain to be isolated.

It is difficult to measure energy partition or to quantify it in absolute units. Energy is described relative to explosive mass and the effect of the explosive is described by the strain energy factor λ_{cc} which is $LM^{-1/3}$ dimensionally.

2.5.4 Summary of Soil Cratering by Explosives and Instrumentation Used by Previous Workers

In 1961 the U.S. Army Engineers produced a summary of previous work together with the following conclusions

a) Crater radius is best described by cube root scaling. Crater depth is best described by $W^{0.3}$ scale factor.

b) Scatter of results in soils: crater radius $\pm$ 20%

crater depth $\pm$ 30%

c) Maximum apparent crater occurs when $-1.0 > \lambda_c > -1.5$

Maximum true crater occurs when $\lambda_c = -2.0$

d) Camouflets are formed in cohesive soils when $\lambda_c > -3.5$

where λ_c = reduced charge depth.

Reduced charge depth = depth of charge burial divided by the cube root of the charge mass.

Townsend et al (1961) studied the mechanics of crater formation in sand and clay using a 'fastax' high speed camera and coloured columns of soil. Fig. 2.16 shows the mechanism for crater formation. This was the only reference found to dynamic instrumentation techniques used in soil cratering by explosives and corresponds to the similar situation found with shaped charge jet impacts on concrete.

2.6 CRATERING OF AIRFIELD PAVEMENTS

Bituminous pavements are outside the scope of this study which concentrates only on plain and reinforced concrete ground slabs.

There has been interest in cratering of pavements for some time and several workers have investigated the problem. However Kvammen (1973) reported that up to 1973 no model scale experiments had been performed.

Pichumani and Dick (1970) carried out some full scale tests on concrete specimens representing real situations and used explosive charges of 1.5 pounds (0.7kg) of an explosive known as C4. Tests were carried out on materials for crushing and tensile stregth, bearing capacity, density, moisture content and grading. Data was collected by high speed cine films and still photography,measurement and weighing of debris. No instrumentation was incorporated in the specimens but significant results from this programme were:

a) Crater volume was greater in clay than sand, and the crater shapes were hemispherical and cylindrical respectively.
b) For central explosive loading the radial cracking of slabs was greater on clay than sand.
c) For central explosive loading on clay, plugs of concrete were blown out.

(For central explosive loading on sand, no plugs were blown out but some spalling occurred.)

d) Soil moisture content was important,that is,higher moisture contents corresponded to more cracking in concrete.

McNeil (1974) reported experiments undertaken to try to determine whether scaling laws were applicable to craters in airfield pavements caused by buried explosive charges. Four charge sizes were used at four depths of burial, the scaling was by the Hopkinson cube root rule for charge weights. The charges were designed to be full, three quarters, half and quarter scale with respect to each other and were located in drilled boreholes under the concrete pavement. Determination of damage was by levelling of the craters, measurement of crater dimensions and the distance travelled by debris.

Two statistical analyses were performed on the test data, one a standard regression analysis and the second, an analysis based on extrapolation errors. The analyses gave similar results and indicated that scaling equations of acceptable accuracy could be derived.

Kvammen (1973) performed a series of experiments on full scale aircraft pavements in-situ. Charges were located at various depths below the pavement in holes formed by shaped charges exploded above the pavement and then augered out.

Measurements were made after each test but no instrumentation was used during the tests. The cube root scaling law was used to determine charge sizes and the results analysed by statistical methods.

Kvammen defined three types of crater produced by charges at different depths. Fig. 2.17 shows the craters. He also found that because the full scale pavements did not satisfy similitude requirements for the charge sizes, cube root scaling law did not predict all damage parameters accurately.

2.7 STRESS WAVES

In dynamic loading situations the specimen under load can be subjected to several types of stress waves. Inkester (1980) has summarised these various stress waves and the full proofs for the equations can be obtained from Goldsmith (1960), Johnson (1972), Kolsky (1953) and Redwood (1966).

Knowledge of stress waves and their interaction at boundaries is necessary for understanding fracture theories. The various stress waves are considered in the following sections and fracture theories are discussed in Chapter 9.

2.7.1 Elastic Waves in an Infinite Medium

Consideration of the equations of motion of a small element related to the stresses and stains in the body through Hooke's law, fig. 2.18,yields a general equation for the propagation of waves through a substance:

$$(G + \lambda) \frac{\partial \varepsilon}{\partial x} + G\nabla^2 U = \rho \frac{\partial^2 u}{\partial t^2} \qquad \text{... 2.85}$$

where G, λ are Lamé constants

∇^2 is the Laplace operator

ρ is the density of the material

u is displacement parallel to 0_x at time t

v is displacement parallel to 0_y at time t

w is displacement parallel to 0_z at time t

ε is strain

The solution of equation 2.85 indicates that there are two types of wave, equivoluminal waves and irrotational waves.

Equivoluminal waves are also known as transverse or shear waves and in abbreviated form 'S' waves. Particle movement is parallel to the wave front.

Deformation with no change in volume producing only distortion and rotation can be expressed by $\frac{\partial \varepsilon}{\partial x} = 0$.

Substitution in equation 2.85 gives

$$\frac{\partial^2 u}{\partial t^2} = \frac{G}{\rho} \cdot \nabla^2 u \qquad \text{... 2.86}$$

This represents an equivoluminal body wave with a speed of propagation of C_t where

$$C_t = \sqrt{\frac{G}{\rho}}$$

Irrotational waves are also known as dilatational or longitudinal waves and in abbreviated form, 'P' waves. Particle movement is perpendicular to the wave front and in the direction of propagation of the wave.

If straining is irrotational then the rotation terms in equation 2.85 go to zero. That is

$$\frac{\partial^2 u}{\partial t^2} = \left(\frac{\lambda + 2G}{\rho}\right) \nabla^2 U \qquad \ldots 2.87$$

Equation 2.87 describes an irrotational wave with a wave speed of C_d where $C_d = \sqrt{\left(\frac{\lambda + 2G}{\rho}\right)}$.

Superposition of irrotational and equivoluminal waves accounts for any disturbance in an isotropic elastic solid, that is

$$\frac{C_d}{C_t} = \sqrt{2 + \frac{\lambda}{G}} \quad \text{and } C_d > C_t$$

In addition, if an isotropic solid has a boundary then a third type of elastic wave may occur. These waves, known as Rayleigh waves, decrease in effect rapidly with depth and are sometimes known as surface waves. Their velocity of propagation is slightly less than the equivoluminal wave velocity C_t. High frequency Rayleigh waves are attenuated more rapidly with depth than low frequency waves.

Rayleigh waves travel with particle movement only in two dimensions, parallel to the wave front and vertically through the material, hence their intensity falls off more slowly than equivoluminal or irrotational waves and they tend to be more important in earthquake situations.

Rayleigh waves which have only particle movement parallel to the wave front and no vertical component of particle movement are known as Love waves. Such waves are accounted for by assuming the elasticity and density of the Earth's crust varies with depth. In this study Love waves are much less important than Rayleigh waves equivoluminal or irrotational waves.

2.7.2 Reflection and Refraction of Waves at Interfaces

The amplitude and direction of reflected and refracted waves at interfaces depend not only on the angle of incidence but also the boundary conditions at the interfaces. The two factors involved are the relative densities and the relative wave speeds in the two materials adjacent at an interface. In the case of a solid/air interface, the difference in properties is so great that air can be considered to be a vacuum. Thus transmission of waves is not considered, only reflection and refraction. Two types of wave can be produced on reflection at a solid/air interface. transverse and irrotational. The boundary condition is that stresses normal and parallel to a free air surface must be zero at that surface.

The boundary conditions at a solid/solid boundary require that displacements and stresses at the interface shall be continuous.

An obliquely incident irrotational wave at a solid/air interface produces two reflected waves, an irrotational wave and a transverse wave as shown in figure 2.19.

At a boundary the rate of travel along the boundary of a point of constant phase is known as the phase velocity, c in fig. 2.20. The phase velocity for both the irrotational and the transverse waves must be the same since one wave is generated from another. Hence for the irrotational wave

$$c = C_d/\sin\alpha$$ and for the transverse wave

$$c = C_t/\sin\beta$$

where C_d and C_t are the irrotational and transverse wave velocities respectively and α and β are the angles shown in figure 2.20.

$$\text{Therefore} \quad \frac{\sin\alpha}{C_d} = \frac{\sin\beta}{C_t} \qquad \ldots\ 2.88$$

A boundary between two isotropic solids will reflect and transmit an oblique incident irrotational wave as shown in fig. 2.21. Both irrotational and transverse waves are transmitted and reflected.

For transverse waves with particle motion perpendicular to an interface plane, that is vertically polarised, the result is similar to an irrotational wave incident on a solid/solid interface.

Transverse waves with particle motion parallel to the interface plane, that is horizontally polarised, reflect and transmit only transverse waves at a solid/solid interface as shown in figure 2.22. The relationship between the refracted transverse wave velocity C_{tB} and the reflected transverse wave velocity C_{tA} is given by:

$$\frac{\sin\alpha_1}{C_{tA}} = \frac{\sin\beta_3}{C_{tB}} \qquad \ldots\ 2.89$$

where α_1 and β_3 are the angles shown in figure 2.22. Reflection of a transverse wave at a solid/air interface conforms to the same relationship between angles and velocities for the reflected wave. There are no refracted waves.

2.7.3 Plastic Waves

Plastic waves occur when stresses produced by an impact exceed the elastic limit of the material. Experimental work on plastic waves in rods by Kolsky (1953) has contributed much to the theory of plastic wave propagation.

If a long bar is loaded to a stress σ_o instantaneously, then the strain associated with normal stress $\sigma_o = \varepsilon_p$. At any time t three areas of strain can be defined as shown in figure 2.23 where x is the distance along the bar from the point of impact.

a) $C_p t > x > 0$ Strain is constant at ε_p

b) $C_o t > x > C_p t$ Strain varies

c) $x > C_o t$ The bar is unstressed

where C_p is the rod wave speed at constant strain

C_o is the rod wave speed at non uniform elastic plastic strain

t is time

To propagate a force increment $d(A_o \sigma_o)$ at a stress level σ_o along an element of bar of length dx takes a time of dt

$$dt = \frac{dx}{C_p} \text{ or substituting } C_p$$

$$dt = dx/\sqrt{(d\sigma_o/d\varepsilon)/\rho_o} \qquad \text{... 2.90}$$

Applying the momentum equation to the element of the bar gives

$$(\rho_o A_o dx)dv = d(A_o \sigma_o)dt$$

where dv = increment in speed of the element due to excess force $d(A_o \sigma_o)$

Eliminating dt from the above equations yields

$$dv = \frac{d\sigma_o}{\rho_o \sqrt{\frac{d\sigma_o / d\varepsilon}{\rho_o}}} \qquad \text{... 2.91}$$

From which the total velocity V acquired by the element in attaining the stress level σ_o is given by:

$$V = \int_o^{e_p} \frac{d\sigma\, d\varepsilon}{\rho_o}, \; d\varepsilon \qquad \text{... 2.92}$$

where e_p is plastic strain.

At a critical velocity the maximum plastic strain corresponds to the ultimate strength of the rod. At this critical velocity the end of the bar moves as fast as the propagation of particle movement from the loaded end of the bar. The critical impact velocity for the bar is when the velocity of the loaded end causes fracture in the bar under tension.

Plastic waves behave in the same fashion as elastic waves at solid/solid and solid/air interfaces.

If an elastic wave meets a plastic wave, where the waves are travelling towards each other, the plastic wave may propagate further along the material or it may be arrested and the elastic wave only continues. This depends on the relative magnitude of the plastic wave to the elastic wave. In either case an elastic wave is always reflected backwards along the path of the incident elastic wave.

Where a plastic wave and an elastic wave are travelling in the same direction the elastic wave will overtake the plastic wave because attenuation of the plastic wave speed occurs rapidly after the initial propagation. Not only will the elastic wave overtake, but the plastic wave may degrade into an elastic wave and reinforce the elastic wave.

The instantaneous removal of an impact load which is producing a plastic wave will produce an elastic unloading wave. The elastic unloading wave travels faster than the plastic wave and so at some point it will catch the plastic wave front and be reflected. This reduces the amplitude of the plastic wave but not the velocity of the plastic wave front.

2.7.4 Waves in Elastic Rods

Rigorous solutions of the three dimensional wave equations for a finite elastic rod have not yet been obtained because it has not been possible to satisfy simultaneously the boundary conditions on the sides and ends of the bar. Normally for a long thin rod the problem is assumed to be two dimensional and various workers in the 19th century developed theories for the propagation of sinusoidal elastic waves in an infinite rod.However non-sinusoidal waves are dispersed because the components have different wavelengths and thus travel with different velocities.

Dispersion is therefore the change of shape of a wave. A frequency equation can be derived with multiple roots of the form:

$$\frac{c}{C_o} = f(\nu, \frac{a_r}{A_w}) \qquad \ldots\ 2.93$$

where ν = Poisson's ratio

A_w = wavelength

a_r = radius of the rod

C_o = rod velocity

c = phase velocity

Each root of the function in equation 2.93 corresponds to a particular mode of vibration and the function shows that a band of waves propagated along the rod is dispersed. Short wavelength waves travel more slowly than longer wavelength waves and thus the wave train is progressively stretched with time.

2.7.5 Attenuation of Waves

Attennuation is the change in amplitude of a wave. This change in amplitude occurs when a boundary intervenes and distributes the energy of a wave into several other waves or when wave energy is dissipated by internal friction or fracture. Goldsmith et al (1968) studied the attennuation characteristics of several concrete-like mixtures. The results showed that the higher the impact veloity the greater the attenuation because there is greater proportional loss of energy in fragmentation at the impact point. It was also found that damping in concrete decreased with age, reduced water content and increased compressive strength. Damping increased with maximum strain amplitude and frequency of vibration up to a limit of 2.5 Hz.

2.8 MODELLING TECHNIQUES FOR EXPLOSION TESTING

In studying the dynamic response of a structure to transient loading, the high energy involved can make full scale testing both expensive and impractical. Explosion and impact tests on scale models can be performed and full scale results predicted if the scaling rules are correctly deduced. The scaling of explosives has already been partly discussed. In this section the scaling of the model concrete and soil test specimens, the response of these to blast loading and further scaling of the shaped charge explosives are dicussed. Previous related work and problems associated with model testing are considered.

2.8.1 The Scaling of Shaped Charges

Baker et al (1973) investigated penetration by shaped charge jets using the Buckingham Pi theorem. This theorem states that any complete physical relationship can be expressed in terms of a set of independent dimensionless products composed of the relevant physical parameters. Dimensionless products, Pi terms, are products of variables.

Twenty such variables were identified by Baker et al (1973) as being significant in shaped charge jet penetration. These were reduced to sixteen Pi terms and eighteen scaling factors. Table 2.1 lists the twenty variables and their fundamental dimensions, table 2.2 lists the derived Pi terms and table 2.3 lists the scaling factors. The full mathematical derivation of these can be found in Baker et al (1973). All sixteen Pi terms in table 2.2, can be satisfied theoretically by a replica model, which is a physically smaller but geometrically similar model employing the same materials throughout as the prototype and at the same temperature.

With such a model,

length scales as λ_s

$$L_m = \lambda_s L_p \qquad \ldots\ 2.94$$

where L denotes length

m denotes model

p denotes prototype

λ_s denotes the scale factor

Velocity V scales as

$$V_m = V_p \qquad \ldots\ 2.95$$

but V = L/T where T is time

thus time scales as length

$$T_m = \lambda_s T_p \qquad \ldots\ 2.96$$

2.8.2 Scaling Explosive Blast Effects on Concrete Models

Dobbs and Cohen (1970) carried out some blast loading tests on reinforced concrete models. They demonstrated that the model law for high explosives can be determined by a consideration of the equations describing the motion of a shocked fluid. The pressures and other properties of the shock wave would be unchanged if the length and time scales were changed by the same factor as the dimensions of the loading source. Using equtions 2.94, 2.95, 2.96 and $W_m = \lambda_s^3 W_p$, (where W_m and W_p are the charge masses, and the density scale ρ_p/ρ_m is unity) then the scale factor λ_s for charge masses M_m and M_p is given in equation 2.97

$$M_m = \lambda_s^3 M_p \qquad \ldots 2.97$$

where subscript m denotes model and subscript p denotes prototype. It has also been shown that the same geometric scaling governing shock transmission also governs the model's structural response to blast generated pressures. If the motion of the structure is expressed by Newton's second law $F = MT^{-2} L$ then

$$F_m = \lambda_s^2 F_p \qquad \ldots 2.98$$

where F denotes force.

In the plastic region,model and prototype similitude is satisifed when the dimensionless ratio of the external work to the stored strain energy is the same for both model and prototype. Thus the kinetic energy of the structure due to blast loading equals the strain or potential energy of the structure in both model and prototype systems.

Kinetic energy, KE, may be expressed as impulse I where impulse is a function of force and time such that $KE = I^2/2M$.

$$KE_m = \lambda_s^3 KE_p \qquad \ldots 2.99$$

Potential energy, PE, is equivalent to the area under the resistance deflection curve for a structure and is also a function of force and time.

$$PE_m = \lambda_s^3 PE_p \qquad \ldots 2.100$$

Although structural response to transient loading follows the same similitude principle as the transient load, there are some limitations in the application of the scaling laws. Using similar arguments for the derviation of equations 2.99 and 2.100 itis possible to derive a scale for each parameter in the study. Table 2.4 gives a summary.

2.8.3 Limitations and Assumptions on Replica Scaling

Modelling has been used previously for reinforced concrete structures by Dobbs and Cohen (1970), for soil dynamics by Westine (1966) and for penetration mechanics by Baker et al (1973). Davis (1978) reviewed the use of models in studying response to dynamic loading and concluded that initiators and very small explosive charges did not scale especially when the mass of explosive in the initiator was significant compared to the mass of explosive in the main charge. Similarly, tolerances in the manufacture of charges did not scale because a practical limit was reached before the scale limit could be applied. Scaling explosives by geometric replica scaling resulted in time needing to be scaled. This was impossible because the reaction rate of the explosive could not be altered. If velocities were not scaled then the detonation velocity of the explosive and any projectile velocity resulting from the charge remainded unaffected.

The second major difficulty in scaling was the scaling of gravity. Gravity can distort dead loads and the distances travelled by fragments and debris. Westine (1966) found that the gravity effects on dead load could be reduced in soil models by layering the soil to vary the soil shear strength with depth. This did not remove problems with the scaling of fragment dispersion. Although pore pressure dissipation and strain rate effects are difficult to scale

Westine (1966) claimed to have achieved correlation between model and prototype response to dynamic loading within 5%. He found sands to be strain rate insensitive but cohesive soils had a wide range of sensitivity. Nevertheless he concluded that at one fifth scale strain rate effect in any soil was relatively insignificant.

White and Clark (1978) studied reinforced microconcrete models and found that lack of similitude existed between model and prototype moment-curvature relationships, crack widths and the number of cracks. The cause was attributed, at least in part, to a fundamental difference in the local bond mechanism between microconcrete and the reinforcing wire compared with the mechanism between prototype concrete and reinforcement.

Table 2.1

List of Parameters for Modelling Shaped Charge Jet Impact

Variables	Symbols	Dimensions
Diameter of jet	d_j	L
Length of jet	L_j	L
Nose radius of jet	r_j	L
Angle of leading end of jet	α_1	-
Angle of obliquity of attack	β'	-
Jet density	ρ_j	FT^2/L^4
Jet velocity	V_j	L/T
Target thickness	h_t	L
Target density	ρ_t	FT^2/L^4
Target temperature	θ_t	θ
Specific heat of target	c_t	$L^2/\theta T^2$
Heat of fusion of target	n_t	L^2/T^2
Jet temperature	θ_j	θ
Specific heat of jet	c_j	$L^2/\theta T^2$
Heat of fusion of jet	n_j	L^2/T^2
Ultimate stress of target	S	F/L^2
Ultimate stress of jet	σ_u	F/L^2
Other stresses or target strengths	S_i	F/L^2
Other stresses or jet strengths	σ	F/L^2
Strain	ϵ	-

Table 2.2

Projectile Impact Pi Terms

P_i Terms	Comments
$\pi 1 = \alpha_1$	Geometric similarity. All lengths scale similarly and angles remain constant.
$\pi 2 = \beta'$	
$\pi 3 = L_j/d_j$	
$\pi 4 = r_j/d_j$	
$\pi 5 = h_t/d_j$	
$\pi 6 = \rho_j/\rho_t$	Similar density ratios between projectile and target materials.
$\pi 7 = \varepsilon$	Constitutive simarlity. Similarity of stress strain curves implied.
$\pi 8 = \sigma_u/S$	
$\pi 9 = S_i$	
$\pi 10 = \sigma$	
$\pi 11 = \sigma_j/\sigma_t$	Similar temperature
$\pi 12 = n_j/n_t$	Similar heats of fusion
$\pi 13 = c_j/c_t$	Similar specific heats
$\pi 14 = \rho_t^{1/2} V_2/S^{1/2}$	Energy ratios
$\pi 15 = \rho_r \sigma_r c_t/S$	
$\pi 16 = \rho_t n_t/s$	

Table 2.3

Replica Model Scale Factors

Variable	Symbols	Scale factor
Lengths	d_j, L_j, r_j, h_t	λ_s
Angles	α_1, β'	1
Stress	σ_u, S	1
Strain	ε	1
Density	ρ_t, ρ_j	1
Temperature	θ_t, θ_j	1
Velocity	V_j	1
Specific heats	c_t, c_j	1
Heats of fusion	n_t, n_j	1

Table 2.4

Summary of Ideal Scale Factors

Quantity	Symbol	Dimensions	Ideal Scale
Slab length	l_s	L	$l_{sm}/l_{sp} = \lambda_s$
Slab depth	d_s	L	$d_{sm}/D_{sp} = \lambda_s$
Slab area	A_s	L^2	$A_{sm}/A_{sp} = \lambda_s^2$
Slab mass	M	M	$M_m/M_p = \lambda_s^3$
Reinforcement area	A_r	L^2	$A_{rm}/A_{rp} = \lambda_s^2$
Reinforcement area/unit length	A'_r	L	$A'_{rm}/A'_{rp} = \lambda_s$
Unit resistance	w_r	$\frac{M}{T^2 L}$	$w_{rm}/w_{rp} = 1$
Total resistance	R_t	$\frac{ML}{T^2}$	$R_{tm}/R_{tp} = \lambda_s^2$
Charge	W_{cm}	M	$Wcm_m/Wcm_p = \lambda_s^3$
Distance	r_d	L	$r_{dm}/r_{dp} = \lambda_s$
Scaled distance	z_d	$\frac{L}{\left(\frac{ML^2}{T^2}\right)^{1/2}}$	$z_{dm}/z_{dp} = 1$
Total impulse	I	$\frac{ML^2}{T^2}$	$I_m/I_p = \lambda_s^3$
Unit impulse	i	$\frac{M}{T^2}$	$i_m/i_p = \lambda_s$
Scaled impulse	$\bar{i}$	$\frac{\left(\frac{M}{T^2 L}\right)}{\left(\frac{ML^2}{T^2}\right)^{1/3}}$	$\bar{i}_m/\bar{i}_p = 1$
Pressure	p_r	$\frac{M}{T^2 L}$	$p_{rm}/p_{rp} = 1$
Kinetic energy	KE	$\frac{ML^2}{T^2}$	$KE_m/KE_p = \lambda_s^3$

Table 2.4 cont'd

Quantity	Symobol	Dimensions	Ideal Scale
Density	ρ	$\frac{M}{M^3}$	$\rho_m/\rho_p = 1$
Elastic modulus	E_d	$\frac{M}{T^2 L}$	$E_{dm}/E_{dp} = 1$
Deflection	δ	L	$\delta_m/\delta_p = \lambda_s$
Moment	M_o	$\frac{ML^2}{T^2}$	$M_{om}/M_{po} = \lambda_s^3$
Moment/unit length	$\bar{M}$	$\frac{ML}{T^2}$	$\bar{M}_m/\bar{M}_p = \lambda_s^2$
Shear	V_z	$\frac{ML}{T^2}$	$V_{zm}/V_{zp} = \lambda_s^2$
Shear/unit length	$\bar{V}$	$\frac{M}{T^2}$	$\bar{V}_m/\bar{V}_p = \lambda_s$
Stress	σ	$\frac{M}{T^2 L}$	$\sigma_m/\sigma_p = 1$
Strain	ε	-	$\varepsilon_m/\varepsilon_p = 1$
Velocity	V	$\frac{L}{T}$	$V_m/V_p = 1$
Time	t	T	$t_m/t_p = \lambda$
Moment of inertia	$\bar{I}$	L^4	$\bar{I}_m/\bar{I}_p = \lambda_s^4$
Frequency	f	$\frac{1}{T}$	$f_m/f_p = 1/\lambda_s$
Angle	$\bar{\alpha}$	-	$\bar{\alpha}_m/\bar{\alpha}_p = 1$
Temperature	θ	-	$\theta_m/\theta_p = 1$
Specific heat	C_u	$\frac{L^2}{T^2}$	$C_{um}/C_{up} = 1$
Heat of fusion	n_o	$\frac{L^2}{T^2}$	$n_{om}/n_{op} = 1$

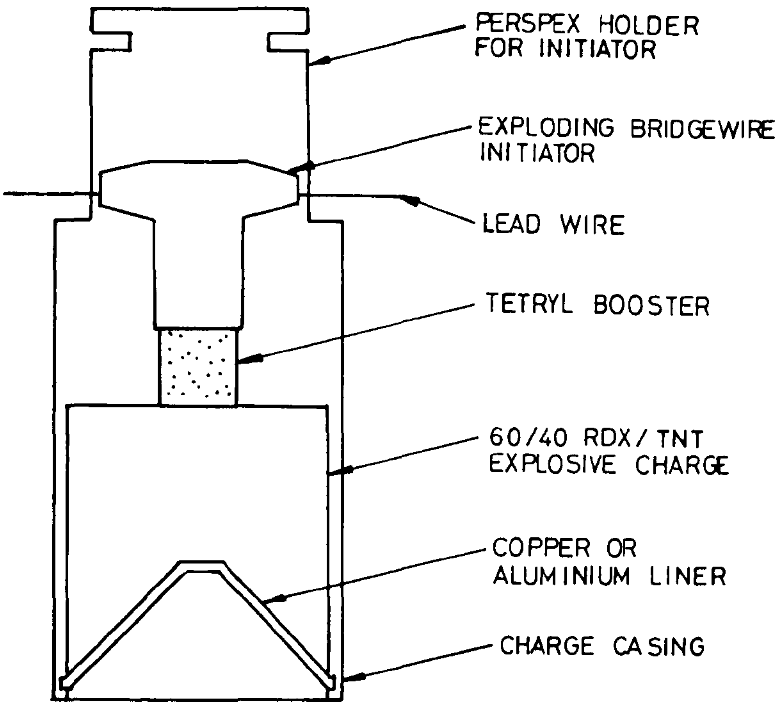

FIGURE 2.1 CROSS SECTIONAL VIEW OF A SHAPED CHARGE

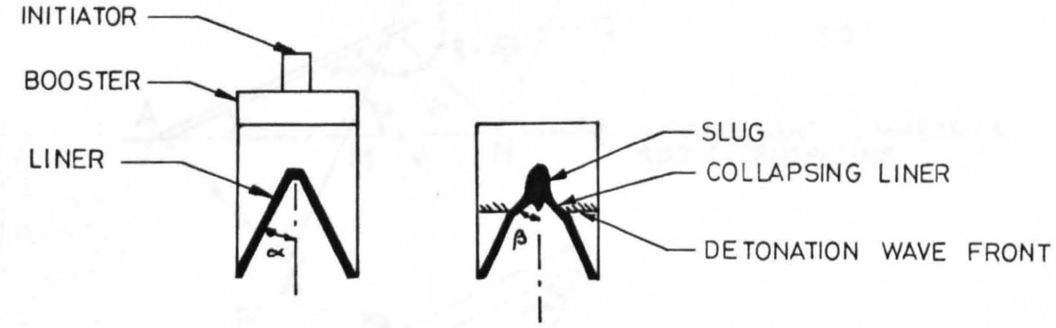

FIGURE 2.2 COLLAPSE OF A SHAPED CHARGE LINER
(AFTER JOHNSON 1972)

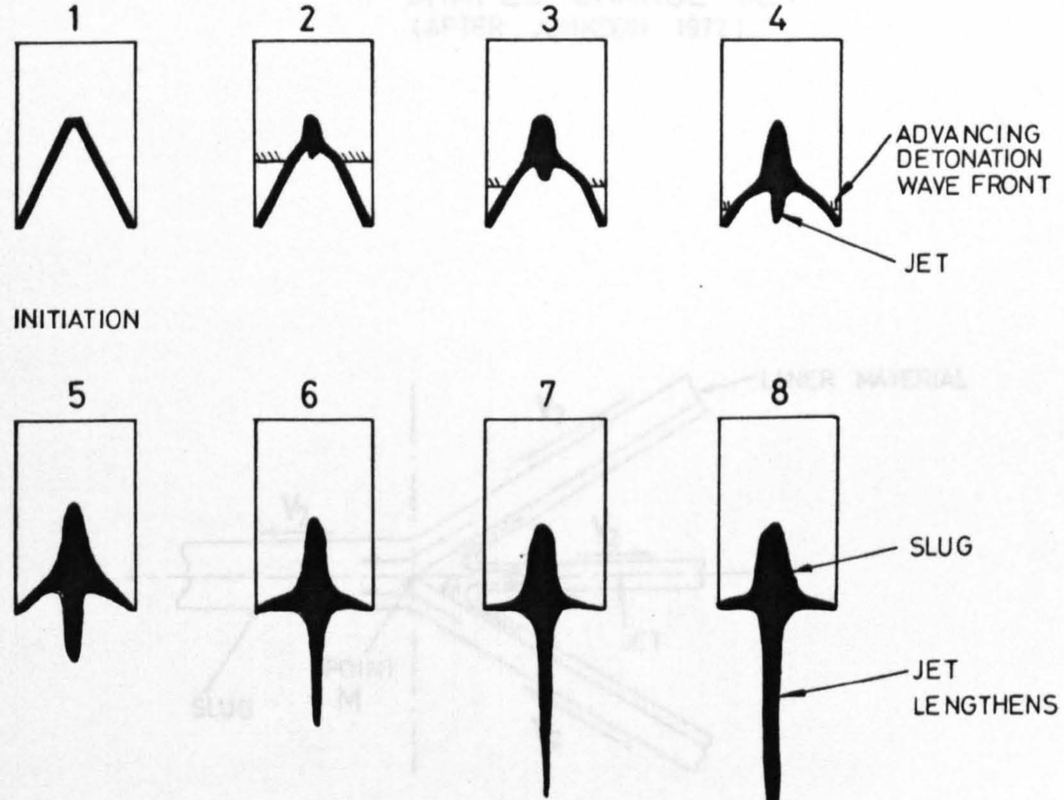

FIGURE 2.3 FORMATION OF A SHAPED CHARGE JET
(AFTER COUSINS 1968)

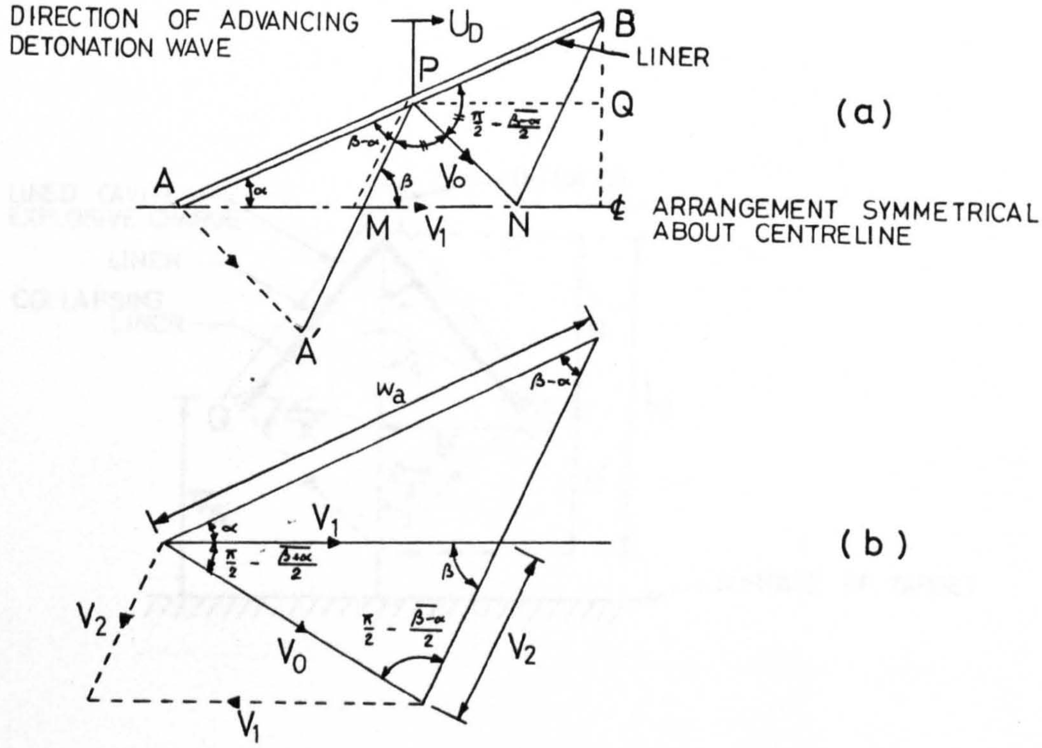

FIGURE 2.4 VELOCITY DIAGRAMS FOR THE FORMATION OF A SHAPED CHARGE JET (AFTER JOHNSON 1972)

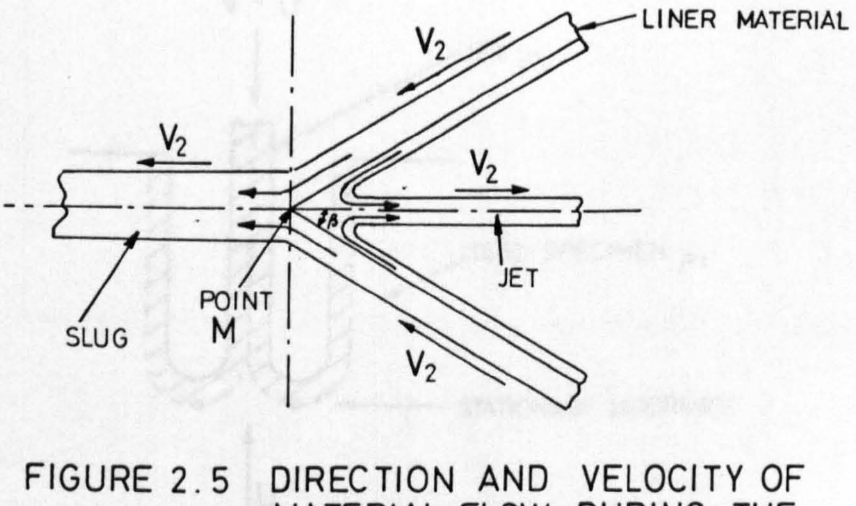

FIGURE 2.5 DIRECTION AND VELOCITY OF MATERIAL FLOW DURING THE FORMATION OF A SHAPED CHARGE JET (AFTER JOHNSON 1972)

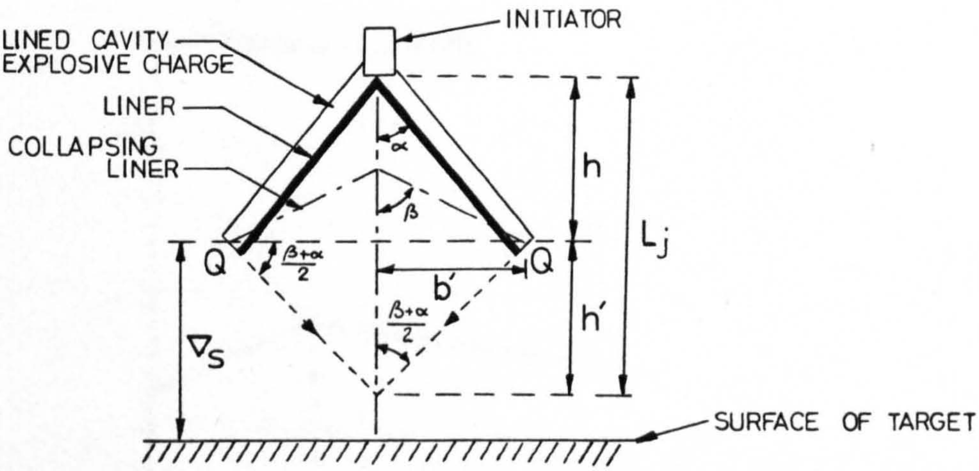

FIGURE 2.6 THE LENGTH OF A SHAPED CHARGE JET - GEOMETRY CONSIDERATIONS
(AFTER JOHNSON 1972)

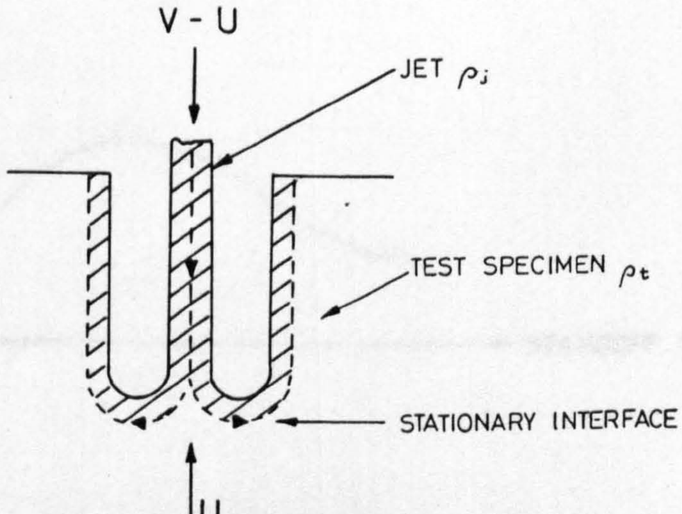

FIGURE 2.7 PENETRATION OF A SEMI-INFINITE MEDIUM BY A SHAPED CHARGE JET
(AFTER JOHNSON 1972)

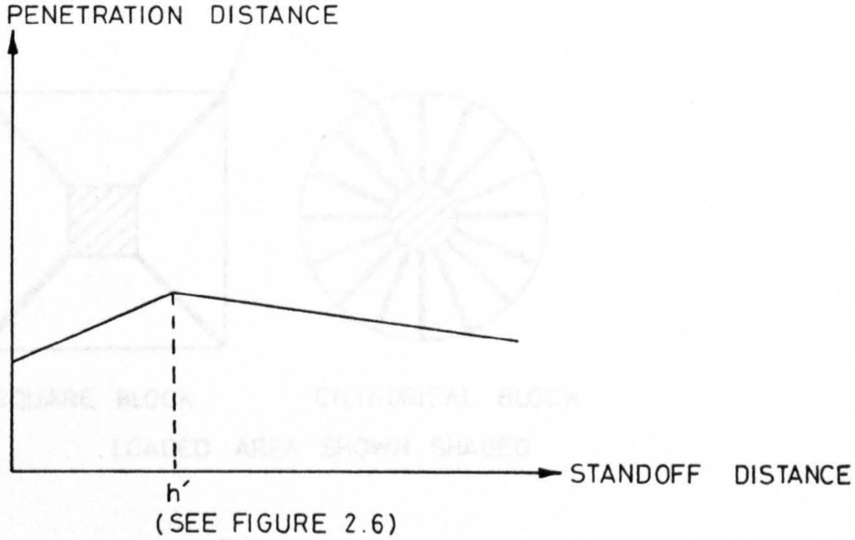

FIGURE 2.8 IDEALISED PENETRATION - STANDOFF RELATIONSHIP FOR SHAPED CHARGE JET IMPACT (AFTER JOHNSON 1972)

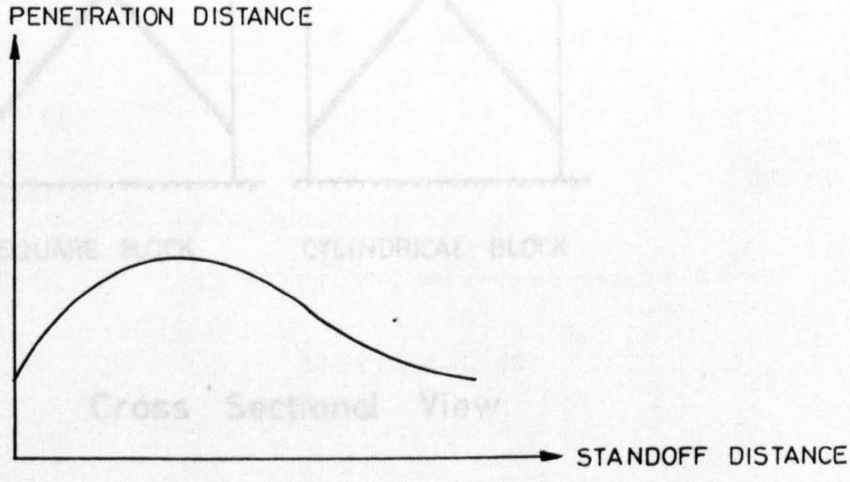

FIGURE 2.9 ACTUAL PENETRATION - STANDOFF RELATIONSHIP FOR SHAPED CHARGE JET IMPACT (AFTER JOHNSON 1972)

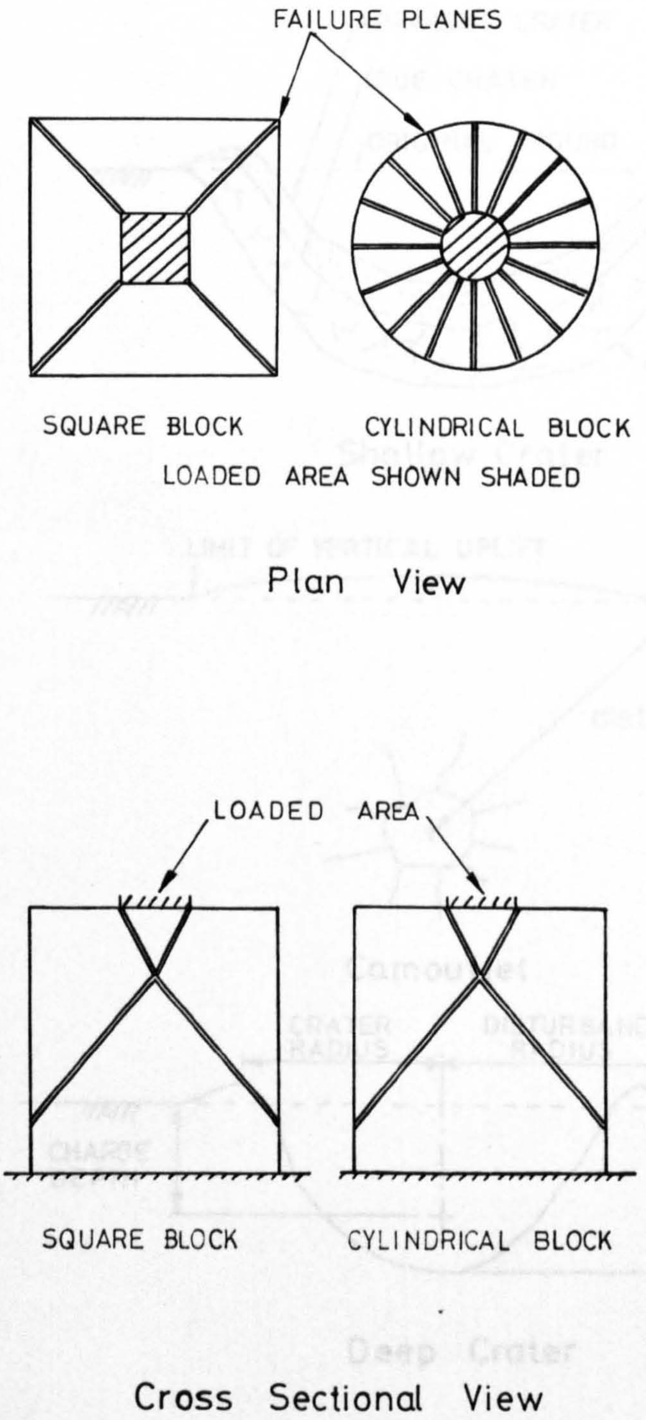

FIGURE 2.10 BEARING CAPACITY OF ROCK UNDER POINT LOADING
(AFTER CHEN 1969)

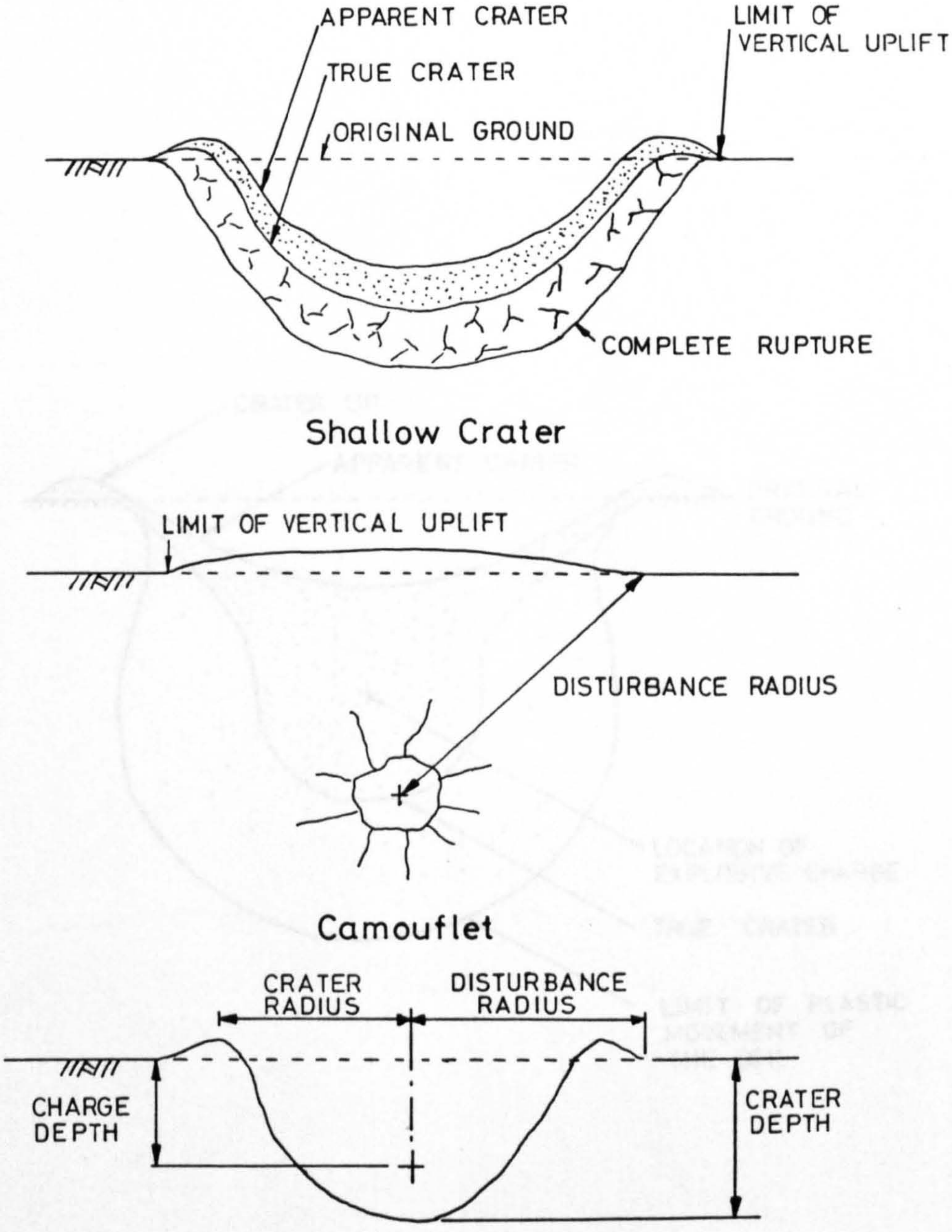

FIGURE 2.11 CRATER AND CAMOUFLET NOMENCLATURE

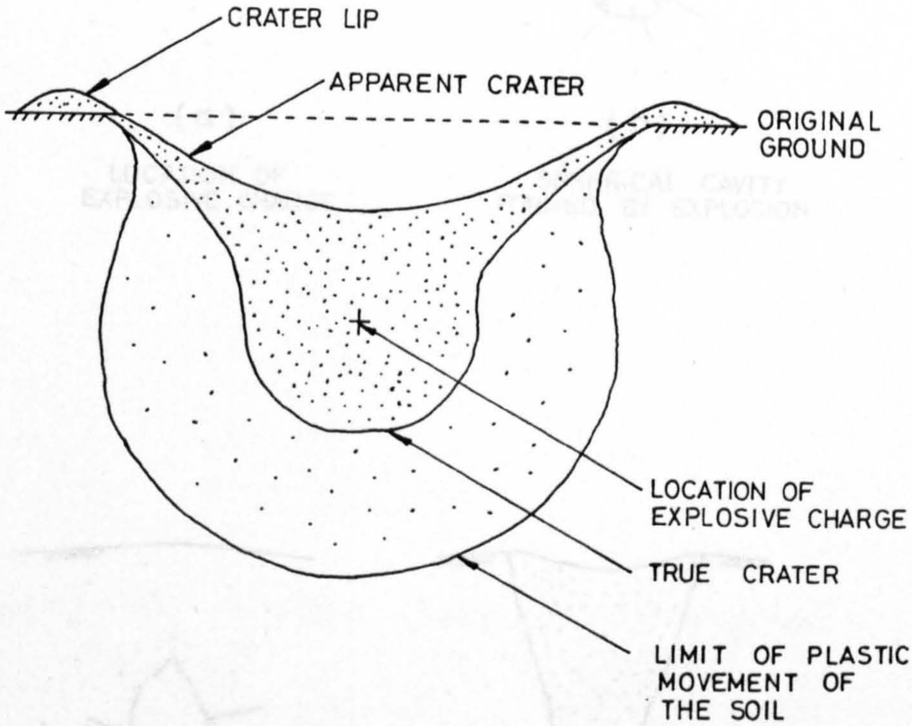

FIGURE 2.12 APPARENT AND TRUE CRATER NOMENCLATURE

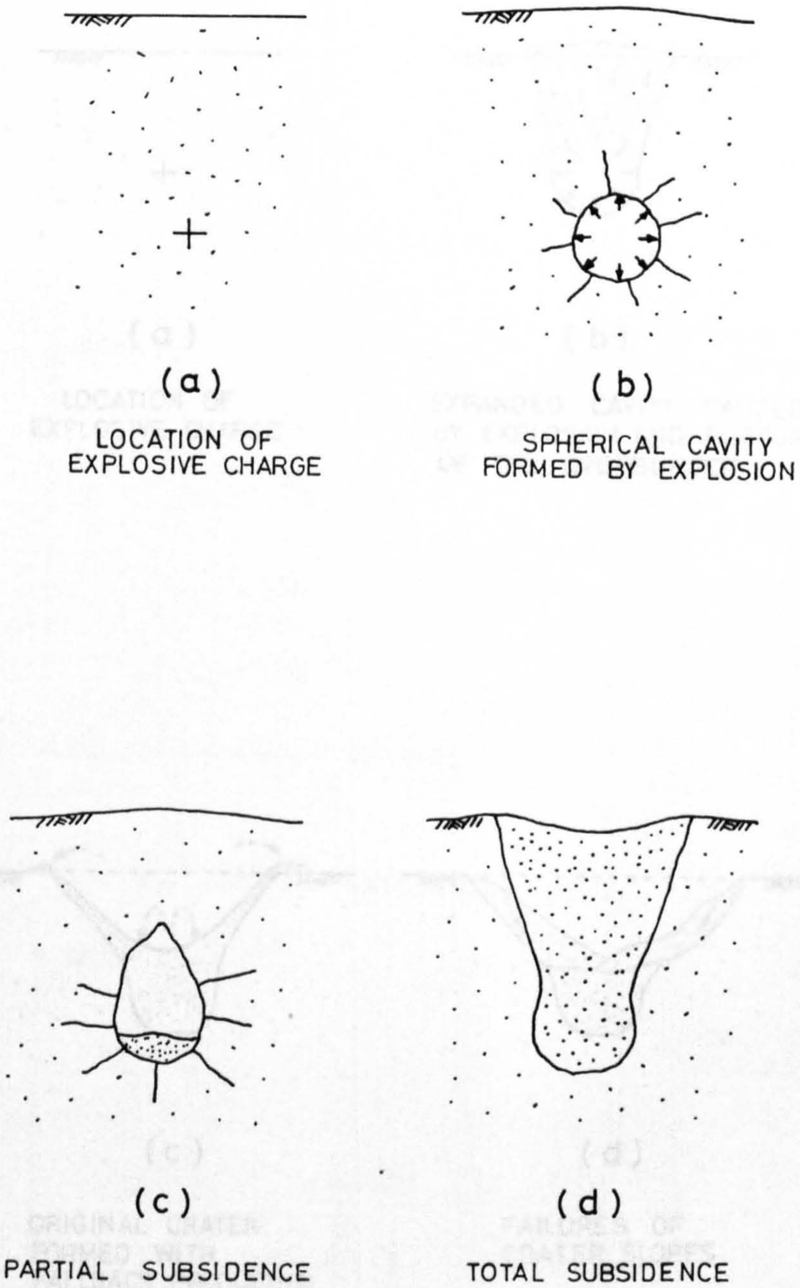

FIGURE 2.13 THE MECHANISM OF CRATERING FOR DEEP BURIED EXPLOSIVE CHARGES

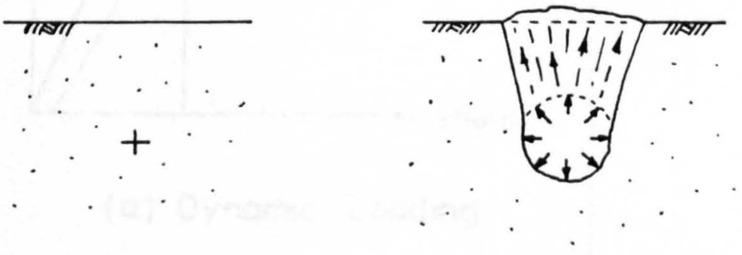

(a)

LOCATION OF
EXPLOSIVE CHARGE

(b)

EXPANDED CAVITY CAUSED
BY EXPLOSION AND RUPTURE
OF THE OVERBURDEN

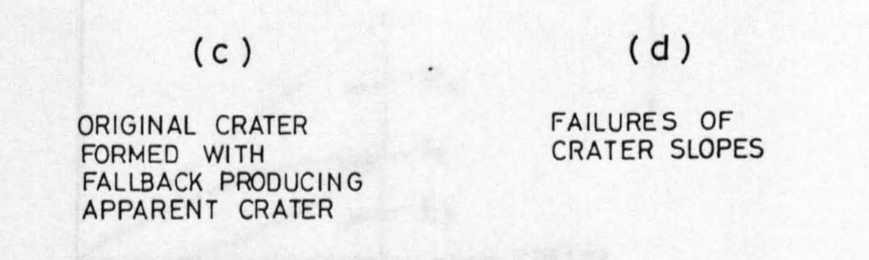

(c)

ORIGINAL CRATER
FORMED WITH
FALLBACK PRODUCING
APPARENT CRATER

(d)

FAILURES OF
CRATER SLOPES

FIGURE 2.14 THE MECHANISM OF CRATERING FOR EXPLOSIVE CHARGES AT MODERATE DEPTH

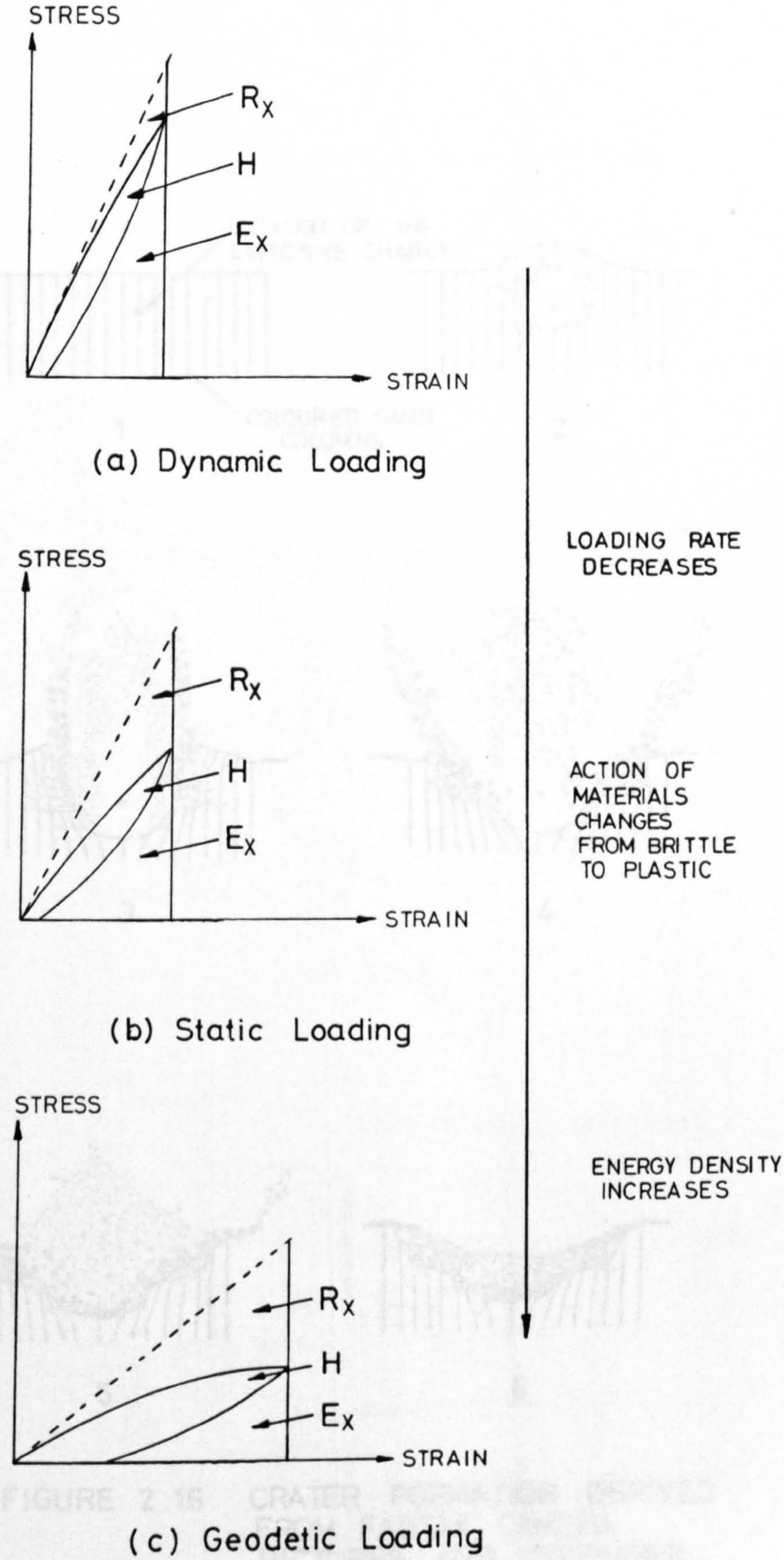

FIGURE 2.15 STRESS-STRAIN DIAGRAMS FOR MATERIAL BEHAVIOUR AT DIFFERENT LOADING RATES

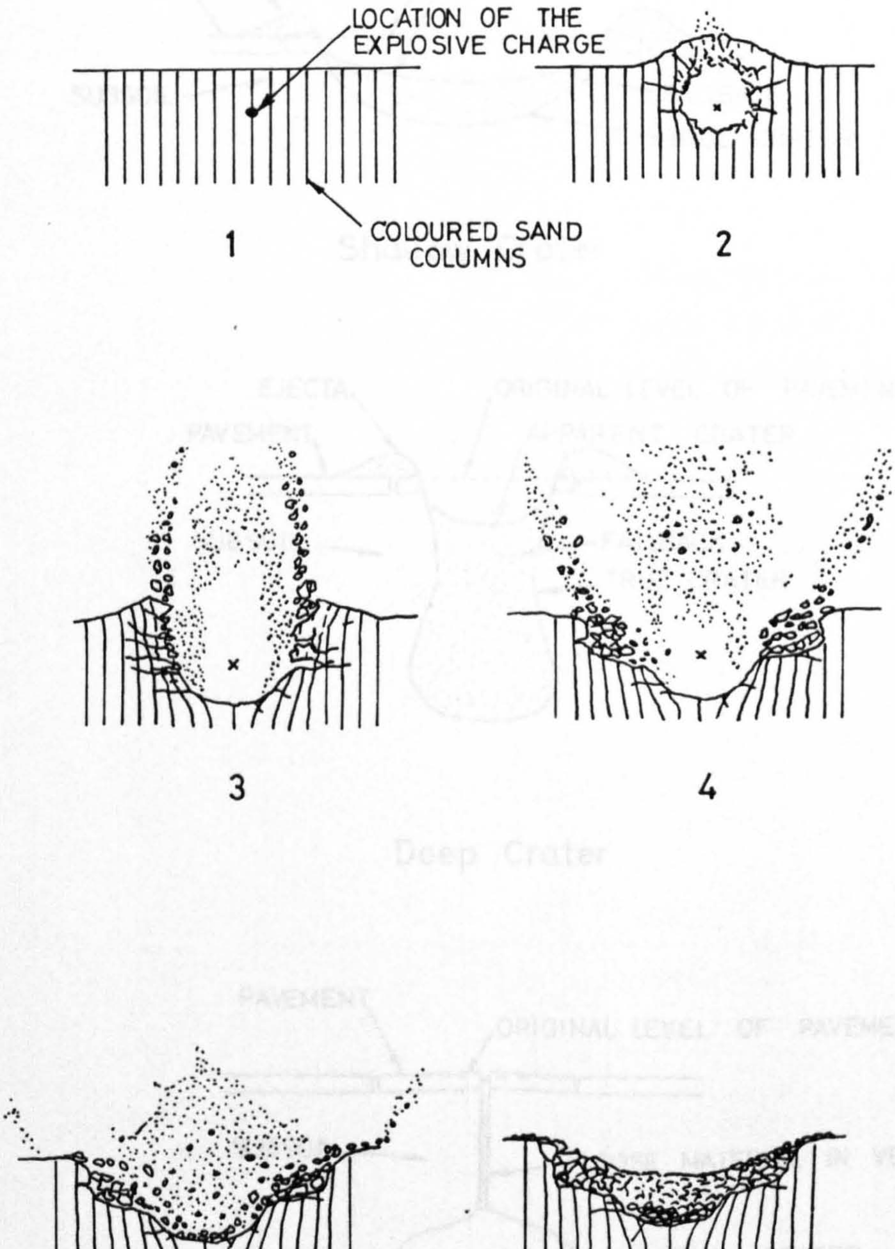

FIGURE 2.16 CRATER FORMATION DERIVED FROM FASTAX CAMERA PICTURES AND COLOURED SAND COLUMN TECHNIQUE (AFTER TOWNSEND 1961)

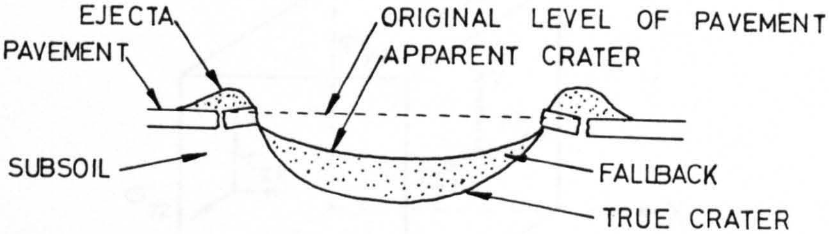

Shallow Crater

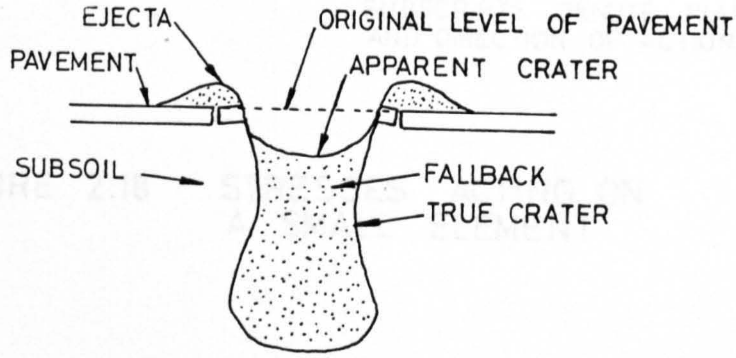

Deep Crater

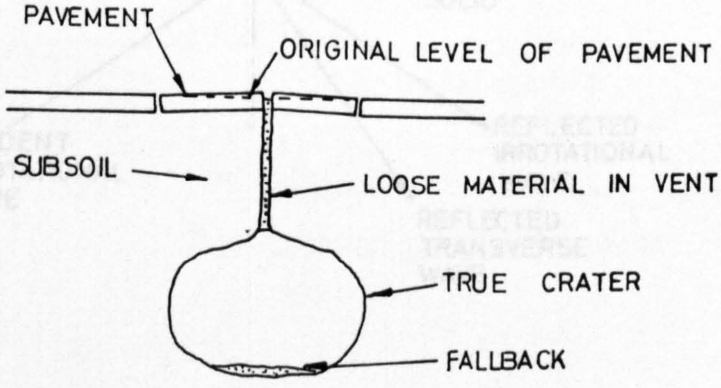

Camouflet Crater

FIGURE 2.17 CRATERS PRODUCED BY EXPLOSIVE CHARGES BURIED UNDER PAVEMENTS (AFTER KVAMMEN 1973)

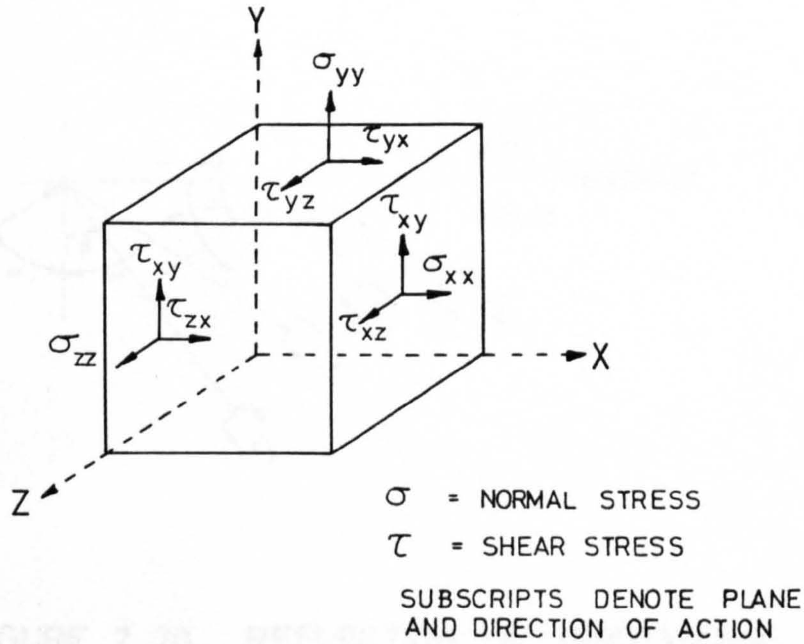

FIGURE 2.18 STRESSES ACTING ON A SMALL ELEMENT

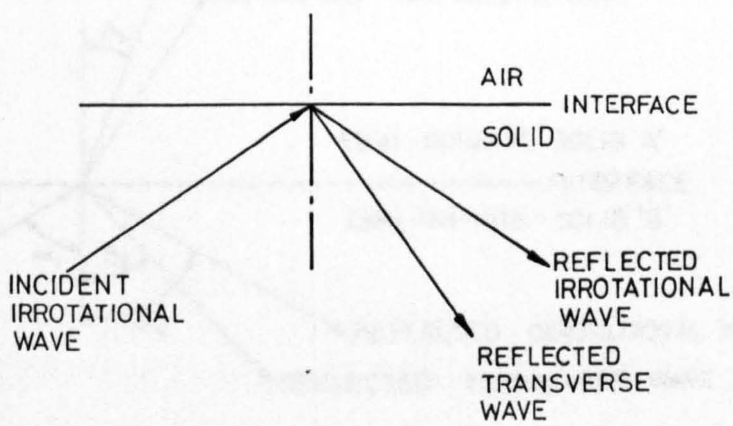

FIGURE 2.19 REFLECTED STRESS WAVES AT AN INTERFACE

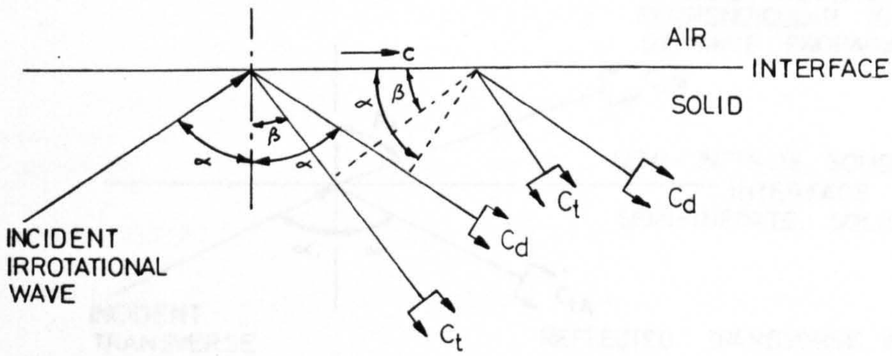

FIGURE 2.20 REFLECTION OF IRROTATIONAL WAVES AT A SOLID/AIR INTERFACE

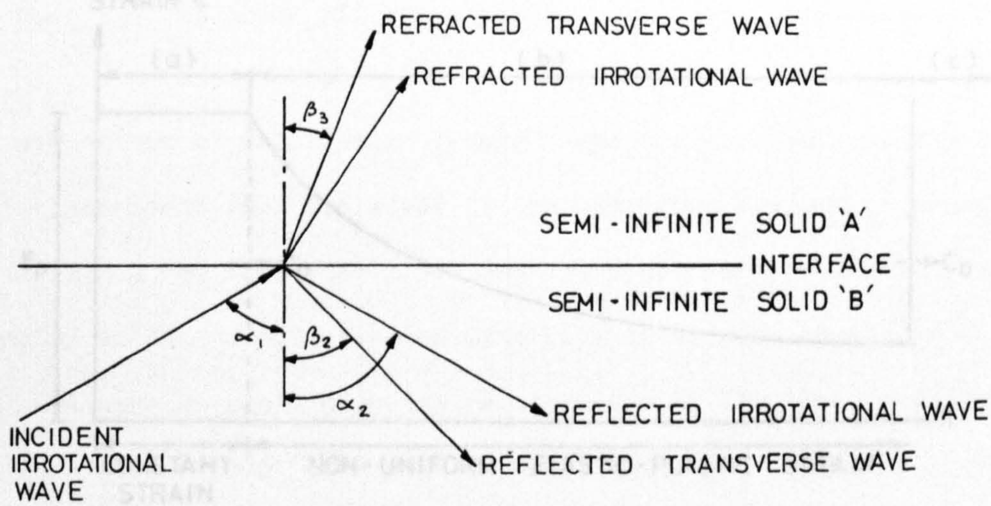

FIGURE 2.21 REFLECTION OF AN IRROTATIONAL WAVE OR A VERTICALLY POLARISED TRANSVERSE WAVE

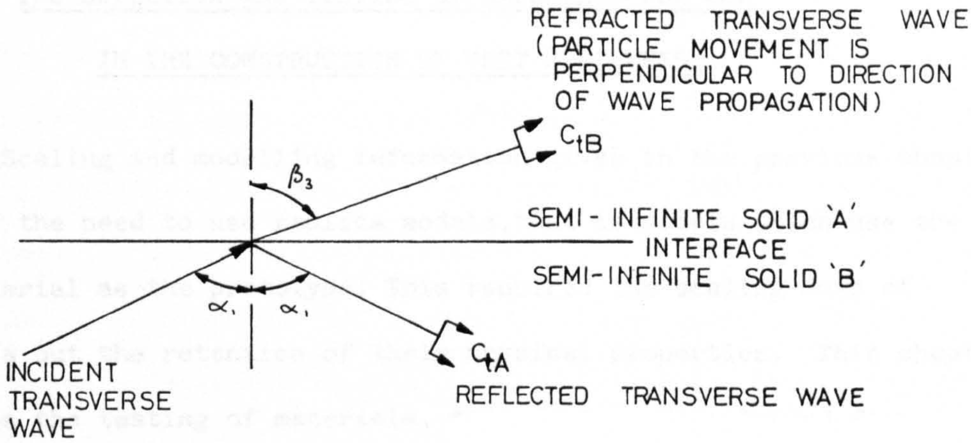

FIGURE 2.22 REFLECTION AND REFRACTION OF A HORIZONTALLY POLARISED TRANSVERSE WAVE

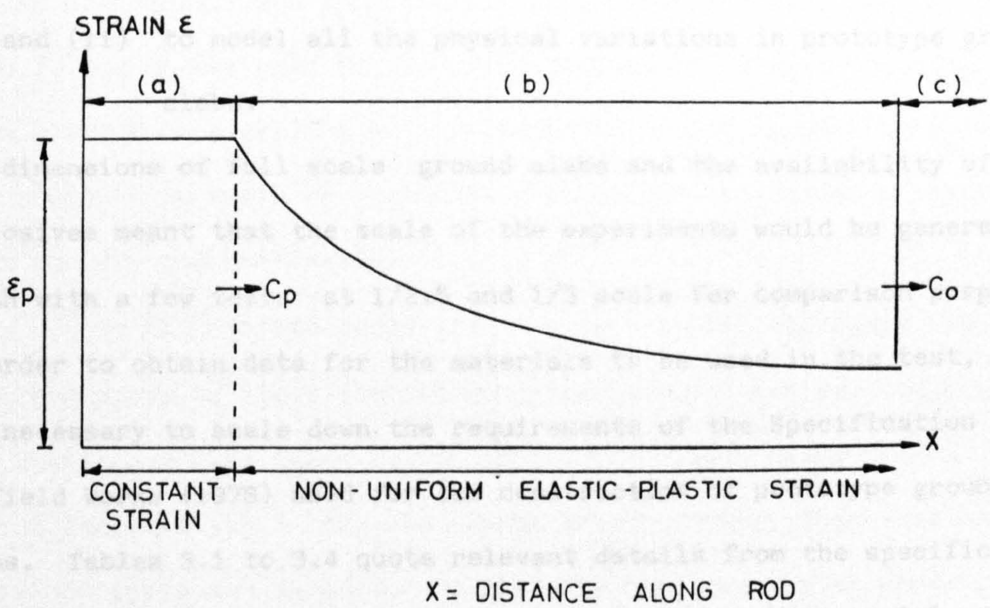

FIGURE 2.23 PLASTIC IMPACT STRAIN DISTRIBUTED IN A ROD

CHAPTER 3

THE SELECTION AND TESTING OF MATERIALS FOR USE IN THE CONSTRUCTION OF TEST SPECIMENS

Scaling and modelling information given in the previous chapter dictated the need to use replica models,that is models which use the same material as the prototype. This required the scaling down of materials but the retention of their physical properties. This chapter describes the testing of materials, testing methods selected for use during the experimental programme and the limitations and effects of practical tolerances.

3.1 REQUIREMENTS AND GENERAL DETAILS OF THE MODELS USED IN THIS STUDY

The model has two basic requirements

(i) to reproduce the damage caused by the high speed impact of a projectile and the blast damage from an explosion

and (ii) to model all the physical variations in prototype ground slabs.

The dimensions of full scale ground slabs and the availability of explosives meant that the scale of the experiments would be generally 1/5th with a few tests at 1/2.5 and 1/3 scale for comparison purposes. In order to obtain data for the materials to be used in the test, it was necessary to scale down the requirements of the Specification for Airfield Works (1978) used for the construction of prototype ground slabs. Tables 3.1 to 3.4 quote relevant details from the specification for concretes, aggregates and construction joints. Figures 3.1 and 3.2 show respectively details of full scale and proposed model ground slabs.

3.2 AGGREGATES USED IN THE MODELS

Five aggregates were selected for use in models, limestone (sedimentary rock), basalt (igneous rock), barytes (dense rock), crushed river gravel and 'Lytag', a lightweight aggregate formed as a power station by-product. Each aggregate was tested for basic properties at source since the sample sizes there were more representative than with the limited amount obtained for use in concrete trial mixes. Table 3.5 lists basic properties and table 3.6 gives the grading for zone 2 crushed gravel sand listed in table 3.5. Scaling requirements required that aggregates should be scaled so that, for example, a 1/5 scale of 40mm maximum size would be 8mm.

Figures 3.3 and 3.4 respectively show grading limits for pavement and lean mix concretes from the Specification for Airfield Works (1978). Scaled up 1/5 scale grading curves have been superimposed to show the relationship between the practical scaled mix taken from Shacklock (1978) and the prototype. The apparent out of tolerance at the smaller sieve sizes is due to the need to prevent the volume of material passing a 125μm sieve from exceeding 10% by weight in scaled mixes. This is to stop a situation known as oversanding which has the effect of making a mix too dry and unworkable.

To achieve the scale gradings each coarse aggregate was sieved by an 8mm sieve to limit the maximum size to 8mm. For each aggregate both coarse and fine (zone 2) fractions were sieved using sieves to British Standard 410. Fine and coarse fractions were then combined in the ratios given in table 3.7 to give the required scaled grading.

3.3 CONCRETES USED IN THE MODELS

Trial concrete mixes were made for each type of concrete required in the test programme and for each aggregate used for the concretes. For each concrete mix the aggregate was combined in the proportions given in table 3.7. The aggregates, cement and water were all batched by weight, according to the proportions given in table 3.8. In the case of pavement quality concrete air entraining agent was added to the mixing water and thoroughly stirred in. The aggregates and cement were taken and placed in the clean, dry pan of a Cretangle type ME horizontal pan mixer shown in plate 3.1 and mixed for two minutes. The mixer pan was cleaned and dried before each separate trial mix was made and also between batches of a mix to ensure the moisture content remained uniform. The water was added and the concrete mixed for a further two minutes. The density of the fresh concrete was tested in a density can to British Standard 1881 part 2 (1970) and, in the case of pavement quality concrete, for air content using an air content meter to British Standard 1881 part 2 (1970). Table 3.9 contains calibration data for the air content meter since the different aggregates required separate adjustments.

For each trial mix four 100mm cube moulds, three 100mm by 100mm by 500mm concrete beam moulds and three 100mm diameter by 250mm concrete cylinder moulds were coated with Tellus MRO mould release oil. Fresh concrete was cast into each mould and tamped with a tamping foot attached to a Kango 950 electric hammer. Different tamping feet were required for different moulds and different compaction times for lean and pavement quality concrete mixes. Table 3.10 gives details of compaction methods and thicknesses of concrete layers compacted for all the different mixes.

The surface of each concrete specimen was then finished using a plasterer's float and the moulds were covered with a polythene sheet to prevent moisture evaporating from the surface. The concrete specimens were cured for one day in the moulds at 20°C and then in air under a polythene sheet, for a further thirteen days. For each trial mix cube crushing,beam bending and cylinder splitting tests to British Standard 1881 part 4 (1970) were performed on the cubes, beams and cylinders respectively at fourteen days after casting.

Generally the cement used was "Ferrocrete" rapid hardening cement but other types tried were "Swiftcrete" extra rapid hardening cement and ordinary portland cement. It was found that "Swiftcrete" offered no advantages over "Ferrocrete" but "Ferrocrete" was better than ordinary portland cement in its rate of gain of strength. A further benefit was that the cement particles were more finely ground,and hence more to scale than ordinary portland concrete. Table 3.11 gives basic properties of Ferrocrete and typical 14 day strength values of concretes of various aggregates made from "Ferrocete" are listed in table 3.12.

Values of the dynamic modulus of elasticity for each trial mix were calculated from ultrasonic determinations of the compressive wave speed in the concrete. Table 3.13 contains values of the wave speed and the modulus of elasticity which were determined by the "PUNDIT" apparatus. The method used was to transmit a 500kHz pulse from a transmitter to a receiver down a 500mm long prism of concrete and to time this pulse. The transmitter and receiver were each 25mm in diameter and were held firmly against the centre of each 100mm square end face of the prism. Lithium grease was included between the transmitter or receiver and the concrete to achieve a good accoustic coupling. By knowing the transmitted length and the measured time,the velocity of the wave could be computed. From this the elastic modulus was derived from the formula

$$E_d = \rho C_d^2 \qquad \ldots\ 3.1$$

where E_d is the dynamic modulus of elasticity of the concrete

ρ is the density of the concrete

C_d is the elastic wave speed in the concrete

Problems were encountered in producing scaled concrete mixes, especially compaction,due to the extremely low degree of workability. The only practical method was to use a Kango 950 electric hammer with a tamping tool. Another problem was the determination of the water content of as-delivered aggregates. Since concrete mixes assumed completely dry aggregates, the amount of water held by aggregate particles needed to be measured and deducted from the water added to the mix. The siphon can apparatus described in British Standard BS 1337 was found to be both accurate and practical. Table 3.9 gives values for constants related to the aggregate used in this study.

3.4 REINFORCEMENT USED IN MODEL SLABS

Prototype reinforced concrete slabs are reinforced with a light steel mesh near the top surface to control thermal cracking and resist frost damage.

The steel mesh sizes required by the Specification for Airfield Works (1978) were scaled down linearly for bar diameter and spacing. In the models twelve gauge and sixteen gauge wires were used for the main and distribution reinforcement respectively. Stress-strain relationships for the wires were obtained by the Houndsfield extensometer and the results are given in figure 3.5.

Two problems occur with the use of wire in models. The local bond and anchorage characteristics are not representative of prototype reinforcement and welding of wires into a mesh introduces unrepresentative stresses. Inkester (1980) used a machine to make surface deformations on wire to improve bond characteristics. In this study this was not feasible because of the large amount of wire required in the reinforcement mesh. Instead the wires were woven into the required meshes. In this manner anchorage and bond were improved by the interlock and cranking of the wires without residual welding stresses. Cold working in the weaving process was not considered to be significant in altering material properties.

3.5 JOINTS AND SEPARATION LAYERS USED WITH MODEL GROUND SLABS

Prototype ground slabs have three types of joints, construction contraction or expansion joints. These are usually filled with between 10mm and 25mm of a flexible material. The model joints were made from 2mm thick balsa wood strips which extended the full depth of the slab.

The other prototype construction detail to be modelled was the polythene sheet found between the main concrete slabs and the lean concrete base course. A similar sheet was used in the model and had scaled thickness but the tensile strength was not scaled. This does not matter in penetration tests because the strength is insignificant but in slab lifting tests with subsurface charges it may have an effect.

3.6 SOILS USED AS FOUNDATIONS TO MODEL GROUND SLABS

The range of soils available as foundations to prototype ground slabs was considered to be too wide to try to select any one as representative. Two widely different types were selected to try to show any differences in results attributable to the soil foundation. Clay obtained from Naylor Brothers (Clayware) Ltd of Denby Dale, Huddersfield was chosen to represent cohesive soils and zone 2 sand from BCA Ltd, Hednesford, Staffordshire to represent non-cohesive soils.

The clay and the sand were both tested for basic properties. Table 3.6 gives the grading of Zone 2 sand and figure 3.6 shows the relationship between dry density versus moisture content derived from compaction tests for sand. For the clay, table 3.14 gives basic properties and figures 3.7, 3.8 and 3.9 give the relationships amongst dry density, triaxial shear strength and moisture content. All soil tests conformed with the requirements of British Standard 1377 (1975) and no attempt was made to scale either soil particles or soil properties. The scaling of soils is a problem which has not often been solved. Some parameters have been scaled but the problems of scaling all the phases of the material simultaneously and the variation of strength with increasing depth particularly with large masses of soil are almost impossible to solve.

Table 3.1

<u>Requirements for Aggregates</u>

(from Specification for Airfield Works, 1978)

Concrete	Aggregate	10% fines load	Clay and fine silt limit by mass
Dry lean	Coarse aggregates Natural sand Crushed stone sands	$\nless$ 50 kN $\nless$ 50 kN $\nless$ 50 kN	$\ngtr$ 1% $\ngtr$ 3% $\ngtr$ 15%
Pavement Quality	Coarse aggregate Natural sands Crushed stone sands	$\nless$ 100 kN $\nless$ 100 kN $\nless$ 100 kN	$\ngtr$ 1% $\ngtr$ 3% $\ngtr$ 15%

Table 3.2

<u>Grading Limits for Aggregates</u>

(from Specification for Airfield Works, 1978)

Sieve size mm	% Passing		
	Coarse aggregate for PQC	Fine aggregate for PQC (zone 2)	All in aggregate for dry lean mix
75	100	-	100
37.5	95-100	-	95-100
20	35-70	-	45-80
10	10-40	100	-
5	0-5	90-100	25-50
2.26	-	75-80	-
1.18	-	55-90	-
.6	-	35-59	8-30
.3	-	8-30	-
.15	-	0-10*	0-6

* for crushed stone 0 - 20%

Table 3.3

Requirements for Concrete

(from Specification for Airfield Works, 1978)

	Dry lean mix concrete	Pavement Quality Concrete
Mean crushing strength of 100mm concrete cubes at 7 days	8 N/mm^2 (3 cubes)	32.3 N/mm^2 $\pm$ 3.5 N/mm^2 (9 cubes)
Mix proportions		
Aggregate/cement ratio	12:1	6:1
Water/cement ratio	-	0.45
Volume of entrained air	-	3 to 6%
Tolerances - thickness	- 0mm, + 25mm	- 0mm, + 10mm
Undulations	$\ngtr$ 1.15mm dip in 3m	-
Compaction	Vibrating roller to $\nless$ 95% of the standard density	-

Table 3.4

Requirements for Joint and Separation Layers

(from Specification for Airfield Works, 1978)

Separation layer	Natural colour polythene	$\nless$ 125µm thick
Joint filler board	Contraction joints	10mm thick
	Expansion joints	25mm thick

Table 3.5

Properties of Aggregates

	Limestone	Basalt	Gravel	Barytes	'Lytag'
Oven dry s.g.	2.67	2.75	2.57	4.1	0.89-0.95
Sat. surface dry s.g	2.68	2.82	2.60	4.2	NA
Aggregate crushing value %	23	17	NA	40	NA
Aggregate impact value %	23	17	11	NA	NA
10% fines load (kN)	160	250	320	NA	NA

NA indicates results not available.

Table 3.6

Zone 2 Sand Grading

Sieve size to BS 5410	% passing
4mm	97
2mm	80
1mm	67
500μm	38
250μm	4
125μm	0

Table 3.7

Grading of Aggregates

	% PASSING SIEVE SIZE 8mm	4mm	2mm	1mm	0.5mm	0.25mm	0.125mm	Ratio of fine to coarse aggregates required to achieve grading
PQC 1/5 scaled limits	95-100	56-80	41-60	30-37	25-34	17-30	3-10	-
Lean mix 1/5 scaled limits	95-100	45-80	-	25-50	-	-	8-30	-
Sand/gravel actual grading	97	59	48	40	24	2*	0*	60/40
Limestone actual grading	98	65	53	35	29	8*	3*	65/35
Basalt actual grading	100	71	49	33	27	4*	1*	70/30
Barytes actual grading	100	80	59	43	26	9*	1*	80/20
'Lytag' actual grading	98	65	50	38	27	11*	3*	50/50
PQC and lean mix sand/gravel actual grading**	97	70	56	40	28	25	4	40/60

* adjusted to prevent over sanding in scaled mixes

** grading for aggregate for 1/3 and 1/2.5 ground slabs and 760mm concrete cubes

Table 3.8

Concrete Mix Details

Mix Ref.	Concrete Type	Aggregate	Water/cement ratio by weight	Ratio of fine to coarse aggregate	Aggregate/cement ratio by weight	% air entrained (limits)	Density of the hardened concrete kg/m³
1	PQC	Sand/gravel	0.5	60/40	6:1	3 to 6	2350
2	PQC	Limestone	0.5	65/35	6:1	3 to 6	2350
3	PQC	Basalt	0.5	70/30	6:1	3 to 6	2350
4	PQC	'Lytag'	0.6	50/50	2.15	3 to 6	1700
5	PQC	Barytes	0.4	80/20	4.96	3 to 6	3400
6	PQC	Sand/gravel*	0.5	40/60	6:1	3 to 6	2350
7	Lean mix	Sand/gravel	0.96	60/40	15:1	0	2250
8	Lean mix	Limetone	0.96	65/35	15:1	0	2250
9	Lean mix	Basalt	0.96	70/30	15:1	0	2250
10	Lean mix	'Lytag'	1.0	50/50	5.3:1	0	1650
11	Lean mix	Barytes	0.9	80/20	14.5:1	0	3300
12	Lean mix	Sand/gravel*	0.96	40/60	15:1	0	2250
13	Neat/cement**	-	0.5	-	-	-	-
14	Mortar**	Zone 2 sand	0.5	-	2:1	0	-
15	Mortar**	Zone 2 sand	0.5	-	4:1	0	-
16	Mortar**	Zone 2 sand	0.5	-	6:1	0	-
17	Mortar**	Zone 2 sand	0.5	-	8:1	0	-
18	Mortar**	Zone 2 sand	0.6	-	10:1	0	-

In all but one experiment and two trial mixes the cement used was "Ferrocrete" rapid hardening cement.

PQC denotes pavement quality concrete

* proportions for 1/3 and 1/2.5 scale ground slabs and 760mm concrete cubes

** 380mm concrete cubes only

Table 3.9

Constants for Apparatus

Apparatus	Constant	Aggregate	Value
Siphon Can	Values of V_b for: (see British Standard 1377)	Zone 2 sand 8mm gravel limestone sand 8mm limestone basalt fine 8mm basalt 'Lytag' barytes	247 ml 259 ml 239 ml 245 ml 185 ml 199 ml N/A N/A
Air entraining meter	Working pressure	All aggregates	0.06 N/mm^2
	Deductions in measured air volume for concretes made from:	sand/gravel basalt limestone barytes 'Lytag'	1.0% 0.6% 0.6% 0% N/A
Sand cone	Dry density	Zone 2 sand passing a 500 m sieve retained on a 250 m sieve.	1.395 Mg/m^3
	Weight remaining in cone	" "	371 g

N/A means that the apparatus is not suitable for use with these materials

Table 3.10

Casting Details and Compaction Times for

Concrete Trial Mixes

Material	Test Mould	Vibration time for each layer s	Thickness of compacted layer mm	Dimensions of tamping foot mm
Lean mix concrete (all aggregates)	100mm cube	See note 1	30-35	50 x 75
Pavement quality concrete (except Lytag)	100mm cube	3	30-35	50 x 75
	500mm x 100mm x 100mm prism	3	30-35	75 x 100
	100mm dia. x 250mm cylinder	See note 2	30-35	-
Pavement quality concrete (Lytag)	10mm cube	3	30-35	See note 3
	500mm x 100mm x 100 prism	3	30-35	See note 3
	100mm dia. x 250mm cylinder	3	30-35	See note 3

Note 1 Lean concretes were vibrated until no further movement of material under the tamping foot was apparent.

Note 2 100mm diameter by 250mm cylinders were hand tamped to the requirements of British Standard 1881 (1970)

Note 3 A 250mm by 300mm by 25mm thick wooden board was placed on top of each mould and vibrated by a rubber head vibrating attachment fitted to the electric hammer.

Table 3.11

Cement Properties

Type	"Ferrocrete" Rapid Hardening
Standard consistence	31.25%
Setting time (Vicat)	initial 192 minutes final 244 minutes
Soundness (Le Chatelier)	value 9mm expansion 1mm

Table 3.12

Typical Strength Test Results for Concrete Trial Mixes

PQC concrete with aggregate:	Cube crushing strength N/mm^2	Beam bending strength (Tensile) N/mm^2 to BS 1881 part 4 (1970)	Cylinder splitting strength (Tensile) N/mm^2
Sand/gravel	38.8	4.85	4.15
Limetone	41.2	5.06	4.43
Basalt	39.6	4.92	4.4
Barytes	37.2	4.66	3.84
'Lytag'	40.7	4.90	4.52

PQC denotes pavement quality concrete

Table 3.13

Computed Values of the Dynamic Modulus of

Elasticity of Concrete

Concrete Aggregate	Wave Speed c mm/μs	Density kg/m³	Modulus of Elasticity kN/m²	Cube Crushing Strength N/mm²	Modulus of Rupture N/mm²	Tensile Strength (Indirect) N/mm²
Basalt	4.0	2350	37.6	35.0	-	-
Sand/gravel	4.0	2350	37.6	33.4	-	-
'Lytag'	3.6	1700	22.6	41.5	4.28	3.38
Barytes	3.1	3400	29.9	42.4	4.54	3.15
Limestone	4.3	2350	44.4	44.0	4.94	3.97
10/1 Sand/cement	2.7	2007	14.2	12.2	-	-
8/1 Sand/cement	3.0	2048	18.8	17.7	-	-
6/1 Sand/cement	-	-	27.0	19.0	-	-
4/1 Sand/cement	3.5	2024	24.1	21.7	-	-
2/1 Sand/cement	-	-	25.7	32.4	-	-
Neat cement	3.3	1796	19.3	33.3	-	-

Table 3.14

Properties of the Clay Used in Experiments

(Naylor's Fireclay)

Plastic limit 23% Liquid limit 42% Plasticity index 19%		
Maximum dry density	1.88 Mg/m^3	at 15.6% optimum moisture content
Undrained triaxial shear strength	120 kN/m^2	at 15.9% moisture content
CBR Value	5.3%	at 15.8% moisture content
Compaction Hammer	4.5 kg	

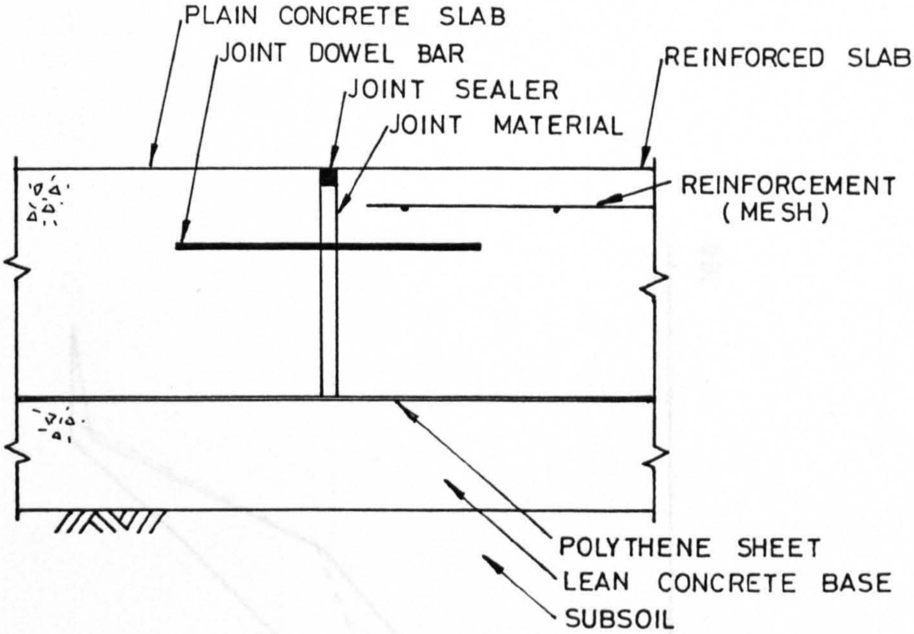

FIGURE 3.1 CROSS SECTION OF A FULL SCALE CONCRETE PAVEMENT (JOINT DETAILS)

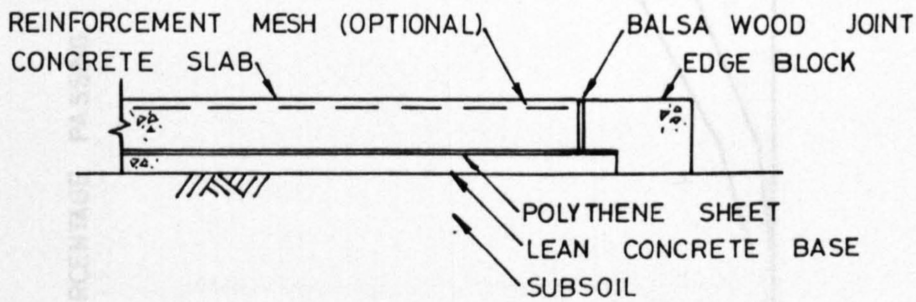

FIGURE 3.2 CROSS SECTION OF A MODEL CONCRETE PAVEMENT

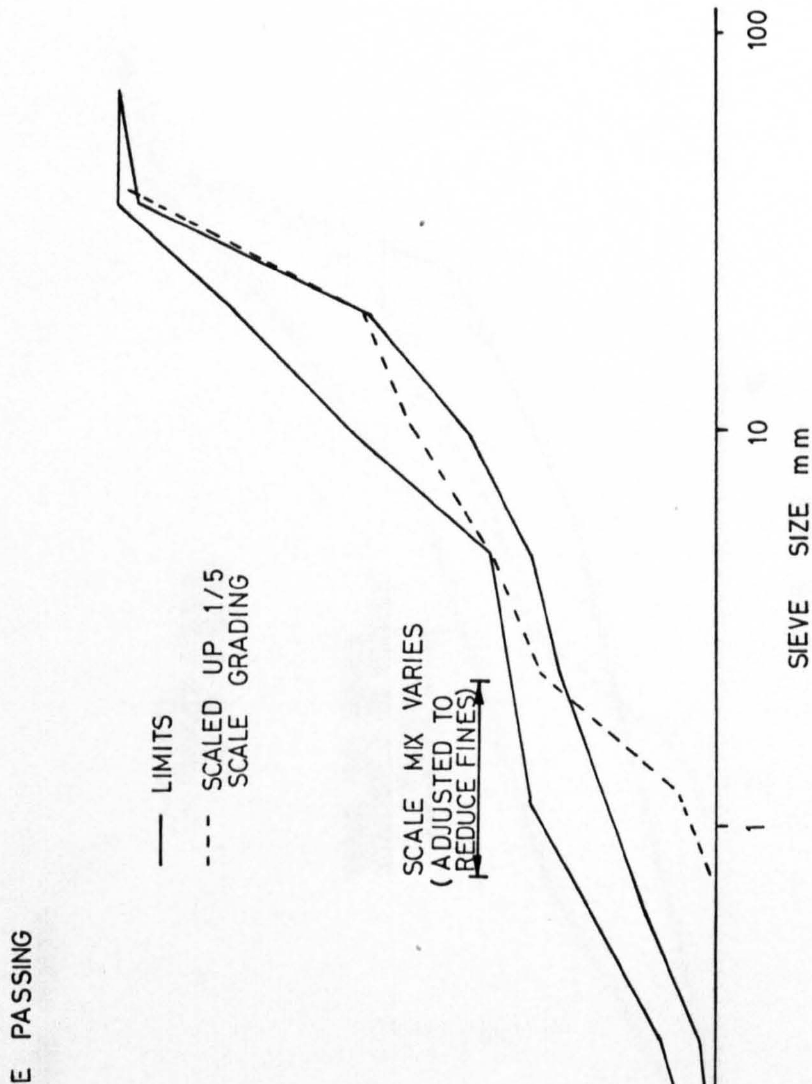

FIGURE 3.3 GRADING LIMITS FOR PAVEMENT QUALITY CONCRETE AGGREGATES (FULL SCALE)

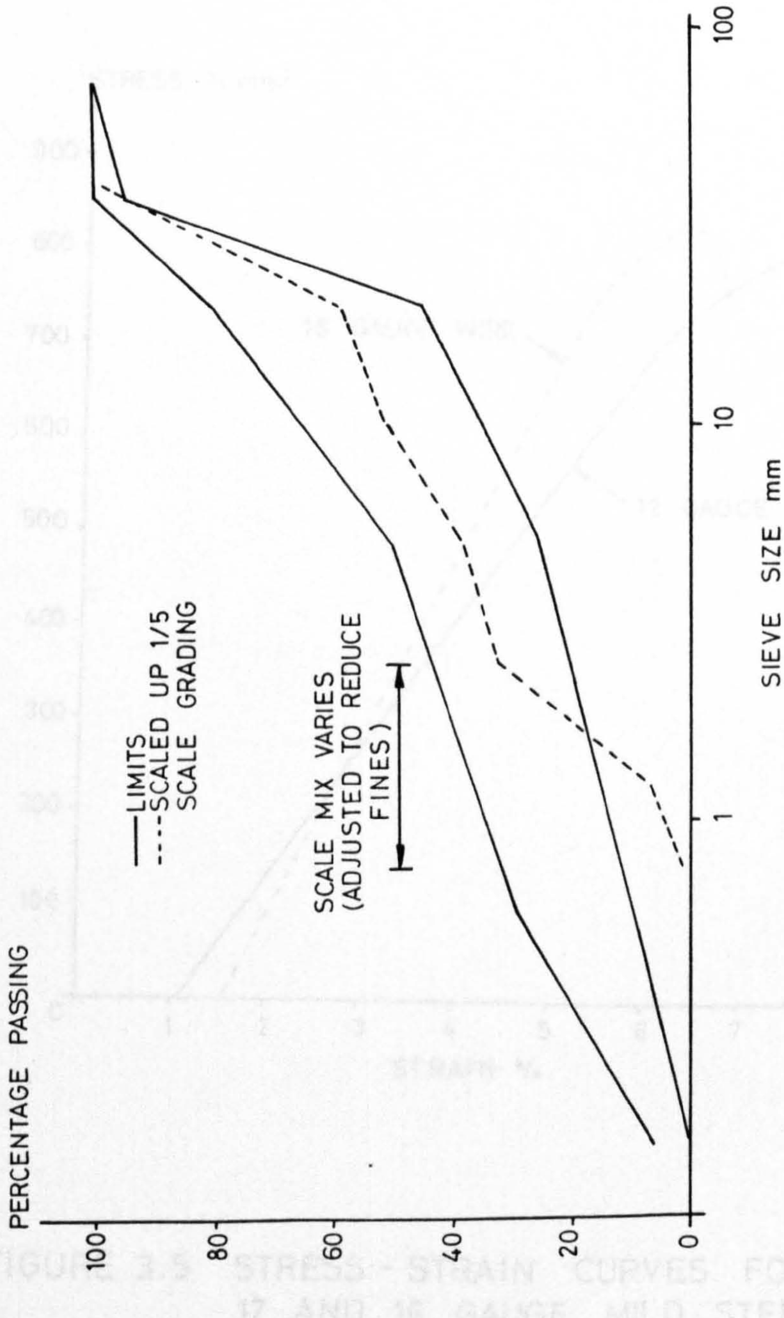

FIGURE 3.4 GRADING LIMITS FOR DRY LEAN MIX CONCRETE AGGREGATES (FULL SCALE)

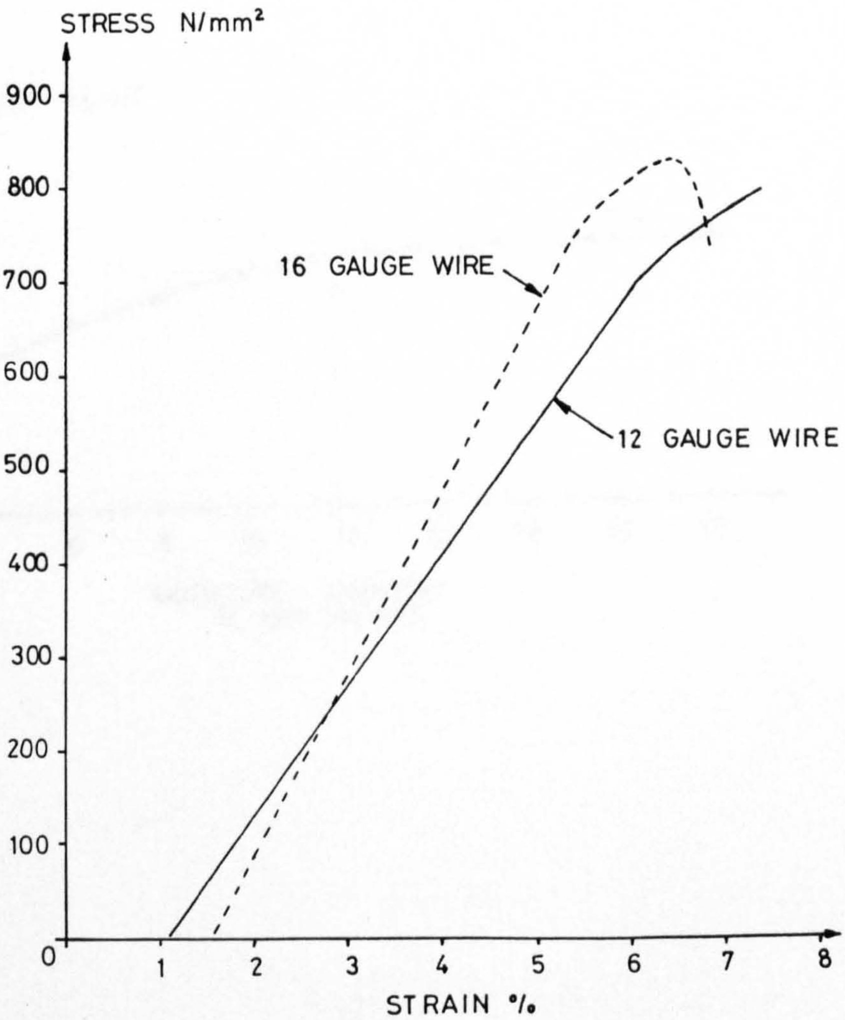

FIGURE 3.5 STRESS - STRAIN CURVES FOR 12 AND 16 GAUGE MILD STEEL WIRE USED AS SCALE REINFORCEMENT IN CONCRETE SLABS

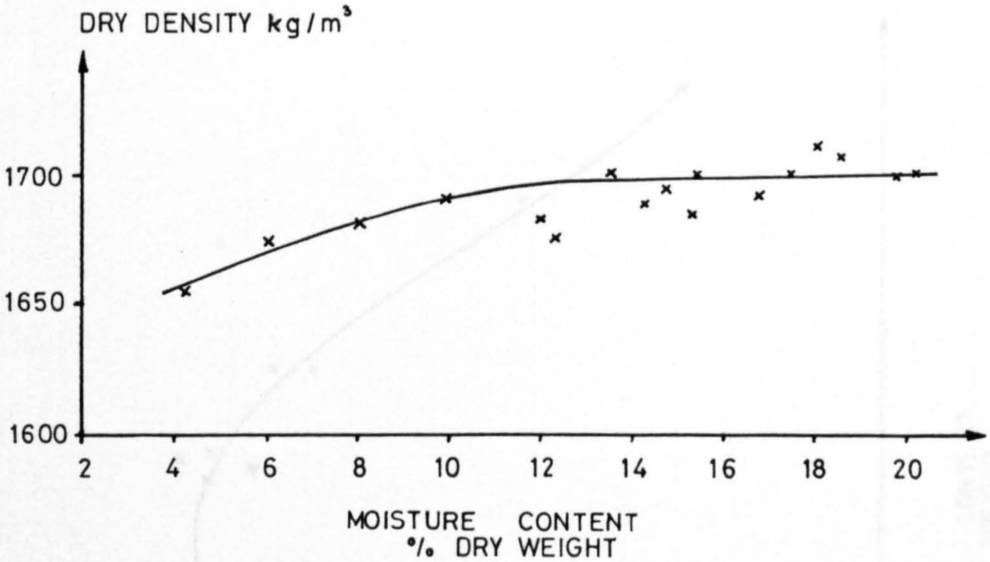

FIGURE 3.6 DRY DENSITY VERSUS MOISTURE CONTENT FOR ZONE 2 SAND

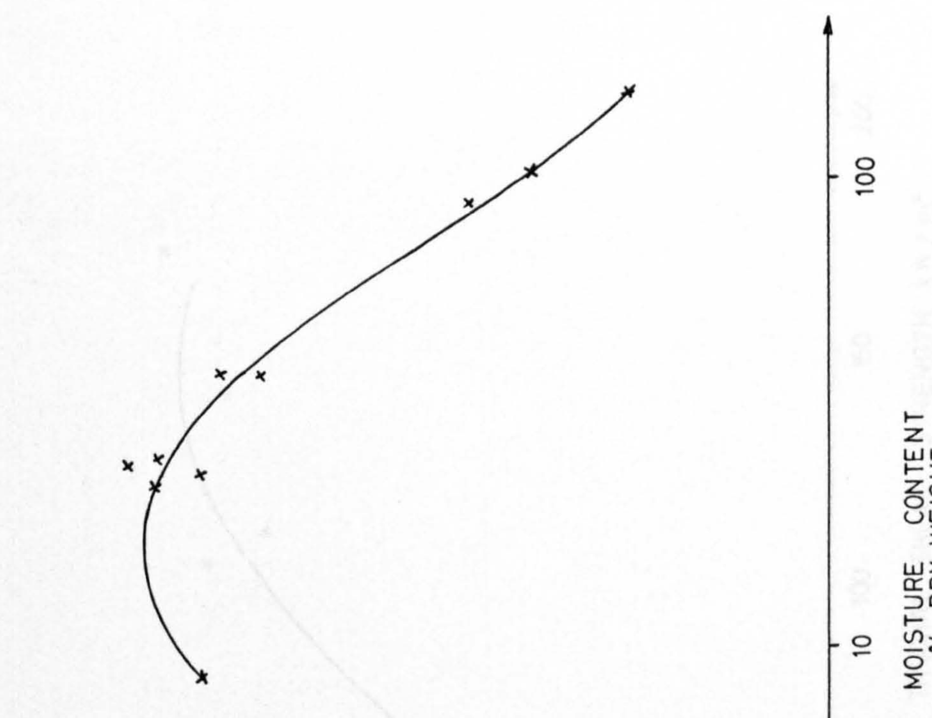

FIGURE 3.7 DRY DENSITY VERSUS MOISTURE CONTENT FOR NAYLOR'S FIRECLAY

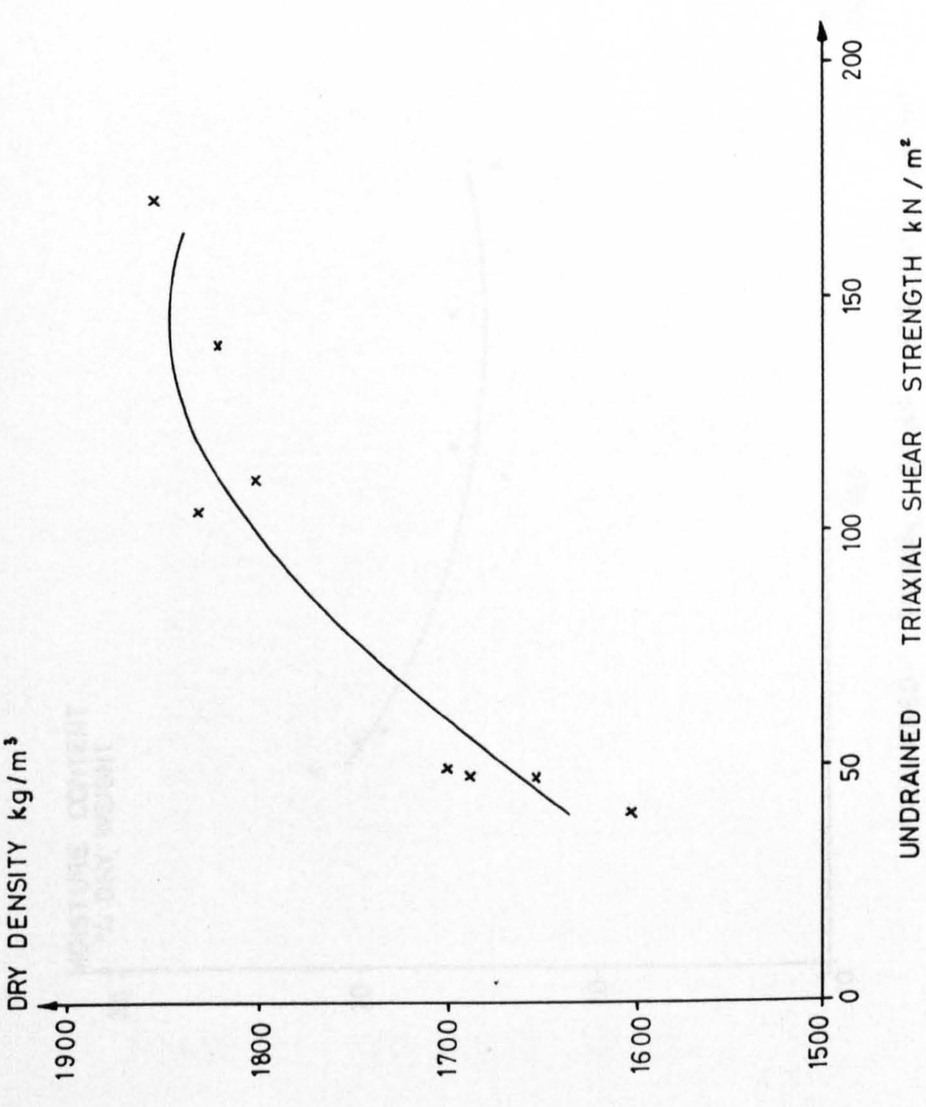

FIGURE 3.8 DRY DENSITY VERSUS UNDRAINED TRIAXIAL SHEAR STRENGTH FOR NAYLOR'S FIRECLAY

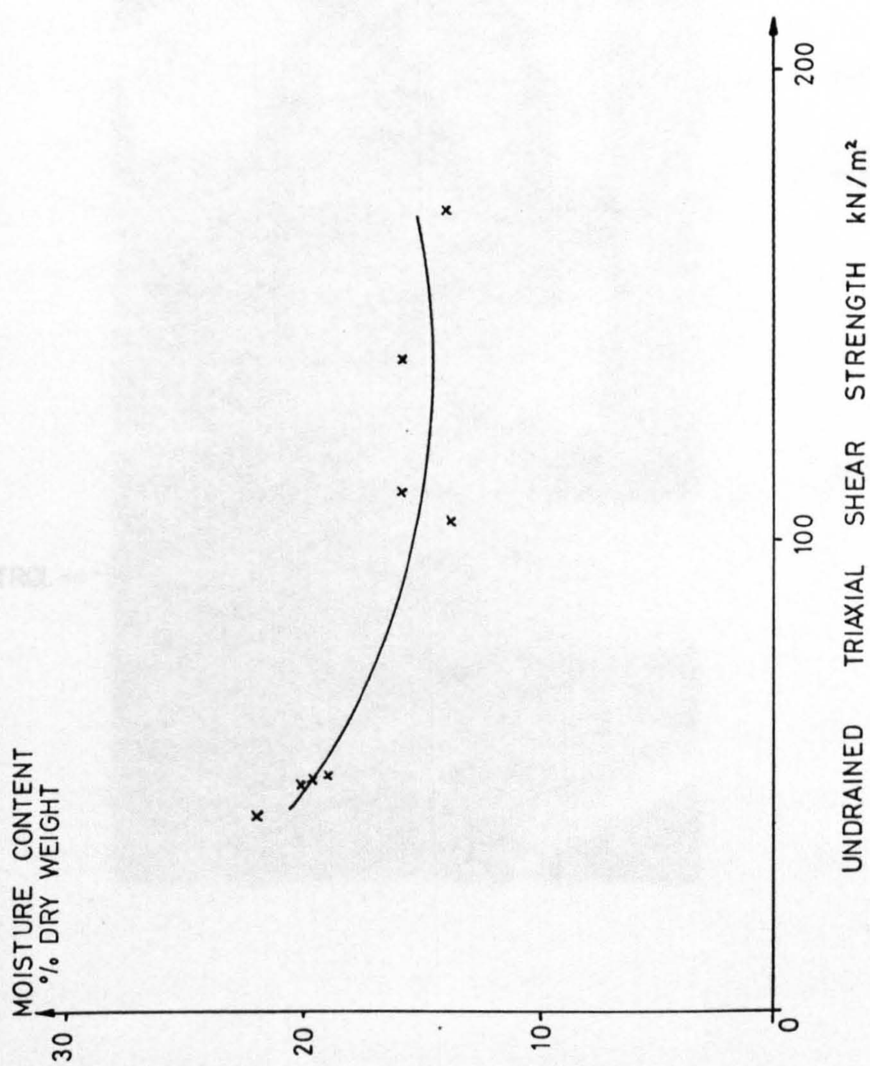

FIGURE 3.9 MOISTURE CONTENT VERSUS UNDRAINED TRIAXIAL SHEAR STRENGTH FOR NAYLOR'S FIRECLAY

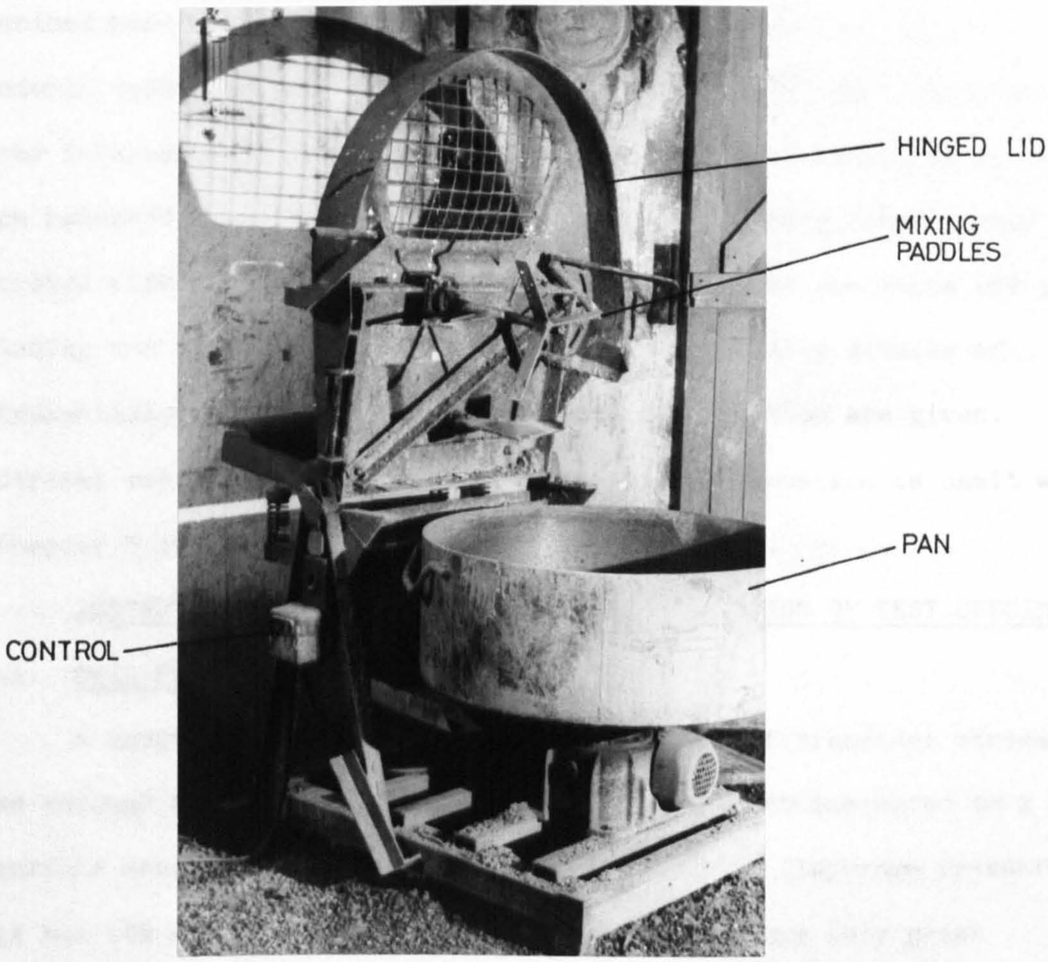

PLATE 3.1 CONCRETE MIXER

CHAPTER 4

THE CONSTRUCTION OF INSTRUMENTATION AND TEST SPECIMENS

Instrumentation was developed in this study as the test programme proceeded. Some methods were improved and the latest developments are described here, these being the most effective. A description of abandoned techniques appears at the end of the chapter for completeness. In the interests of clarity, instrumentation and measurement techniques which required incorporation into test specimens during construction are described first. The methods of construction of test specimens are given including the installation of instrumentation. Finally details of instrumentation applied to specimens after construction are given. Electrical and operational information for instrumentation is dealt with in Chapter 5 in relation to experimental procedures.

4.1 INSTRUMENTATION WORK PRIOR TO THE CONSTRUCTION OF TEST SPECIMENS

4.1.1 Soil Pressure Gauge

A gauge was constructed for the detection of transient stress waves through the subsoil foundation of a ground slab subjected to a subsurface explosion. The gauge was designed as a diaphragm pressure gauge but its relatively crude design could not ensure very great accuracy of measurement. However it would still detect the passage of stress waves and for this reason it was useful for indicating the time of stress wave passage and estimating the order of magnitude of stresses. The gauge is shown in figure 4.1 and consisted of a 6mm mild steel plate onto which an electrical resistance strain gauge had been glued using the following method. The surface of the plate was first ground flat and cleaned with acetone. A thin layer of cyano-acrylate glue was spread onto the cleaned surface and a 20mm long 120Ω Ni/Cu foil strain gauge was firmly pressed onto the glue. After two minutes the glue hardened. Lead wires were soldered to the gauge wires and the whole gauge and connections were covered in silicon rubber to prevent electrical short circuits. The 6mm thick steel plate was then rigidly clamped to a second thick 6mm steel plate using two smaller 6mm thick steel plates as spacers. The gap between the plates was completely sealed with silicon rubber sealant to prevent soil material from subsequently entering the gap.

The gauge was statically calibrated as a beam subjected to central knife edge loading in a compression machine. The stress/strain relationship for the central knife edge load bending moment was recalculated to take into account the uniformly distributed pressure loading assumed to occur with subsurface blasts. It was recognised that any eccentricity in the strain gauge position relative to the calibration loading point would cause errors but since the gauge was a first attempt to monitor subsurface explosions, other considerations such as lack of knowledge of blast pressures and the influence of the soil/gauge interface would have a much greater influence on results. The following calculation gives details of the calibration curve for the gauge which is given in figure 4.2. For calibration purposes the maximum bending moment under a point load = ½ x applied point load x soil gauge length.

Under uniform pressure the maximum bending moment of the gauge would be 1/8 x pressure per unit length x (soil gauge length)^2. By comparing maximum bending moment expressions the action of the uniform pressure per unit length would equal the applied point load divided by 4 x soil gauge length. Hence point load calibration can be equated to blast load pressure.

Figure 4.3 shows the circuit diagram for the strain gauge bridge. The strain gauge in the soil pressure gauge was used in a quarter Wheatstone bridge circuit with three other similar strain gauges fixed to mild steel blocks to provide temperature compensation and balance resistors. The formula for calculating the output from such a strain gauge bridge is well known and for a quarter bridge:

$$\text{Strain} = \frac{4 \text{ x output voltage}}{\text{gauge factor x input voltage}}$$

In a quarter bridge one arm is active and the rest are passive. In half bridge two opposite arms are active and two opposite arms are passive. This system is used to remove strains associated with bending stresses in the strained element and the 4 in the formula is replaced by 2.

4.1.2 Coloured Sand Technique for Soil Movement Detection

The method of determining soil particle movement in the foundations of the ground slabs was developed from a method described by Townsend et al (1961). In Townsend's study columns of coloured sand were used to show lateral soil displacement but the scale of Townsend's experiments was much larger than in this investigation. Townsend formed columns of sand by making holes in the soil and pouring the sand in and this worked because the ratio of the column diameter to the maximum sand particle diameter was large.

In this study, the diameter of the sand columns was to be kept as small as practicable to cause minimum disruption to the soil. In practice 6mm diameter was found to be the smallest practical diameter which meant that very fine grain size sand was required to ensure free flow in the holes forming the column sides. Zone 2 sand to British Standard 882/1201 (1965) was used after being dried for three days in an oven. The dry sand was allowed to cool for a further day and was sieved through a 500µm and a 250µm sieve to British Standard 410 (1976). Only the fraction passing the 500µm and retained on the 250µm sieve was kept. This fraction was then mixed dry with powder paint made by Rowney Ltd at approximately the ratio 10 to 1, sand to paint. Three paint colours were used, crimson, cobalt blue and black to provide contrasts with grey clay and yellow sand. The sand/paint mixture was found to flow easily and because of its single sized grading, it was found to pack without clogging the holes into which it was poured.

4.1.3 'Plasticine' Blocks for Soil Particle Movement Detection

The soil in the foundations to model concrete ground slabs was uniform in colour which did not aid the detection of particle movement under the action of an impacting shaped charge jet. To overcome this in the fireclay, the method chosen was to replace some of the grey clay by a coloured proprietary modelling clay called 'Plasticine' which had similar density. Figures 4.4, 4.5 and 4.6 show the construction details of the three blocks of 'Plasticine' used in this study. The segments for each block were made from different coloured 'Plasticine' in wooden moulds constructed for the purpose. The 'Plasticine' segments of different colours were warmed in a drying oven until they were soft and were then assembled into blocks, care being taken to ensure that adjacent segments were thoroughly joined together. The blocks were rewarmed to enable the joints between segments to completely close and the blocks were then left to cool before further use.

4.1.4 Shaped Charge Jet Penetration Detection Gauge

A gauge was developed to detect the passage of a shaped charge jet, based on the principle that the metal jet conducts electricity.

The jet was used to make a circuit close in the detector gauge thus causing a charged capacitor coupled in parallel to the gauge to be discharged. Figure 4.7 shows the construction and operation of the gauge and figure 4.8 shows the circuit diagram. Each gauge consisted of two brass plates 100mm square by 0.4mm thick and separated by a sheet of ordinary writing paper 140mm square by 7μm thick. The brass plates were taped to each side of the paper and a thick wire was soldered to each plate. For installation in the subsoil under a ground slab or in wet concrete the whole gauge was enclosed in a plastic bag and sealed with electrical insulation tape.

Critical requirements for construction of the gauge were the material thicknesses and the need to use paper which had not been allowed to absorb any moisture. Suitable material thicknesses were found by trial and error and they depend on the distance to be bridged by the jet and continuity between the jet and the brass. It was important to use the minimum of brass to avoid eroding too much of the metal jet. The 0.4mm thick brass was found to be the optimum material. Moisture was a problem because it caused electrical leaks in the detection circuit which were unacceptable where a capacitor was required to maintain an electric charge for any length of time.

4.1.5 Electrical Resistance Strain Gauges for Burial in Concrete

Electrical resistance stain gauges were required to be embedded in concrete test specimens to monitor strains due to transient stresses during testing. The method used was to glue the strain gauges to small precast blocks of concrete and place these into the wet concrete as the test specimens were being constructed. Precast concrete blocks for strain gauges were made in 100mm by 100mm by 500mm beam moulds using the same mixes and method described in section 3.3. After one day the concrete blocks were wire brushed all round to provide a rough surface and cured at room temperature until the fourteenth day when they were sawn up by a wet cut diamond tipped circular saw shown in plate 4.1. Two sizes of blocks were made, 50mm cubes and 50mm x 50mm x 500mm long beams. These were placed in an oven for three days to drive off any moisture.

The sawn surfaces required no further surface grinding and were cleaned with acetone. Immediately after the acetone had evaporated the areas of the surface required for strain gauges were sealed with a thin layer of 'P2' two part epoxy adhesive. After 24 hours a second coat was applied. 20mm long 120Ω Ni/Cu electrical resistance foil strain gauges were located in chosen positions and orientations on the blocks and left for 24 hours. Each gauge was weighted with a small block of metal to ensure it remained wholly in contact with the concrete block. Two plastic coated lead wires were soldered to the wires provided on each gauge and the whole gauge and soldered joints were coated in silicon rubber compound to waterproof and to protect the gauge during installation.

20mm gauges were used throughout the test programme. In practice the gauge should have been three times longer than the maximum aggregate size but this required a gauge 24mm long. In theory the gauge should have been as small as possible to register peak stresses. A long gauge could average short pulses over its length and give an underestimate of the amplitude of the peak stress. However, an estimate of the loading time and the wave propagation velocity in concrete indicated that pulses would be longer than the gauge length and so any averaging effects would be minimised with a 20mm gauge.

Strain gauges on concrete blocks were statically tested in a compression machine to determine a static stress-strain relationship which is a standard procedure in dynamic work. Figure 4.9 contains details of the calibration of the strain gauges which were arranged in quarter Wheatstone bridge arrangement shown in figure 4.3.

The strain gauged concrete blocks were soaked in cold water prior to use, to enable water to soak into the concrete. During casting the absorbed water in the blocks prevented water from being drawn from the fresh concrete and ensured a good bond.

4.1.6 Graphite Rod Spall Detection Gauge

The detection of spalling of concrete from the surface of a test specimen under impact loading was accomplished by a spall detection gauge. The gauge consisted of a graphite rod which was embedded in the concrete and was broken as concrete spalled taking part of the rod with it. An electrical current was continuously passed through the rod which was coupled across a 1MΩ resistor as shown in figure 4.10 and the breaking of the rod was detected by the voltage change across the 1MΩ resistor.

The graphite rods used were 0.5mm diameter by 100mm long clutch pencil leads. A wire was glued to each end of the rod using electrically conducting silver loaded two part epoxy glue supplied by R.S. Components Ltd. The wires and the graphite rods were rigidly held together in blocks of 'Plasticine' modelling clay while the glue was applied and during the one day curing period required to form the joint.

4.2 CONSTRUCTION OF THE TEST SPECIMENS

The following tables summarise the basic data for the experimental programme test specimens.

Tables 4.1 to 4.5	List of test specimens used and instrumentation
Tables 4.6 and 4.7	Properties of pavement and concrete block materials
Table 4.8	Soil foundation properties

Table 4.9	Principal dimensions of main test specimens
Table 4.10	Principal dimensions of minor test specimens

Results quoted are material properties of the specimens as constructed and are not connected with explosion test results.

4.2.1 Construction of Scale Model Concrete Ground Slabs

Scale model concrete ground slabs were constructed to three scales, 1/5, 1/3 and 1/2.5. The method of construction of slabs at all three scales was similar, the only differences being the overall dimensions of the component parts which are listed in table 4.9, and the grading of aggregates for the concrete which is given in table 3.7.

Every ground slab required a soil foundation and in order to retain the soil, a square concrete block wall was built onto the concrete floor of the laboratory. Figure 4.11 shows a cross section through a typical ground slab test bay. Each block wall was double thickness concrete blockwork with mortar in the cavity. Table 4.9 gives the different internal dimensions of the block walls for the soil foundations of 1/5, 1/3 and 1/2.5 scale ground slabs. The mortar in these walls was allowed to cure for two weeks before the test bay was used so that compaction of soil against the wall would not cause damage.

When the soil pressure gauge, described in section 4.1.1, was used it was located on the concrete floor in the test bay under the point of proposed explosions. Sand or clay was introduced into the test bay and compacted in layers using a Kango 950 electric hammer fitted with a tamping foot. Table 4.11 gives full details of the compaction foot, the compaction time for each layer and the thickness of the layer compacted for each scale model soil. These values were derived from preliminary material tests described in section 3.6 and basic material properties are given in Chapter 3.

Sand was compacted at its normal moisture content which in this study was at approximately 3%. After filling the test bay with compacted sand the test bay was flooded with water and left to drain. A layer of polythene was laid over the test bay to prevent evaporation of moisture from the exposed soil surface. In some test specimens water was prevented from draining in order to model a high water table in the soil, a condition which can occur in prototype situations. To prevent drainage occurring a single thickness block wall was constructed around the test bay with a 50mm gap between it and the test bay blockwork. This gap was filled with puddled clay to provide a drainage barrier. The sand in this test bay was flooded in the same way as drained test specimens but sufficient extra water was added to allow for water soaked up by test bay blockwork walls. Seepage under the walls was a problem which was only alleviated by continually replenishing the water in the soil.

Clay for slab foundations was compacted under approximately 75mm of water to ensure that the material was as fully saturated as possible. The water level rose as the test bay was filled with clay. After the test bay was filled the clay was covered by a layer of polythene to prevent evaporation of moisture from the surface. The material was left for four weeks before testing in order to allow the moisture conditions in the material to equalise. Sand was left only as long as other construction details required before testing since moisture movement was complete in less time than the fourteen days required for concrete curing.

After the soil had been compacted the upper surface was trimmed. Scale construction tolerances were derived from the full scale specification for Airfield works (1978), given in table 3.3. For the surface of the soil the scale tolerances on level was -0mm, + 5mm. Both clay and sand foundations were levelled by drawing a metal straightedge across the surface of the soil. This straightedge ran on top of the blockwork wall which had been built to the required scale tolerance. Clay soil was usually levelled after the four weeks allowed for moisture movement but sand was levelled at any time prior to further construction work since moisture migration was not a problem at the surface.

The soil was not subjected to moisture content or in-situ density tests during construction. The only test which was used at this stage was the California Bearing Ratio (CBR) test described in British Standard 1377 (1975). This test involved pushing a plunger a known distance into the surface of the soil and comparing the force required to the force required to push the plunger into a standardised rock sample. Figure 4.12 shows the CBR plunger apparatus connected via a hydraulic jack, which provided the force, to a structural steel frame. This frame spanned the test bay and was bolted to the floor to provide the resistance to the jacking force. Results obtained from CBR tests on scale models are given in table 4.8. Although the test specimens were models, the results were directly comparable with full scale results since neither soils nor the apparatus were scaled.

The surface of the soil was levelled again locally after the CBR tests which were made on four sites on the soil surface half way between the proposed test area and the blockwork walls. The sites were chosen to avoid disturbing the test site and any influences caused by the walls.

For tests which required coloured sand columns a metal frame with a row of 6mm diameter holes was now placed across the centre of the soil mass foundation as shown in figure 4.13. This frame was designed to act as a guide for a 6mm diameter steel rod which was driven into the soil at 50mm intervals. The frame ensured that the rod remained vertical during driving and accurately preserved the 50mm interval. An engraved mark on the rod ensured that each hole was the same depth, 400mm for 1/5 scale models and 600mm for 1/3 scale models. Coloured sand, described in section 4.1.2 was now poured into each hole using a funnel, until the hole was completely filled. The natural moisture in the soil later seeped into the sand and mixed with the powder paint in the coloured sand mixture. Different colours were used so that no two adjacent columns were the same colour. This ensured that any possible lateral movement greater than the 50mm column interval could be easily detected.

Three clay foundations had a hole dug in the surface under the proposed shaped charge impact location. Into the hole was placed one of the three blocks of 'Plasticine' shown in figures 4.4, 4.5 and 4.6, and described in section 4.1.3. Clay was puddled into the gap between the 'Plasticine' block and the boundary of the hole and the soil moisture was allowed to equalise for a further two weeks. The clay was covered with a polythene sheet during this period to prevent evaporation of moisture and shrinkage of the clay away from the 'Plasticine blocks'.

In the case of test specimens which were only to be used with a subsurface explosive charge, it was necessary to prepare a hole in the soil for the charge before any further construction work took place. To form the hole a 22mm diameter steel bar was driven the required depth into the soil at the centre of the soil mass and then removed. A cardboard tube 20mm in diameter was lowered into the hole until it reached the bottom. The tube was longer than the hole depth plus the thickness of a slab and lean mix layer so that it would project above the slab as shown in figure 4.14. The purpose of the tube was to prevent collapse of the sides of the hole and to stop concrete falling into the hole during construction of the slab.

The final operation in preparing the soil foundation was to locate the shaped charge jet penetration detectors described in section 4.1.4 in their positions on the surface of the soil. These gauges were the type enclosed in plastic bags since they would be subjected to wet concrete and soil moisture. In prototype construction lean concrete base is rolled directly onto the prepared formation using metal forms to retain the edge of the material during compaction. In the models the lean mix was compacted in a square metal mould which was used both to retain the edges of the concrete and to regulate the thickness of the material. The mould consisted of a square steel frame constructed from steel angles bolted together. The size of the steel angle was chosen to match the depth of material to be compacted. Table 4.9 gives the dimensions and thicknesses of the lean mix layers used in the three model scales. The mould was laid directly onto the soil mass and levelled using a 1m long builder's level. Small wooden wedges were used to keep the mould level and rigid. Finally Tellus MRO oil was painted onto the mould to aid striking.

Lean mix concrete was batched and mixed according to the method described in section 3.3. The lean mix concrete was compacted into the mould in two layers using a Kango electric hammer fitted with a tamping foot. Table 4.11 gives details of the compaction time and thickness of layers used in all the models. Lean mix concrete was compacted in two equal layers as in prototype construction and excess material above the level of the mould was removed by drawing a steel straightedge across the steel mould. This ensured that the surface level was within the tolerance derived from the specification given in table 3.3. The exposed surface of the lean mix was immediately covered by a layer of polythene to prevent the loss of moisture from the surface.

For each batch of concrete used in the construction four 100mm concrete cubes for crushing strength tests to British Standard 1881 (1970) were cast according to the method detailed in section 3.3 The cubes were placed next to the test specimen to cure for one day at the ambient temperature of the laboratory. After one day the formwork was stripped from both the lean mix layer and the 100mm cubes. The cubes were then stored alongside the test bay until tested at fifteen days. The layer of polythene on the lean mix was left in place to act as an impervious separation layer. Polythene is used in prototype construction and its location is shown in figure 4.11. The 125μm thick polythene sheet used was to scale for 1/5 scale slabs but not for 1/3 and 1/2.5 scale models. It was not possible to obtain material to correctly model at these scales so two layers of 125μm thick polythene were used instead. Shaped charge jet detctors, described in section 4.1.4 were now placed in position on the top of the polythene layer.

The dimensions of pavement quality concrete ground slabs at each scale are given in table 4.9. Formwork for the concrete was constructed from 150mm by 63mm steel channel in the case of 1/5 slabs. For 1/3 scale slabs 108mm by 50mm timber was used and for 1/2.5 scale slabs 130mm by 50mm timber.

Only 1/5 scale slabs were reinforced so each piece of steel channel formwork was prepared to facilitate reinforcement to be fixed in position. The channel was designed to lie flat with both flanges vertical and the flange depth of 63mm corresponded to the thickness of the concete slab. 3mm diameter holes were drilled at 40mm intervals along the inside flange of each piece of channel. This flange was to be the side shutter for the concrete and the holes were located 10mm down from the top of the flange to coincide with the proposed depth of the reinforcement in the slab, that is, 10mm from the upper surface. Figure 4.15 shows the location of these holes in the formwork.

Both the metal and timber types of formwork were bolted together. Each formed a square mould with internal dimensions given in table 4.9 corresponding to the scale of slab to be constructed. The frame was located directly on top of the polythene layer, one day after the lean mix had been cast. This corresponded to full scale ground slab construction practice. The formwork was levelled using a 1m long builder's level and was adjusted by wooden wedges. The slab mould, plus the moulds for 100mm test cubes and the 500mm test beams for British Standard 1881 (1970) tests were oiled with Tellus MRO oil to facilitate shutter striking.

Pavement quality concrete was now batched and mixed as described in section 3.3 and cast into the formwork. The thickness and compaction details for the concrete corresponded to the details given in table 4.11. Small soaked concrete blocks with electrical resistance strain gauges adhering to them as described in section 4.1.5, were located in predetermined positions and orientations as shown in figure 4.16 as construction proceeded. Further fresh concrete was then compacted around the small blocks and care was taken not to damage either them or the strain gauges.

Concrete was cast up to the top of the slab formwork except in the case of reinforced slabs. For these slabs the concrete was left just below the line of holes drilled in the side of the formwork. 12 gauge mild steel wire was threaded through each hole, across the slab and through the corresponding hole in the other side of the formwork. Each wire was individually tensioned by means of a turnbuckle shown in figure 4.15. A mesh of mild steel wire, 16 gauge wire at 40mm centres one way by 12 gauge wire at 20mm centres the other way was laid on these taut wires to act as the reinforcement in the concrete. Further 12 gauge wires were now passed across the slab at right angles to the first set, threaded through holes in the formwork and tensioned by turnbuckles. The wire mesh was thus rigidly held in position between the two sets of wires. Further fresh concrete was now added until the formwork was completely filled.

The surface of the concete was levelled by drawing a straightedge across the formwork. This allowed the slab surface to be finished by a plasterer's float and kept the surface within the scaled tolerance of -0mm to +2mm derived from the specification given in table 3.3. While the concrete was still wet graphite rod spall detectors described in section 4.1.6 were pushed into the concrete at their predetermined locations and orientations as shown in figure 4.17. Six millimetre diameter threaded bars 100mm long were pushed vertically 50mm into the surface of the wet concrete for use with displacement transducers during explosion testing. The slab was then covered by a polythene sheet and left to cure for fourteen days at the ambient temperature of the laboratory.

The fresh concrete was tested for wet density and air content to British Standard 1881 part 2 (1970) and 100mm cubes and 500mm beams were made as described in section 3.3 for strength tests to British Standard 1881 part 4 (1970). The cubes and blocks were cured alongside the slab until tested at fourteen days.

One day after casting, the formwork to the slab and the moulds for the test cubes and beams was stuck. The edges of the concrete were coated in Lithuim grease to prevent loss of moisture and in 1/5 scale models this was also for holding in place strips of balsa wood 1000mm long, 63mm deep and 2mm thick. These strips of balsa were to represent scaled joint material as described in section 3.5, and were merely pushed against the greased concrete, the suction being sufficient to hold them in position. Figure 3.2 shows their location.

1/5 scale model ground slabs were fitted with edge blocks. These were blocks of concrete cast alongside each edge of a slab to simulate the effect of adjacent slabs, found in full scale practice. Figure 4.11 shows their location in the models. Each edge block had a mass equal to one quarter of the mass of a slab since only one quarter of an adjacent slab was assumed to have an influence. The width of the edge blocks was 150mm. The width had been calculated from theoretical stress wave data to prevent the production of reflected tensile stress waves at the free edge of the slab.Section 2.7.2 describes the reflection of incident compression waves on free surfaces.

Formwork for the edge blocks was constructed from 6mm plywood supported by a 'dexion' steel frame. The depth of the formwork, 93mm, was equal to the combined thickness of the slab and lean mix concrete since the blocks extended to the lower limit of the lean mix base course. The balsa wood joint stuck to the free edge of the slab by grease, formed the shutter for the other side of the edge block. The formwork for all four blocks was bolted together for stability and coated with Tellus MRO oil to aid striking. Oil was also poured in the bottom of the edge block shuttering to prevent concrete adhering to the lean mix concrete and the top of the test bay wall.

Concrete for edge blocks was pavement quality concrete. It was batched,mixed and compacted in the same way as the concrete in the adjacent slab, using the method described in section 3.3. Similar aggregate was used, the concrete was air entrained and four 100mm concrete cubes were made for the cube crushing strength test to British Standard 1881 part 4 (1970). The surface of the edge blocks was finished using a plasterer's float to the same level as the adjacent slab. The top of each balsa wood joint between the slab and the blocks was then raked by drawing the edge of the float along the joint to prevent any possibility of concrete laitance bridging the gap. The edge blocks were covered with a polythene sheet to prevent loss of moisture from the surface and cured at the ambient temperature of the laboratory for thirteen days. The four 100mm cubes were cured under polythene sheets alongside the test specimen and tested at thirteen days to coincide with the explosion tests on the test slab.

4.2.2 Construction of Concrete Block Test Specimens

Concrete blocks were constructed in two sizes, 380mm cubes and 760mm cubes. The 380mm cubes were for impacts by 1/5 scale shaped charge jets and the 760mm cubes by 1/2.5 scale jets. 380mm concrete cubes were constructed from all types of pavement quality concrete, and lean mix concrete made from sand/gravel aggregate. 760mm concrete cubes were only constructed from sand/gravel aggregate pavement quality concrete because the availability of explosives was limited.

Formwork for the blocks consisted of 19mm thick plywood sheets braced by 50mm by 50mm timber and bolted together to form a square box. The formwork for the 380mm blocks was bolted to a base consisting of a 25mm thick sheet of timber but the formwork for the 760mm blocks had no base. Instead the four sides of the mould were bolted together and placed on a polythene sheet on a level part of the laboratory floor. The formwork was coated with Tellus MRO oil to aid striking and four 100mm cube and two 500mm long by 100mm by 100mm beam moulds were similarly prepared for making control specimens. One set of beams and cubes was required from each batch of concrete used.

Concrete was batched and mixed as described in section 3.3. Placing and compaction of the concrete were carried out in layers and details are given in table 4.11. During casting small concrete blocks holding electrical resistance strain gauges were located in the concrete as shown in figure 4.16. The procedure was similar to that used for concrete slabs described in section 4.2.1. When the formwork was completely filled with compacted concrete, the concrete surface was levelled by drawing a steel straightedge across and finished with a plasterer's float.

Graphite rod spall detectors described in section 4.1.6 were pushed into the surface of the wet concrete in their predetermined locations and orientations as shown in figure 4.17. The surface of the concrete was covered with a polythene sheet and the specimen was left to cure at the ambient temperature of the laboratory for fourteen days. The formwork was not struck until seven days after casting in order to prevent loss of moisture from the sides of the test specimen. Cube and beam moulds for control specimens were stripped after one day and kept on the surface of the test block under a polythene sheet until they were tested at fourteen days.

4.2.3 Construction of Other Test Specimens

Table 4.10 gives details of the dimensions of all test specimens described in this section of which fourteen were solid blocks of metal. The blocks were machined to give uniform dimensions and square faces. Ten blocks were mild steel cylinders 100mm diameter by 250mm long, two blocks were EN28 steel 80mm diameter by 250mm long and two blocks were aluminium 100mm square section by 250mm long.

Five test specimens consisted of plates. Two of these were composed of copper plates as shown in figures 4.18 and 4.19 respectively. Brass plate shaped charge jet detectors as described in section 4.1.4 were included for penetration rate measurements. The third layered test specimen was a 380mm sand/aggregate concrete cube constructed as described in section 3.3. A 12mm thick 300mm square 'Perspex' plate coated with Tellus MRO oil was placed in the concrete during casting in the position shown in figure 4.20. The plate had been oiled to prevent concrete adhering to it.

The remaining two test specimens were constructed from a stack of plates of sand/gravel pavement quality concrete. Figures 4.21 and 4.22 show the two test specimens, one of which was included in a 1/5 scale ground slab, the construction of which is described in section 4.2.1.

The concrete for these plates was batched and mixed as described in section 3.3. It was then placed in a 200mm square mould constructed from two plates of 12mm thick transparent 'perspex' held rigid and 20mm apart by bolts and spacers. The spacers prevented loss of concrete on two sides and the base. The mould was oiled with Tellus MRO oil and concrete was placed in 25mm layers. It was tamped using a 6mm diameter brass rod from the British Standard 812 (1975) siphon can apparatus and tamping continued until no air spaces were visible through the transparent sides of the mould. The concrete was left for 14 days to cure and then the mould was stripped. The 200mm square concrete plate was now sawn into four 100mm square plates by the diamond tipped saw shown in plate 4.1.

4.3 CONSTRUCTION OF EXPLOSIVE CHARGES AND CHARGE HOLDERS

4.3.1 Shaped Charges

Three types of shaped charge were supplied by the Ministry of Defence for use in this study. 127 copper lined and 15 aluminium lined shaped charges were for use with 1/5 scale test specimens. Six copper lined shaped charges were for use with 1/2.5 scale test specimens. Table 4.12 gives the details of the construction of these three types of charges and figures 4.23 and 4.24 show cross sectional views through the charges for 1/5 scale and 1/2.5 scale tests respectively.

Shaped charges were held in position above the test specimen by holders made in the form of a platform on legs. Figure 4.25 shows a typical charge holder made from 'perspex' and mild steel threaded bar. The standoff and angle of incidence, given in table 4.12 were varied by altering the lengths of the legs. A second or third platform was incorporated as shown in figure 4.25 to hold brass plate jet detectors described in section 4.1.4.

4.3.2 Subsurface Charges

Two subsurface charges were used in 1/5 scale slab tests and one for 1/3 scale. Figure 4.26 shows the three charges and the upper two charges shown were the alternative charges used at 1/5 scale. The explosive used was military plastic explosive known as PE4 activated by either an L2A1 or an EBW type 3 military initiator. The charges were made by cutting the required mass of explosive from a 1 kg stick. The explosive was moulded by hand into the desired shape and taped to a 2mm silver steel rod using electrical insulation tape. The initiator was pushed into the end of the charge and taped to the rod. The joint between the main charge and the initiator was also taped to prevent loss of coupling during installation of the charge under a slab. Table 4.13 gives details of the explosives used.

4.4 INSTRUMENTATION OF TEST SPECIMENS AFTER CONSTRUCTION

4.4.1 Conducting Silver Paint Crack Detector

The method used to detect cracking in concrete was to incorporate a conducting material with the concrete so that any crack would break not only the concrete but also at the same time the conductor. The break in the conductor was detected by electrical means. Cracks in concrete were detected on the concrete surface by painting lines using electrically conducting paint, supplied by R.S. Components Ltd., across the areas of the test specimen which were expected to crack. Figures 4.27 and 4.28 show the typical locations of these painted crack detectors on slabs and blocks respectively.

The surface of the concrete to be painted was first sealed by a layer of varnish dissolved in amyl acetate. This was the same solvent used in the conducting paint. This varnish was left for at least 24 hours to harden. Two brass contacts 100mm square by 0.1mm thick were then glued to the surface of the concrete using two part epoxy adhesive, one at each end of the varnish track. A wire was immediately soldered to each contact so that the heat applied in the soldering process would accelerate the curing of the epoxy adhesive. Conducting silver paint was now applied in a 2mm wide line along the varnished track and over the brass contacts up to the wires themselves. The paint had to be taken to the wire since dirt and solder by-products on the contacts could result in poor electrical conductivity. The paint was allowed to dry and after 24 hours the resistance of the circuit was checked. Values of resistance of 250Ω on 200mm long tracks and up to 1 kΩ on 500mm tracks were the maximum allowed. Values over these limits needed additional paint to be applied usually at the brass contacts to bring the resistance down to within these limits. The limits were set at these values so that the maximum error in the detection circuits would be 0.1%. Figure 4.29 shows the circuit diagram for conducting silver paint crack detectors.

4.4.2 Shaped Charge Jet Velocity Detector

Section 4.1.4 describes the construction of brass plate shaped charge jet detectors. These detectors were used in air, besides being buried in test specimens, to monitor the velocity of shaped charge jets prior to impact. The detectors were placed on 150mm square 'perspex' plates which had 75mm diameter holes machined in them to allow the unhindered passage of a shaped charge jet. Figure 4.25 shows a jet detector holder, which was usually combined with a shaped holder described in section 4.3.1. The jet detector was stretched across the hole and fixed to the 'perspex'plate by insulation tape.

4.4.3 Explosion Blast Detector

In subsurface charge work where an explosive charge was lowered down a hole through the concrete, a detector was located on the surface of the hole to monitor the arrival of the explosive blast. Figure 4.30 shows the location and construction of the gauge which consisted of two brass plates, separated by a piece of ordinary writing paper. The materials used were the same as in the construction of shaped charge jet detectors described in section 4.1.4, that is, 0.4mm thick brass and 7μm thick writing paper. The paper did not completely separate the brass strips so that when the explosion gases arrived, they would be able to cause the brass strips to touch. These plates were incorporated into an electrical circuit similar to the circuit used for shaped charge jet detection. It is shown in figure 4.31.

4.4.4 Displacement Gauge

The vertical displacement of ground slabs under shaped charge jet impact loading was measured by a potentiometric linear variable displacement transducer. This was a Novatech R102 25Ω wire track transducer supplied by Novatech Ltd., Croydon, and it worked on the potentiometer principle. A push rod in the device moved a potential splitter along a resistance wire, the change in resistance being related to the change in displacement. The device was rigidly mounted to a 150mm by 150mm rolled steel joist spanning over the test specimen and is shown in figure 4.32. The push rod was then screwed to the piece of 6mm diameter mild steel threaded bar cast in the slab during construction as described in section 4.2.1. The displacement of the slab was measured during the test relative to the rolled steel joist which was independent of the test specimen and did not move. Figure 4.33 shows the circuit diagram used with the gauge.

4.4.5 High Speed Photography

Both shaped charge jet impact and subsurface explosion tests were recorded photographically. A Barr and Stroud high speed rotating mirror camera supplied by Hadlands Ltd., Hemel Hempstead, and shown in plates 4.2 and 4.3 was used. This camera was capable of taking 30 pictures at interframe times of between 0.5μs and 15μs though in practice only five interframe times were used because of lighting difficulties. Figure 4.34 shows the location of the camera and its flash light relative to the test specimen.

4.5 TECHNIQUES ABANDONED OR IMPROVED

4.5.1 Coloured Sand Column Technique for Measuring Soil Particle Movement When Used With Shaped Charges

The technique described in sections 4.1.2 and 4.2.1 was only used for subsurface explosions. For soil particle movement under shaped charge jet impact 'plasticine' was used in clays as described in sections 4.1.3 and 4.2.1. In sands columns of coloured sand were tried but the diameter of the resulting impact hole was small and disruption of the soil so minimal that the system did not work well. A second problem was the accuracy of positioning the columns under the expected impact point in relation to the expected hole diameter and disruption zone.

4.5.2 Electrical Resistance Strain Gauges as Crack Detectors

Instead of conducting silver paint crack detectors as described in section 4.4.1, foil electrical resistance strain gauges were tried as an alternative. Problems were encountered in achieving an adequately smooth ground surface on the concrete specimens for the gauges to adhere to. The only satisfactory surface was a concrete surface cast against a steel form. However in this study such surfaces were rarely available. The second problem was using a long enough gauge to cover the large area where a crack could form. It was possible to predict cracking areas but not with sufficient accuracy to allow the use of even 100mm long gauges.

Foil gauges were used in preference to wire so that cracking would be more likely to break them. However the suitability of epoxy resin glue was questionable and in some cases the glue yielded before the gauge thus giving a poor signal.

4.5.3 RACAL Timers

RACAL timers were used prior to and later in conjunction with a GOULD OS4000 storage oscilloscope, described in Chapter 5 . The major problem was that the signals from instruments could not be observed. Any events being timed need not be the actual events if the signals were jumbled or had a large interference component. In addition the timers tended to interfere with each other and the oscilloscope. This tended to trigger start and stop circuits and the oscilloscope trigger circuit. For these reasons the use of timers was abandoned and all subsequent tests were monitored on the oscilloscope screen. This enabled the signals to be interpreted better.

4.5.4 Resistance Circuit for Shaped Charge Jet Detector

Figure 4.8 shows the capacitance circuit used for shaped charge jet detectors described in sections 4.1.4 and 4.4.2. This circuit was used in preference for shaped charge jet detectors even though each detector required a separate recording channel. The resistance circuit shown in figure 4.35 was used initially but the signal received was poor even when only one gauge was used. In the diagram three gauges are shown. In theory as the shaped charge jet shorted out each gauge the change in overall resistance of the circuit should have been recorded as a discrete voltage change. In practice once the jet passed a gauge the short circuit at that gauge tended to open and caused a second voltage change. This resulted in confusing traces and was abandoned.

Table 4.1

List of Test Specimens and Instrumentation Details

for Shaped Charge Tests on Slabs

Specimen	No. of impacts	Aggregate	Instrumentation	Purpose of test	Remarks
S1	1	SG		Initial damage data	
S2	1	SG		Initial damage data	Reinforced
S3	1	SG		Initial damage data	
S4	1	SG		Initial damage data	Reinforced
S5	1	SG		Boundary effect on cracking. Impact damage by another projectile	
S6	1	SG		Initial damage data	O.P.C.
S7	1	SG		Initial damage data	
S8	1	LIM		Initial damage data	
S9	1	SG	CD	Crack detection	
S10	1	SG	PW	Crack detection	
S11	1	SG	PW PB	Crack detection Particle movement	
S12	1	SG	PB	Target size effects	500mm square slab
S13	1	SG	DT	Displacement	
S14	1	SG	SG HSP	Stress analysis	
S15	3	SG	JD	Damage and Charge repeatability. Variation of concrete aggregates.	
S16	3	SG	JD	"	
S17	3	LIM	JD	"	
S18	3	LIM	JD CD	"	
S19	3	LIM	JD PD	"	
S20	3	LIM	JD PD	"	Reinforced
S21	3	BAR	JD CD	"	
S22	3	BAR	JD CD	"	
S23	3	LYT	PD	"	
S24	3	LYT	PD	"	
S25	1	SG	SG	Stress analysis	
S26	1	SG	SG	Stress analysis	
S27	3	SG	SG	Stress analysis	
S28	1	SG	PD	Repeatability of results	
S29	1	SG		Influence of oblique impacts	
S30	1	SG		Influence of oblique impacts	
S31	1	SG	CD	Target size effects	1.67m square slab
S32	1	SG		Scale effects	298g charge 760mm square slab
S33	5	SG	JD CD PD	Comparison between copper and aluminium charge damage	Aluminium and copper lined charges
S34	5	SG	JD CD PD	"	Aluminium and copper lined charges

For explanation of abbreviations see Table 4.5

Table 4.2

List of Test Specimens and Instrumentation Details

for Shaped Charge Tests on Concrete Blocks

Specimen	No. of impacts	Aggregates	Instrumentation	Purpose of test	Remarks
B1	1	SG		Initial damage data	
B2	1	SG		Initial damage data	
B3	1	SG		Age effects	
B4	1	LIM		Initial damage data	
B5	1	BAR	JD	Information on jet velocities	
B6	1	LYT	JD	"	
B7	1	SG	CD	Crack detection	
B8	1	SG	PD	Penetration measurement	
B9	1	LYT	CD	Crack detection	
B10	1	SG	PD	Penetration measurement	
B11	1	SG	SG	Stress analysis	
B12	1	SG	SG	Stress analysis	
B13	1	LYT	CD	Crack detection	
B14	1	BAR	CD	Crack detection	
B15	1	SG		Charge standoff variation	
B16	1	SG	JD	"	
B17	1	SG	JD	"	
B18	1	SG	JD	"	
B19	1	SG		"	
B20	1	SG		Influence of oblique impact	
B21	1	SG	JD	Influence of modified impacting jet	
B22	1	SG	JD	"	
B23	1	SG	JD	"	
B24	1	SG	JD	"	
B25	1	C		Influence of cement content in the mix	
B26	1	SG	Perspex plate insert	Investigation of local damage	
B27	1	SC		Influence of cement content in the mix	
B28	1	SC		"	
B29	1	SC		"	
B30	1	SC		"	
B31	1	SC		"	
B32	1	SG	CD SG	Stress analysis	
B33	1	SG	CD SG	"	
B34	1	SG	CD SG	"	
B35	1	SG	CD SG	"	
B36	1	SG	CD SG	"	
B37	1	SG	CD SG	"	
B38	1	BAS	CD SG	"	
B39	1	BAS	CD SG	"	
B40	1	BAS	CD SG	"	
B41	1	LIM	CD SG	"	
B42	1	LIM	CD SG	"	
B43	1	SG	SD	Break up and particle movement	
B44	1	SG	SD	"	

Table 4.2 cont'd

Specimen	No. of impacts	Aggregates	Instrumentation	Purpose of test	Remarks
B45	1	SG		Standard block for comparison purposes with aluminium charge tests	
B46	1	SG		Modified charge initiation	
B47	1	SG		Initial damage data	Aluminium lined charge
B48	1	SG	CD	Damage and charge repeatability	"
B49	1	SG	JD SP	Variation of concrete aggregates	"
B50	1	LYT	SD CD	"	"
B51	1	LIM	JD CD	"	"
B52	1	SG	CD	"	"
B53	1	SG	HSP	Break up and particle movement	
B54	1	SG	HSP	"	
B55	1	SG	HSP	"	
B56	1	SG	HSP	"	
B57	1	SG	HSP	"	
B58	1	SG	HSP	"	
B59	1	SG	HSP	"	
B60	1	SG	JD	Scale effects	298g charge
B61	1	SG	JD	"	" "
B62	1	SG	CD	"	298g charge
B63	1	SG	SG	"	" "
B64	1	SG	SG	"	" "
B65	1	SG		Liner effects	Unlined charge

For explanation of abbreviations see Table 4.5

Table 4.3

List of Test Specimens and Instrumentation for Shaped Charge Tests on Other Materials

Specimen	No. of impacts	Instrumentation	Purpose of test	Remarks
M1	1	JD	Charge repeatability	Mild steel block
M2	1	JD	"	"
M3	1	JD	"	"
M4	1	JD	"	"
M5	1	JD	"	"
M6	1		"	"
M7	1		"	"
M8	1		"	"
M9	1		"	"
M10	1		"	"
M11	1	JD	Data for calculations	EN28 steel
M12	1	JD	"	"
M13	1		"	Steel block. Aluminium lined charge
M14	1	SG	"	Copper lined charge. Aluminium block.
M15	1		"	Aluminium block. Aluminium lined charge.
M16	1	PD	"	Copper plate stack
M17	1	PD	"	Copper plate stack
M18	1	PD	"	Concrete plate stack
M19	1	JD	Particle movement data	Plasticine block

For explanation of abbreviations see Table 4.5

Table 4.4

List of Test Specimens and Instrumentation for Subsurface Charge Tests on Concrete Slabs

Specimen	Size of charge gms	Aggregate	Soil	Instrumentation	Purpose of test	Remarks
U1	16	SG	S		Initial damage data	
U2	16	SG	S		"	Reinforced slab
U3	16	SG	C		"	
U4	16	SG	C		"	Reinforced slab
U5	16	SG	S		"	
U6	16	SG	S	HSP	Observation of events	
U7	16	SG	S		Influence of not forming the hole explosively	No shaped charge used
U8	16	SG	S	CSC	Particle movement measurement	
U9	16	SG	S	CSC	"	No shaped charge used
U10	16	SG	S	CSC	"	
U11	16	SG	C	CSC SPG	"	
U12	74	SG	S	CSC	Scale effects	No shaped charge used

For explanation of abbreviations see Table 4.5

Table 4.5

List of Abbreviations Used in Tables 4.1 to 4.4

Abbreviations used for instrumentation

CD	Conducting silver paint crack detectors
CSC	Coloured sand columns
DT	Linear variable displacement transducer
HSP	High speed photography
JD	Brass plate shaped charge jet detector
PB	'Plasticine' block to reflect soil particle movement
PD	Brass plate shaped charge jet penetration detector
PW	Paint wash on concrete surface
SD	Graphite rod spall detector
SG	Electrical resistance strain gauge
SPG	Soil pressure gauge

Abbreviations used for aggregates

BAR	Barytes
BAS	Basalt
C	Neat cement only
LIM	Limestone
LYT	'Lytag' lightweight aggregate
SC	Sand/cement mortar
SG	Sand and gravel

Abbreviations used for soils

C	Clay
S	Sand
SS	Saturated sand

Table 4.6

Properties of Pavement Materials

Specimen	PQC crushing strength N/mm²	PQC Air. content %	Lean mix crushing strength N/mm²	Concrete Mix Ref. to Table 3.8	Age at test date. days	Remarks
S1/U1	43.9	5.3	11.7	1&7	64	
S2/U2	44.1	4.3	12.4	1&7	56	Reinforced
S3	56.6	4.4	17.4	1&7	20	
S4/U3	34.6	4.5	13.1	1&7	7	
S5	31.0	3.9	12.8	1&7	11	
S6	34.5	3.6	12.8	1&7	28	O.P.C.
S7/U4	23.3	3.4	11.3	1&7	7	Reinforced
S8	37.9	2.5	11.7	2&8	7	
S9/U5	41.8	4.4	12.4	1&7	14	
S10	43.6	2.8	17.1	1&7	9	
S11	46.8	4.5	10.1	1&7	14	
S12	46.8	4.5	10.1	1&7	15	
S13	38.1	4.6	12.3	1&7	43	
S14/U6	51.9	5.2	11.3	1&7	105	
U7	38.8	4.2	14.3	1&7	21	
S15	33.8	6.5	10.1	1&7	14	
S16	37.3	4.6	13.3	1&7	14	
S17	48.3	4.7	19.9	2&8	14	
S18	47.1	3.0	19.6	2&8	14	
S19	42.4	4.1	21.2	2&8	14	
S20	30.9	4.1	21.2	2&8	14	Reinforced
S21	35.2	4.5	17.3	5&11	14	
S22	45.5	4.2	40.3	5&11	14	
S23	42.9	3.0-6.0*	33.4	4&10	14	
S24	40.2	3.0-6.0*	34.0	4&10	14	
S25/U8	38.0	4.3	12.7	1&7	127	
U9	49.5	4.1	16.6	1&7	14	
S26/U10	26.0	6.0	14.8	1&7	126	
S27	52.8	3.1	17.7	1&7	120	
S28/U11	32.3	4.5	11.6	1&7	22	
U12	32.3	4.5	10.6	6&12	15	1/3 scale
S29	29.2	4.6	12.5	1&7	14	
S30	29.2	4.9	12.3	1&7	13	
S31	39.2	3.6	13.0	1&7	130	
S32	20.4	3.0-6.0*	18.8	6&12	14	1/2.5 scale
S33	36.1	4.1	-	1&7	14	
S34	36.4	4.4	-	1&7	14	

* Lightweight aggregate. Air content calculated.

O.P.C. Ordinary Portland Cement

Table 4.7

Properties of Concrete Block Materials

Specimen	PQC crushing strength N/mm^2	PQC air content %	Concrete mix code to Table 3.8	Age at test date. days	Remarks
B1	43.4	4.0	1	14	
B2	59.9	4.6	1	223	
B3	31.7	4.6	1	91*	
B4	59.0	3.6	2	108	
B5	35.6	3.6	5	129	
B6	43.2	3.0-6.0**	4	134	
B7	16.4***	0	1	118	
B8	30.8	3.0	1	14	
B9	33.2	3.0-6.0**	4	21	
B10	30.1	4.5	1	14	
B11	19.3	4.5	1	15	
B12	23.5	4.2	1	14	
B13	32.8	3.0-6.0**	4	15	
B14	32.0	3.9	5	14	
B15	20.2	4.2	1	12	
B16	18.2	3.8	1	17	
B17	17.7	4.1	1	16	
B18	31.1	3.8	1	15	
B19	35.7	4.1	1	14	
B20	20.7	6.0	1	66	
B21	18.6	5.5	1	50	
B22	17.2	-	1	81	
B23	17.2	-	1	80	
B24	34.8	-	1	77	
B25	33.3	-	1	77	Perspex sheet buried
B26	31.3	-	13	63	Neat cement
B27	19.0	-	16	14	
B28	32.4	-	14	13	
B29	12.2	-	18	76	
B30	17.7	-	17	76	
B31	21.7	-	15	75	
B32	31.3	4.6	1	132	
B33	29.7	4.0	1	131	
B34	26.9	3.8	1	132	
B35	18.4	4.6	1	85	
B36	20.2	4.7	1	131	
B37	22.1	4.5	1	130	
B38	12.1	4.5	3	43	
B39	16.9	5.1	3	43	
B40	21.0	4.5	3	43	
B41	34.1	4.0	2	43	
B42	28.0	3.7	2	43	
B43	19.7	3.9	1	5	
B44	19.6	4.0	1	5	
B45	36.0	4.0	1	14	
B46	33.4	4.2	1	14	
B47	37.2	3.7	1	14	
B48	41.8	4.0	5	14	
B49	24.0	4.7	3	14	
B50	40.1	3.0-6.0**	4	14	

Table 4.7 cont'd

Specimen	PQC crushing strength N/mm^2	PQC air content %	Concrete mix code to Table 3.8	Age at test date days	Remarks
B51	22.5	4.5	2	14	
B52	36.1	4.0	1	14	
B53	20.2	4.2	1	15	
B54	34.2	4.3	1	(14)	Same mix Strength is at 14 days. Tested at various dates
B55	34.2	4.3	1	(14)	
B56	34.2	4.3	1	(14)	
B57	34.2	4.3	1	(14)	
B58	34.2	4.3	1	(14)	
B59	34.2	4.3	1	(14)	
B60	32.5	4.6	6	14	1:2.5 scale
B61	51.9	4.5	6	14	
B62	43.5	4.5	6	14	
B63	43.4	4.6	6	14	
B64	23.4	4.7	6	14	
B65	31.7	4.6	1	91*	

Notes

* Air blast at 91 days. Shaped charge at 355 days

** Lightweight aggregate. Air content calculated

*** Lean mix concrete

Table 4.8

Soil Foundation Properties

Specimen	Soil type	Dry density Mg/m^3	Degree of saturation %	Moisture content %	Remarks
S1/U1	Sand	1.80	36	6.5	CBR 4.0%
S2/U2	Sand	1.73	34	6.5	CBR 3.6%
S3	Sand	1.80	15	2.6	CBR 5.2%
S4/U3	Clay	1.84	97	16.3	CBR 2.5%
S5	Sand	1.80	16	3.0	CBR 4.9%
S6	Sand	1.80	16	3.0	CBR 4.9%
S7/U4	Clay	1.91	88	13.0	CBR 2.6%
S8	Sand	1.80	18	3.3	CBR 4.8%
S9/U5	Sand	1.78	59	11.1	Test bay flooded prior to test
S10	Clay	1.87	88	14.0	CBR 2.8%
S11	Clay/Plasticine	1.89	-	-	Clay untouched by shaped charge jet
S12	Clay/Plasticine	1.89	-	-	Clay untouched by shaped charge jet
S13	Sand	2.00	17	3.5	CBR 4.8%
S14/U6	Sand	1.95	100	26.3	Water table maintained immediately below lean mix
U7	Sand	1.91	29	4.2	CBR 4.0%
S15	Sand	1.88	25	3.9	CBR 4.0%
S16	Clay	1.88	87	13.6	CBR 2.9%
S17	Sand	1.87	24	4.1	CBR 4.0%
S18	Clay	1.99	97	3.9	CBR 4.7%
S19	Sand	1.77	22	4.2	CBR 4.1%
S20	Sand	1.77	22	4.2	CBR 4.2%
S21	Sand	1.76	20	3.8	CBR 4.0%
S22	Clay	1.83	82	14.1	CBR 3.1%
S23	Sand	1.97	28	3.5	CBR 4.6%
S24	Clay	1.85	79	15.5	CBR 2.5%
S25/U8	Sand	2.0	24	3.1	CBR 4.9%
U9	Sand	1.82	23	4.1	CBR 4.1%
S26/U10	Sand	1.80	15	3.7	CBR 4.0%
S27	Sand	1.86	17	2.7	CBR 5.0%
S28/U11	Clay	1.95	100	15.1	CBR 2.7%
U12	Sand	2.14	66	6.0	Test bay flooded prior to test
S29	Clay	1.95	100	15.1	CBR 2.7%
S30	Sand	1.86	17	2.7	
S31	Sand	1.84	17	2.5	CBR 5.0%
S32	Sand	1.96	24	3.0	
S33	Clay	1.91	88	12.9	
S34	Sand	1.80	36	6.5	

CBR California Bearing Ratio

Table 4.9

Principal Dimensions of Main Test Specimens

Specimen	Number of tests	Scale	DIMENSIONS			
			Subsoil	Lean mix	Concrete	Ref. Number
Ground slab	35	1/5	(Internal dimensions of square blockwork wall) 1100mm x 1100mm x 470mm deep	1100mm x 1100mm x 30mm thick	1000mm x 1000mm x 63mm thick*	S1 to S30, S33 and S34**
Ground slab	1	1/3	1670mm x 1670mm x 940mm deep	1670mm x 1670mm x 50mm thick	1670mm x 1670mm x 108mm thick	S31
Ground slab	1	1/2.5	760mm x 760mm*** x 760mm deep	760mm x 760mm*** x 60mm thick	760mm x 760mm*** x 130mm thick	S32
Block	54	1/5	-	-	380mm cube	B1 to B53 and B65
Block	5	1/2.5	-	-	760mm cube	B60 to B64
Block	6	-	-	-	100mm cube	B54 to B59

*** Lateral dimensions reduced for practical purposes from 2m to 0.76m

** Includes three slabs for tests U1, U9 and U12 on which shaped charges were not used

* Slab 12 was sawn down to 500mm by 500mm by 63mm thick for target size effects

Table 4.10

Principal Dimensions of Minor Test Specimens

Type	No.	Material	Dimensions	Notes
Cylinder	11	Mild Steel	100mm diameter by 250mm long	M1 to M10 and M13
Cylinder	2	EN28 steel	80mm diameter by 250mm long	M11 and M12
Block	2	Aluminium	100mm by 100mm by 250mm long	M14 and M15
Plate	1	'Perspex'	300mm by 200mm	'Perspex' is methyl methacrylate. Plate was encased in PQC concrete (Block B26).
Plate stack	1	Copper	75mm by 75mm by 144mm thick	12 plates each 12mm thick placed in a stack (M16).
Plate stack	1	Copper	75mm by 75mm by 210mm thick	As above except 6mm air gaps introduced between plates by using four 6mm perspex spacers between each pair of plates (M17).
Plate stack	1	Concrete	100mm by 100mm by 20mm thick	Sand/gravel aggregate concrete (M18).
Plate stack	1	"Plasticine"	See figure 4.6	(M19)

Table 4.11

Compaction Details for Materials Used in Test Specimens

Material	Thickness of compacted layer (mm)	Vibration time for each layer (secs)	Size of compaction foot (mm by mm)	Test specimens
Clay soil	70-80	5	100 x 150	1/5, 1/3 and 1/2.5 scale model ground slabs
Sand soil	70-80	3	100 x150	
Lean mix concrete (All aggregates)	15 25 30 30-35	See note 1 " " "	100 x 150 100 x 150 100 x 150 50 x 75	1/5 scale ground slabs 1/3 " " " 1/2.5 " " " 100mm test cubes
Pavement quality concrete (Except Lytag aggregate concrete)	20-25 50-60 60-70 30-35 30-35	3 5 5 3 3	100 x 150 100 x 150 100 x 150 50 x 75 75 x 100	1/5 scale ground slabs 1/3 scale ground slabs 1/2.5 scale ground slabs 380mm cubes 760mm cubes 100mm test cubes 500mm by 500mm by 100mm test beams 100mm diameter by 250mm test cylinders (see note 2)
Pavement quality concrete (Lytag aggregate concrete)	20-25 60-70 30-35	3 3 3	See note 3 See note 4 See note 4	1/5 scale ground slabs 380mm cubes 100mm test cubes 100mm by 100mm by 500mm test beams

Notes

1. Lean mix concretes were vibrated until no further movement of material under the tamping foot was apparent.

2. 100mm diameter by 250mm long pavement quality concrete test cylinders were hand tamped to the requirements of British Standard 1881 Pt. 2 (1970).

3. A 250mm by 300mm by 25mm thick wooden board was placed on the wet concrete and vibrated by a rubber head vibrating attachment fitted to the electric hammer.

4. The formwork for the specimen was vibrated by a rubber head vibrating tool fitted to the electric hammer.

Table 4.12

Details of Shaped Charges

Number	127 No.	15 No.	6 No.
Type	1/5 scale 43g	1/5 scale 43g	1/2.5 scale 298g
Liner material	Copper	Aluminium	Copper
Liner thickness	0.36mm	0.92mm	1.52mm
Core angle	85°	85°	62.5°
% tuncated	80%	80%	80%
Booster	Tetryl	Tetryl	Tetryl
Booster mass	1.24g	1.24g	19.4g
Main charge	RDX/TNT 60/40	RDX/TNT 60/40	RDX/TNT 60/40
Main charge mass	43g	43g	298g
Diameter (inside case)	34mm	34mm	56mm
Normal standoff	102mm	102mm	204mm
Normal angle of incidence	90°	90°	90°
Variable standoff	68mm (A) 136mm (B) 153mm (C) 204mm (D) 518mm (E)	-	-
Alternative angle of incidence	60° (F)	-	-
Test specimens on which charges were used.* **	S1 to S31, S33 and S34 B1 to B46, B53 to B59, B65 M1 to M12, M14, M16 M17 and M19	S33 and S34 B47 to B52 M13, M15 and M18	S32 B60 to B64

* In the test on block B46 the initiator was detonated peripherally.

** In the tests on blocks B21 to B24 the shaped charge jet penetrated a steel plate before impact

A Test B17
B Test M19
C Test B16
D Test B18
E Test B19
F Tests B20, S29, S30

Table 4.13

Details of Explosives

Charge component	Explosive	Mass	Velocity of detonation
EWB III initiator	PETN	350mg	-
L2A1 initiator	Tetryl	1.55g	-
PE4 Plastic Explosive	RDX/Wax	16g 74g	8.34mm/μsec
Shaped charge booster (43g charge) Shaped charge booster (298g charge)	Tetryl	1.24g 19.4 g	7.2mm/μsec
Shaped charge (Main charge)	60/40 RDX/TNT	43g 298g	7.85mm/μsec

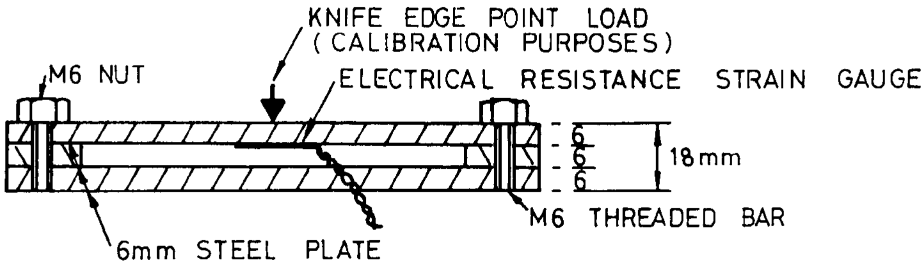

Cross Section

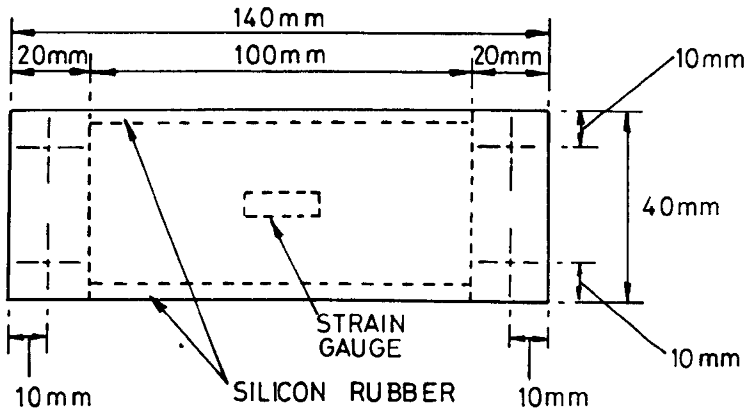

Plan

FIGURE 4.1 SOIL PRESSURE GAUGE DETAILS

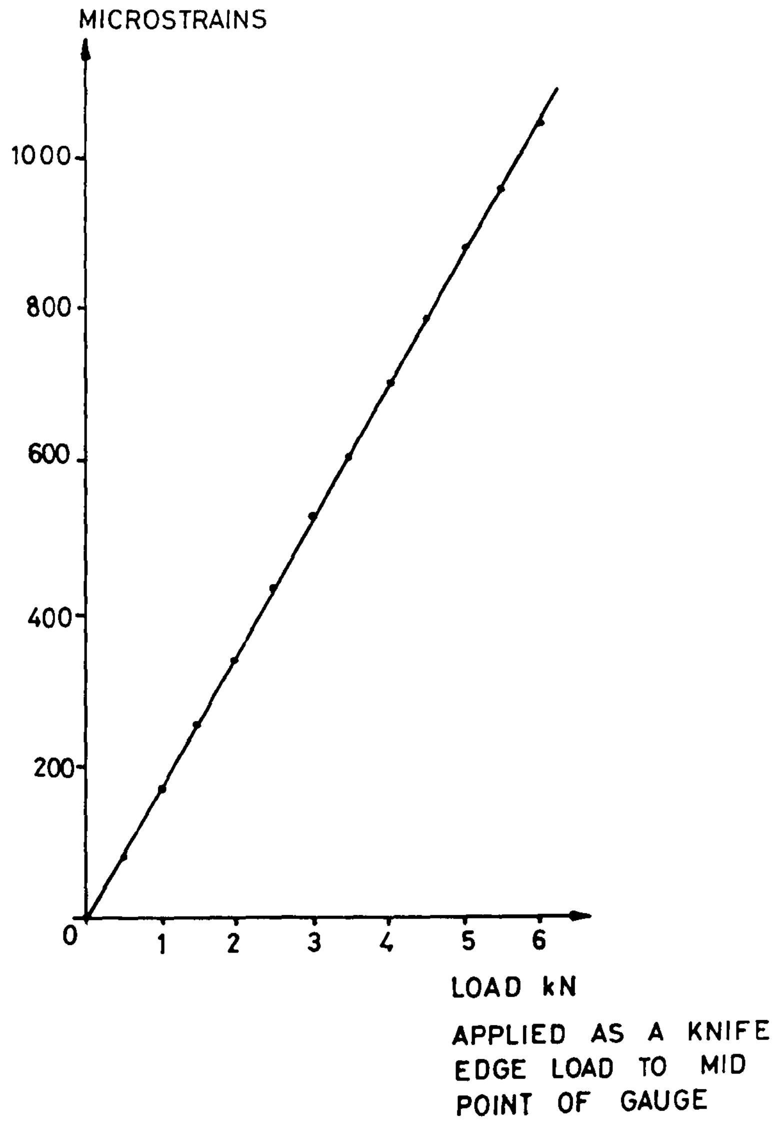

FIGURE 4.2 CALIBRATION GRAPH FOR THE SOIL PRESSURE GAUGE

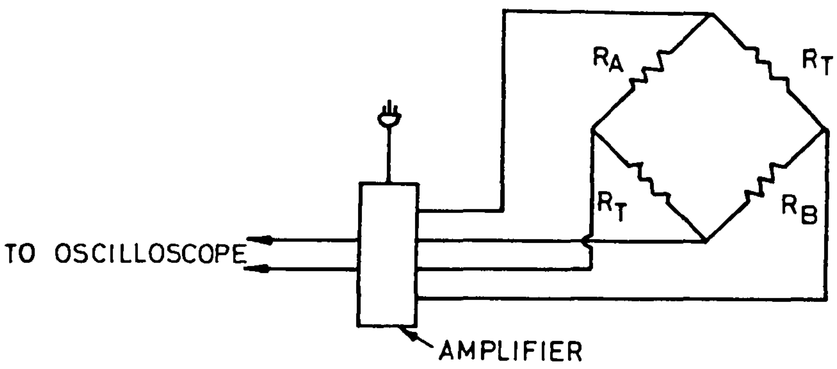

R_A = ACTIVE GAUGE

R_B = ACTIVE GAUGE (1/2 BRIDGE)
PASSIVE GAUGE (1/4 BRIDGE)

R_T = TEMPERATURE COMPENSATION GAUGE

FIGURE 4.3 WHEATSTONE BRIDGE CIRCUIT FOR ELECTRICAL RESISTANCE STRAIN GAUGES

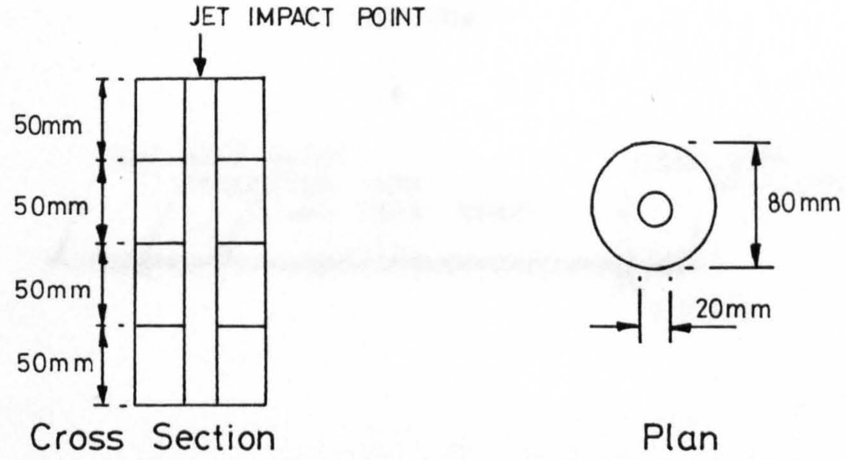

FIGURE 4.4 'PLASTICINE' BLOCK No.1 DETAILS

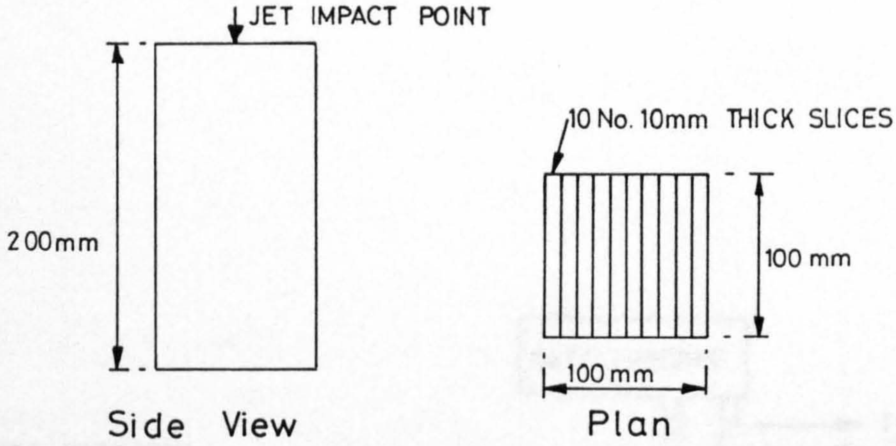

FIGURE 4.5 'PLASTICINE' BLOCK No. 2 DETAILS

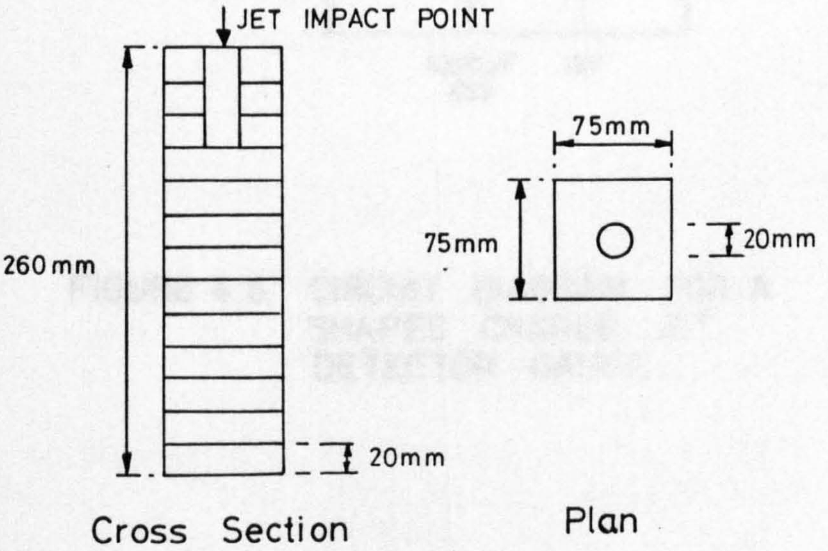

FIGURE 4.6 'PLASTICINE' BLOCK No.3 DETAILS
(TEST M19)

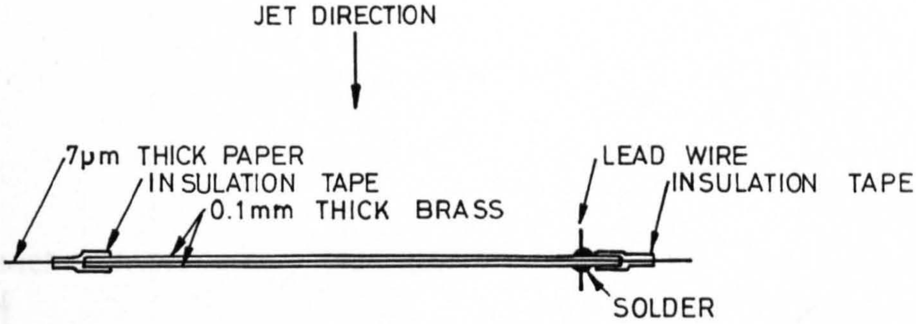

FIGURE 4.7 CROSS SECTION OF A SHAPED CHARGE JET DETECTOR GAUGE

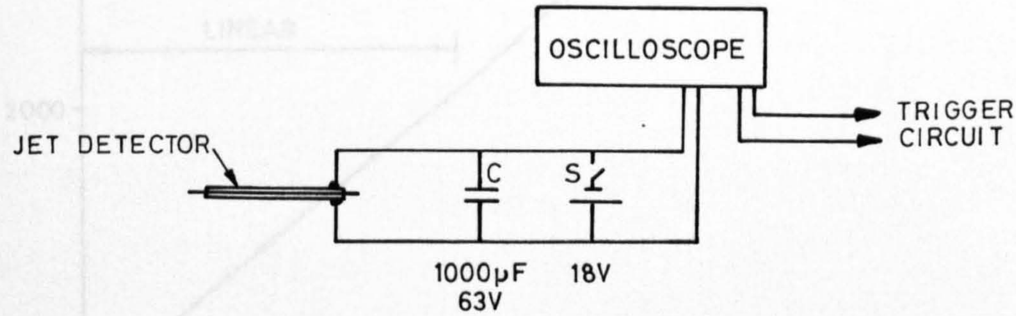

FIGURE 4.8 CIRCUIT DIAGRAM FOR A SHAPED CHARGE JET DETECTOR GAUGE

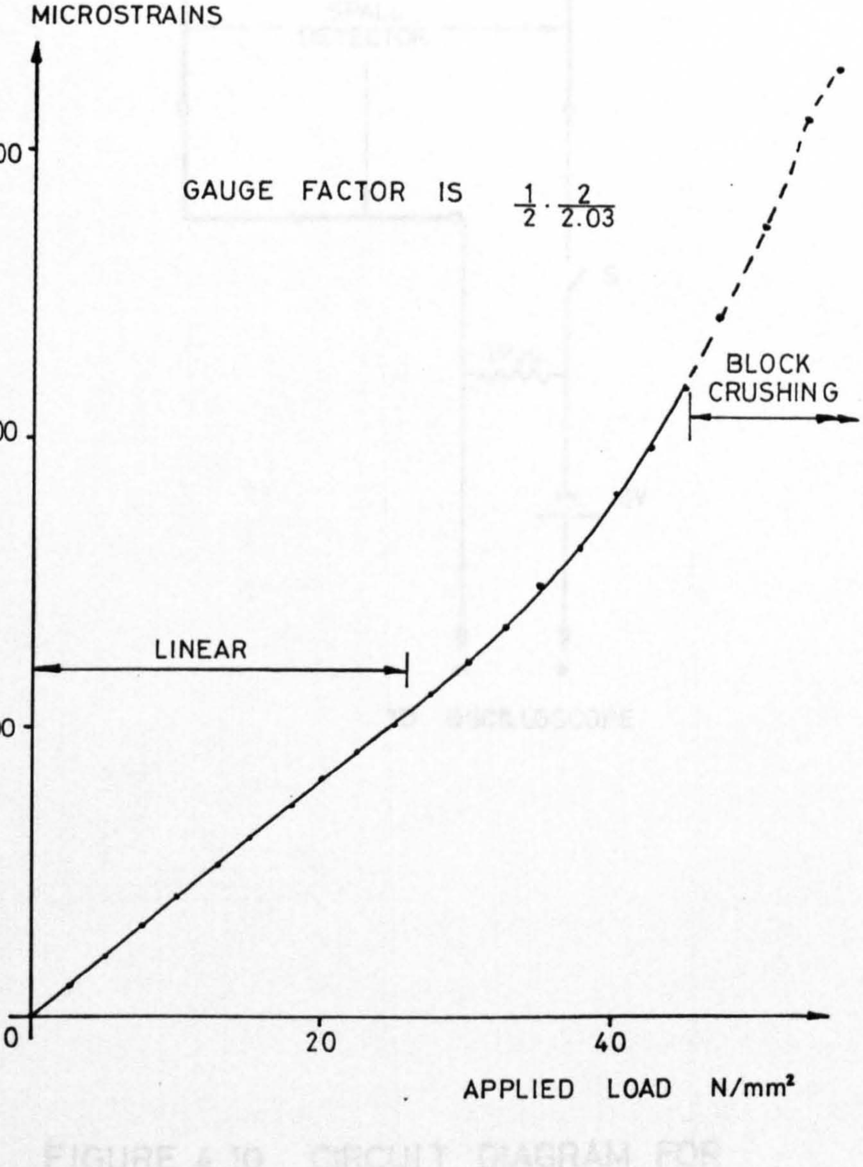

FIGURE 4.9 CALIBRATION GRAPH FOR ELECTRICAL RESISTANCE STRAIN GAUGES FIXED TO SMALL CONCRETE BLOCKS

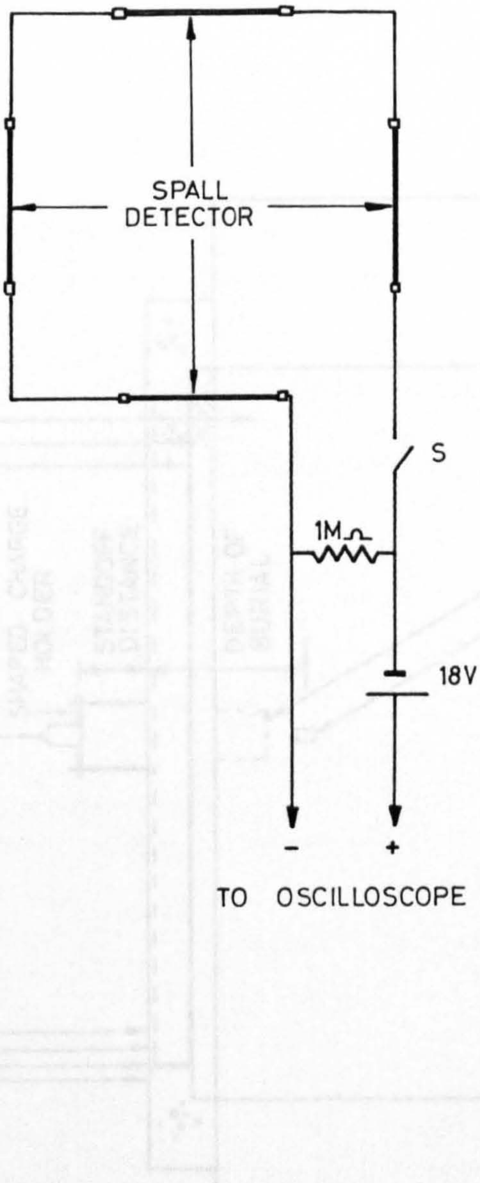

FIGURE 4.10 CIRCUIT DIAGRAM FOR GRAPHITE ROD SPALL DETECTORS

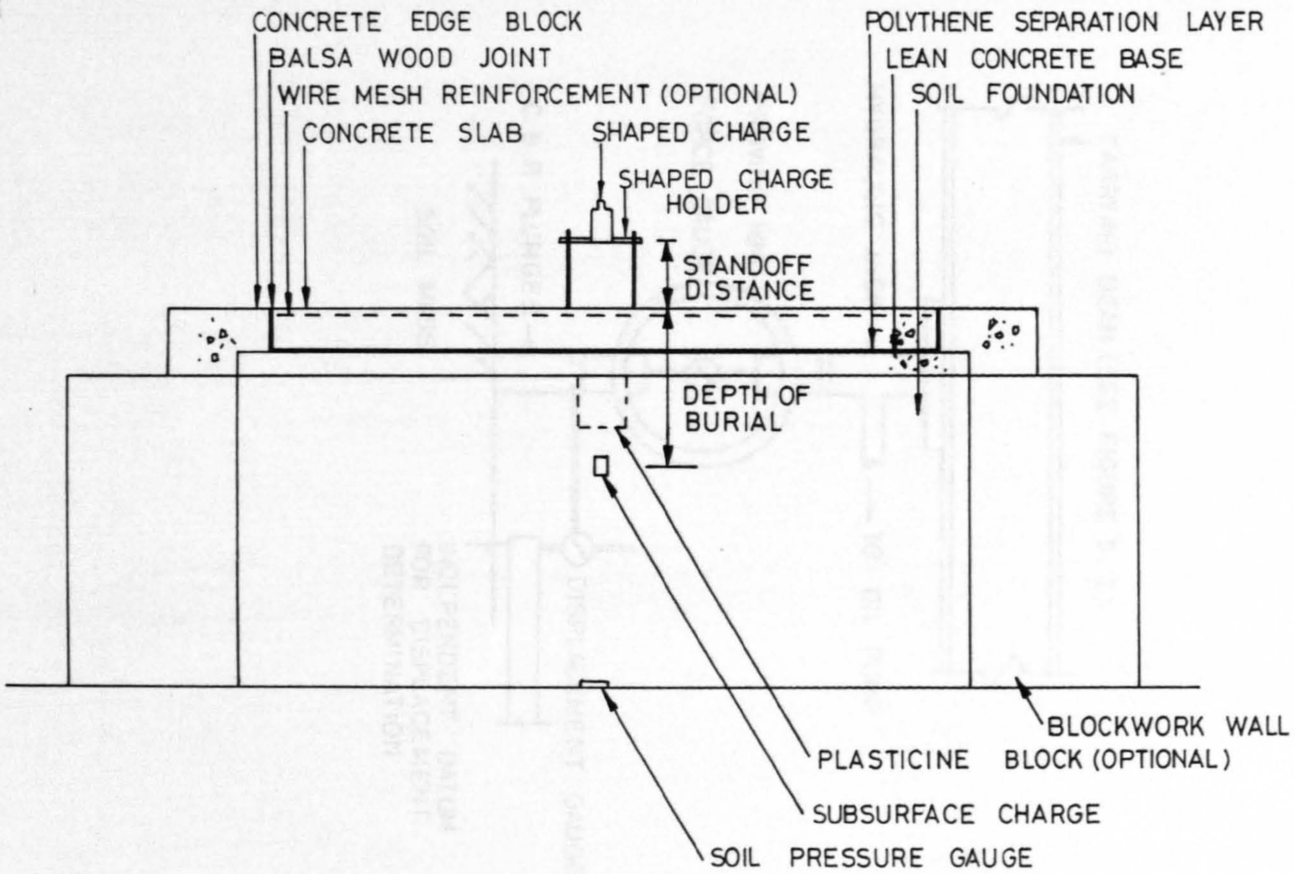

FIGURE 4.11 CROSS SECTION OF A TYPICAL TEST BAY SHOWING EXPLOSIVE CHARGE LOCATIONS AND CONSTRUCTION DETAILS

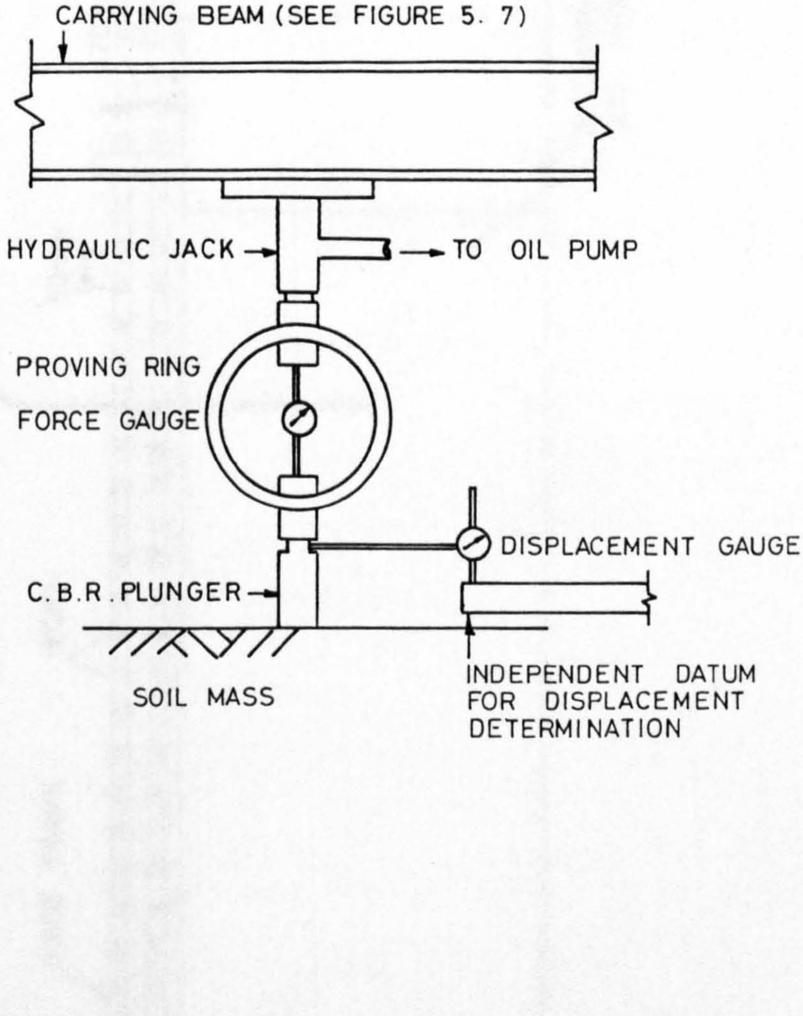

FIGURE 4.12 CALIFORNIA BEARING RATIO TEST ARRANGEMENTS

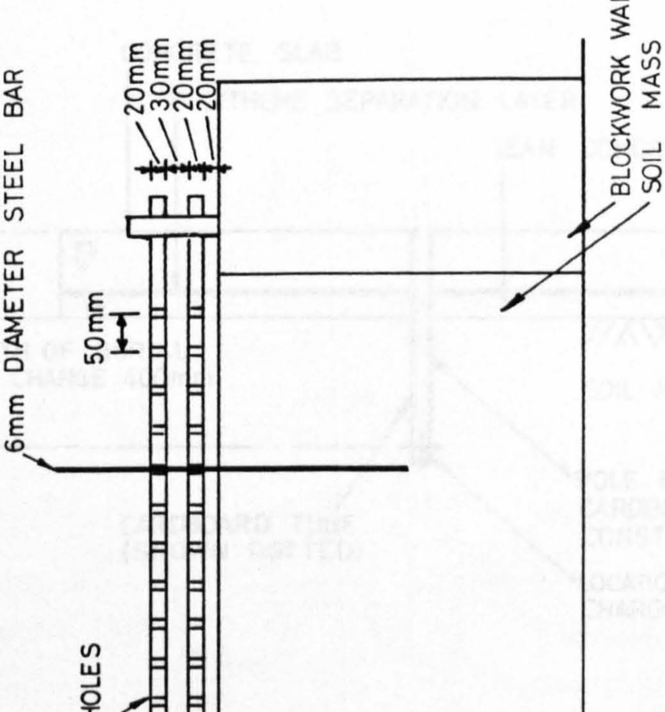

FIGURE 4.13 GUIDE FRAME FOR MAKING HOLES FOR COLOURED SAND COLUMNS IN SOILS

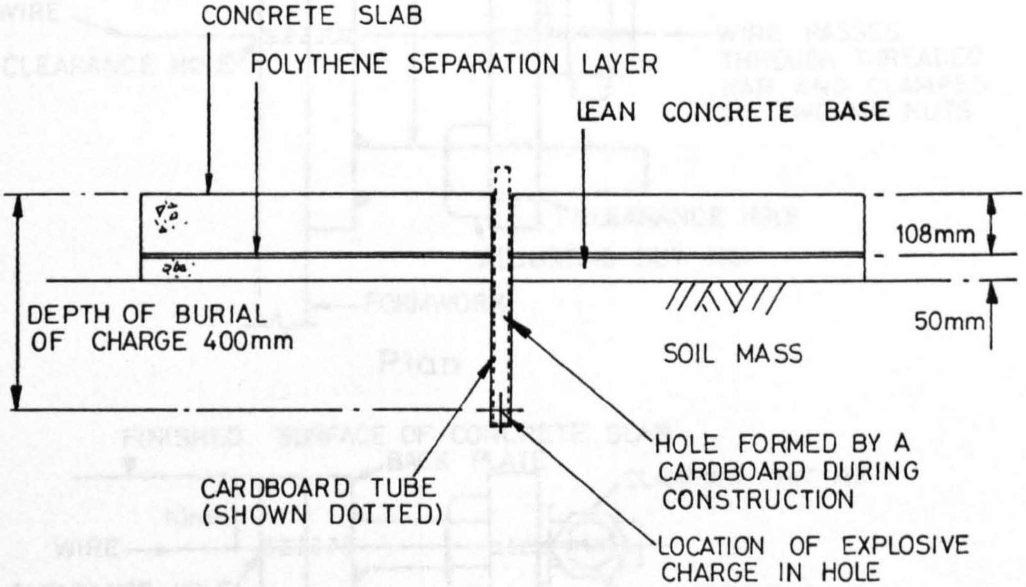

FIGURE 4.14 EXPERIMENTAL DETAILS FOR A 1/3 SCALE TEST SPECIMEN

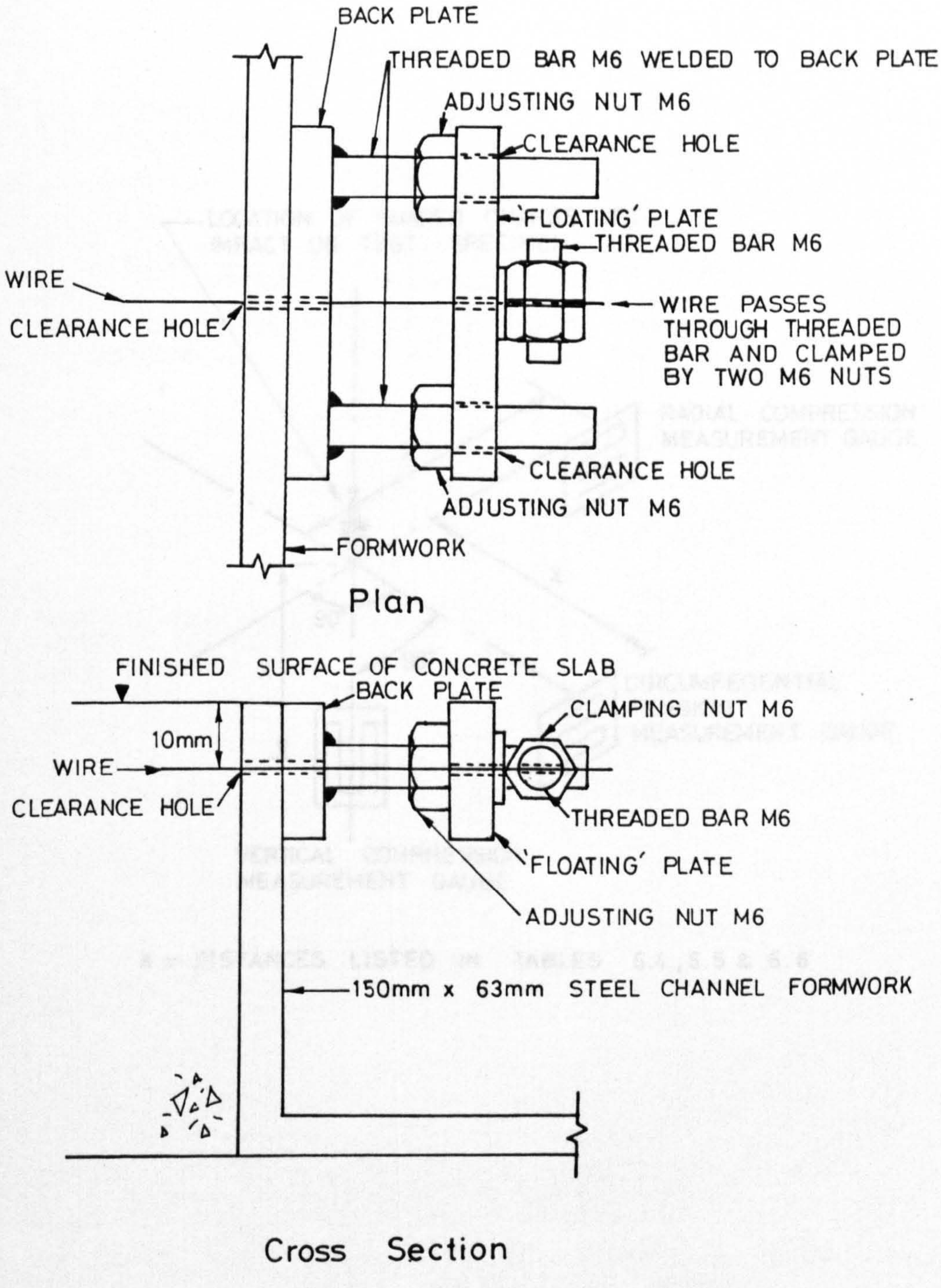

FIGURE 4.15 DETAILS OF THE TURNBUCKLE FOR TENSIONING HOLDING WIRES FOR REINFORCEMENT MESH IN CONCRETE SLABS

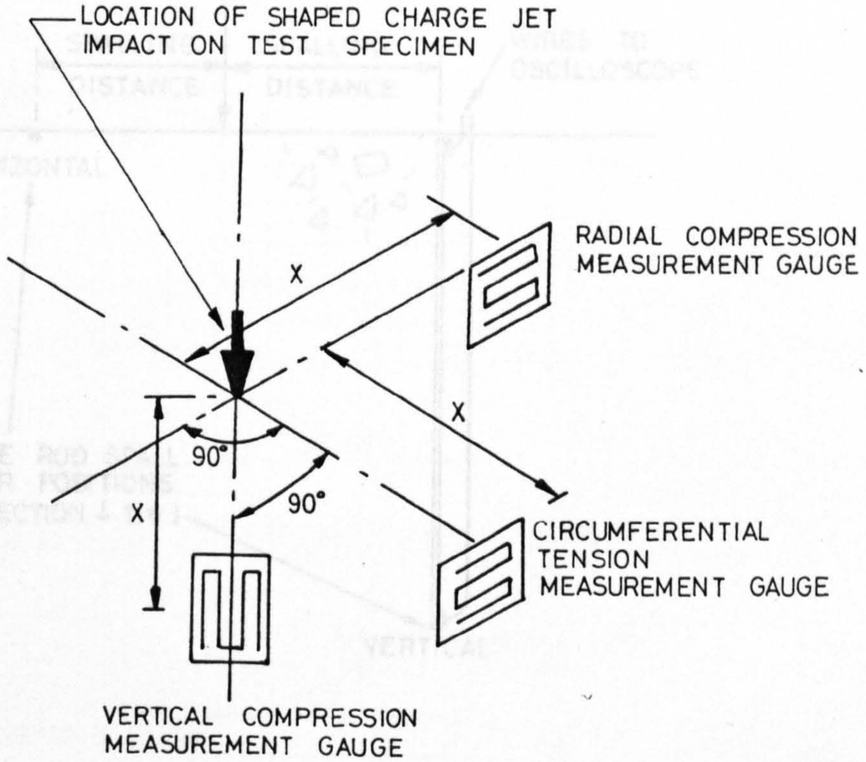

X = DISTANCES LISTED IN TABLES 6.4 , 6.5 & 6.6

FIGURE 4.16 ORIENTATIONS OF ELECTRICAL RESISTANCE STRAIN GAUGES BURIED IN CONCRETE TEST SPECIMENS

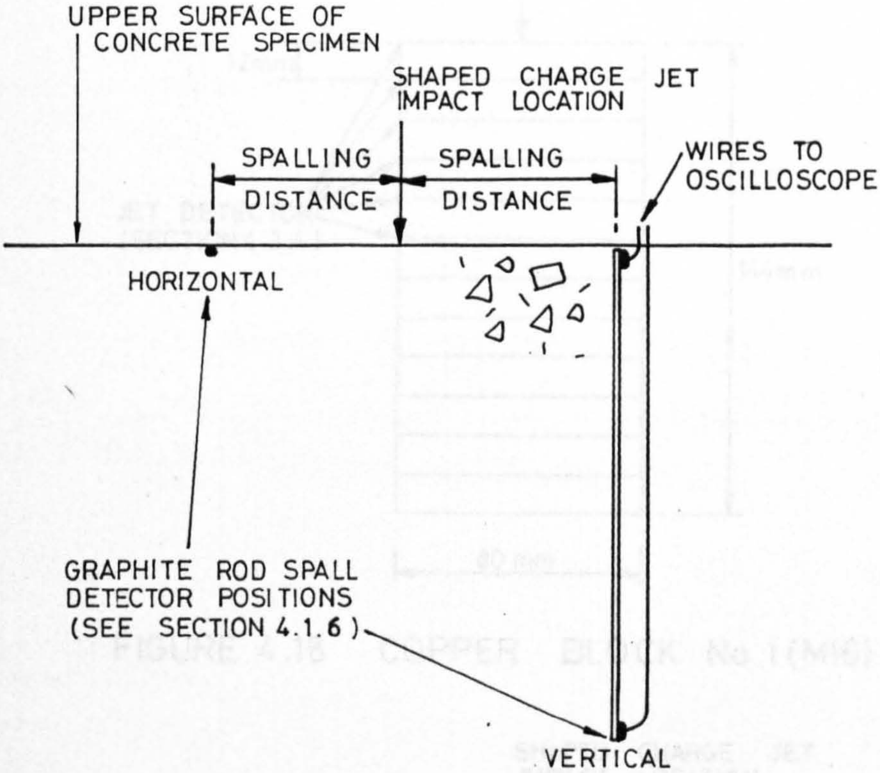

FIGURE 4.17 LOCATIONS OF GRAPHITE ROD SPALL DETECTORS BURIED IN CONCRETE TEST SPECIMENS

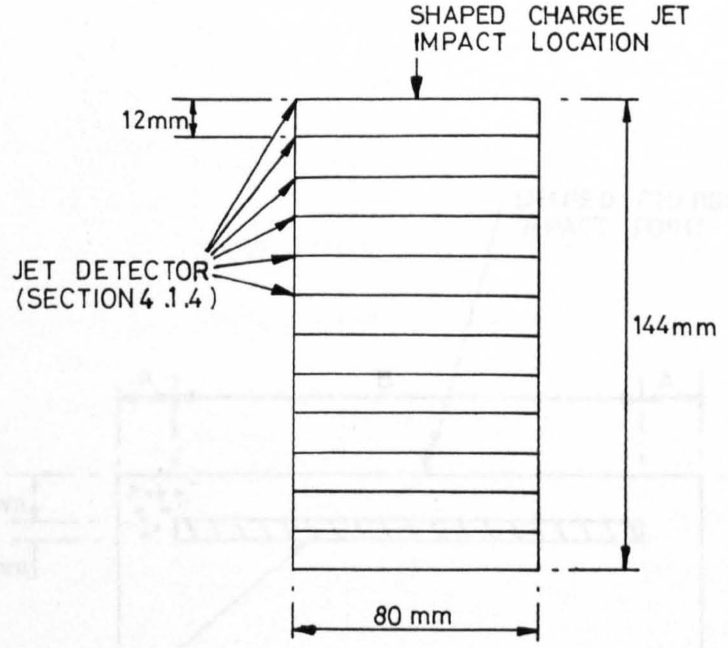

FIGURE 4.18 COPPER BLOCK No.1 (M16) DETAILS

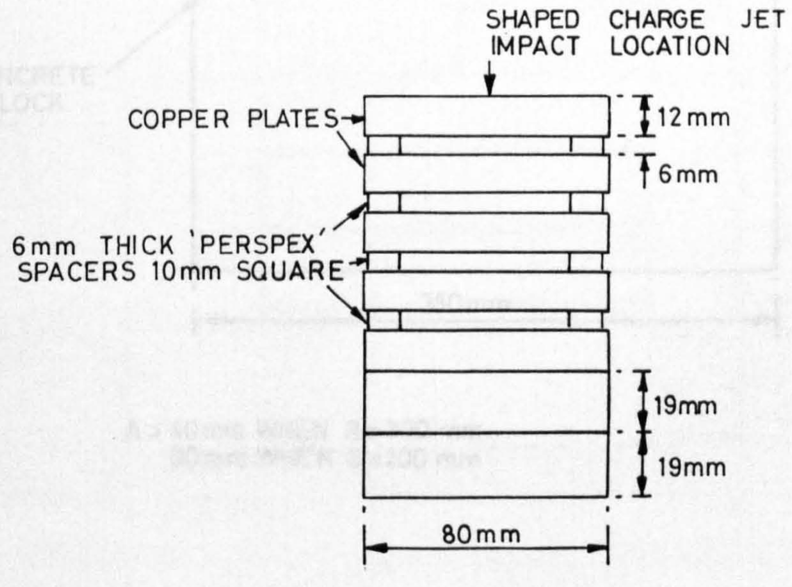

FIGURE 4.19 COPPER BLOCK No.2 (M17) DETAILS

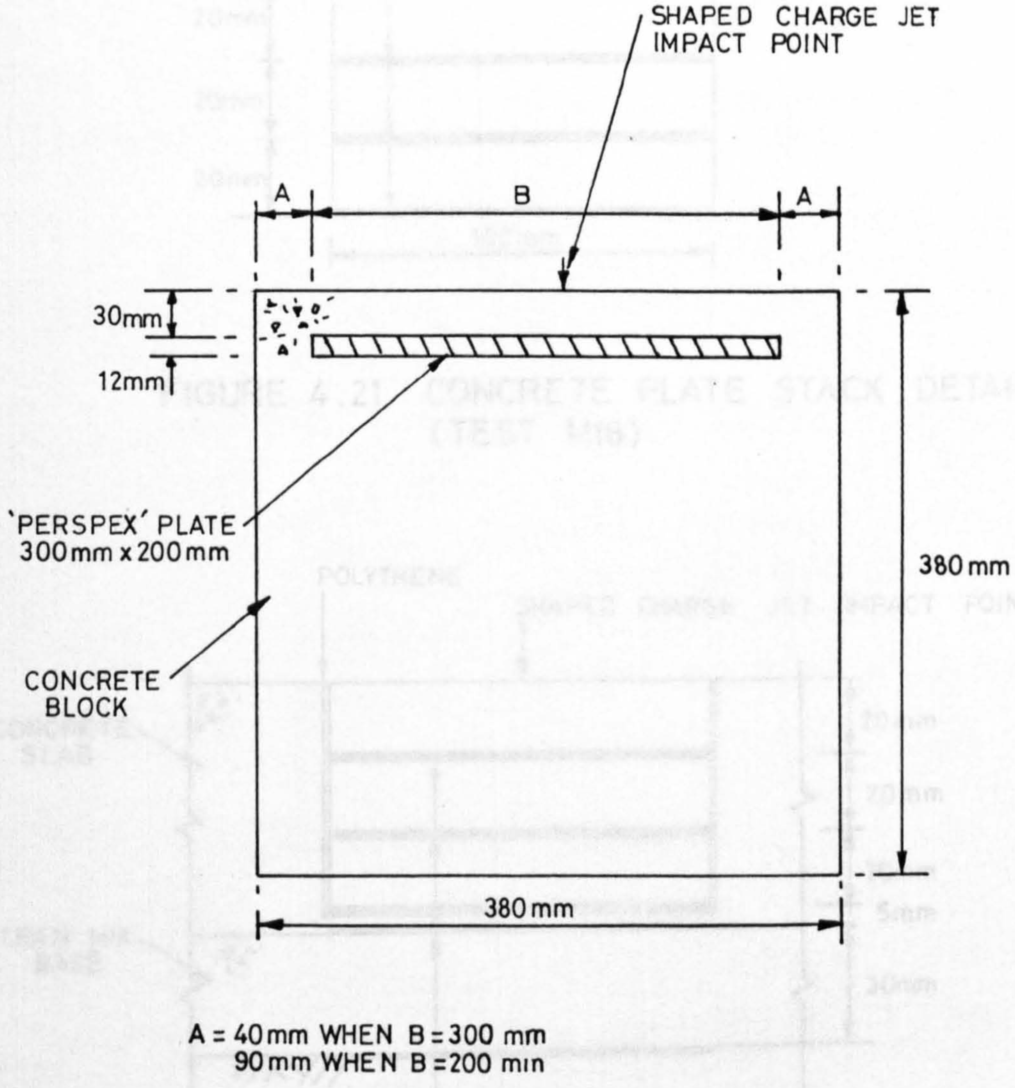

FIGURE 4.20 CROSS SECTION OF BLOCK B26 WITH BURIED 'PERSPEX' PLATE

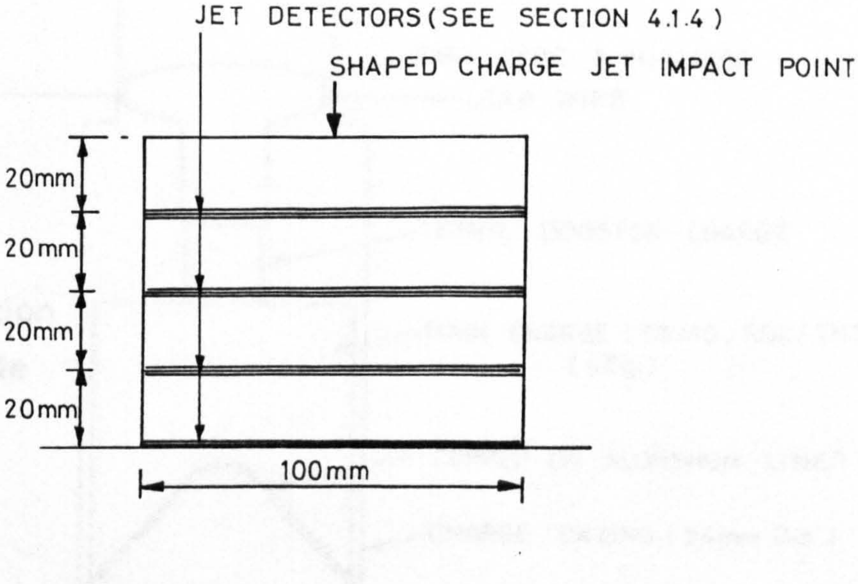

FIGURE 4.21 CONCRETE PLATE STACK DETAILS (TEST M18)

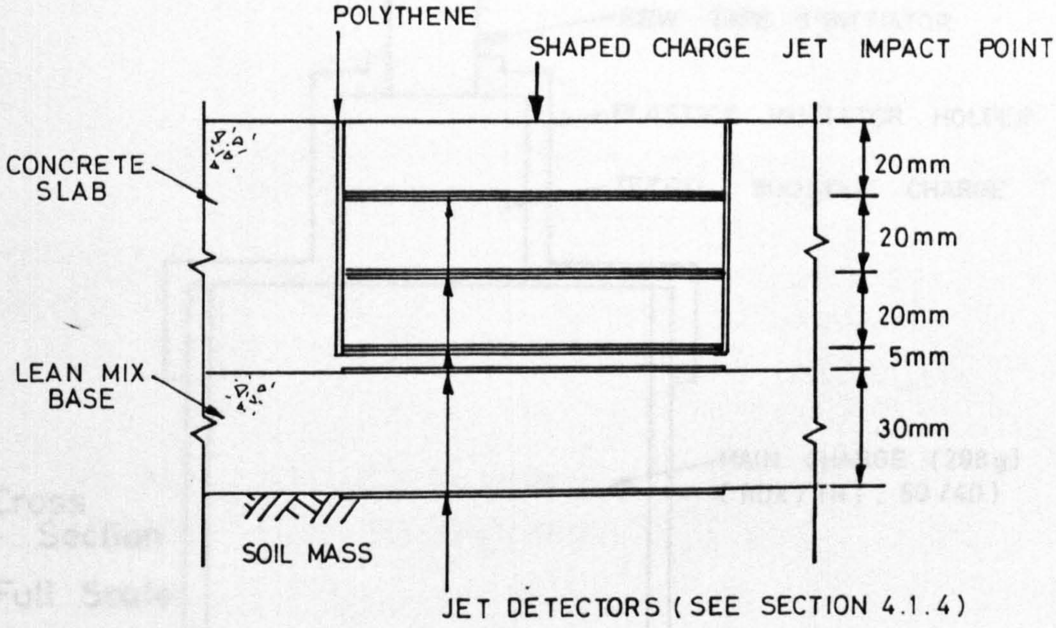

FIGURE 4.22 CONCRETE PLATE STACK EMBEDDED IN SLAB S28

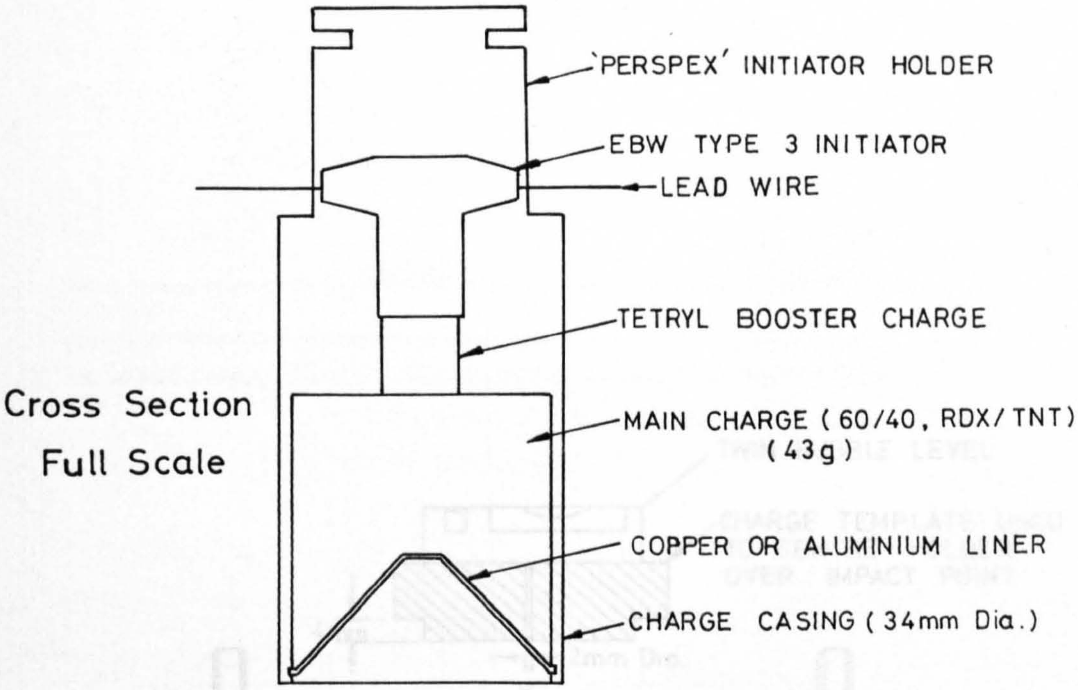

FIGURE 4.23 43g. 34mm. dia. SHAPED CHARGE

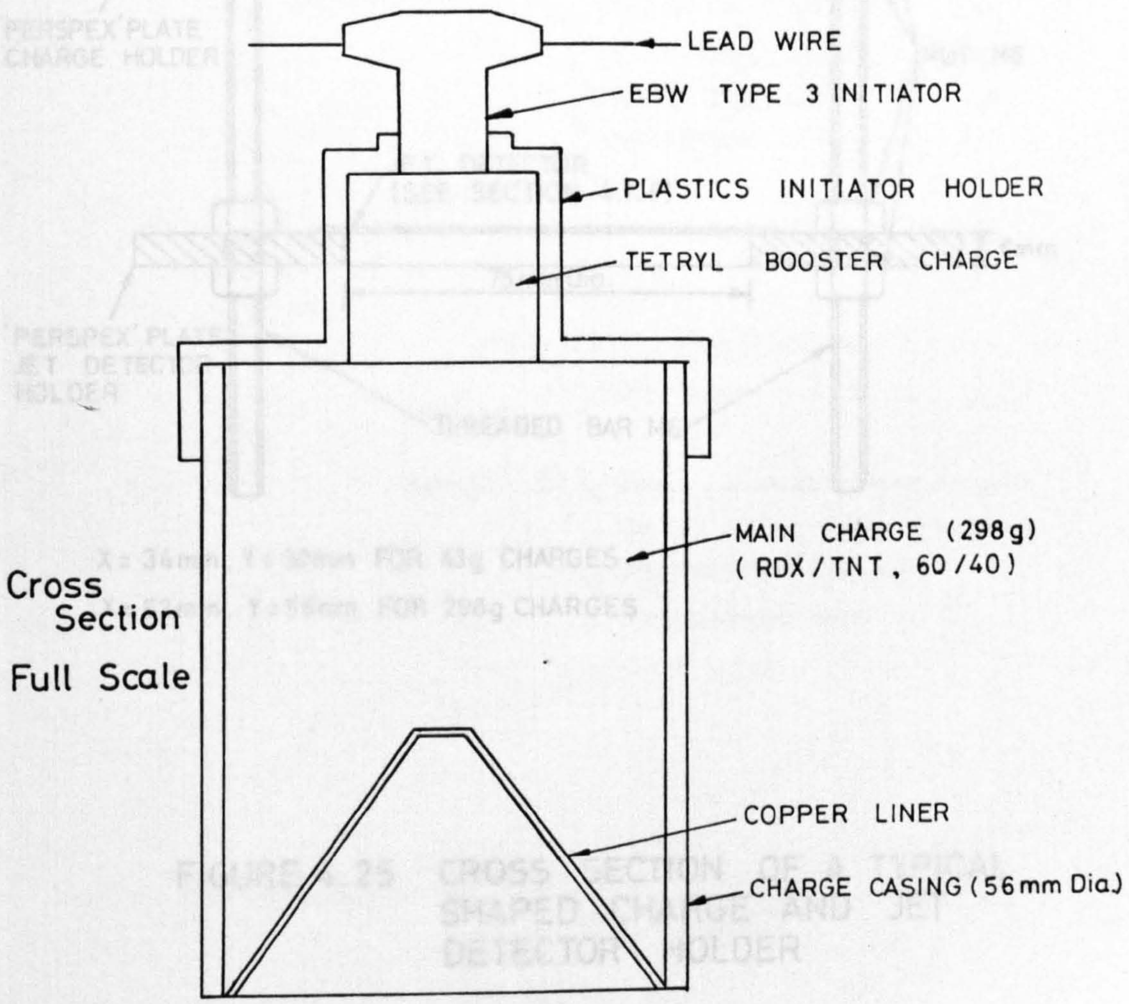

FIGURE 4.24 298g. 56mm. dia. SHAPED CHARGE

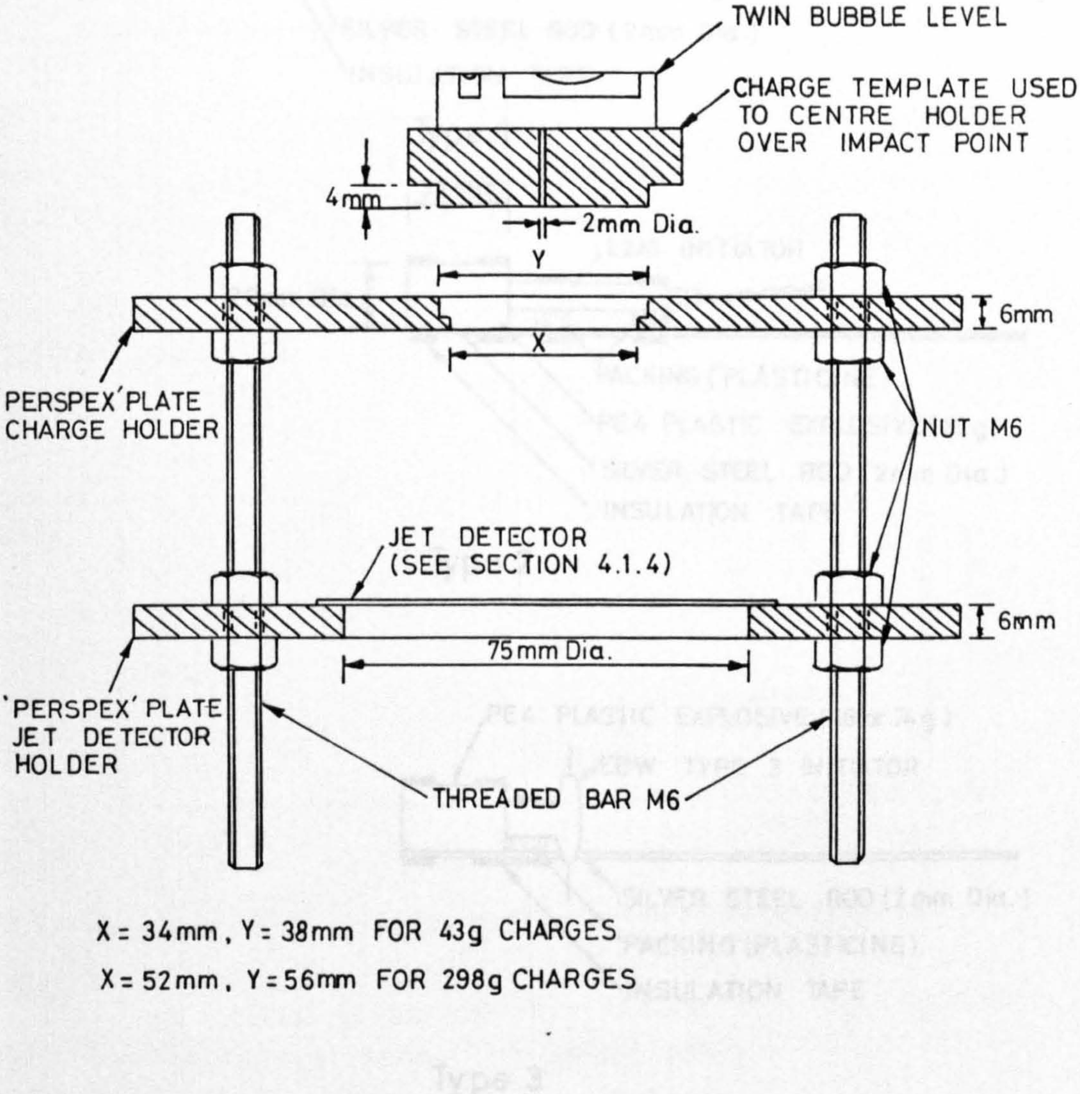

FIGURE 4.25 CROSS SECTION OF A TYPICAL SHAPED CHARGE AND JET DETECTOR HOLDER

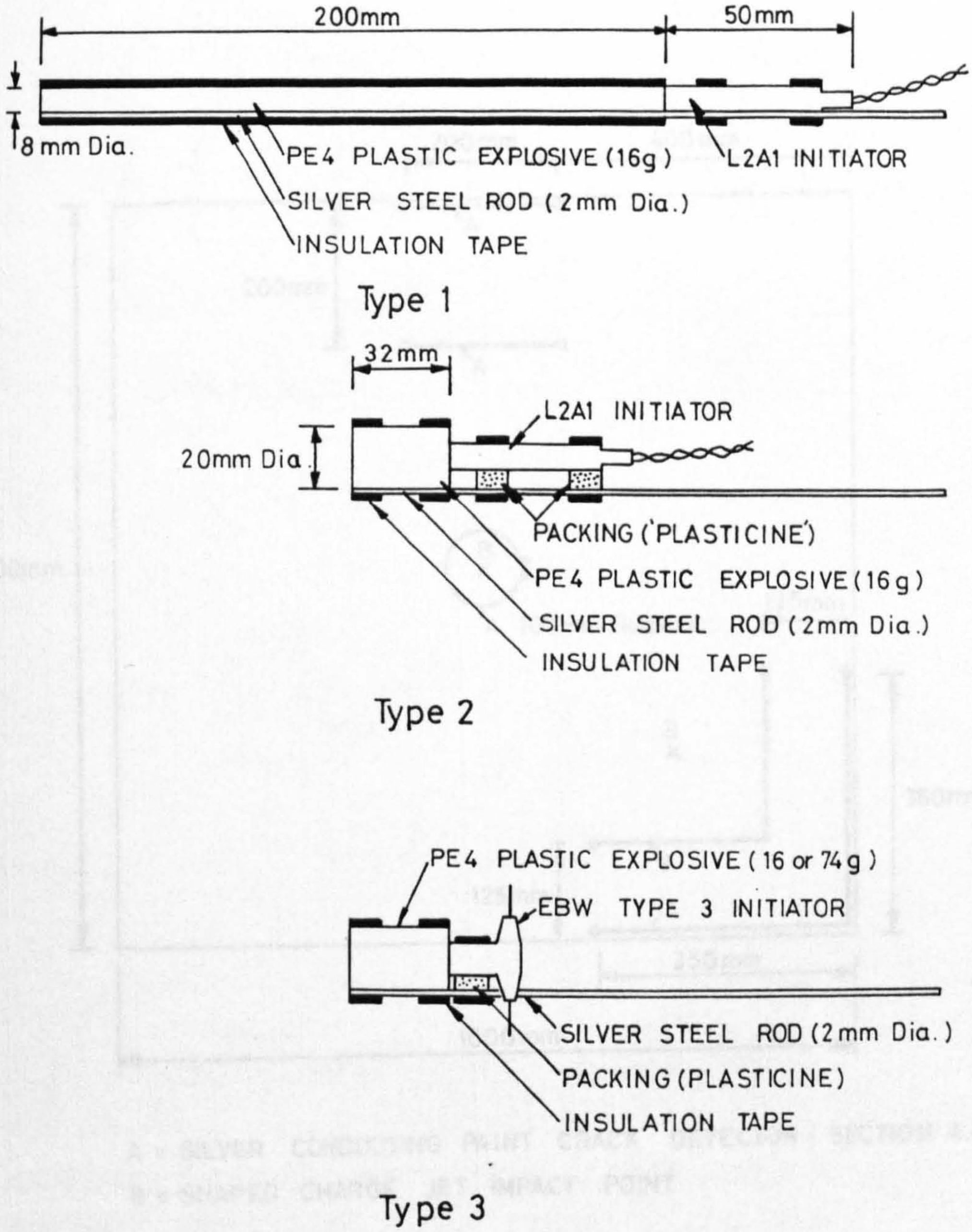

FIGURE 4.26 DETAILS OF BURIED EXPLOSIVE CHARGES

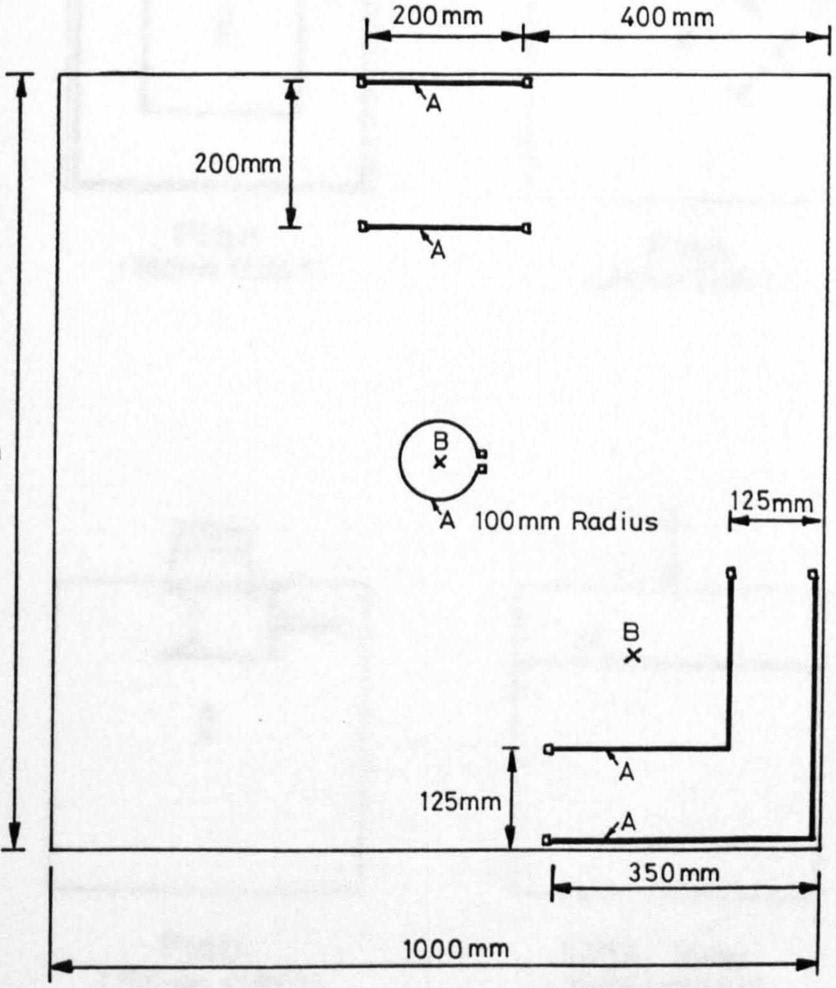

A = SILVER CONDUCTING PAINT CRACK DETECTOR (SECTION 4.4.1)
B = SHAPED CHARGE JET IMPACT POINT

FIGURE 4.27 TYPICAL LOCATIONS OF CRACK DETECTORS ON CONCRETE SLABS

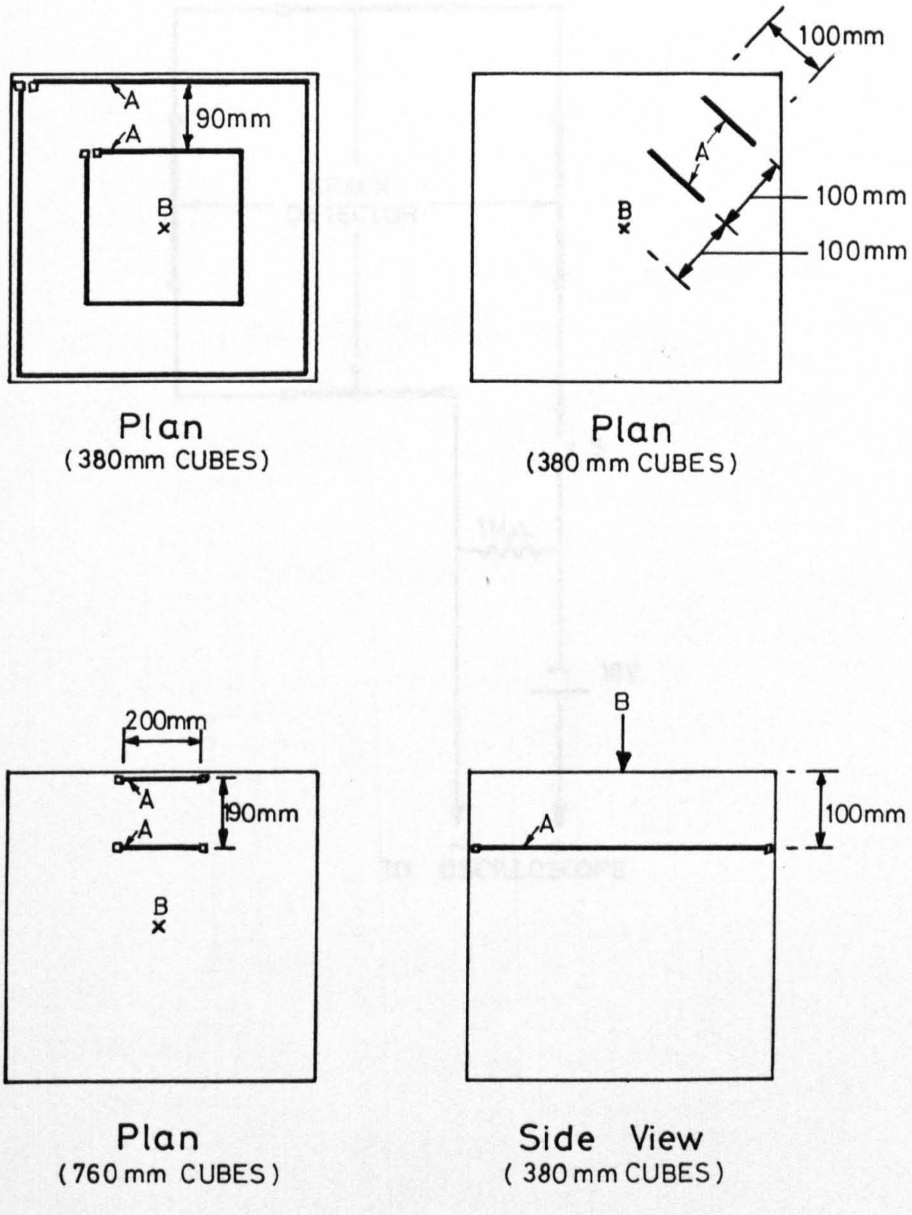

A = SILVER CONDUCTING PAINT CRACK DETECTOR (SECTION 4.4.1)

B = SHAPED CHARGE - JET IMPACT POINT

FIGURE 4.28 TYPICAL LOCATIONS OF CRACK DETECTORS ON CONCRETE BLOCKS

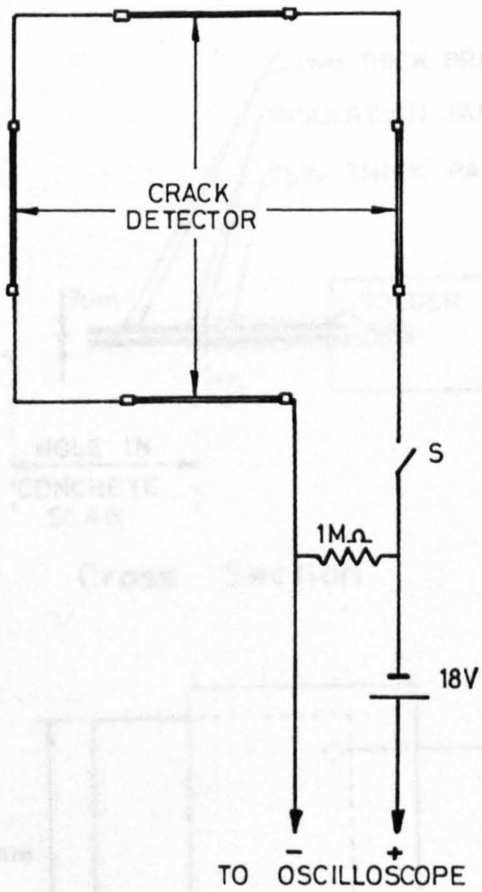

FIGURE 4.29 CIRCUIT DIAGRAM FOR CONDUCTING SILVER PAINT CRACK DETECTORS

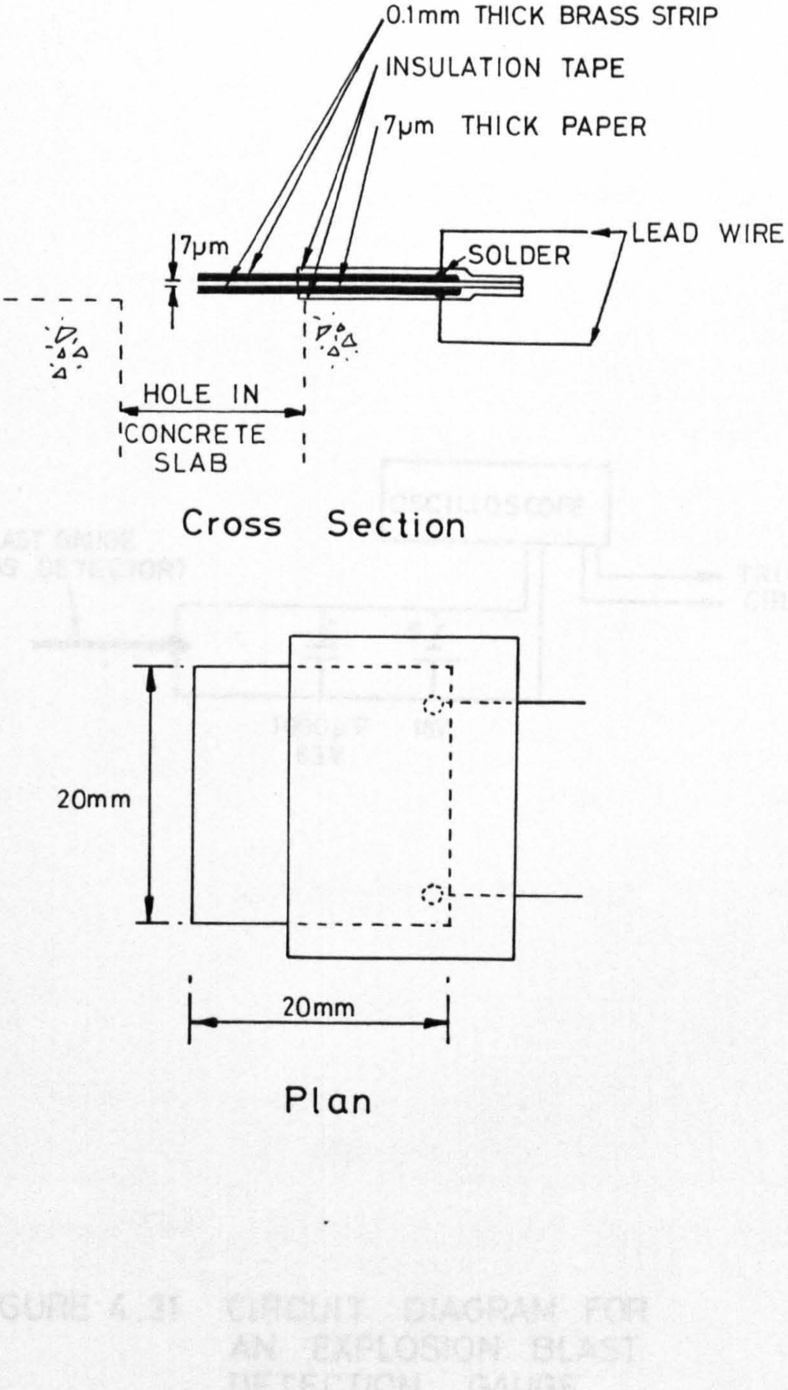

FIGURE 4.30 LOCATION AND DETAILS OF AN EXPLOSION BLAST DETECTION GAUGE

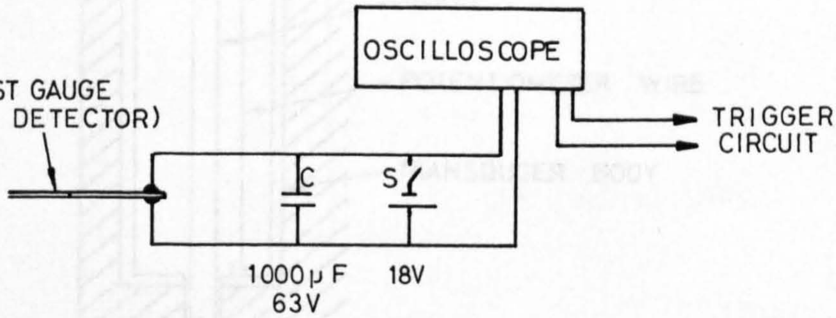

FIGURE 4.31 CIRCUIT DIAGRAM FOR AN EXPLOSION BLAST DETECTION GAUGE

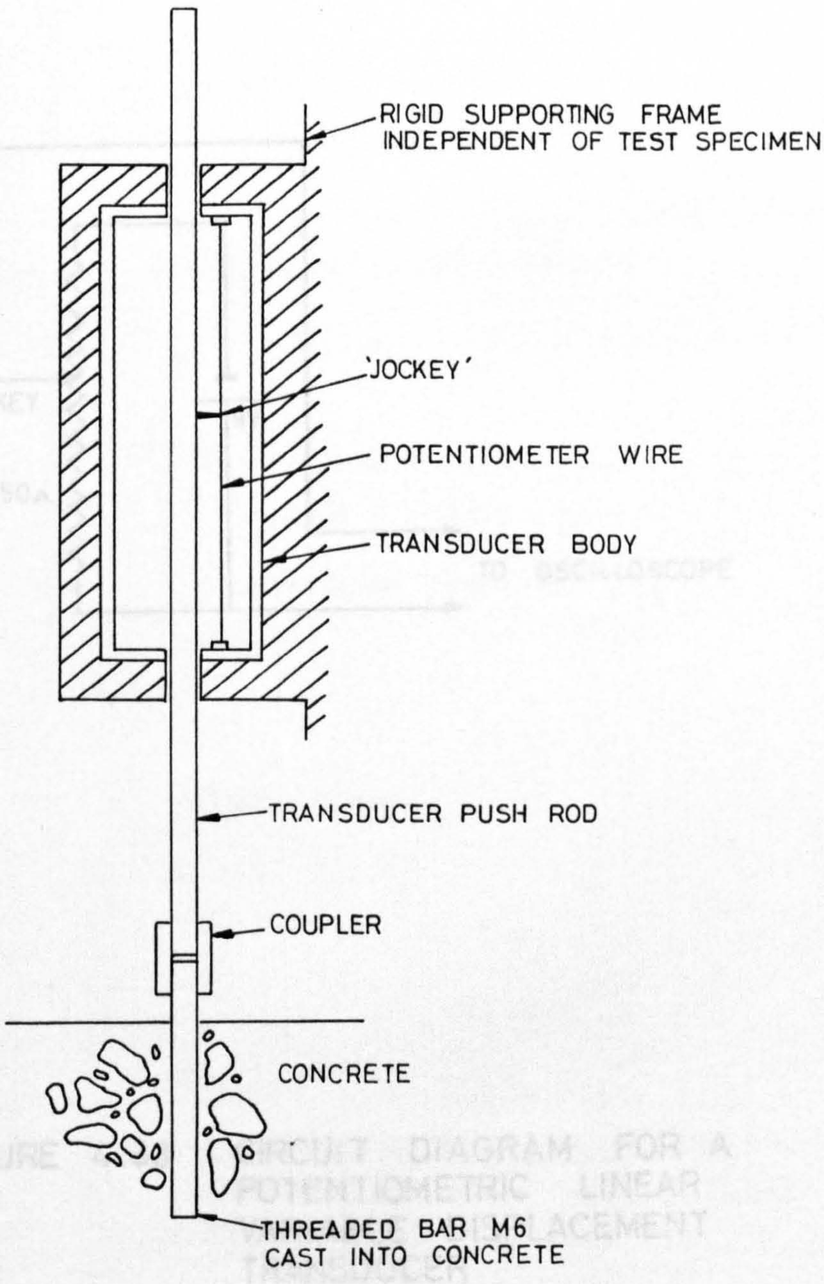

FIGURE 4.32 CROSS SECTION OF A POTENTIOMETRIC LINEAR VARIABLE DISPLACEMENT TRANSDUCER SHOWING BASIC DETAILS

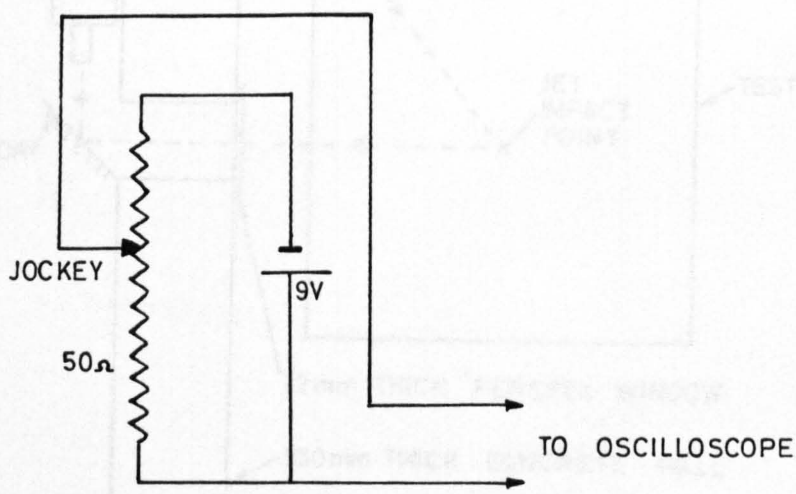

FIGURE 4.33 CIRCUIT DIAGRAM FOR A POTENTIOMETRIC LINEAR VARIABLE DISPLACEMENT TRANSDUCER

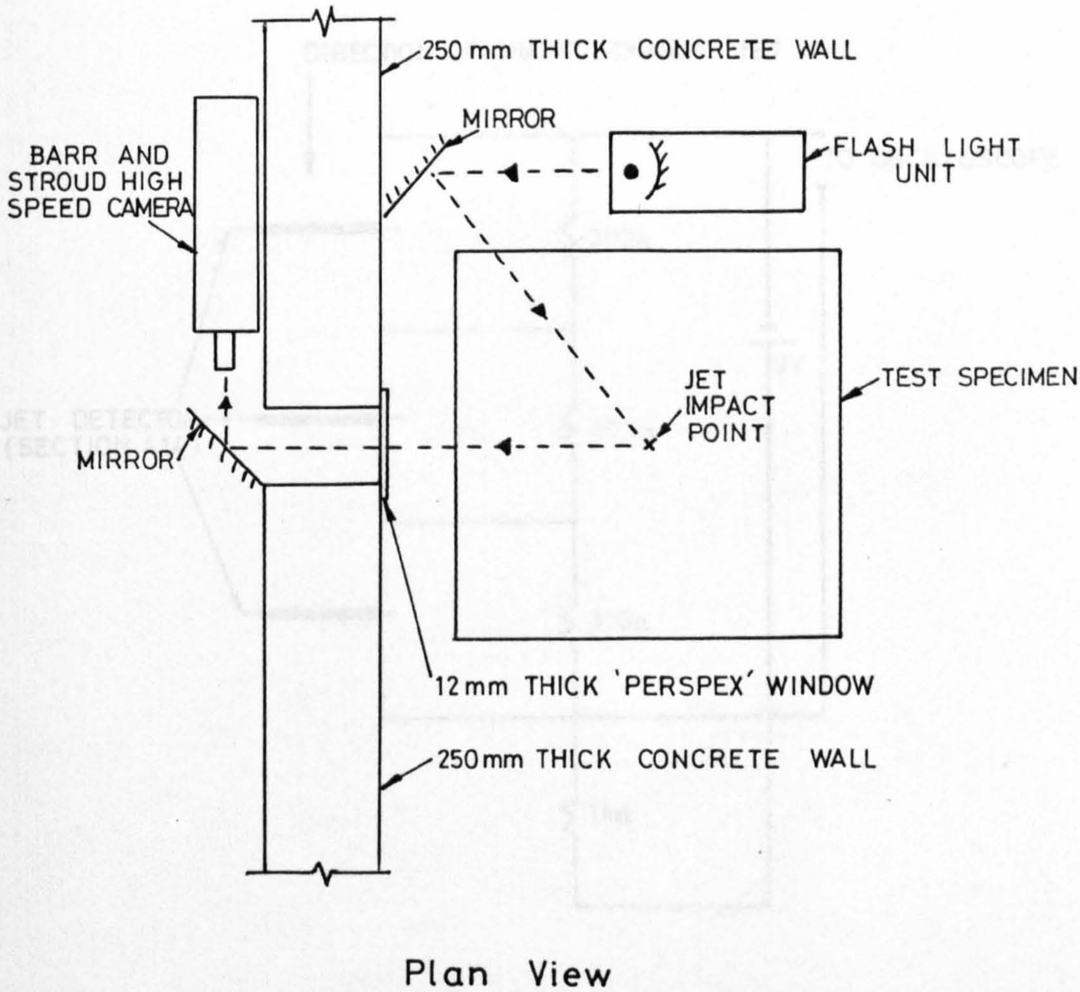

FIGURE 4.34 EXPERIMENTAL DETAILS FOR USING THE BARR AND STROUD HIGH SPEED CAMERA

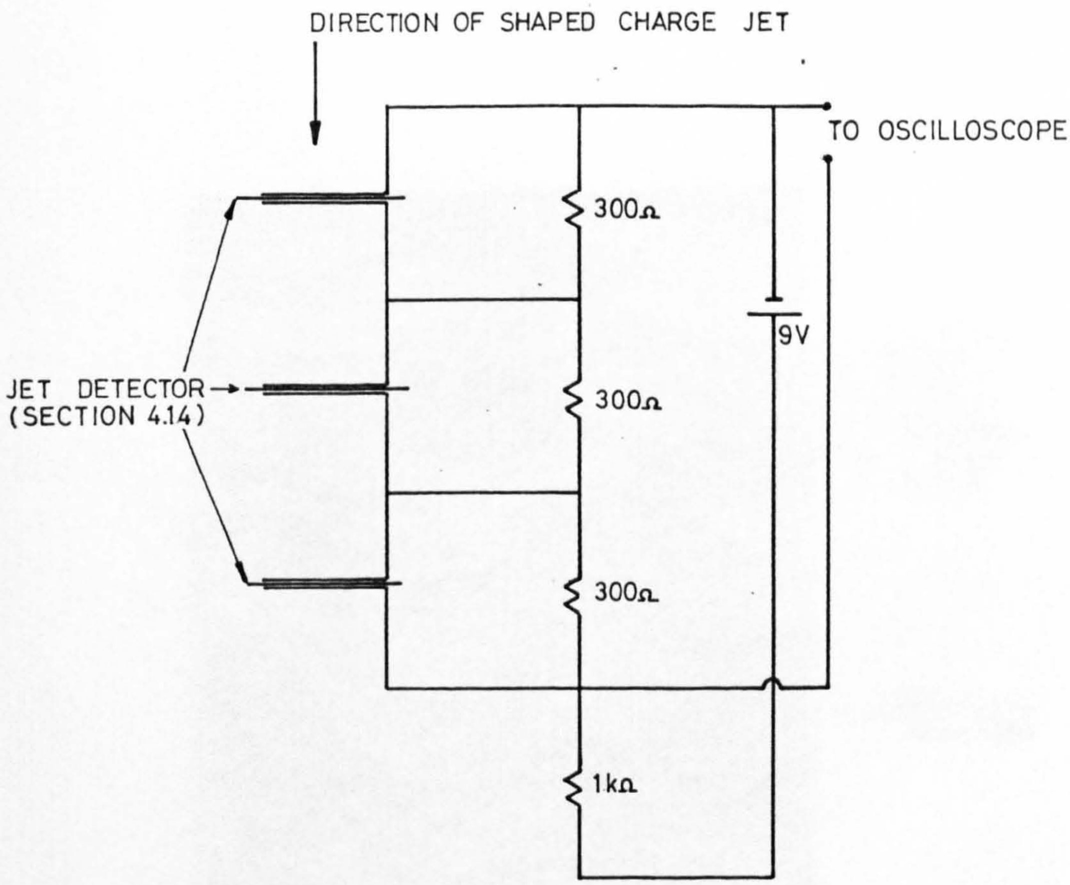

FIGURE 4.35 RESISTANCE CIRCUIT DIAGRAM FOR SHAPED CHARGE JET DETECTORS

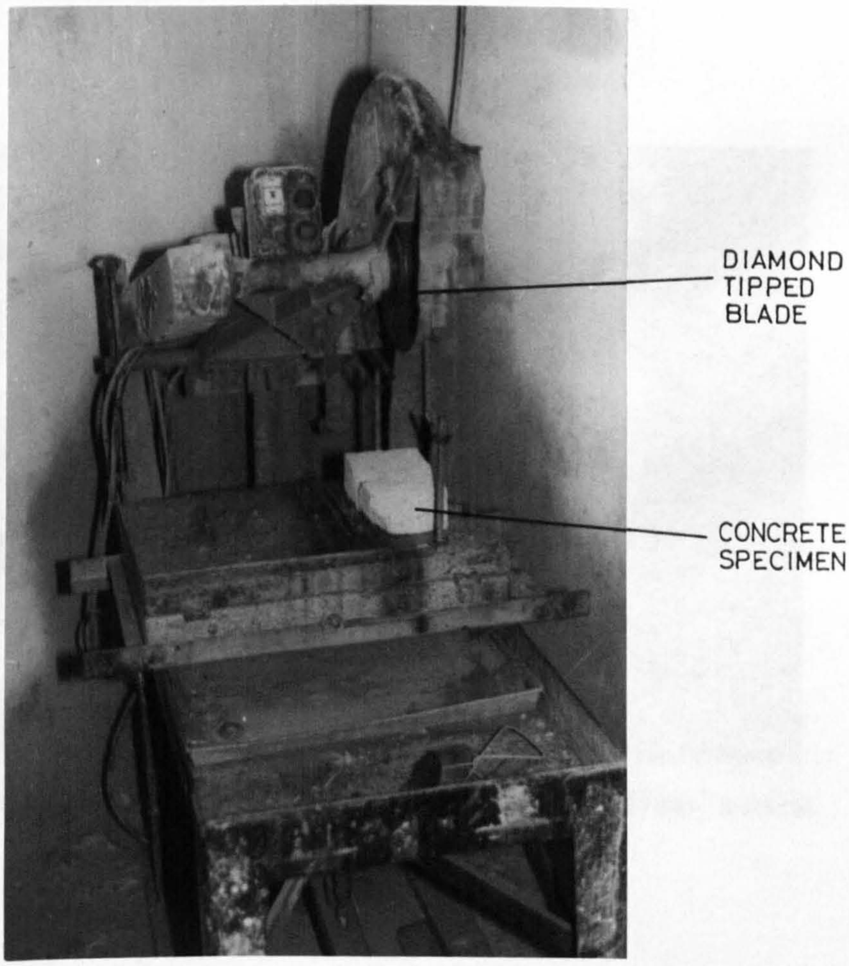

PLATE 4.1 CONCRETE SAW

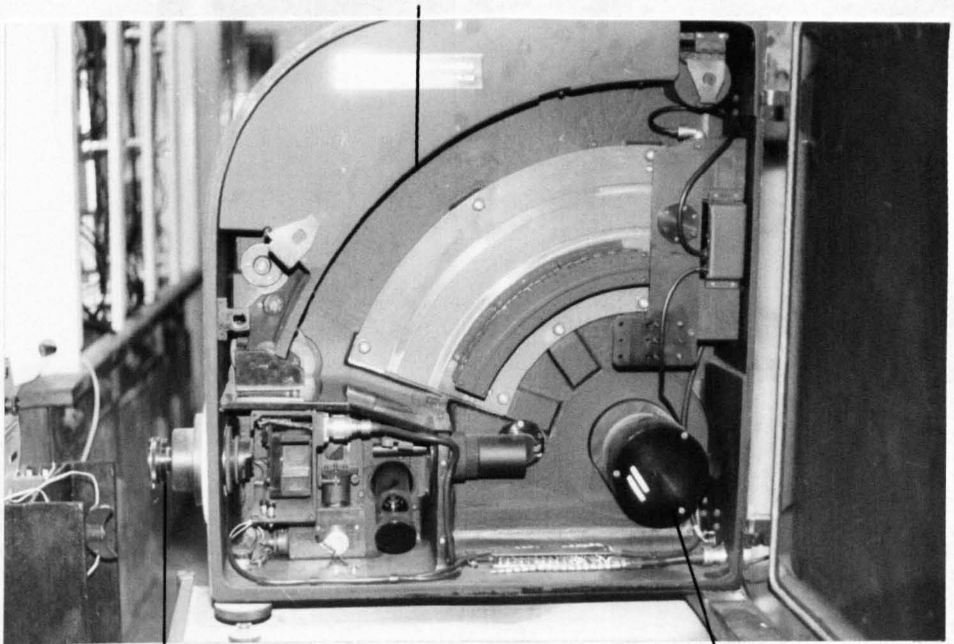

PLATE 4.2 BARR AND STROUD HIGH SPEED ROTATING MIRROR CAMERA (INTERIOR VIEW)

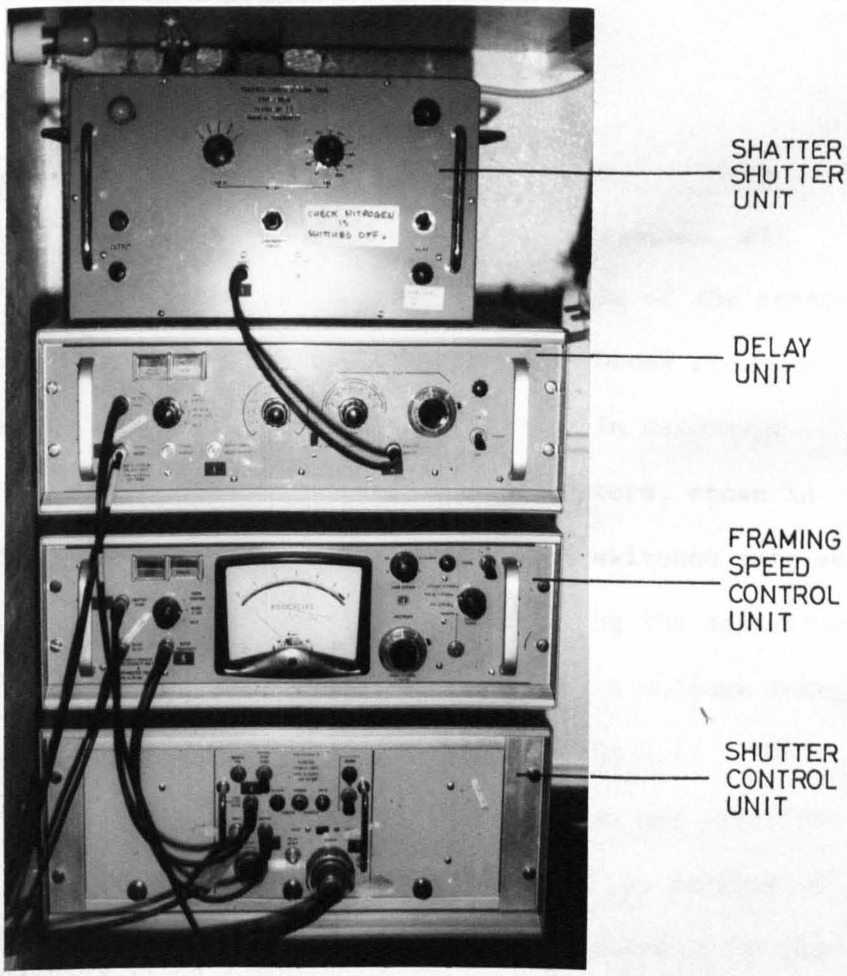

PLATE 4.3 BARR AND STROUD CAMERA OPERATING UNITS

CHAPTER 5

EXPERIMENTAL PROCEDURES AND THE MEASUREMENT OF DAMAGE PARAMETERS

This chapter describes the methods of carrying out the experiments including techniques used for determining damage caused by the explosives.

5.1 EXPERIMENTAL PROCEDURES

5.1.1 Pre-test Electrical Instrumentation Checking Procedure

Before the charge was brought to the test specimen, all instrumentation was checked. The electrical details of the instrumentation were of four types, discharge circuits, break circuits, resistance circuits and potentiometric circuits. In discharge circuits for jet detectors and explosion gas detectors, shown in figures 4.8 and 4.31, the battery was momentarily switched into and out of the circuit. This had the effect of charging the capacitor and was registered on the storage oscilloscope as a voltage change. The oscilloscope, a Gould OS4000, is shown in plate 5.1. The capacitor was then discharged by shorting the jet or gas detector plates with a piece of wire. This was to simulate the passage of a jet or the arrival of explosion gases and was registered on the oscilloscope by the trace returning to its original position.

Break circuits shown in figures 4.10 and 4.29 were used for electrically conducting silver paint crack detectors and graphite rod spall detectors. The circuit was tested by opening the switch included in the shunt arm. This simulated the breaking of a detector and was registered as a voltage change on the oscilloscope. During explosion testing the switch was kept closed.

Figure 4.3 shows a Wheatstone bridge circuit with a single active arm and three temperature compensation gauges. This circuit was used with electrical resistance strain gauges buried in concrete and also used in the soil pressure gauge. A resistance meter was used to check electrical conductivity and the circuit was then connected to a FE359TA bridge amplifier supplied by Fylde Ltd, Preston. The output from this was monitored as a voltage by the OS4000 oscilloscope. The signal amplification factor through the bridge amplifier was 500 times when it was operated with a 10V input to the bridge. The bridge amplifier had balancing circuits in the internal electronics and these were varied in conjunction with the voltage controls on the oscilloscope to provide a steady voltage on the oscilloscope.

The fourth electrical circuit was the potentionmetric circuit shown in figure 4.33 , used for the potentiometric variable displacement transducer. The storage oscilloscope monitored the change in voltage as the displacement of the slab relative to the gauge caused the push rod rider on the resistance wire in the gauge to move. The gauge was set up with its push rod fixed to the slab via a threaded bar as shown in figure 4.32 . The voltage at this positon was taken as zero on the oscilloscope screen to provide a datum for relating displacements.

5.1.2 Shaped Charge Jet Impact Test Procedure

After all electrical checks described in section 5.1.1 were complete, all power to gauges was switched off and capacitors were discharged to prevent spurious electrical signals affecting explosives' circuits. Appendix 2 gives actual detailed charge firing rules. The shaped charge holder described in section 4.3.1 was now adjusted for final standoff, level and angle of incidence, the details of which are given in table 4.12. This was done by altering the screwed rod legs until the required position was obtained. A small bubble level was used to ensure that the charge holder remained level. The holder was held in position on the test specimen by small lumps of 'plasticine' moulded around the bases of the legs.

The high speed camera described in section 4.4.5 was then arranged as shown in figure 4.34 and a trial exposure made to ensure that the camera and flash light were operating correctly. Instructions on the use of the camera are specialised and reference should be made to the literature accompanying the instrument. The charge firing circuit, a Reynolds FS10 EBW System shown in plate 5.2 was laid out and connected to the camera circuitry and the oscilloscope as shown in figure 5.1. The camera was run again without exposing the film to ensure that all control circuits for the charge firing system and the oscilloscope were functioning.

The shaped charge was now placed on its holder. The EBW initiator was connected to two lead wires. Each wire was a 2m long 'uniradio 43' solid copper core screened coaxial cable. These wires were kept shorted together before the initiator was connected to ensure that no potential difference existed between them. The EBW initiator was located in its position on top of the charge as shown in plate 5.3. The lead wires from the initiator were connected into the firing system along with three firing circuit wires. Each of these was a 20m long 'uniradio 43' coaxial cable. The safety key was removed from the firing module and placed in the control module.

Instrumentation was now energised and allowed to 'warm up' for ten minutes. This ensured that resistors in internal electronic circuits in the amplifiers and the strain gauges themselves reached a stable temperature. The oscilloscope and bridge amplifiers were then adjusted to zero any voltage drift. The firing circuit was now energised and electrical control given to the high speed camera electronic circuitry to deliver the firing pulse. This pulse was delivered when the camera reached its operating speed for the interframe time required. Table 5.1 gives details of delays in the camera and firing systems and figure 5.2 gives a schematic diagram showing the signals between the camera, the firing system and the oscilloscope. Throughout the firing procedure it was necessary to manually hold the arming switch on the firing circuit. Thus although the high speed camera controlled the firing, the release of this switch could at any time abort the explosion. This ensured the safety of personnel.

5.1.3 Subsurface Explosive Charge Test Procedure

Basically the same procedure was followed for subsurface explosion tests as for shaped charge jet impact tests and Appendix 2 gives detailed rules for carrying out tests involving subsurface explosive charges.

The electrical instrumentation used in subsurface charge tests consisted of buried electrical resistance strain gauges, a buried soil pressure gauge and a blast detector gauge. These were checked as described in section 5.1.2 before the test and were then switched off. All capacitors were discharged. In test slabs already perforated by a shaped charge jet no further preparation was required. Slabs which had not been previously tested had a cardboard tube projecting up from the soil under the slab through the concrete as described in section 4.2.1. The cardboard tube was now removed, its Tellus MRO oil coating prevented the material sticking to the concrete or disintegration occurring due to dampness from moisture in the soil.

The high speed camera, described in section 4.4.5, was then operated as described in section 5.1.2. to ensure correct operation of the camera system. The charge firing circuit was set up as shown in figure 5.1 and the camera was run again without exposing the film to ensure that the firing pulse and the oscilloscope triggering pulse were correctly delivered.

The explosive charge was prepared as described in section 4.3.2 and taped to a 2mm diameter silver steel rod made to the length needed for the depth of burial required. A hook on the end of the rod allowed the rod to hang from the top of the slab concrete. The initiator was connected to a pair of shorted lead wires each consisting of 2m of 'uniradio 43' screened coaxial cable. After the initiator was pushed in contact with the explosive charge and taped to the rod, the junction between the initiator and the main explosive charge was also securely taped to the steel rod using insulation tape. The rod and its charge were lowered into the hole in the test specimen and the hook on the rod was taped to the surface of the concrete to prevent accidental movement. A blast detector gauge,described in section 4.4.3, was then set in its operating position over the hole as shown in figure 4.30.

The lead wires from the initiator were coupled into the charge firing module and this was coupled in turn into the control module as shown in figure 5.1. All instruments were switched on and left to warm up for ten minutes as in the case of shaped charge explosion tests. Strain gauge amplifiers were adjusted to zero any voltage drift on the oscilloscope. The firing circuit was now energised and electrical control of the charge firing transferred to the high speed camera system. The high speed camera was run up to speed and the camera system opened the camera shutter and fired the explosive charge. A pulse was also delivered to the oscilloscope to initiate storage of signals as shown in figure 5.2. The arming switch was the safeguard for personnel in this test procedure just as in the shaped charge tests.

5.1.4 Post Test Procedures

After any test involving explosives, all firing and instrumentation circuits were switched off and checked by a multimeter to ensure that they were electrically dead. The site of the explosion was inspected to ensure that the explosive had completely and correctly detonated. Appendix 2 contains detailed rules governing this procedure and also prescribes the courses of action to be followed in the case of partial or non-detonation of any component in the explosive charge.

The output from the instrumentation was stored as traces on the oscilloscope screen. These traces were now measured and photographed. Figures 5.3 to 5.6 show representative traces for the output from respectively, a potentiometric variable displacement gauge, two resistance strain gauges,a brass plate jet or blast detector and silver paint crack or a graphite rod detectors. The Ilford HP5 400 ASA film from the high speed camera was developed as 16oo ASA to aid definition due to low light problems. Plates 5.4 and 5.5. from such a film show a 1/5 scale copper shaped charge jet in air and perforating a brass plate jet detector respectively.

The 100mm concrete cubes and the 100mm by 100mm by 500mm concrete beams, made from each batch of concrete used in the test specimen, were all tested for strength on the same day as the explosion test was performed. The results of these strength tests, to British Standard 1881 part 4 (1980) are given in tables 4.6 and 4.7.

5.2 POST TEST INVESTIGATION TECHNIQUES FOR THE DETERMINATION OF DAMAGE PARAMETERS

5.2.1 Paint Wash Technique to Determine the Extent of Surface Cracking

After a shaped charge jet impact a thin black water paint wash made from Rowney fixed powder paint was applied to the surface of the concrete test specimen. The water paint was allowed to dry so that paint could impregnate cracks and then the surface of the concrete was cleaned with a damp sponge. The paint in the cracks remained and was used to aid the tracing of cracks normally invisible to the naked eye.

This technique was used before impacts in early tests but it was found that no shrinkage cracking was detectable. Hence the method was eventually used only as a post test procedure.

5.2.2 Physical Measurements and Still Photography

All test specimens were physically measured and photographed using still photography after testing to record damage such as cracking, cratering and permanent displacements. The test specimens were then carefully dismantled and at each stage further measurements and photographs were taken. The measurements obtained are given in tables 5.2 to 5.12 for all impact tests and tables 5.13 and 5.14 for all impulse tests. In addition several other tests were performed on materials and samples were taken for further analysis. These are described in the following sections.

5.2.3 Stereoscopic Photography of Craters

The impact of a shaped charge jet left a crater in the surface of the concrete. A stereo-pair of photographs was taken of the crater using a pair of Wild CAD stereocameras mounted on a structural steel gantry 1.2m above the test specimens. Figure 5.7 shows the arrangement of the cameras and plate 5.6 shows the crater as seen by each camera. The photographic plates were later set in a sterecomparator and viewed sterescopically. From this,data were obtained of the coordinates and relative levels of points on the surface of the crater. The punched output tape from the comparator was run through the Universty of Sheffield's ICL 1907S computer using a program written to convert the data into a form useful for plotting cross sections. The program in Fortran IV is listed in Appendix 3 together with a sample of the output. The output was plotted by hand as cross sections to true scale for further measurements to be taken. Figure 5.8 shows a typical set of cross sections.

5.2.4 Sawing and Coring of Test Specimens by Diamond Tipped Tools for Electron Microscope Inspection and Crushing Strength Tests

Concrete slabs and blocks were sawn using a diamond tipped saw shown in plate 4.1 to investigate the depths of cracks and to take cross sections through craters. Plate 5.7 shows a typical cross section of a shaped charge jet impact crater in a 1/5 concrete ground slab.

Concrete cores were taken using either a 10mm or a 25mm diameter diamond tipped coring tool attached to a pillar drill. The 10mm diameter cores were taken through damaged surfaces for samples to be viewed in the University's Philips scanning electron microscope. Plate 5.8 is a typical photograph of the magnified view of the surface of a sample of damaged concrete.

25mm diameter concrete cores were taken from concrete ground slabs at various distances from the point of impact of a shaped charge jet. These cores were trimmed top and bottom to 50mm length and crushed in a longitudinal direction in a compression machine. The test was performed to investigate any reduction in strength in the material at various points in the slab due to the passage of stress waves through the slab during explosion impact testing. Figure 5.9 gives the results of compression tests on a typical set of cores taken from a slab.

5.2.5 Soil Property Tests

The pavement quality concrete slab and the lean mix concrete base layer were removed after all measurements and photography were completed. The exposed surface of the soil foundation was then sampled to provide moisture content information. This was obtained using the drying oven method described in British Standard 1377 (1975) and is listed for each test specimen in table 4.8.The in-situ density of the soil foundation was then determined using the sand cone method of British Standard 1377 (1975) and this information appears in table 4.8. Calibration data for the sand cone is given in table 3.8.

5.2.6 Investigation of Craters in Soil Foundations by Wax and Cement Castings

The shape of the crater formed in soil foundations was preserved by making a casting either in wax or in neat cement paste. Craters formed in sand and clay by shaped charge jets and were filled by pouring molten paraffin wax straight in and allowing it to cool. Craters in clay were larger in diameter than in sand as can be seen from plates 5.9 and 5.10. These show wax castings of holes in clay and sand respectively. The larger volume of wax in clay craters tended to shrink on cooling so the crater needed to be topped up the day after the cast was first made.The wax was then left for a further day to allow the extra wax to solidify before removal from the soil. Wax castings in sand could be removed after one day and needed no further topping up.

The crater formed by a subsurface explosion in clay soil was too large to be filled with wax. The casting material used in this case was a neat cement plaste made from 'Ferrocrete' rapid hardening cement to which just sufficient water was added to form a smooth paste. This paste was poured into the crater and worked into fissures in the crater sides by hand. Since cement is caustic, rubber gloves were required. The crater was topped up and left to harden for three days under a layer of polythene to prevent evaporation of moisture. The paste was in contact with cool material and so shrinkage was not a problem. The cast was removed from the soil after three days and was clearly seen to accurately model the crater shape by the material adhering to it, especially in fissures.

Subsurface charge craters in sand soils were impossible to fill with any wax or cement paste because the crater roof and sides fell into the crater and filled it with loose material. In this case the crater was carefully exposed by diggging sand out until a vertical face of sand was exposed through the centre of the crater. At the same time, the vertical coloured sand columns described in sections 4.1.2 and 4.2.1 were also exposed. Plates 5.11 and 5.12 show these in sand and in clay respectively. Measurements of particle displacement were now made relative to their original positions by comparing the location of coloured sand columns with their installed locations. In sands this needed to be done quickly because the exposure of the vertical face to the drying action of the air quickly caused instability of the material. If this was expected before the investigation began a 75mm deep face was exposed measured and removed before proceeding with a further 75mm face, until the whole depth of soil had been measured.

Table 5.1

High Speed Camera Delay Data

Interframe time µs	Delay from firing pulse to first frame µs	Delay between firing pulse and charge initiation µs	Maximum event viewing time from first frame µs	Delay for flash build up µs	Flash duration µs
1	6.8	14.5	30	60	200
4	27.2	14.5	120	60	200
5	34	14.5	150	60	200
8	54.4	14.5	240	60	200

Table 5.2

Measurements of Cracking and Local Damage

by 43g Copper Lined Shaped Charge Jet Impacts on Concrete Slabs

Slab Code	Surface Crack Number of Each Type PQC R	RC	RM	C	P	A	Total Length (PQC) cm	Jet Penetration Depth (mm)	Maximum Hole Diameter in Concrete (mm)	Notes
S1	-	-	1	-	1	-	-	250	15	
S2	-	-	-	-	-	-	-	245	15	R
S3	-	-	1	-	2	-	85	191	12	
S4	-	-	-	-	-	-	-	261	14	R
S5	Shattered						-	186	15	A
S6	-	-	-	-	-	-	-	248	12	
S7	-	-	2	-	-	-	60	240	16	
S8	-	-	-	-	-	-	-	210	15	
S9	-	-	2	-	-	-	55	310	14	
S10	-	-	1	-	-	-	50	258	14	
S11	-	-	-	-	-	-	-	272	13	
S13	-	-	-	-	-	-	-	160	11	B
S14	-	-	-	-	-	-	-	262	15	
S15	-	-	-	-	-	-	-	192	16	
S15	3	1	2	-	-	-	145	158	16	
S15	1	1	2	-	-	-	120	132	17	
S16	-	-	1	-	-	-	55	65	19	
S16	3	-	2	-	-	-	125	247	15	
S16	4	-	2	-	1	-	185	272	15	
S17	-	-	1	-	-	-	55	338	12	
S17	1	-	2	-	3	1	175	252	15	
S17	2	-	2	-	2	-	116	108	17	
S18	-	-	1	-	-	-	55	234	15	
S18	3	-	2	-	2	-	153	140	12	
S18	3	1	2	-	4	-	206	281	12	
S19	2	-	2	-	2	1	142	225	12	
S19	2	1	2	-	2	2	175	135	16	
S20	-	-	-	-	-	-	-	205	14	R
S20	3	-	2	-	2	-	136	94	18	R
S20	3	-	1	-	4	-	91	70	15	R
S21	-	-	4	-	-	-	185	127	12	
S21	7	1	2	-	7	1	273	205	15	
S21	6	1	1	-	5	1	217	72	16	
S22	-	-	4	-	3	-	247	215	12	
S22	6	1	1	-	6	2	277	210	12	
S22	6	-	2	-	6	2	317	145	13	
S23	2	1	2	-	-	-	268	195	14	
S23	3	1	-	1	4	-	196	337	14	
S23	8	-	2	3	4	-	270	160	18	

Table 5.2 (cont'd)

Slab Code	Surface Crack Number of each Type PQC R	RC	RM	C	P	A	Total Length (PQC) cm	Jet Penetration Depth (m)	Maximum Hole Diameter in Concrete (mm)	Notes
S24	-	1	4	4	1	-	336	215	12	
S24	5	1	2	1	4	-	362	73	14	
S24	10	3	2	5	-	-	276	163	15	
S25	-	1	2	-	-	-	166	-	16	
S26	2	1	2	-	-	-	274	-	15	
S27	-	-	2	-	-	-	(103)	-	18	
S27	5	1	-	1	4	1	261	-	15	
S27	4	1	2	-	2	-	212	-	14	
S28	-	-	-	-	-	-	-	-	16	C
S29	-	-	-	-	-	-	83	222	20	D
S30	-	-	-	-	-	-	-	176	14	D
S32	1	3	4	-	-	-	256	575	35	E
S33	2	-	2	-	-	-	132	-	-	
S33	5	-	2	-	-	-	162	-	-	
S34	1	-	-	-	3	1	137	-	-	
S34	2	-	-	-	2	-	121	-	-	

Slabs listed several times received several impacts in the order listed.

Key to crack types

R - radial, RC - radial to corner of slab,
RM - radial along minimum distance to side of slab
C - circumferential, P - parallel to sides of slab
A - across slab corner

Key to notes

A - 500mm square slab. Main slab previously impacted by an armour piercing bullet
B - Cracks influenced by large blocks carrying strain gauges
C - Jet detectors embedded in slab influenced cracking Penetration depth invalid.
D - Oblique impact
E - 298g copper lined shaped charge
R - Reinforced concrete slab

Table 5.3

Measurements of Cracking and Local Damage by 43g Aluminium Lined Shaped Charge Jet Impacts on Concrete Slabs

Slab Code	Surface Crack Number of each Type PQC						Total Length (PQC) mm	Jet Penetration Depth (mm)	Minimum Hole Diameter in Concrete (mm)
	R	RC	RM	C	P	A			
S33	-	-	4	-	-	-	189	257	19
S33	3	1	-	-	3	2	194	235	25
S33	3	1	1	-	-	-	132	-	-
S34	-	-	-	-	-	-	-	185	20
S34	1	1	2	-	2	0	119	-	24
S34	1	-	2	-	2	0	111	211	20

Key to cracks types

R - radial, RC - radial to corner of slab, RM - radial along minimum distance to side of slab, C - circumferential, P - parallel to sides of slab, A - across slab corner.

Slabs listed several times received several impacts in the order listed.

Table 5.4

Measurements of Cracking and Local Damage

by 43g Copper Lined Shaped Charge Jet Impacts on Concrete Blocks

Block Code	SURFACE CRACKS								Jet Penetration Depth (mm)	Minimum Hole Diameter (mm)	Notes
	Number of each Type					Total Length (cm)					
	R	RC	RM	S	SP	Top	Sides	Base			
B3	-	-	-	-	-	-	-	-	150	13	A
B4	4	4	4	9	4	222	296	-	89	10	
B5	7	3	4	11	5	230	396	-	160	16	
B6	6	3	4	15	9	271	537	-	115	-	
B7	-	-	2	-	-	380	760	380	216	30	
B8	-	-	-	-	-	-	-	-	165	-	B
B9	-	-	-	-	-	-	-	-	210	-	
B10	-	-	-	-	-	-	-	-	136	-	B
B11	-	-	-	-	-	-	-	-	177	14	C
B12	-	-	-	-	-	-	-	-	216	15	C
B13	-	-	-	-	-	-	-	-	221	-	D
B14	-	-	-	-	-	-	-	-	140	15	E
B25	3	3	4	9	-	171	262	-	255	-	
B26	2	2	3	6	-	114	125	-	-	-	
B27	2	-	4	4	-	84	68	-	200	20	
B28	5	4	4	5	-	228	179	-	204	-	F
B29	1	-	4	5	1	85	192	-	260	15	F
B30	-	-	4	4	4	76	251	-	178	15	F
B31	-	1	4	5	-	103	167	-	179	-	F
B32	-	-	2	2	-	30	33	-	194	11	
B33	-	-	4	4	-	61	44	-	174	10	
B34	1	-	4	5	-	86	86	-	101	9	
B35	-	-	2	2	-	30	42	-	190	13	
B36	-	1	3	2	-	67	38	-	195	12	
B37	-	-	3	3	-	44	44	-	205	13	
B38	-	-	2	2	-	32	47	-	122	18	
B39	-	1	3	3	-	68	76	-	218	13	

Table 5.4 (cont'd)

Block Code	SURFACE CRACKS								Jet Penetration Depth (mm)	Minimum Hole Diameter (mm)	Notes
	Number of each Type					Total Length (cm)					
	R	RC	RM	S	SP	Top	Sides	Base			
B40	-	-	4	4	-	66	108	-	175	18	
B41	-	-	3	3	3	47	72	-	226	11	
B42	1	-	4	5	-	85	141	-	122	12	
B45	-	1	4	4	-	89	106	-	170	14	
B46	7	1	4	10	2	181	267	-	110	20	G
B65	1	2	4	4	4	99	164	-	130	11	

Key to crack types

R - radial, RC - radial to corner, RN - radial to mid point side.
All R cracks are on impact suface (Top)
S - cracks parallel to jet axis, SP - cracks perpendicular to jet axis.
All S cracks are on cube surfaces perpendicular to impact surface (Sides)

Key to Notes

- A Did not crack
- B Cracks influenced by penetration detectors
- C Cracks influenced by blocks for strain gauges
- D Block shattered - no details
- E Block splintered - no details
- F Base cracked
- G Different initiator

Table 5.5

Measurements of Cracking and Local Damage by Modified Copper Lined Shaped Charge Jets on Concrete Blocks

Block Code	SURFACE CRACKS: Number of Each Type: R	RC	RM	S	SP	Total Length (cm): Top	Sides	Base	Jet Penetration Depth (mm)	Minimum Hole Diameter (mm)	Notes
B16	-	-	-	-	-	0	0	0	242	15	A
B17	-	-	-	-	-	0	0	0	187	8	A
B18	-	-	4	4	4	68	174	0	167	10	
B19	-	-	-	-	-	0	0	0	36	-	
B20	7	1	1	3	-	110	47	0	162	14	
B21	-	-	-	-	-	0	0	0	73	20	
B22	2	-	1	1	-	48	26	0	152	16	
B23	-	-	-	-	-	0	0	0	120	20	B
B24	-	-	-	-	-	0	0	0	72	10	B
B60	5	1	4	4	-	267	265	75	646	20	
B61	10	-	4	4	-	346	228	75	625	22	
B62	1	1	4	3	-	171	158	0	640	12	
B63	2	-	1	1	-	95	75	0	500	15	
B64	2	-	3	3	--	150	129	0	695	20	

Key to crack types

R - radial, RC - radial to corner, RM - radial to mid point of side.
All R cracks are on impact surface (Top)
S - cracks parallel to jet asix, SP - cracks perpendicular to jet axis.
All S cracks are on cube surfaces perpendicular to impact surface (Sides)

Key to Notes

A - No cracks. Standoff too large
B - No cracks. Insufficient jet energy

Table 5.6

Measurements of Cracking and Local Damage by 43g

Aluminium Lined Shaped Charge Jet Impacts on Concrete Blocks

Block Code	SURFACE CRACKS								Jet Penetration Depth (mm)	Minimum Hole Diameter (mm)
	Number of Each Type					Total Length (cm)				
	R	RC	RM	S	SP	Top	Sides	Base		
B47	10	-	2	7	4	161	188	0	123	15
B48	7	1	4	14	2	229	408	0	-	-
B49	6	-	3	6	-	141	110	0	104	23
B50	12	1	4	9	-	245	174	0	160	20
B51	3	-	4	6	-	122	76	0	115	23
B52	3	-	3	5	-	99	99	0	127	33

Key to crack types

R - radial, RC - radial to corner, RM - radial to mid point of side.
All R cracks are on impact surface (Top)
S - cracks parallel to jet axis, SP - cracks perpendicular to jet axis.
All S cracks are on cube surfaces perpendicular to impact surface (Sides)

Table 5.7

Measurements of 43g Copper Lined Shaped Charge Jet Impact Holes in Concrete Slabs

Slab Code	DIMENSIONS OF HOLE IN EACH IDEALISED ZONE TO FIGURE 5.10 (mm)													
	1		2		3		4		5		6		7	
	MAX DIA	DEPTH	MAX DIA	DEPTH	MAX DIA	DEPTH	MAX DIA	DEPTH	MAX DIA	DEPTH	MAX DIA	DEPTH	MAX DIA	DEPTH
S1	91	-	-	-	30	-	x	x	x	x	x	x	x	x
S2	x	x	x	x	x	x	x	x	x	x	x	x	x	x
S3	95	25	22	15	12	23	-	-	-	-	-	-	-	-
S4	x	x	x	x	x	x	x	x	x	x	x	x	x	x
S5	120	15	29	20	15	25	65**	6	15	20	65**	10	25	90
S6	80	20	25	30	12	15	33**	3	13	15	60**	12	-	-
S7	120	14	45	25	16	26	x	x	x	x	x	x	x	x
S8	115	22	24	19	15	4	125//	22	19	22	49**	5	-	-
S9	-	-	-	-	-	-	-	-	-	-	-	-	-	-
S10	80	27	-	-	14	30	40**	18	19	23	50*	19	70	146
S11	70	5	27	45	13	1	40**	20	19	25	30*	1	80	175
S13	47	6	21	32	10	22	33**	9	13	9	70**	29	30	53
S14	x	x	x	x	x	x	x	x	x	x	x	x	x	x
S15	90	25	43	1	16	33	50**	17	19	20	-	-	-	-
S15	60	43	25	1	16	12	40//	17	19	23	-	-	-	-
S15	50	17	-	-	17	27	80//	26	23	25	-	-	-	-
S16	95	18	-	-	27	22	100//	+	+	+	+	+	+	+
S16	80	13	35	21	34	31	28//	+	+	+	+	+	+	+
S16	80	23	32	22	15	15	27//	+	+	+	+	+	+	+
S17	85	16	-	-	24	44	25//	+	+	+	+	+	+	+
S17	70	15	-	-	20	50	20//	+	+	+	+	+	+	+
S17	50	20	-	-	17	29	90//	+	+	+	+	+	+	+
S18	90	22	37	1	15	43	-	+	+	+	+	+	+	+
S18	50	14	-	-	18	34	70//	+	+	+	+	+	+	+
S18	70	12	30	5	24	48	28//	+	+	+	+	+	+	+
S19	94	20	25	20	-	-	75//	25	18	30	21	5	27	125
S19	60	23	-	-	16	17	140//	33	25	12	76*	20	40	30
S20	105	30	20	20	14	15	-	-	15	30	75**	10	30	100
S20	50	15	25	15	18	10	103//	54	-	-	-	-	-	-
S20	120	15	21	-	15	50	140//	8	-	-	-	-	-	-
S21	80	13	25	21	15	7	58//	24	29	30	40	1	40	32
S21	70	23	23	18	15	24	20**	-	20	30	22*	20	20	90
S21	90	13	50	24	16	-	110//	35	-	-	-	-	-	-
S22	80	14	30	13	12	35	30//	10	8	19	84*	11	103	113
S22	40	16	20	16	12	18	40//	21	8	7	100*	27	93	105
S22	70	17	35	30	15	18	18//	1	15	17	77*	26	77	37
S23	60	5	25	33	14	20	70//	+	+	+	+	+	+	+
S23	70	10	29	27	13	13	70//	+	+	+	+	+	+	+
S23	70	9	38	56	18	-	-	-	-	-	-	-	-	-

Table 5.7 (cont'd)

Slab Code	DIMENSIONS OF HOLE IN EACH IDEALISED ZONE TO FIGURE 5.10 (mm)														
	1		2		3		4		5		6		7		
	MAX DIA	DEPTH	MAX DIA	DEPTH	MAX DIA	DEPTH	MAX DIA	DEPTH	MAX DIA	DEPTH	MAX DIA	DEPTH	MAX DIA	DEPTH	
S24	55	28	30	-	15	37	40**	5	15	25	97	-	134	120	
S24	80	36	40	-	14	9	120//	28	-	-	-	-	-	-	
S24	50	10	30	55	19	-	+	+	+	+	+	+	110	72	
S25	60	13	25	9	16	43	+	+	+	+	+	+	+	+	
S26	35	29	19	18	15	18	+	+	+	+	+	+	+	+	
S27	75	11	30	11	18	43	40**	5	20	25	-	-	-	-	
S27	65	23	22	27	17	15	15**	1	15	29	-	-	-	-	
S27	80	22	20	23	14	-	90//	25	20	25	-	-	-	-	
S28	70	15	26	15	16	30	16	-	16	35	-	-	-	-	
S29	110	30	54	7	20	40	60//	3	30	32	100*	-	90	110	B
S30	110	24	60	10	14	42	50//	2	30	33	-	-	35	65	B
S32	140	75	85	85	-	-	50	14	35	37	40	24	40	340	A

Slabs listed several times received several impacts in the order listed.

Key to symbols

// Diameter in pavement concrete
** Diameter in Lean mix concrete
* Diameter in soil
x Data not recovered due to subsurface charge
\+ Data not recovered due to repeated use of the lean mix concrete

Notes

A 298g copper lined shaped charge
B Oblique impact

Table 5.8

Measurements of 43g Aluminium Lined

Shaped Charge Jet Impact Holes in Concrete Slabs

Slab Code	DIMENSIONS OF HOLE IN EACH IDEALISED ZONE TO FIGURE 5.10 (mm)													
	1		2		3		4		5		6		7	
	MAX DIA	DEPTH	MAX DIA	DEPTH	MAX DIA	DEPTH	MAX DIA	DEPTH	MAX DIA	DEPTH	MAX DIA	DEPTH	MAX DIA	DEPTH
S33	80	25	25	15	19	12	25	13	-	-	140*	30	165	162
S33	80	26	-	-	25	37	35	2	35	30	57*	-	200	140
S33	90	26	-	-	35	37	40	2	-	-	-	-	-	-
S34	70	18	35	22	20	25	-	-	20	30	-	-	40	90
S34	85	20	30	30	24	5	40	18	25	-	40	23	-	-
S34	70	25	25	33	20	-	40	9	30	3	40	25	40	116

Slabs listed several times received several impacts in the order listed.

* Diameter in soil

Table 5.9

Measurement of 43g Copper Lined Shaped

Charge Jet Impact Holes in Concrete Blocks

Block Code	DIMENSIONS OF HOLE IN EACH IDEALISED ZONE TO FIGURE 5.10 (mm)							
	1		2		3		TAPERED SECTION	
	MAX DIA	DEPTH	MAX DIA	DEPTH	MAX DIA	DEPTH	MAX DIA	DEPTH
B3	-	-	-	-	-	-	-	-
B4	85	25	-	-	10	64	-	-
B5	100	23	25	17	16	49	16	71
B6	-	-	-	-	-	-	-	-
B7	82	14	-	-	30	57	12	145
B8	-	-	-	-	-	-	-	-
B9	-	-	-	-	-	-	-	-
B10	-	-	-	-	-	-	-	-
B11	60	26	24	50	14	85	14	15
B12	60	19	25	19	15	87	13	91
B13	-	-	-	-	-	-	-	-
B14	62	19	25	19	15	37	13	65
B25	-	-	-	-	-	-	-	-
B26	-	-	17	20	12	115	-	-
B27	90	12	35	5	20	108	12	75
B28	72	12	25	20	13	98	13	74
B29	110	15	35	55	15	105	15	85
B30	-	-	-	-	-	-	-	-
B31	-	-	-	-	-	-	-	-
B32	55	16	22	22	12	123	10	33
B33	42	25	16	5	10	140	10	4
B34	80	20	25	50	9	31	-	-
B35	57	30	20	20	15	90	10	50
B36	80	25	20	40	13	79	10	51
B37	65	32	20	13	15	95	15	65
B38	62	16	40	24	18	82	-	-
B39	60	16	25	62	13	97	13	43
B40	70	18	30	14	18	115	13	28
B41	60	31	25	36	11	54	10	105
B42	105	30	35	42	12	50	-	-
B45	90	10	50	45	14	105	14	10
B46	127	27	65	33	20	50	-	-
B65	78	10	50	20	11	100	-	-

Table 5.10

Measurements of Modified Copper Lined Shaped Charge Jet Impact Holes in Concrete Blocks

Block Code	DIMENSIONS OF HOLE IN EACH IDEALISED ZONE TO FIGURE 5.10 (mm)							
	1		2		3		TAPERED SECTION	
	MAX DIA	DEPTH	MAX DIA	DEPTH	MAX DIA	DEPTH	MAX DIA	DEPTH
B16	75	9	30	27	15	154	15	52
B17	110	16	35	72	8	54	8	45
B18	60	14	25	61	10	50	20	42
B19	140	20	x	x	x	x	x	x
B20	110	23	59	12	14	127	-	-
B21	63	9	-	-	20	64	-	-
B22	50	12	20	-	16	80	16	60
B23	40	17	-	-	20	36	20	67
B24	60	5	25	20	10	47	-	-
B47	130	37	30	58	15	28	-	-
B60	145	42	42	62	20	256	18	286
B61	160	35	43	70	22	156	22	364
B63	130	50	30	130	12	110	20	350
B63	140	55	30	15	15	330	15	100
B64	140	35	50	205	20	210	20	245

Key

x Untypical hole - long standoff

Table 5.11

Measurements of 43g Aluminium Lined Shaped

Charge Jet Impact Holes in Concrete Blocks

Block Code	DIMENSIONS OF HOLE IN EACH IDEALISED ZONE TO FIGURE 5.10(mm)							
	1		2		3		TAPERED SECTION	
	MAX DIA	DEPTH	MAX DIA	DEPTH	MAX DIA	DEPTH	MAX DIA	DEPTH
B48	-	-	-	-	-	-	-	-
B49	90	17	48	23	23	18	23	46
B50	60	48	25	31	20	81	-	-
B51	80	30	30	15	23	60	23	10
B52	80	15	40	27	22	63	22	22

Table 5.12

Summary of Results from Impact

Experiments on Non Cementitious Specimens

Specimen Code	Jet Penetration Depth (mm)	DIMENSIONS OF HOLE IN EACH IDEALISED ZONE TO FIGURE 5.10 (mm)							
		1		2		3		TAPERED SECTION	
		MAX DIA	DEPTH	MAX DIA	DEPTH	MAX DIA	DEPTH	MAX DIA	DEPTH
M1	80								
M2	82								
M3	63								
M4	80								
M5	60								
M6	82								
M7	82								
M8	72								
M9	79								
M10	77								
M11	48	*	*	*	*	*	*	*	*
M12	61	*	*	*	*	*	*	*	*
M13	49	(50)	(5)	28	30	-	-	9	19
M14	153	(45)	(2)	19	33	9	17	8	103
M15	75	(60)	(4)	30	40	-	-	13	35
M16	85	(50)	(4)	26	40	-	-	11	45
M17	48	(40)	(2)	21	24	11	12	17	12
M19	242	368	20	230	40	-	-	70	182
S11	270++					75	100	75	75
S12	210+					45	115		

Key to Symbols

() Dimensions of surface heave (not crater)
+ 95mm penetration through PQC and lean concrete slabs, 115mm in plasticine
++ 95mm penetration through PQC and lean cocrete slabs, 175mm in plasticine
* Material too hard to section

Table 5.13

Summary of Crater Data from

Impulse Experiments

Test Code	PE4 EXPLOSIVE CHARGE Dimensions (mm)	Mass (g)*	Depth (mm) ***	SUBSOIL CRATER Depth (mm) App.	True	Max. Dia. (mm)	Slab Vertical Displacement (mm)**	Notes
U1	8 dia x 200	16	240	-	240	370	25	
U2	8 dia x 200	16	240	240	240	270	10	
U3	8 dia x 200	16	240	-	250	300	58	
U4	8 dia x 200	16	240	260	260	420	41	
U5	8 dia x 200	16	240	-	295	300	35	
U6	8 dia x 200	16	240	126	206	350	75	
U7	16 dia x 50	16	240	55	205	430	30	
U8	16 dia x 50	16	240	79	214	310	29	
U9	16 dia x 50	16	240	52	305	400	35	A
U10	16 dia x 50	16	240	65	205	330	25	
U11	36 dia x 20	16	240	-	300	220	-	
U12	34 dia x 50	74	425	212	562	600	32	A
U13	16 dia x 50	16	240	140	350	620	0	
U14	16 dia x 50	16	240	280	380	500	10	

Key to symbols

*   Mass includes L2A1 initiator explosive (1.3g)
**   Residual deflection after explosion
*** Depth to centre of gravity of charge

Key to notes

A   Slab had not been impacted prior to the impulse experiment

Table 5.14

Summary of Concrete Slab

Cracks from Impulse Experiments

Test Code	NUMBER OF EACH TYPE OF SLAB CRACKS												
	PQC						LC						
	R	RC	RM	C	P	Parts	R	RC	RM	C	P	A	Parts
U1	4	-	2	-	-	6*	9	2	1	4	4	2	6
U2	2	3	4	-	4	4	4	3	-	3	4	1	8
U3	2	-	3	5	-	12*	10	-	-	10	1	-	25
U4	12	1	4	-	1	4	8	3	2	20	-	-	15
U5	2	1	4	6	-	6*	3	3	4	13	-	-	15
U6	4	-	1	-	-	5	4	2	1	-	5	-	11
U7	5	-	2	-	-	7*	b	b	b	b	b	b	b
U8	2	-	1	-	-	4	b	b	b	b	b	b	b
U10	2	1	2	-	-	6	b	b	b	b	b	b	b
U11	4	1	3	7	-	15*	b	b	b	b	b	b	25
U12	5	-	-	-	-	9	b	b	b	b	b	b	b
U13	Sand surcharge 120mm deep. No concrete slabs												
U14	Clay surcharge 120mm deep. No concrete slabs												

Key to symbols

* Major disruption of the broken parts of the slab

Key to crack types

PQC pavement quality concrete slab
LC lean concrete base
R radial
RC radial to corner of slab
RM radial along minimum distance to side of slab
C circumferential (usually circumferential cracks joined each other)
P parallel to sides of slab
A across slab corner

Notes

b Lean mix cracks not investigated in these tests.

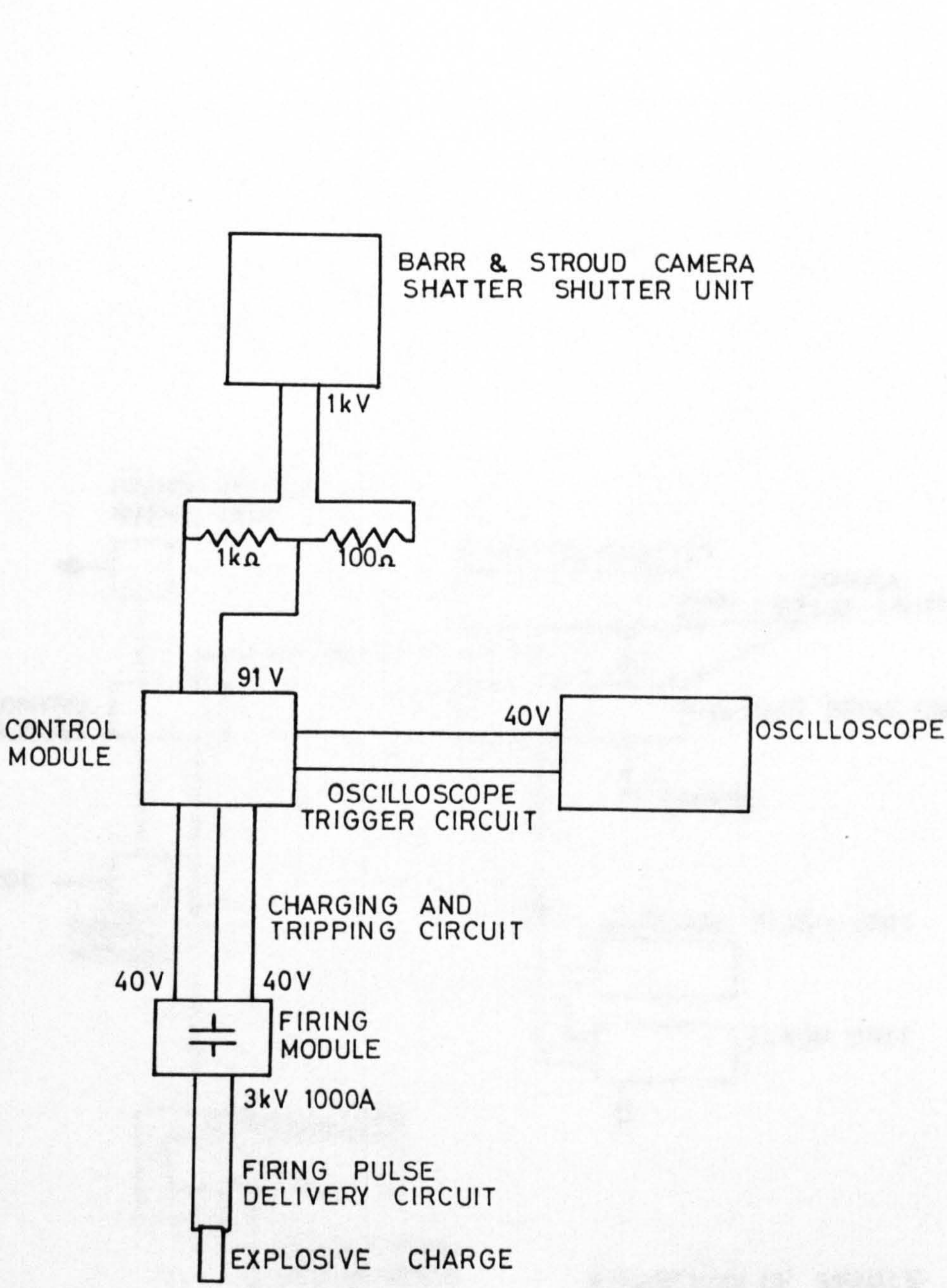

FIGURE 5.1 EXPLOSIVE CHARGE FIRING CIRCUIT DIAGRAM

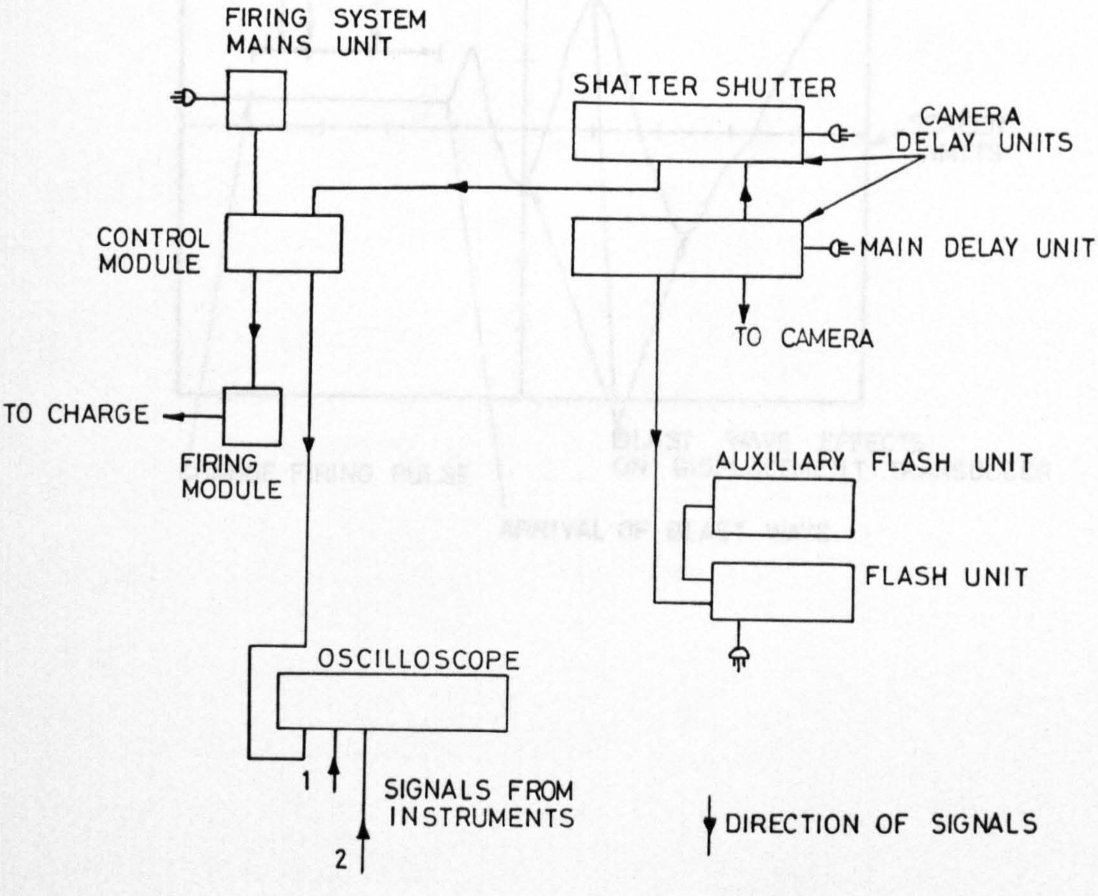

FIGURE 5.2 DIAGRAMMATIC CIRCUIT FOR ALL TEST EQUIPMENT USED WITH THE BARR AND STROUD HIGH SPEED CAMERA

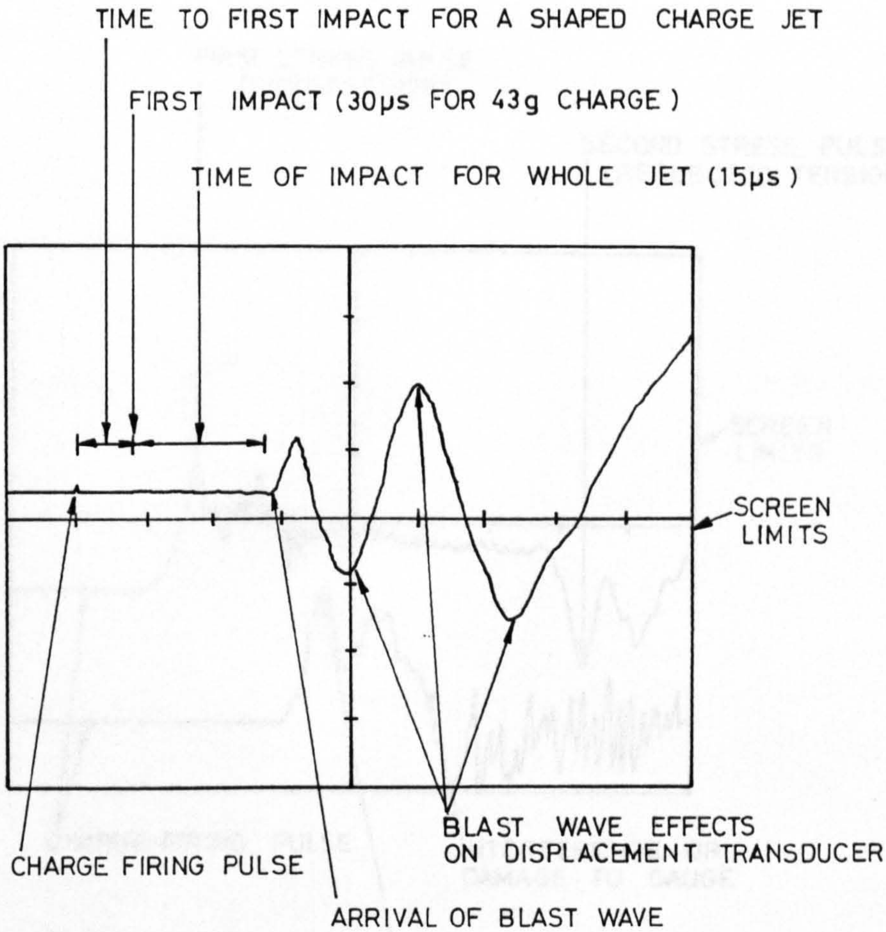

FIGURE 5.3 OSCILLOSCOPE TRACE OF OUTPUT FROM A POTENTIOMETRIC LINEAR VARIABLE DISPLACEMENT TRANSDUCER

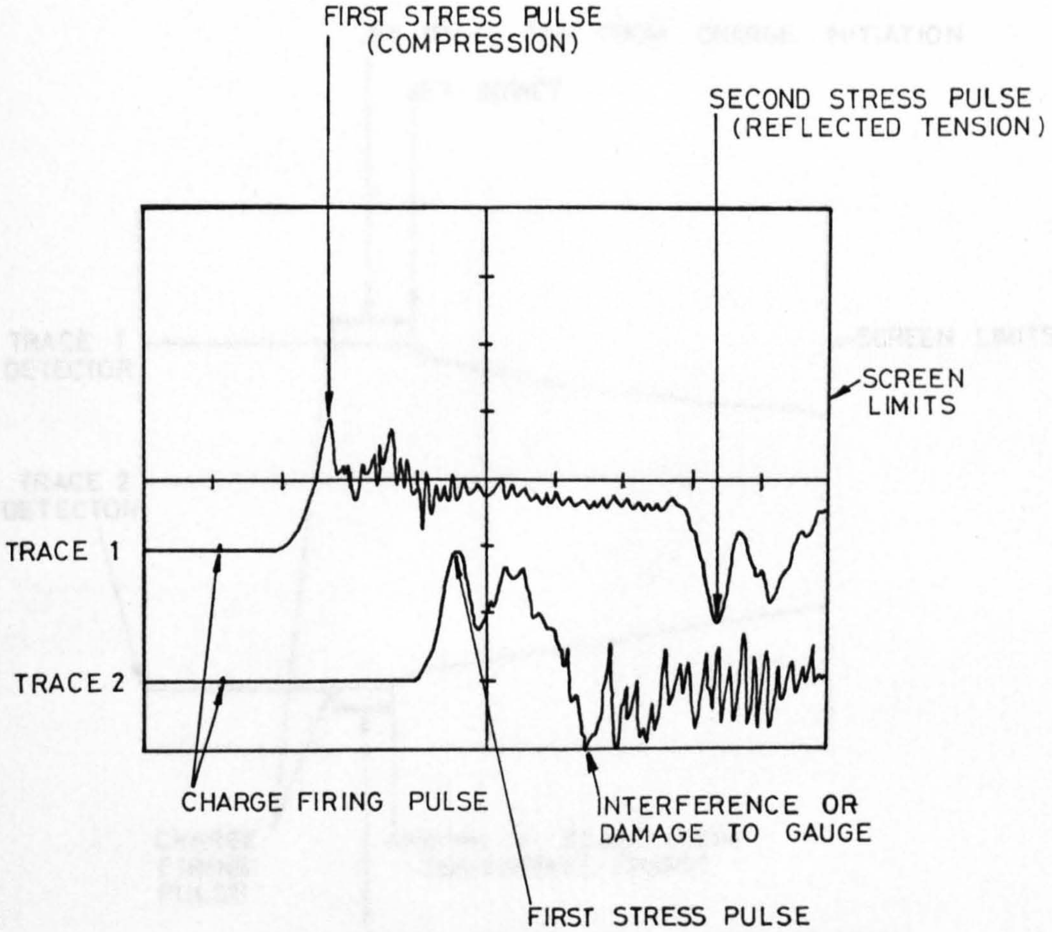

FIGURE 5.4 OSCILLOSCOPE TRACE OF THE OUTPUT FROM TWO ELECTRICAL RESISTANCE STRAIN GAUGES

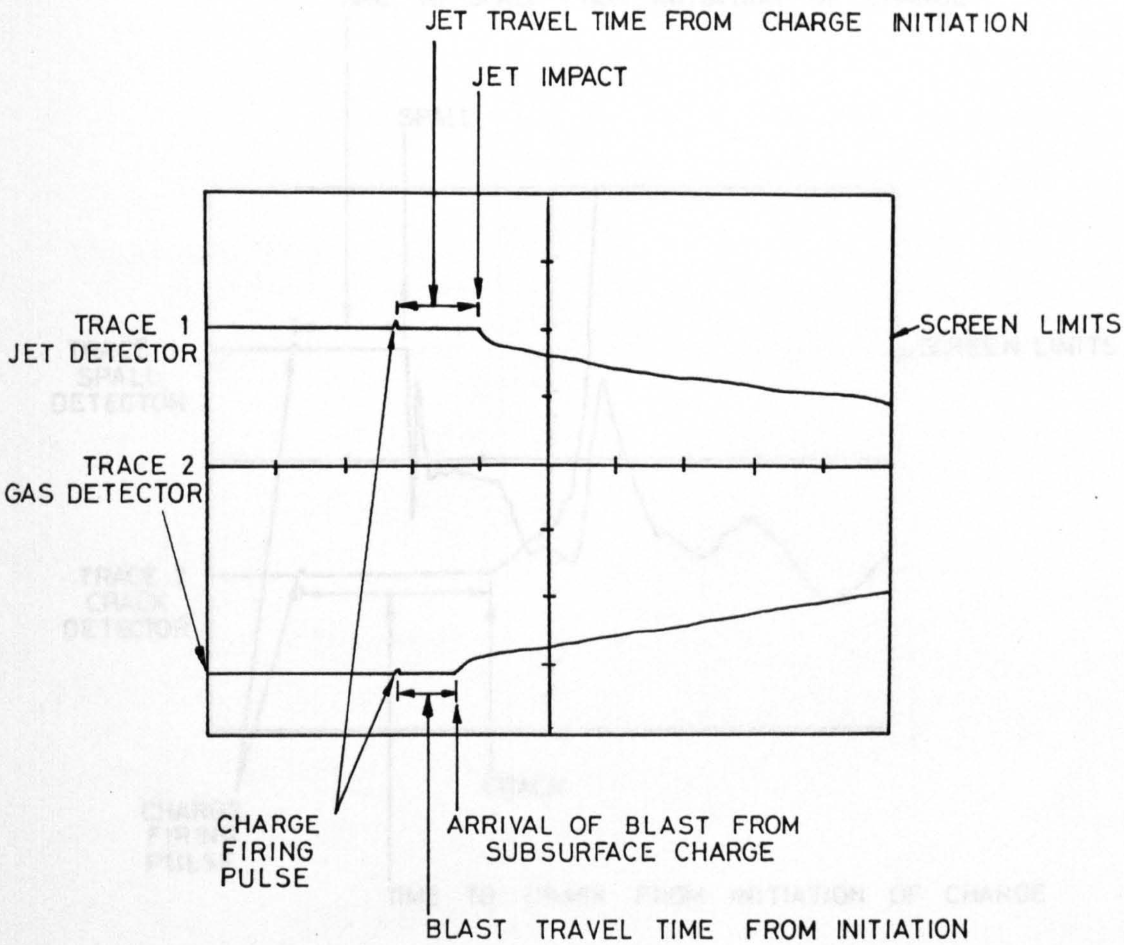

FIGURE 5.5 OSCILLOSCOPE TRACE OF THE OUTPUT FROM A JET OR BLAST DETECTOR GAUGE

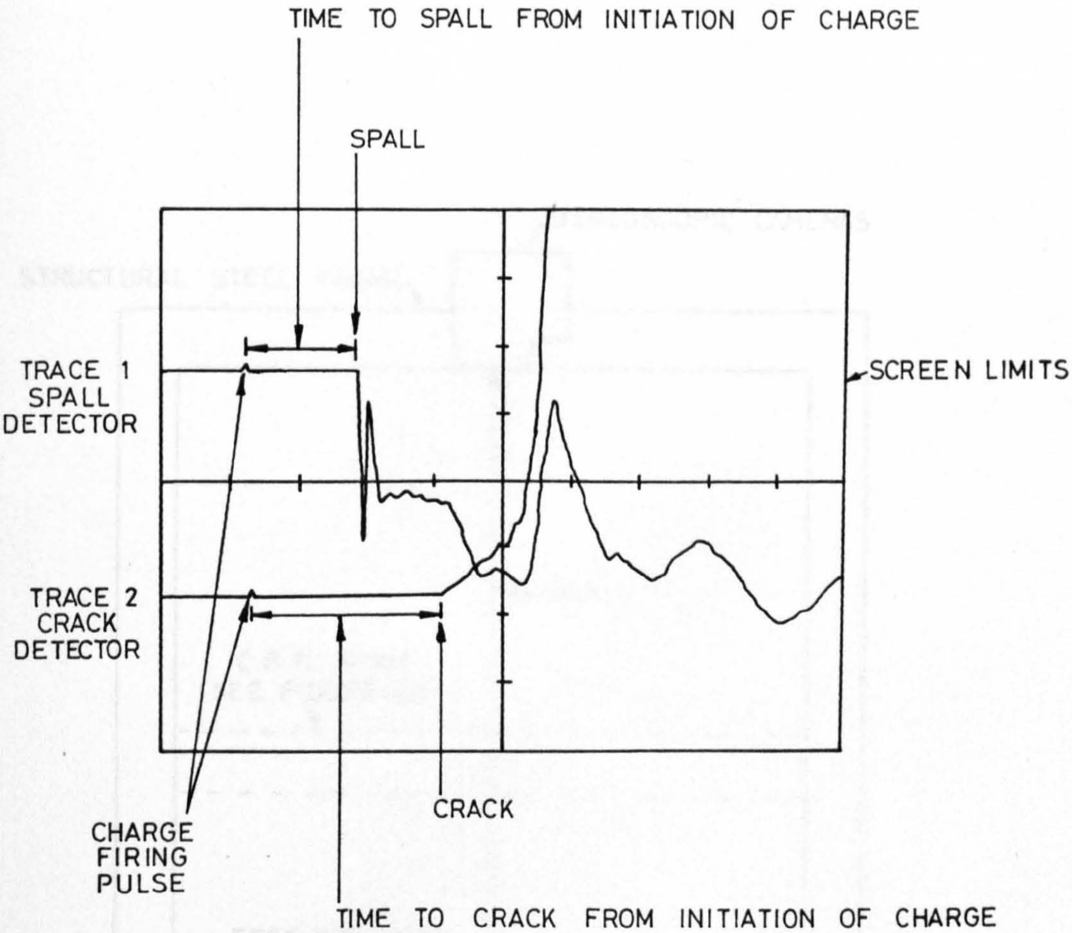

FIGURE 5.6 OSCILLOSCOPE TRACE OF THE OUTPUT FROM ELECTRICALLY CONDUCTING SILVER PAINT CRACK DETECTORS AND GRAPHITE ROD SPALL DETECTORS

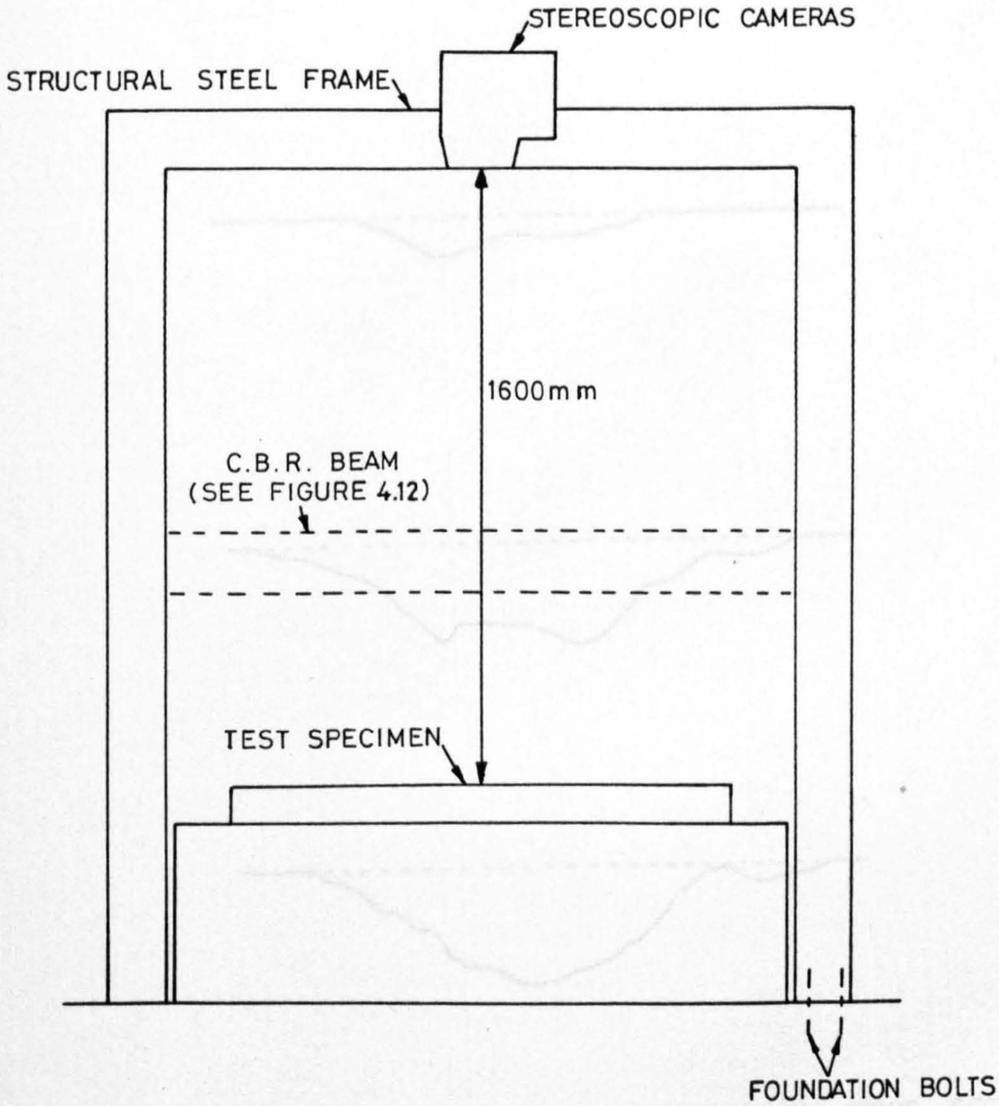

FIGURE 5.7 LOCATION OF STEREOSCOPIC CAMERAS OVER A TEST SPECIMEN

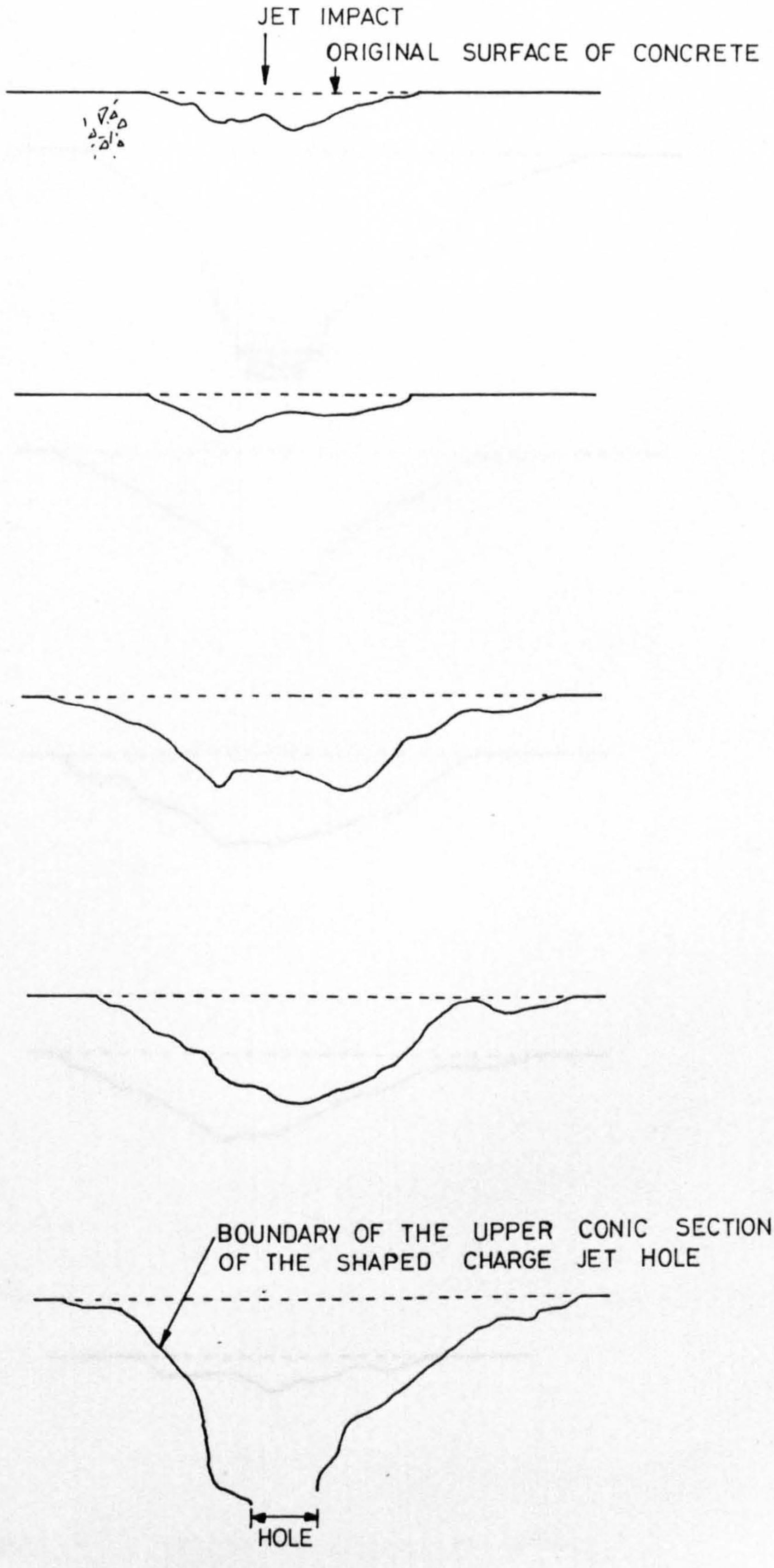

FIGURE 5.8 CROSS SECTIONS AT 6mm INTERVALS OF A SHAPED CHARGE JET HOLE IN CONCRETE FROM STEREOSCOPIC PHOTOGRAPHY

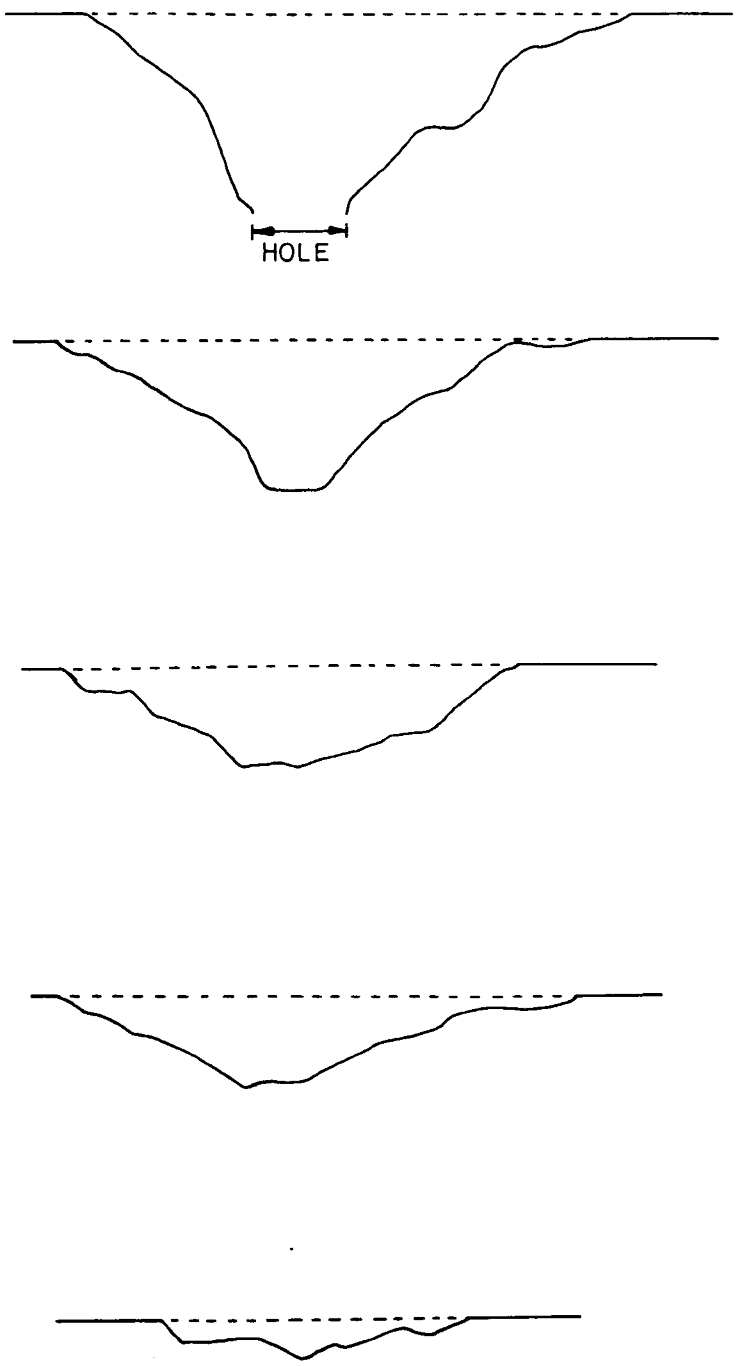

FIGURE 5.8 (Continued)

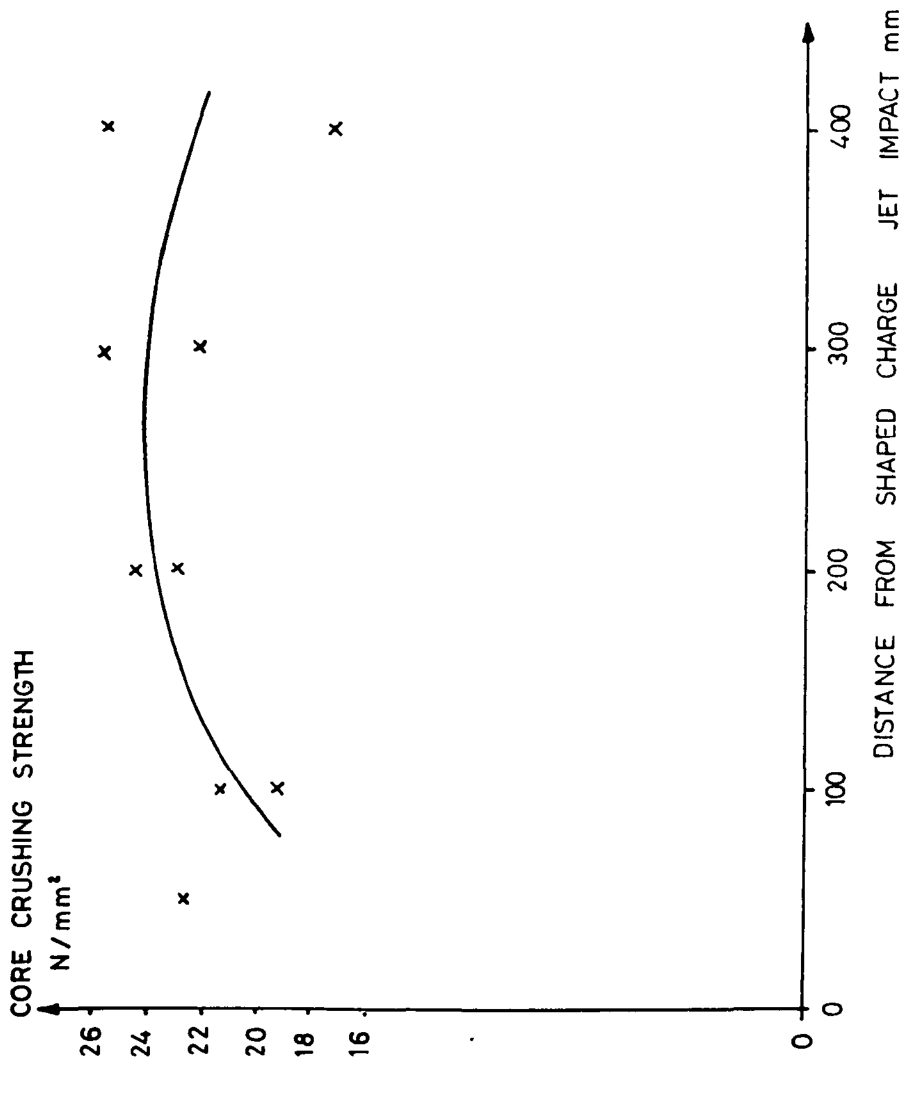

FIGURE 5.9 CRUSHING STRENGTH VERSUS DISTANCE FROM IMPACT FOR 25mm. dia. CONCRETE CORES FROM A SLAB IMPACTED BY A 43g. SHAPED CHARGE JET

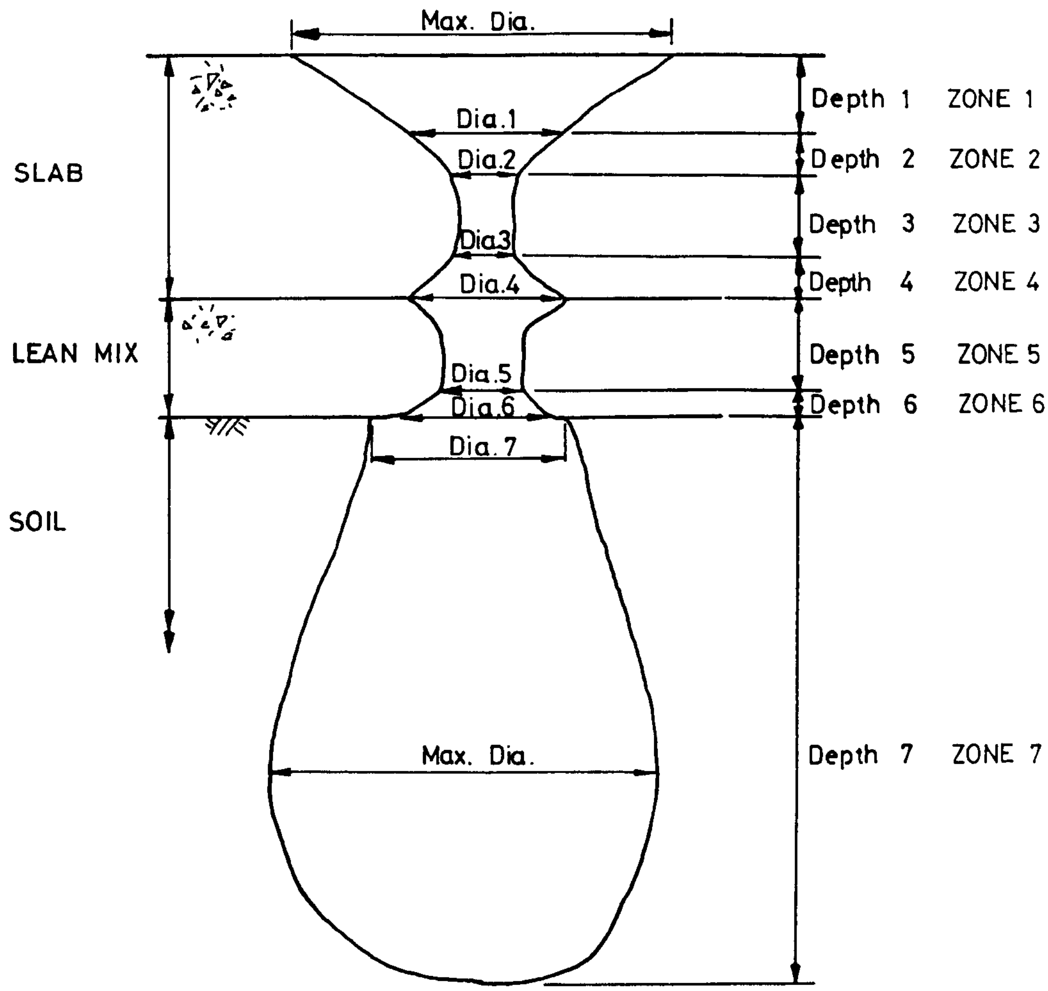

DIMENSIONS FOR ALL TESTS APPEAR IN TABLES 5.7 TO 5.12

FIGURE 5.10 IDEALISED SHAPED CHARGE JET HOLE IN A CONCRETE SLAB FOR MEASUREMENT PURPOSES

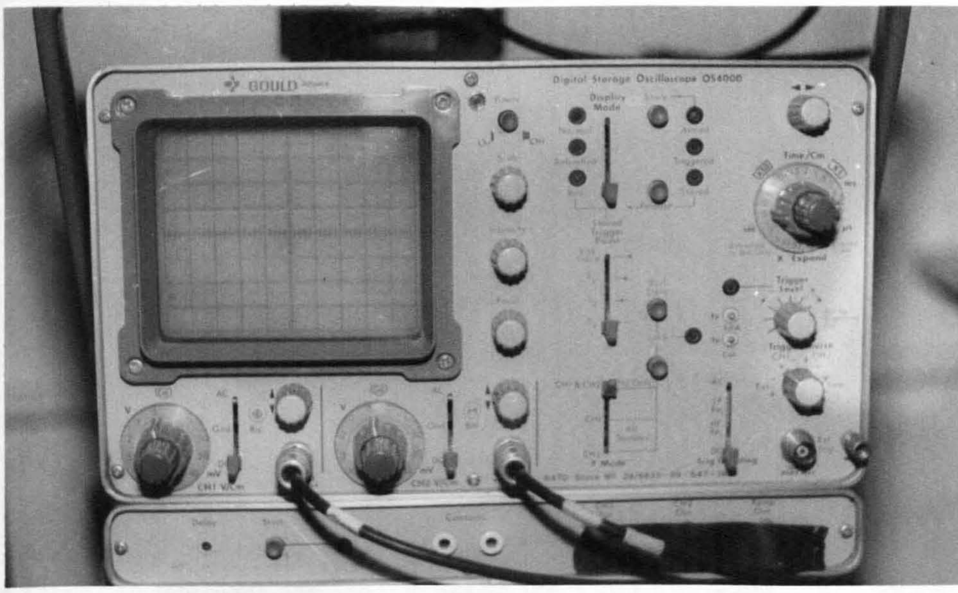

PLATE 5.1 GOULD OS4000 DIGITAL STORAGE OSCILLOSCOPE

MAINS TRANSFORMER

FIRING MODULE

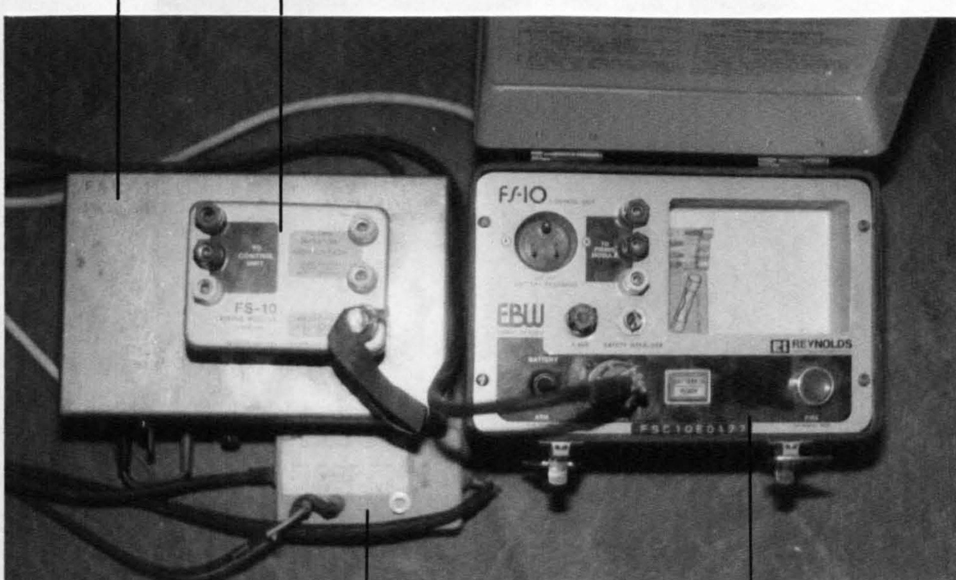

PULSE (FROM SHATTER SHUTTER) SPLITTER BOX (SEE PLATE 4.3)

CONTROL MODULE

PLATE 5.2 REYNOLDS FS10 EBW FIRING SYSTEM

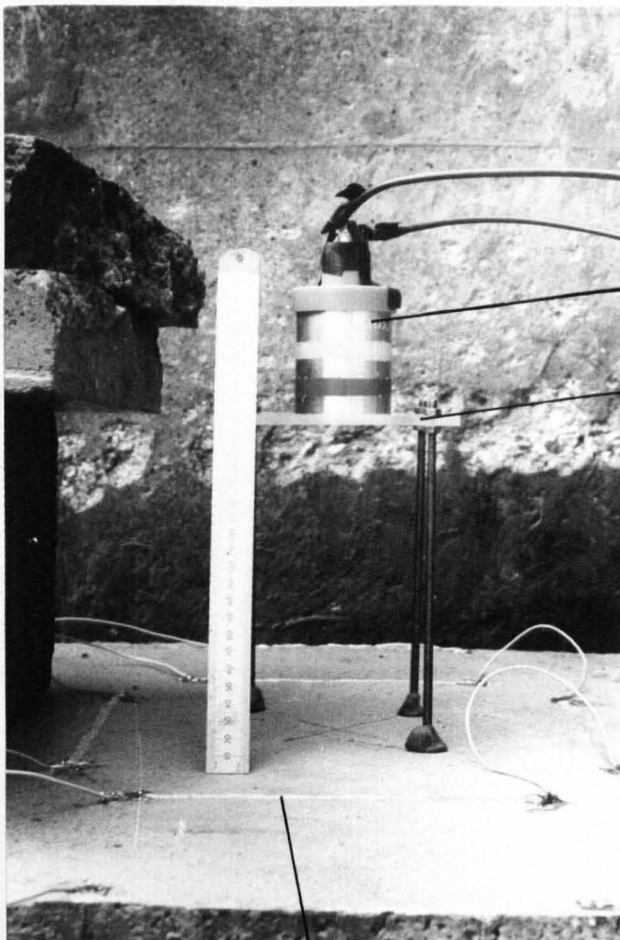

PLATE 5.3 A 298g. 56mm dia. SHAPED CHARGE IN POSITION ON A CONCRETE TEST SPECIMEN

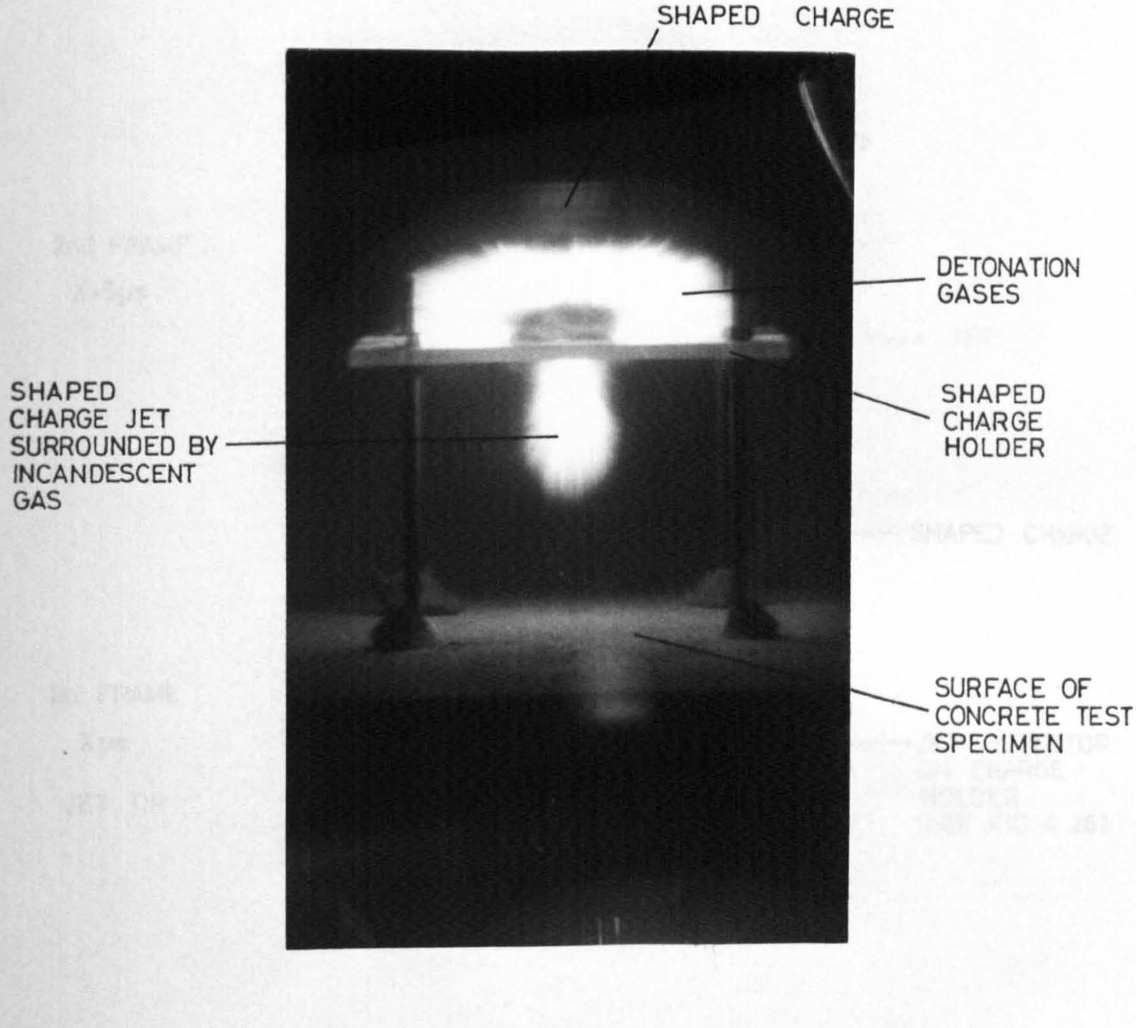

PLATE 5.4 HIGH SPEED CAMERA FRAME OF A 43g. SHAPED CHARGE JET IN AIR (BEFORE IMPACT)

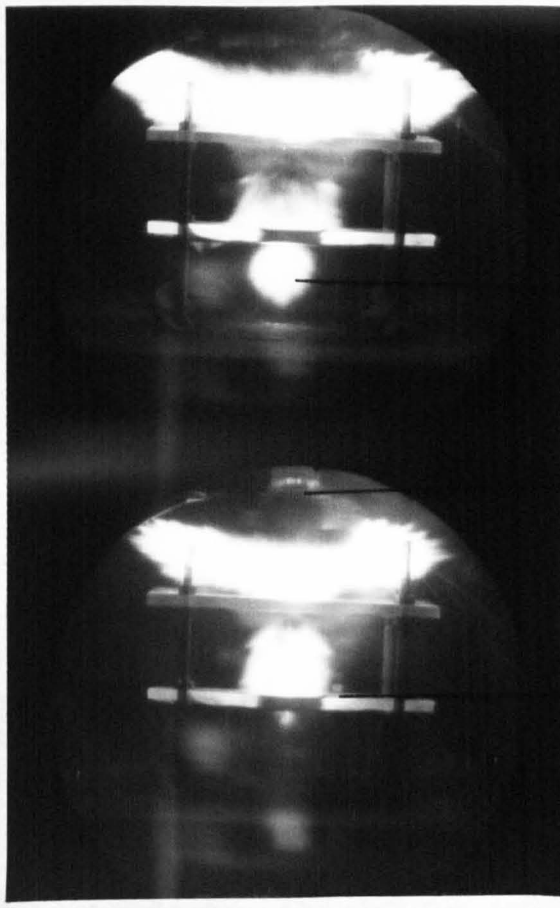

PLATE 5.5 TWO HIGH SPEED CAMERA FRAMES OF A 43g. SHAPED CHARGE JET PERFORATING A JET DETECTOR

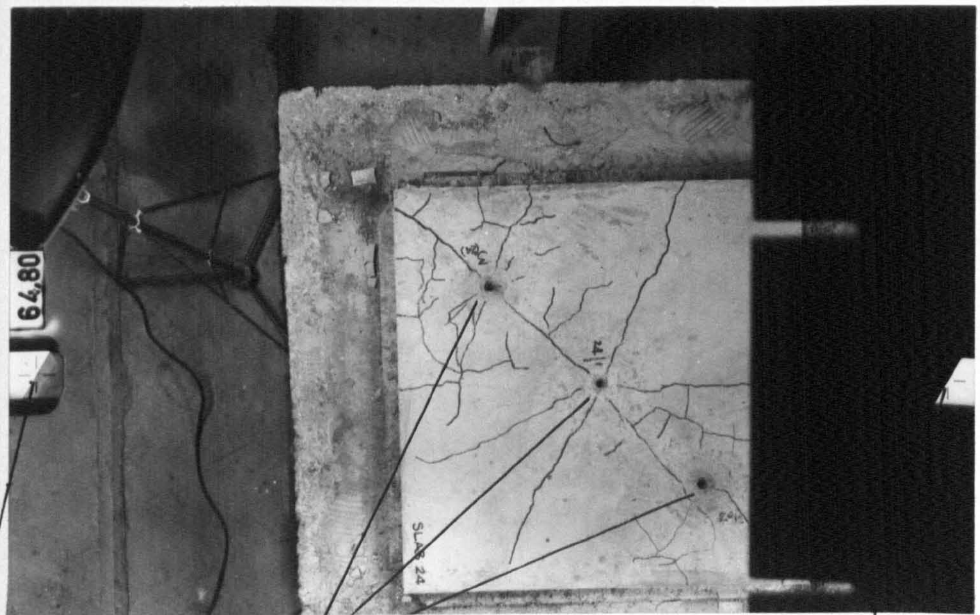

CONTROL POINT　　SHAPED CHARGE JET IMPACTS (1m. SQUARE SLAB)　　CONTROL POINT

PLATE 5.6 TYPICAL STEREO CAMERA FRAME OF THREE 43g. JET IMPACTS ON A CONCRETE SLAB

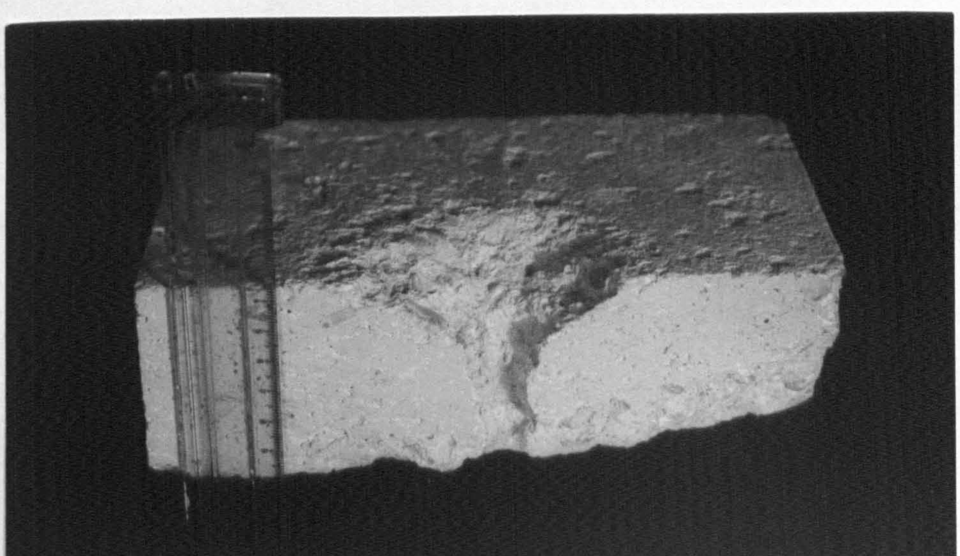

PLATE 5.7 CROSS SECTION OF A TYPICAL 43g. SHAPED CHARGE JET HOLE IN A 65mm. THICK CONCRETE SLAB

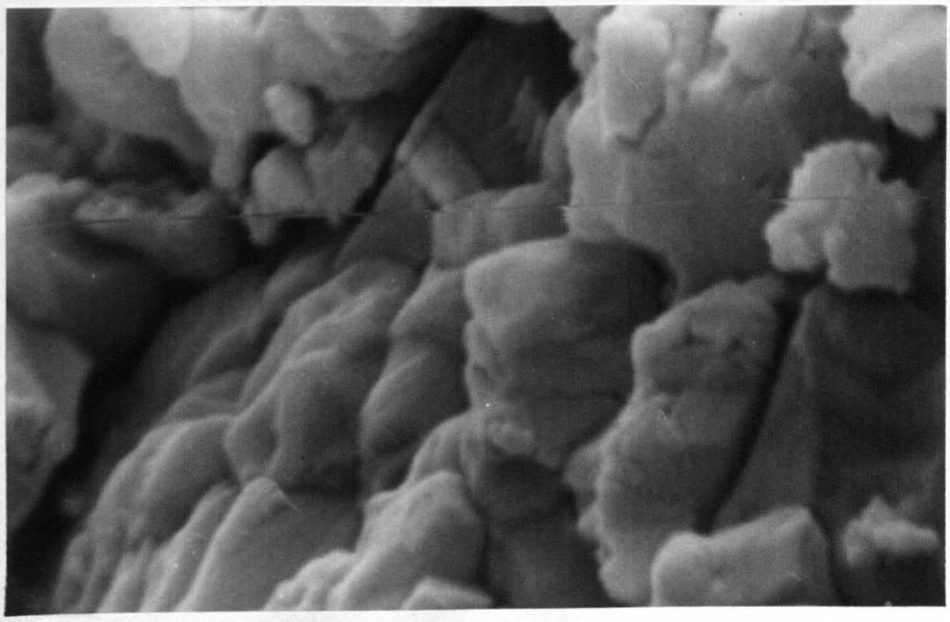

MAGNIFICATION 1280 TIMES

PLATE 5.8 SCANNING ELECTRON MICROSCOPE FRAME OF THE LOWER SPALL ZONE OF A SHAPED CHARGE JET HOLE IN BARYTES AGGREGATE CONCRETE

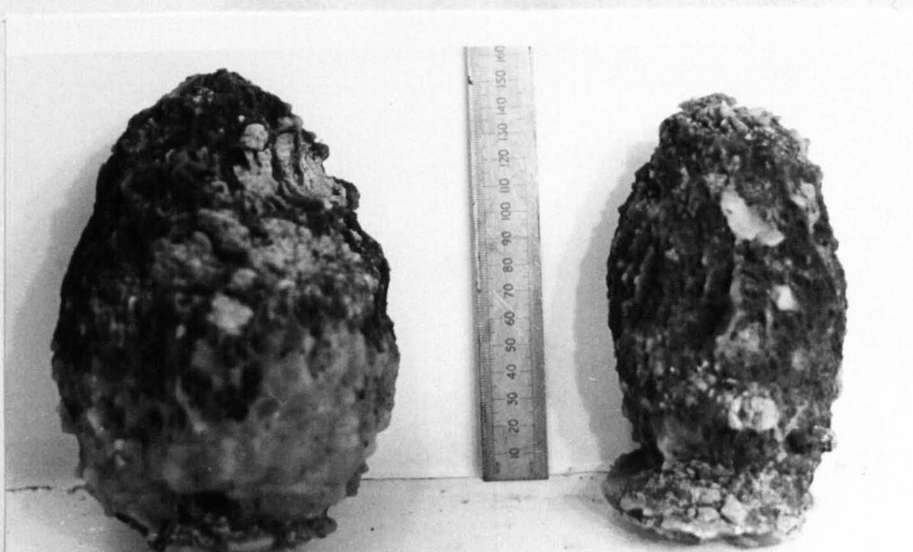

PLATE 5.9 WAX CASTINGS OF 43g. SHAPED CHARGE JET HOLES IN CLAY SOIL

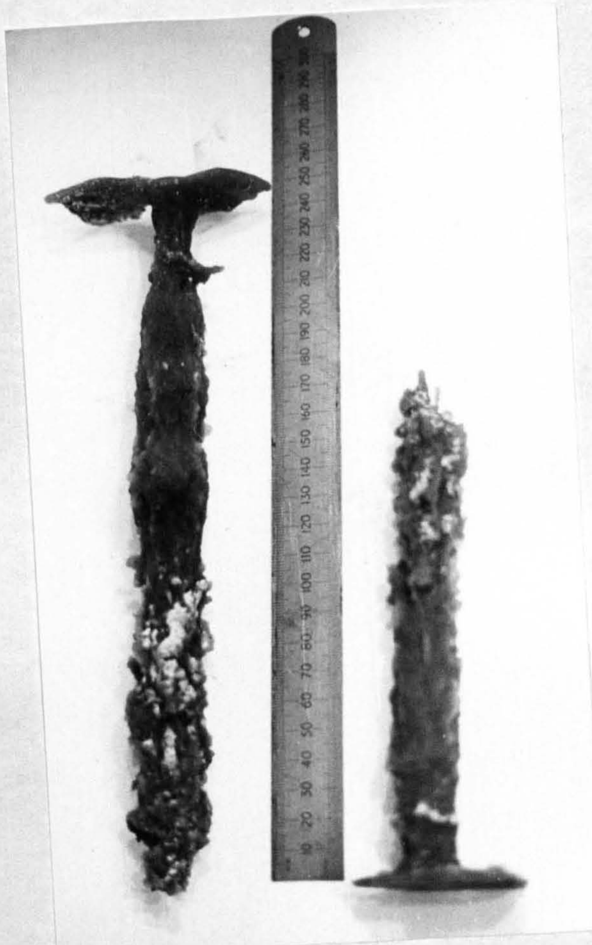

PLATE 5.10 WAX CASTINGS OF 43g. SHAPED CHARGE JET HOLES IN SAND SOIL

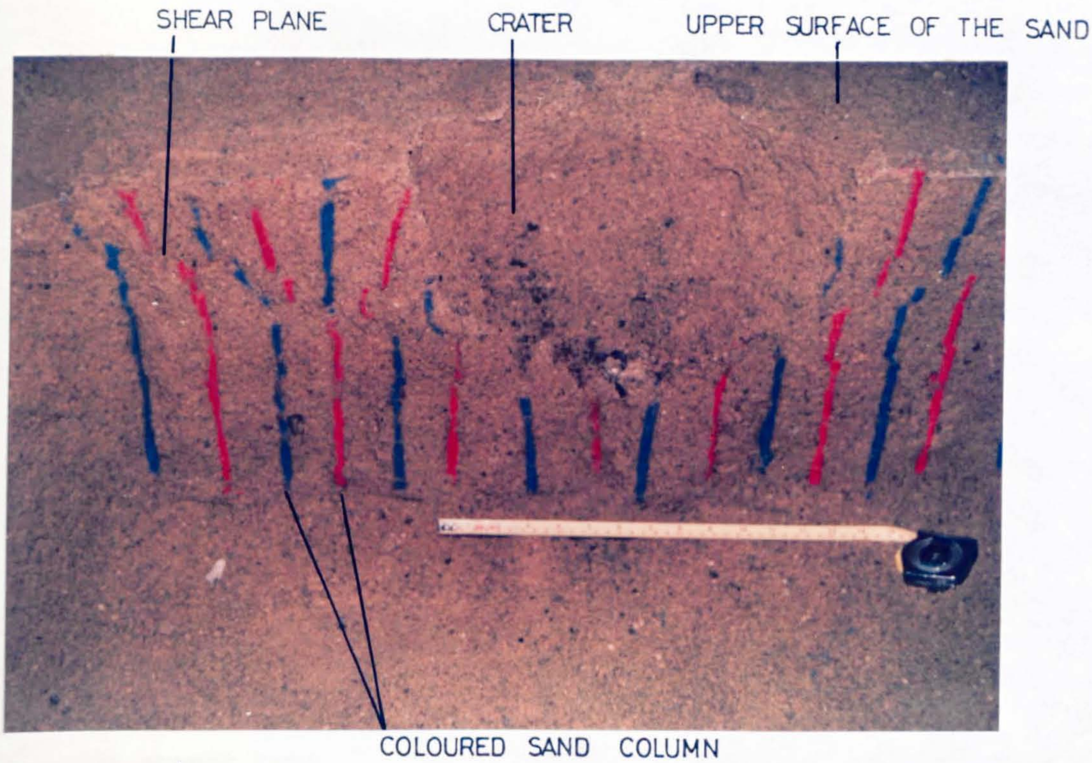

PLATE 5.11 COLOURED SAND COLUMNS IN SAND SOIL AFTER A 16g. CHARGE SUBSURFACE EXPLOSION

PLATE 5.12 COLOURED SAND COLUMNS IN CLAY SOIL AFTER A 16g. CHARGE SUBSURFACE EXPLOSION

CHAPTER 6

EXPERIMENTAL RESULTS FROM THE SHAPED CHARGE TEST PROGRAMME

6.1 INTRODUCTION

Table 6.1 gives a summary of the number of tests performed on the various specimens described in chapter 4. A total of 148 shaped charges were used of which 127 were 34mm diameter 43g copper lined, 15 were 34mm diameter 43g aluminium lined and 6 were 56mm diameter 298g copper lined.

The main programme consisted of the majority of the 127 43g copper lined shaped charge tests. These tests were to obtain data on the response of concrete to impact loading by a high speed metal jet. Some 43g copper lined charges were used with metal and non-metal blocks to determine by experiment,data required for calculations.

The fifteen 43g aluminium lined charges and the six 298g copper lined charges were for comparison purposes with the 127 charges in the main test programme. Only a representative set of experiments was possible with the limited number of these two types of charge available. Chapter 4 contains details including the instrumentation of every test specimen used in the study in tables 4.1 to 4.3.

Where possible instrumentation was duplicated, repeated in different tests or independently checked by other means, for example, by high speed photography, to ensure that the results were as reliable as possible.

6.2 SHAPED CHARGE JET VELOCITY MEASUREMENTS

The velocities in air of the jet produced by all three types of shaped charge described in section 6.1 were obtained by using jet detector gauges, described in section 4.1.4. These were located at various points in the flight paths of the shaped charge jets as shown in figure 4.25. From the data obtained by these gauges listed in table 6.2, figure 6.1 was drawn for the three types of shaped charges, 43g copper lined, 43g aluminium lined and 298g copper lined. The slope at any point of the curve for a particular jet is the velocity of the jet at the distance represented by the point on the x axis. Jet velocity was independently checked in the case of 43g copper lined charges using high speed photography to time the jet tip as it passed points a known distance apart. Plates 5.4 and 5.5 show respectively single frames from high speed films of the shaped charge jet surrounded by incandescent gases in air and perforating a jet detector. The gas surrounding the jet cannot in theory travel faster than the tip of the jet so, although gas is masking the jet the gas at the tip is being dragged by the jet and the jet tip is at the edge of this gas cloud. Work by the Ministry of Defence and Hunting Engineering (1982) using flash radiography has confirmed this to be true.

Data on jet velocities were required in penetration calculations based on formulae presented in section 2.2. All three types of shaped charge were found from figure 6.1 to have a final jet tip approach velocity of appproximately 5000 m/s. In the scaling rules given in table 2.4 velocity was not scaled and so the identical velocities of the 34mm and 56mm diameter charges, 1/5 and 1/2.5 scale respectively, were consistent with the rules.

Flash radiograph work by Richards (1983) on similar charges to those used in this study has confirmed the jet tip velocity at 102mm standoff to be approximately 5000 m/s. No indication of the error in the measurements by radiography was given.

6.3 SHAPED CHARGE JET PENETRATION RATE MEASUREMENTS

Shaped charge jet penetration rates were measured using jet detector gauges described in section 4.1.4. These were buried in concrete test specimens, separated by plates of material as in the case of two copper plate stacks, shown in figures 4.18 and 4.19 or set between concrete plate stacks as shown in figures 4.21 and 4.22. The shaped charge jet penetration rate in test M17 was checked by high speed photography as the jet penetrated the copper plate stack described in section 4.2.3. Plate 6.1 shows a frame from the high speed film in which the incandescent gas surrounding the jet can be seen in the gap between the copper plates.

Figure 6.2 shows the 43g copper lined shaped charge jet penetration v time relationships for concrete and copper test specimens and the 43g aluminium lined shaped charge jet relationship in concrete. The copper jet into concrete relationship shows that copper jet penetration is similar to aluminium jet penetration in concrete up to about 63mm depth. After this the penetration rate for aluminium jets is less than for copper jets. The penetration relationship for copper jets into copper shows that the penetration rate is less than the penetration rate into concrete and it does not stay steady. Table 6.3 gives test data and derived penetration velocities from which figure 6.3 was obtained. This figure gives the relationships between velocity and distance penetrated for various combinations of concretes and shaped charge jets.

6.4 STRESS PULSES IN CONCRETE DUE TO SHAPED CHARGE JET IMPACTS

Strain gauges were installed in three orthogonal directions in concrete specimens as shown in figure 4.16 and decribed in sections 4.1.5 and 4.2.1. These gauges detected and measured strains associated with stress waves from shaped charge jet impacts. Figure 6.4 shows the three stress pulses associated with the strains measured in the test programme and the following sections contain details of each strain measured.

6.4.1 Radial Compression Pulse

Data obtained on the radial compression stress pulse are given in table 6.4. The strains obtained were converted into stresses by using the static stress-strain relationship for concrete blocks given in figure 4.9. The data in table 6.4 is not completely in agreement because not only was it difficult to obtain data in practice but also interpretation of results was not always easy. Figure 5. 4, which was drawn from a photograph of an oscilloscope trace, highlights the difficulty of picking out the strain gauge signal from the electrical interference caused by the explosion. For this reason it is important to consider trends in the results rather than absolute values, and to place more emphasis on corroborated results rather than the significance of spurious values.

From the data given in table 6.4 the stress pulse velocity in sand/gravel aggregate concretes was found to be similar, that is between 2.38 and 2.5mm/μs. This was true whether the pulse was generated by a 43g or by a 298g shaped charge jet. In basalt and limestone aggregate concretes the stress pulse speed was also similar, 0.83 to 0.95 mm/μs, but only one result is available for concrete made from each aggregate. However the value of 0.36 mm/μs for a slab subjected to a 298g shaped charge jet impact does not corroborate the 2.38 mm/μs speed obtained for a similar charge jet impacting a block. Table 3.13 contains values of the elastic wave speed measured in various concretes by ultranonic means. The value of pulse speed measured in this way varies from the value derived from strain gauge measurements by about one third. The reason for this is not clear but the use of the ultrasonic method depends on an accurate value for the dynamic modulus of elasticity of concrete. This is difficult to achieve so any error in this value could cause the discrepency in the values. The influence of the value of the modulus of elasticity (E_d) can be seen from table 3.13 and the amounts of cracking in concrete specimens impacted by shaped charge jets given in tables 5.2 to 5.6. In general except for barytes, the greater the value of the modulus of elasticity the lesser the amount of cracking produced by the jet impact in concretes. This also holds for the series of experiments performed on sand/cement mortar.

The amplitude of the compression stress wave has been calculated at various points. The actual values do tend to contradict each other but again there is a trend. The value of stress decreases with increasing distance from the impact point of the jet roughly by 50% for a doubling of the distance. This trend applies with reflected pulses which are tensile when the incident pulse is compressive and can be seen from the results obtained on block B63 in particular. The results from tests using 43g and 298g charges show that the amplitude of the stress pulses are not the same at similar points even though the wave speed is identical.

6.4.2 Circumferential Tensile Pulse

Associated with a longitudinal compression pulse is an orthogonal tensile pulse which propagates at a speed which is half the speed of the compression pulse. This tensile pulse shown in figure 6.4 was monitored and the strain results obtained in experiments appear in table 6.5. Strains have been converted to stresses by using the static stress-strain relationship given in figure 4.9. Similar problems to those described in section 6.4.1 existed in interpreting strain gauge traces on the oscilloscope. In examining the data it is again important to consider trends rather than absolute values.

The circumferential pulse velocity data in table 6.5 varied more than for the radial pulse velocity described in section 6.4.1. However there were three values of 1.36 mm/μs measured for sand/gravel concrete which approximate to half the value of the compressive wave speed in sand/gravel aggregate concrete. In basalt aggregate concrete there is a similar ratio even though pulse velocity values for both radial and circumferential waves were much lower. No corroborative pulse velocity values were obtained experimentally for 43g and 298g shaped charge jets.

Derived stresses appear to show a reduction in amplitude with increasing distance from the jet impact point as expected. The values are significantly higher than for the corresponding longitudinal compressive stress pulse at the same point. However, at the time the circumferential tension was detected at a distance from the impact 'x', the longitudinal compression pulse would have moved on a similar distance that is to a distance '2x'. Therefore the values of stress given in tables 6.4 and 6.5 obtained at the same point cannot be compared as they occurred at different times.

6.4.3 Vertical Compression Pulse

Table 6.6 contains data from vertical compression pulses shown in figure 6.4. This pulse is a longitudinal compression pulse similar to the pulse described in section 6.4.1 but in this case it is propagated along the axis of the shaped charge jet impact and not orthogonal to the axis. In reality the pulses are the same and propagate as the surface of a hemisphere but in the test specimens the pulse was treated as being in two orthogonal directions for measurement purposes.

The pulse velocities in sand/gravel aggregate was similar to the value of 2.38 to 2.5mm/μs obtained for radial compression pulses. The value of pulse velocity in basalt concrete was similar to the concrete made from sand/gravel aggregate but contradicted the value obtained for radial compression in basalt, given in table 6.4. No agreement was found between pulse velocities obtained from tests using 43g and 298g shaped charges.

The derived stresses obtained at various points directly under the jet impact point were found to be so variable that no trend was obvious and there was no agreement with values quoted in table 6.4. However measurements along the impact axis, while being on the hemisphere of radiating pulses, are a special case. This is because the impacting jet initially penetrates faster than the longitudinal stress pulse generated by it. Thus the pulse is modified along this axis in particular throughout the period the penetration rate exceeds the pulse velocity. Only after the penetration rate drops below the pulse speed does the pulse precede the penetrating jet. This may account for different results for points on the jet axis to points at similar distances but on other axes radiating from the jet impact point. Analytical models usually assume a uniform penetration velocity.

6.5 CRACK AND SPALL MEASUREMENT

6.5.1 Cracking

This section is concerned with the dynamic characteristics of single cracks, namely the initiation time, the speed and the direction of propagation. Data was collected from concrete specimens made from all aggregates and subjected to three types of shaped charge jet impact. Table 6.7 contains all data obtained from these experiments.

The data collected was varied and is difficult to compare directly, for example, as demonstrated in figure 6.5. This is a plot of all data in table 6.2. It was necessary to look for trends in the same way as the stress pulse data was analysed in section 6.4.

At a distance of 190mm from the shaped charge impact point a crack was found to develop between 120 and 230μs after initial jet impact, irrespective of the type of charge used. This occurred in concretes made from natural rocks, that is sand/gravel, basalt, barytes or limestone aggregate but 'Lytag' appeared to crack earier at 60μs. However only a single result was obtained for 'Lytag.' At 500mm from the shaped charge impact point the initiation of a crack could take from 170 to 320μs but the amount of data recovered is limited.

Table 6.7 gives values of circumferential tensile pulse data measured when a crack appeared at the distances and time from impact recorded in each test. For sand/gravel aggregate concrete the values were similar to the values obtained from strain gauge signals given in table 6.5. The data collected was limited but it would indicate that cracking is connected with the circumferential tensile stress wave, that is the shear wave, and the hoop stresses related to the compressive wave.

It was found that these cracks propagated from the edges of the specimen at the nearest point on an edge to the impact point of the jet on the specimen. Furthermore, cracks extended vertically through the specimen and travelled as a plane. This was detected by simultaneously monitoring a crack detected on the edge of the upper surface and on the side of the specimen. In full scale tests by Watson et al (1983) it was found that the crack did not extend through the full depth of the slab. Cracks travelled in towards the impact point at speeds listed in table 6.8 for concretes made from different aggregates.

The analysis of the data is limited by the paucity of results and is restricted to comparisons. The velocity of cracks in sand/gravel aggregate concrete, 2.1 to 3.17 mm/μs, appeared to be similar for impacts by 43g coper and 43g aluminium lined charges but approximately between one and a half and twice as fast, 4.76 mm/μs, when a 298g charge was used. The crack is thought to be driven by a reflected tensile wave in a stressed tensile zone which may account for the difference in speeds since, in section 6.4.1 it was seen that the stresses generated were higher with 298g shaped charge jet impacts. The stressed state of the specimen could account for crack speeds higher than are predicted by theories in which only cracks propagating in unstressed specimens are usually considered.

The limited number of tests on barytes and 'Lytag' aggregate concrete specimens yielded a range of crack speeds from 2 mm/μs to 6.3 mm/μs. Test specimens made from these aggregates were cracked much more than specimens made from concretes containing other aggregates. This may be conected with total energy considerations but scarcity of theoretical and experimental data means that this explanation can only remain a possibility at present.

6.5.2 Spalling

The definition of spalling was not taken to be its usual meaning, that is the movement of material from a face on the specimen remote from the impact, caused by the reflection of a compression wave. Spalling in this study is shown diagrammatically in figure 6.6 and was defined as being the movement of material on the same face or an adjacent face due to the penetration of a shaped charge jet.

Table 6.9 gives spalling data collected from tests on a variety of concretes and in which 43g copper or aluminium lined charges were used to produce the shaped charge jet. The table contains data on both surface and side spalling. The difference between surface and on side spalling are shown in figure 6.6. It is convenient to compare the results for surface spalling by dividing the distance from the spall gauge to the impact point by the time taken to spall to obtain a 'spalling velocity'. The 'spalling velocity' value for 43g copper lined shaped charge jet impact on sand/gravel concrete was found to compare directly with 43g aluminium lined shaped charge jet impact 'spalling velocities' on sand/gravel, basalt and 'Lytag' concretes. The results are in close agreement, lying between 1.0 and 1.33 mm/μs. This range is close to the velocity of the shear wave which was described in section 6.4.2.

The results of two tests, namely B43 and B44 in table 6.9, appear to contradict the agreement between results,but in practice the spalling distances of 15 to 20mm were too short for accurate measurement on the oscilloscope because of interference generated by the charge firing circuit. These results have not been discarded but the trend of the results and the corroborative nature of other results casts some suspicion on them.

A similar interference problem with short distances to gauges occurred in the side spall results listed in table 6.9. The short distance to the first detector on block B53 meant that the signal detected was still in the period when interference from the charge firing circuit was still affecting the stability of the oscilloscope trace. Repeated experiments checked by high speed photography on specimens B56 and B57 showed a 6μs discrepency which was clearly more significant on short duration timing rather than longer timing intervals. Even so at intervals of 50μs this still amounts to a 12% error but in dynamic testing this may be regarded by some researchers as acceptable.

The high speed photography also showed that concrete appeared to bulge and that there was a time lag between passage of the jet, calculated from penetration data taken from figure 6.2, and spalling. The photographs, of which plate 6.2 is an example, show the bulging and spalling, but it is unclear whether the concrete first flowed plastically under the pressure generated or cracked microscopically and moved as discrete particles. To suggest that a brittle material could be induced under pressure to flow plastically may seem inconceivable when comparisons are made with behaviour under normal loading rates. However the loading rate in this study was of the order of 15 to 20μs duration with a pressure calculated in Chapter 8 of between 2.64 $\times 10^3$ N/mm^2 and 1.315 $\times 10^4$ N/mm^2.

6.6 OVERALL CRACKING OF CONCRETE TEST SPECIMENS

In general terms there were four factors which were recognised as affecting the amount of cracks formed in a concrete test specimen under shaped charge jet impact loading. These factors were: the size of the specimen, the influence of different aggregates, the influence of the cement content of the mix and the influence of shaped charge jet parameters. These factors were not all totally independent. The following sections describe the effect of each variable and any degrees of inter-relationship with each other. Crack data for each test are given in tables 5.2 to 5.6.

6.6.1 Influence of the Size of Test Specimens

Cousins (1968) reported that brittle materials such as concrete, 'perspex' and cast iron shattered under impact loading from a shaped charge jet. This was true in this study for small test specimens such as 100mm concrete cubes subjected to 43g shaped charge jet impacts. 380mm concrete cubes did not usually shatter under impact from 43g shaped charge jets and 760mm concrete cubes did not shatter when 298g shaped charges were used. This demonstrates that there is a point or more importantly a charge:target ratio at which brittle materials cease to shatter. That is, when the energy is too low to drive cracks. In addition, doubling both the test specimen size and the charge size, according to scaling rules given in section 2.8.2, produced similar crack patterns. This can be seen in figures 6.7 and 6.8. These figures show respectively, crack patterns due to a 43g shaped charge jet impact on a 380mm concrete block and a 298g charge impact on a 760mm concrete block.

Concrete slabs were found to follow the same rules concerning scaling and overall specimen size as blocks. In slabs there was another parameter which affected cracking. This was the jet impact point in relation to the edges of the slab. In block tests described above, the impact was always in the centre. In slabs the position of the impact point varied. Figure 6.9 shows the crack pattern usually found in 1/5 scale sand/gravel aggregate slabs subjected to a 43g copper or aluminium lined shaped charge jet impact. Reinforcement in the slab did not affect this pattern though main cracks were parallel to the direction of the main reinforcement wires. Insufficient data was obtained to prove any conection other than coincidence. Figure 6.10 shows the crack pattern of Slab S12 which was a 500mm square sand/gravel concrete slab subjected to a 43g copper lined shaped charge jet impact. This slab was only one quarter the size of the slabs shown in figure 6.9 and was shattered, thus demonstating the influence of overall specimen size on the cracking damage caused. Figure 6.11 shows an off-centre impact on a 1/5 scale sand/gravel aggregate concrete slab. The overall dimensions of the slab were similar to those of the slabs in figure 6.9 but the jet impact point was in the same position relative to the edges of the slab as for the smaller slab, S12, shown in figure 6.10. Although there was more cracking around the impact point the slab shown in figure 6.11 did not shatter, hence the overall size of the slab was important even though only one quarter was directly involved with the impact. This is further evidence of the need to consider the total energy effect of the impact and the diminishing of inputted energy by material in the specimen not seemingly directly influenced by the impact.

The foregoing conclusions were based on a single size of charge and specimens formed from the same concrete mix. However, the influence of the modulus of elasticity, discussed in section 6.4.1 should also be included since two similar sized specimens of different concretes will crack differently. Hence the level of strain at a boundary which affects cracking is dependent both on the distance to the boundary and the modulus of elasticity of the material forming the specimens.

6.6.2 Influence of Different Aggregates

Not all 380mm concrete cubes could resist a 43g shaped charge jet impact without shattering. Concrete blocks made from 'Lytag' aggregate and, to a lesser extend barytes aggregate cracked so extensively as shown in figures 6.12 and 6.13 respectively that they could be described as shattered. In this study shattered is taken to be fragmented, splintered and broken into a great many pieces. In general limestone and basalt concrete blocks cracked as shown in figure 6.7.

Concrete ground slabs cracked in similar configurations to concrete blocks. Eleven one fifth scale concrete slabs made from different aggregates were subjected to three 43g shaped charge jet impacts and the resultant crack patterns are shown in figures 6.14 to 6.16. Figure 6.14 shows the general formation of cracks in a typical sand/gravel, limestone or basalt aggregate concrete slab. There were no obvious differences in cracking amongst concrete slabs made from these aggregates. Figures 6.15 and 6.16 show respectively the more extensive crack patterns in 'Lytag' and barytes concrete slabs. Comparison between the 380mm blocks and 1/5 scale slabs clearly show similar trends in cracking amongst the various aggregate concretes.

6.6.3 Influence of the Cement Content of the Mix

'Lytag' and barytes concrete mixes were richer in cement than the natural rock aggregate mixes. It was suspected that the increased cement content and not just the aggregates themselves could be responsible for the increase in cracking in the test specimens. 'Lytag' concrete required more cement because the relative densities of the aggregate and cement altered the batching weight. 'Lytag' particles also have a different surface area. Barytes concrete required more cement for relative density effects on batching weights and also to counteract the sulphate in the aggregate. Sulphates have the effect of reducing the crushing strength of concrete.

To try to quantify the influence of cement content on normal aggregates, a series of 380mm sand/cement mortar blocks were constructed and subjected to 43g charge copper lined shaped charge jet impacts. The mix proportions for the blocks were varied as given in table 6.10. After each test the lengths of the cracks on each face were measured and recorded. The total length of the cracks was then divided by the side length of the specimen, that is 380mm, to give a dimensionless number. This number could then be compared with any other number derived for any specimen used, that is other 380mm blocks and 760mm blocks. The length of cracking found in 760mm blocks was divided by the block size, 760mm. Figure 6.17 shows the normalised crack length, that is the total crack length divided by the size of the test specimen, versus the aggregate/cement relationship for sand/cement mortar. The relationship shows that for normal 6:1 aggregate/cement the cracking is minimised whereas for increased or decreased cement content the amount of cracking increases. For richer mixes this might be because the relatively larger volume of cement mortar which has a different longitudinal have velocity relative to the aggregate, could cause differential cracking. For leaner mixes the extra cracking could be caused by the diminished tensile strength of the material.

The influence of the cement content of the mix and the influence of the type of aggregate used are difficult to separate and quantify since they are interdependent in the mix design process.

6.6.4 Influence of the Shaped Charge Parameters

43g copper lined and aluminium lined charges produced different crack patterns in sand/gravel aggregate 1/5 scale concrete slabs. Figure 6.9 shows the effect of the different jet impacts on identical concrete slabs. That is, on slabs cast from the same materials and at the same time. The increased cracking was thought, within practical constraints, to be caused entirely by the different impacting material.

Aluminium lined shaped charge tests on 380mm concrete blocks comprising the whole range of aggregates showed no noticeable increase in cracking due to the different impacting material.

6.7 SHAPED CHARGE HOLE DIAMETER AND PENETRATION DEPTH

The hole formed in concrete by a shaped charge jet impact was similar for all three types of charge used in the test programme, that is, 43g charge copper lined charges, 43g aluminium lined charges and 298g copper lined charges. Although dimensions of the hole varied depending upon the charge used, the basic shape of all the holes conformed to the composite picture shown in figure 6.18. Plate 6.3 shows the shape of a 298g shaped charge jet hole in a 760mm sand aggregate concrete block and this shape is common to all shaped charge holes in concrete made from all aggregate types. Physical dimensions of all the holes produced during the test programme are given in tables 5.7 to 5.12 and the locations of measurements are shown in figure 5.10.

6.7.1 Influence of the Type of Aggregate

Figure 6.19 shows the hole diameter frequency for all 43g charge copper jet impacts on all pavement quality concretes. 47 of the 69 results quoted for hole diameter were found to be between 12 and 15mm. The mean result was 14mm. Figure 6.20 shows the hole diameter frequency for four aggregates. Basalt was not included as insufficient results were obtained. The frequency graphs show that all aggregates had the most results in the 12 to 15mm diameter band and therefore there was no significant difference in hole diameter amongst the different aggregate concretes for 43g charge copper jet impacts.

43g charge aluminium jet impacts produced larger hole diameters in concrete as shown in figure 6.21. No definite range of preferred hole diameters is apparent from figure 6.21 since the number of results is only eleven. Nevertheless, the mean hole diameter is about 22mm which is 50% greater than for copper jet holes and this is significant.

43g charge copper jets produced larger hole diameters in lean mix base course than in pavement quality concrete slabs. Figure 6.22 shows the range of hole diameters to be from 13mm to 21mm with a mean of 17mm. Too few results exist to show any specific aggregate effects but if the lean mix results reflect the pavement quality concrete results then aggregate type should not cause any difference in hole diameters obtained in lean mix concrete. No results were obtained for holes in lean mix produced by 43g aluminium lined shaped charge jets.

Shaped charge jet penetration depth was not found to be as consistent as hole diameter. This inconsistency is seen in figures 6.23 to 6.25 which show respectively 43g shaped charge jet penetration depth in all slabs, penetration depth in slabs on sand soil and penetration depth in slabs on clay soil. Figure 6.23 shows that though the range of penetration depths is large, a signifiant proportion of results lie in the 230 to 280mm band. Figures 6.24 and 6.25 show that while penetration in clay soils agrees with the 230 to 280mm range, penetration in sand is very variable with 73% of results lying outside this range. This also occurs when penetration depth frequency in concrete blocks is examined as in figure 6.26. The range of shaped charge jet penetration depths is large and no specific penetration depth value appears to prevail in the results.

The results of penetration depth determinations for 43g aluminium shaped charge jets in concrete slabs on soils and concrete blocks are given in figures 6.27 and 6.28 respectively. The results are too few in number to identify any trends except that in both slabs and blocks the overall penetration depth ranges are lower than for 43g copper jet impact depths. Thus while aluminium jets produce holes wider than copper jets by about 50% , penetration is reduced to about 75% or 80% of copper jet penetrations.

6.7.2 Influence of the Shaped Charge Parameters

In section 6.7.1 the influence of the difference in shaped charge liner was discussed in terms of hole diameter and penetration depth .

Differences in hole diameter and penetration were found by altering the characteristics of the impacting shaped charge jet.

The jet was modified in test B19 by removing the initiator system and replacing it with a radial rather than a point initiation system as shown in figure 6.29. This had the effect of reducing penetration by the 43g copper lined shaped charge jet to 80mm but also increasing the hole diameter from 14mm to 20mm.

The influence of the speed and mass of the impacting shaped charge jet was investigated by causing copper jets to penetrate different thicknesses of steel plate, as shown in figure 6.30, before impacting concrete. The penetration of the steel removed a part of the front of the jet and hence reduced its mass. Since a velocity gradient extends down a jet, this had the effect of reducing the speed of the new jet tip arriving at the surface of the concrete. This is shown in in table 6.11 along with the values of hole diameter and penetration depth found. In general, lower jet tip speed gave a wider but less deep hole.

The correlation between hole diameter, penetration depth and shaped charge scale was not found to hold quite so well as overall cracking, described in section 6.6.1 and illustrated in figures 6.7 and 6.8. For 298g shaped charges the predicted hole diameter should have been 28mm taking the mean value of 14mm from figure 6.19. However results obtained were in the range 10mm to 20mm. Penetration depth in concrete was predicted to be 340mm from figure 6.26 and 500mm from figure 6.23 but results were in the range 500mm to 695mm. The 695mm penetration was in sand soil. Thus scaling was not accurately achieved but some parameters of the 298g charge, such as charge diameter and liner angle were slightly different to the 43g charges and this may have been the reason for the differences. Within the study there was no scope for independently checking this with the few charges available.

6.7.3 Influence of Charge Standoff and the Obliquity of the Jet Impact

The influence of the standoff of a shaped charge on hole diameter and penetration depth can be clearly seen in figure 6.31. The majority of shaped charges used in this study were at 102mm standoff for 43g charges and 204mm standoff for 298g charges. This corresponded to three times the charge diameter for 34mm 43g charges but for 298g 56mm diameter charges the standoff was scaled from the 102mm used for 43g charges since the charge was generally twice the scale of the 43g charges except in diameter. The charges can be seen in figures 4.24 and 4.23 respectively.

The shape of the curves for hole diameter and penetration depth versus standoff for concrete shown in figure 6.31 were found to be similar to those for shaped charge jet impacts into metals and were not merely a function of the nature of the test specimen.

Shaped charge jet impacts in this study were usually at normal incidence but the effects of changing the angle of incidence were studied on a limited number of test specimens as listed in table 6.12. The results given in table 6.12 showed that there was no measurable effect on the shaped charge jet hole diameter or penetration depth even though a relatively thicker concrete specimen was penetrated in two cases due to the angle of incidence of the impact. Figure 6.32 shows the crack pattern caused to a 380mm concrete cube by a 43g copper charge jet. Comparison of this with figure 6.7, which is a block impacted at normal incidence, shows the variation in cracking observed. The major effects seemed to be that cracking was concentrated in front of the jet impact point instead of all around the block as in normal impact.

6.7.4 Influence of the Soil Foundation

The shape of the hole formed in soil by a shaped charge jet was dependent on the soil type. This is demonstrated in plates 5.9 and 5.10 which show wax castings of shaped charge holes in clay and sand soils respectively. The penetration depth of a shaped charge jet was similar in both soils but as the plates show the hole diameter could be up to ten times larger in clay than in sand.

The holes were found to be caused by expansion of the cavity produced by the penetrating jet and evidence of this has been found in 'Plasticine' blocks buried in the subsoil as described in sections 4.1.3 and 4.2.1. Plate 6.4 shows one of the 'Plasticine' blocks used and the brown copper coated cavity can clearly be seen. The different coloured layers of 'Plasticine' were not deformed vertically showing that no vertical movement of material had taken place except locally at the end of penetration. This is further demonstrated in figure 6.33 which shows two other cavities in 'Plasticine' blocks.

6.8 TEST SPECIMEN MOVEMENT UNDER IMPACT

The test slabs, the 380mm and the 760mm concrete cubes all remained in position during testing except those blocks which shattered or cracked, where parts moved laterally. The potentiometric displacement transducer described in section 4.4.4 registered no vertical movement under jet impact loading but some small vertical movement was observed (0.25mm) probably due to the blast from the shaped charge explosive after the impact.

Test specimens smaller than those mentioned above generally shattered laterally but no information was obtained on any vertical movements. Air blast tests using plastic explosive PE4 were conducted to determine the blast effects on concrete surfaces. The surfaces used were flat or flat with 14mm diameter holes drilled in to simulate shaped charge jet holes. The charge was the same mass, standoff and was shaped in the same way as a 43g shaped charge but it was unlined. The effect of the air blast at 102mm standoff was to remove some laitance from the surfce of the concrete. Thus air blast damage was deemed to be insignificant when compared to impact damage.

6.9 LIMITATIONS OF THE TEST PROGRAMME

Experiments involving explosive charges presented special problems with safety, the speed of the events, damage to instrumentation and the impossibility of stopping or repeating the test exactly. Where possible, slab test specimens were impacted several times to try to obtain some repeated results. This was not as extensive as would be desired due to limited explosive resources and the damage caused to instrumentation installed for subsequent tests on the specimens. Approximately 50% of all electrical instrumentation was lost or damaged during construction and testing for a variety of reasons, but mainly due to the blast of the explosive. The verification and checking of instrumentation was achieved by doubling up instrumentation or by using a different system such as high speed photography. This checking showed that results were reliably detected and collected but the values of individual signals and their interpretation were not always easy to determine, especially where there had been a lot of electrical interference during the test. Extensive screening arrangements were employed but the proximity of instrumentation to the explosions meant that the disruption was still great.

Although explosive resources were limited, a statistical check was made on the repeatability of a 43g copper lined shaped charge. Tables 6.13 and 6.14 contain details of the penetration of copper jets into mild steel and concrete blocks respectively. The use of so many charges was deemed necessary before reliable conclusions could be drawn. The mild steel was uniform but the results for the concrete were taken from the test specimens in the main test programme and which were nominally similar. It was thought unlikely that a set of absolutely identical concrete blocks could be made so it was felt tht this was acceptable. The conclusions of the statistical exercise on the jet penetration of steel and concrete were that the charges were repeatable and hence results on the test programme would not be likely to contain any systematic errors due to charge variables. There always remained the chance though that with so much instrumentation being damaged, the relatively few experiments and the variable nature of concrete that any rogue results due to charge variable effects could slip through undetected. For this reason the results obtained should be used with regard as to whether they were corroborated or not by simultaneous or subsequent results.

Table 6.1

Summary of Shaped Charge Jet Impact Tests

Type of Specimen	Specimen Numbers	Scale or size	Number of Specimens	Number of Impacts per Specimen	Type of Explosive Charge
Concrete slab	S1-S14 S25/S26 S28/S29/S30 S31	1/5 scale	20	1	Copper lined charge
Concrete slab	S15-S24 S27	1/5 scale	11	3	Copper lined charge
Concrete slab	S33-S34	1/5 scale	2	5	3 Aluminium and 2 copper lined charges
Concrete slab	S32	1/2.5 scale	1	1	Copper lined charge
Concrete block	B1-B46/B53 B65	380mm cube	48	1	Copper lined charge
Concrete block	B47-B52	380mm cube	6	1	Aluminium lined charge
Concrete block	B60-B64	760mm cube	5	1	Copper lined charge
Concrete block	B54-B59	100mm cube	6	1	Copper lined charge
Metal and non metal	M1-M12	-	16	1	Copper lined charge
Metal and non metal	M13/M15 M18	-	3	1	Aluminium lined charge

Table 6.2

Shaped Charge Jet Flight

Time and Velocity Data

Shaped Charge Type	Distance Travelled in Air from Initiation Position mm	Time from Initiation μs	Velocity mm/μs	Specimen Reference
43g copper lined	72	26	5.0	M19
	132	38		
	24	18		M16
	23	17		M17
	102	30± 3		S15 to S28
	57	22		B5
	55	20		B6
	52	20± 1	4.5 to 5.5	M1 to M5
	102	29± 1		
298g copper lined	118	29	6.25	B60
	168	37		
	154	34	4.17	B61
	204	46		
43g aluminium lined	57	21	5.0	S33
	102	30		
	62	22	5.0	S34
	102	30		
	102	30		B49
	102	26		B51
43g copper lined	-	6⁺	3.33*	B22
	-	8⁺	2.5**	B23
	-	13⁺	1.54***	B24

\+ Time for jet to travel 20mm in air after penetrating the plates listed below

* After penetrating 10mm mild steel
** After penetrating 20mm mild steel
*** After penetrating 30mm mild steel

Table 6.3

Shaped Charge Jet Impact

Penetration Data

Shaped Charge Type	Distance Penetrated mm	Time to Penetrate μs	Velocity of Penetration mm/μs	Material Penetrated	Specimen Number
43g copper lined	12	3	4	copper plates	M16
	24	8	3		
	36	15	2.4		
	48	24	2		
	60	40	1.5		
	12	10	1.2	copper plates with air gaps between	M17
	30	21	1.42		
	48	34	1.41		
	65	28	2.32	barytes concrete	S21
	65	40	1.63	barytes concrete	S22
	65	22	2.95	'Lytag' concrete	S23
	65	23	2.83	'Lytag' concrete	S24
	65	20	3.25	sand/gravel concrete	S27
	14	8	2.8	sand/gravel concrete	B8
	28	13			
	50	18			
	100	36	2.8	sand/gravel concrete	B3
43g aluminium lined	63	20	3.15	sand/gravel concrete	S33
	95	53	1.79	sand/gravel PQC and lean mix concrete	S33
	63	24	2.63	sand/gravel concrete	S34
	95	56	1.70	sand/gravel PQC and lean mix concrete	S34

Table 6.4

Stress Pulse Data from Shaped Charge Jet Impact Tests

(Radial Compression)

Shaped Charge	Specimen Type	Specimen Number	Aggregate	Distance to Gauge mm	Time of arrival of Pulse μs	Pulse Velocity mm/μs	Amplitude of Pulse N/mm²
43g copper lined	Slab	S25	sand/gravel	{150	60	2.5	50
				400	165	2.42	25
	Block	B34	sand/gravel	170	70	2.43	20
	Block	B40	basalt	190	200	0,95	85
	Block	B42	limestone	190	230	0.83	45
289g copper lined	Block	B63	sand/gravel	{190	80	2.38	86
				190	150	-	47*
				190	240	-	16
	Slab	S32	sand/gravel	{180	500	0.36	45
				180	680	-	75+

* reflected

\+ tension

Table 6.5

Stress Pulse Data from Shaped Charge Jet Impact Tests

(Circumferential Tension)

Shaped Charge Type	Specimen Type	Specimen Number	Aggregate	Distance to Gauge mm	Time of Arrival of Pulse μs	Pulse Velocity mm/μs	Amplitude of Pulse N/mm^2
43g copper lined	Slab	S14	sand/gravel	200	85	2.35	-
	Slab	S26	sand/gravel	150	110	1.36	250
			sand/gravel	300	250	1.36	62.5
	Block	B11	sand/gravel	95	70	1.36	187.5
	Block	B32	sand/gravel	190	80	2.38	40
	Block	B39	basalt	190	370	0.51	45
298g copper lined	Slab	B64	sand/gravel	170	500	0.34	68

Table 6.6

Stress Pulse Data from Shaped Charge Jet Impact Tests

(Vertical Compression)

Shaped Charge Type	Specimen Type	Specimen Number	Aggregate	Distance to Gauge mm	Time of Arrival of Pulse μs	Pulse Velocity mm/μs	Amplitude of Pulse N/mm^2
43g copper lined	Slab	S29	sand/gravel	67	28	2.39	31.3
	Block	B12	sand/gravel	190	70	2.71	187.3
	Block	B33	sand/gravel	180	50	3.6	35
				360	150	2.4	30
	Block	B38	basalt	380	130	2.92	45
298g copper lined	Block	B64	sand/gravel	190	200	0.95	68

Table 6.7

Concrete Cracking Times from Shaped Charge Jet Impact Tests

Shaped Charge Type	Specimen Type Specimen Number	Aggregate	Distance of Crack Initiation point from Impact mm	Crack Initiation Time for Impact μs	Velocity of Circumferential Tensile Pulse		Distance ÷ 3.65* μs
					Distance ÷ Time mm/μs	Distance ÷ (Time-50μs) mm/μs	
43g copper lined	Slab S27	sand/gravel	250	120	2.08	3.13	68
	Block B32	" "	190	130	1.46	2.28	52
	Block B33	" "	190	170	1.12	1.58	52
	Block B37	" "	190	140	1.36	2.11	52
	Slab S18	limestone	500	320	1.56	1.85	132
	Slab S21	barytes	500	170	2.94	4.16	137
	Slab S22	"	500	225	2.22	2.86	137
	Block B38	basalt	190	165	1.15	1.65	52
	Block B40	"	190	200	0.95	1.26	52
	Block B7	sand/gravel lean mix	190	90	2.11	4.75	52
43g aluminium lined	Slab S33	sand/gravel	180	120	1.5	2.57	49
	Block B52	" "	190	120	1.58	2.71	52
	Block B48	barytes	190	170	1.12	1.58	52
	Block B50	Lytag	190	60	3.16	19	52
	Block B51	limestone	190	230	0.82	1.06	52
298g copper lined	Block B62	sand/gravel	370	102	3.63	7.12	101
	Slab S32	" "	170	174	0.97	1.37	47

* 3.65 mm/μs is the most commonly quoted value of stress wave velocity in concrete

Table 6.8

Speed of Cracks Formed by Shaped Charge Jet Impacts

Shaped Charge Type	Specimen Type	Specimen Number	Aggregate	Distance travelled by crack mm	Time to travel μs	Speed mm/μs
43g copper lined	Slab	S9	sand/gravel	200	91	2.1
	Slab	S27	" "	45	20	2.77
	Block	B3	" "	95	40	2.38
	Slab	S22	barytes	250	350	0.72
	Block	B14	"	95	20	4.8
	Block	B13	'Lytag'	95	15	6.3
43g aluminium lined	Slab	S33	sand/gravel	190	60	3.17
	Block	B52	" "	70	30	2.33
298g copper lined	Block	B62	sand/gravel	200	42	4.76

Table 6.9

Spalling Data from Shaped Charge Jet Impacts

Shaped Charge Type	Specimen Number	Aggregate	Distance of spall from impact point mm	Time to spall μs	Distance / Time mm/μs	Impact Surface or Side Spall
43g copper lined	B43	sand/gravel	20	27	0.74	Surface
	B44	" "	15	26	0.58	Surface
	S31	" "	60	45	1.33	Surface
	B53	" "	25	32	0.78	Side
			100	52	1.92	
	B56	" "	30	14	2.14	Side
			70	56	1.25	
	B57	" "	30	20	1.50	Side
			70	50	1.40	
43g aluminium lined	S33	sand/gravel	30	30	1.0	Surface
	S34	" "	30	24	1.25	Surface
	B49	basalt	40	30	1.33	Surface
	B50	'Lytag'	40	32	1.25	Surface

Table 6.10

Normalised Crack Lengths of Specimens Subjected to a Shaped Charge Jet Impact

Specimen Number		B26	B28	B31	B27	B30	B29
Sand/cement ratio		Neat cement	2/1	4/1	6/1	8/1	10/1
Jet penetration depth, mm		255	204	179	200	178	260
Hole diameter, mm		*	13-25	12-20	12-20	15	15
Upper crater diameter, mm		*	80	*	90	*	110
Total length of cracks, mm		4286	4826	2774	1482	3268	3306
Crack width (max) mm		*	*	*	*	*	*
Crack length per side ÷ 380	(a)	140	100	40	30	160	100
(% of side length of	(b)	100	100	150	50	170	105
380mm) mm	(c)	200	100	100	30	170	160
	(d)	250	170	100	70	160	140
Crack length of top surface ÷ 380 (% of top surface width of 380mm) mm	(e)	450	600	270	220	200	225
Total normalised cracking value (a + b + c + d + e)		1140	1070	660	400	860	730

* data unavailable because of extensive damage and material movement

Table 6.11

Reduction in Shaped Charge Jet Penetration in Concrete by Steel Plates

Specimen Number	Thickness of steel penetrated mm	Hole Diameter in concrete mm	Penetration depth in concrete mm	Jet Tip Speed mm/μs
B22	10	20	152	3.33
B23	20	20	120	2.5
B21	25	20	73	-
B24	30	10	72	1.54

Table 6.12

Data from Oblique Impacts of 43g Shaped Charge Jets on Concrete

Specimen No	Specimen Type	Subsoil	Penetration mm	Hole Diameter mm	Radius of Upper Crater mm
B20	Block	-	162	14	90 - 110
B29	Slab	Clay	234	14	100 - 110
B30	Slab	Sand	234	14	90 - 110

Table 6.13

Statistical Data from 43g Shaped Charge

Jet Impacts on Mild Steel

Specimen No	Penetration mm	Hole Diameter at 20mm Depth mm	At 40mm Depth mm
M1	80	10	6.5-7
M2	82	8	7.5-8
M3	63	9	7-8
M4	80	10	6.5-7
M5	60	5-6	5.5-7
M6	82	10	8
M7	82	10	6.5-7
M8	72	10	7
M9	79	10	7-8
M10	77	11	7-7.5

Penetration depth

mean 75.7mm
standard deviation σ_{n-1} 8.097mm
σ_n 7.682mm

Hole diameter at 20mm depth

mean 9.35mm
standard deviation σ_{n-1} 1.564mm
σ_n 1.484mm

at 40mm depth

mean 7.15mm
standard deviation 0.54mm

Table 6.14

Statistical Data from 43g Shaped Charge Jet Impacts on Concrete Specimens

Block Number	Penetration mm	Hole Diameter mm
B1	130	11
B3	150	-
B8	165	-
B10	136	-
B11	177	14
B12	216	13
B32	194	11
B33	174	10
B34	101	9
B35	190	13
B36	195	12
B37	205	13

Penetration

mean 169.416mm
standard deviation σ_{n-1} 34.307mm
σ_n 32.844mm

Hole diameter

mean 11.778mm
standard deviation σ_{n-1} 1.641mm
σ_n 1.548mm

All specimens were sand/gravel aggregate pavement quality concrete

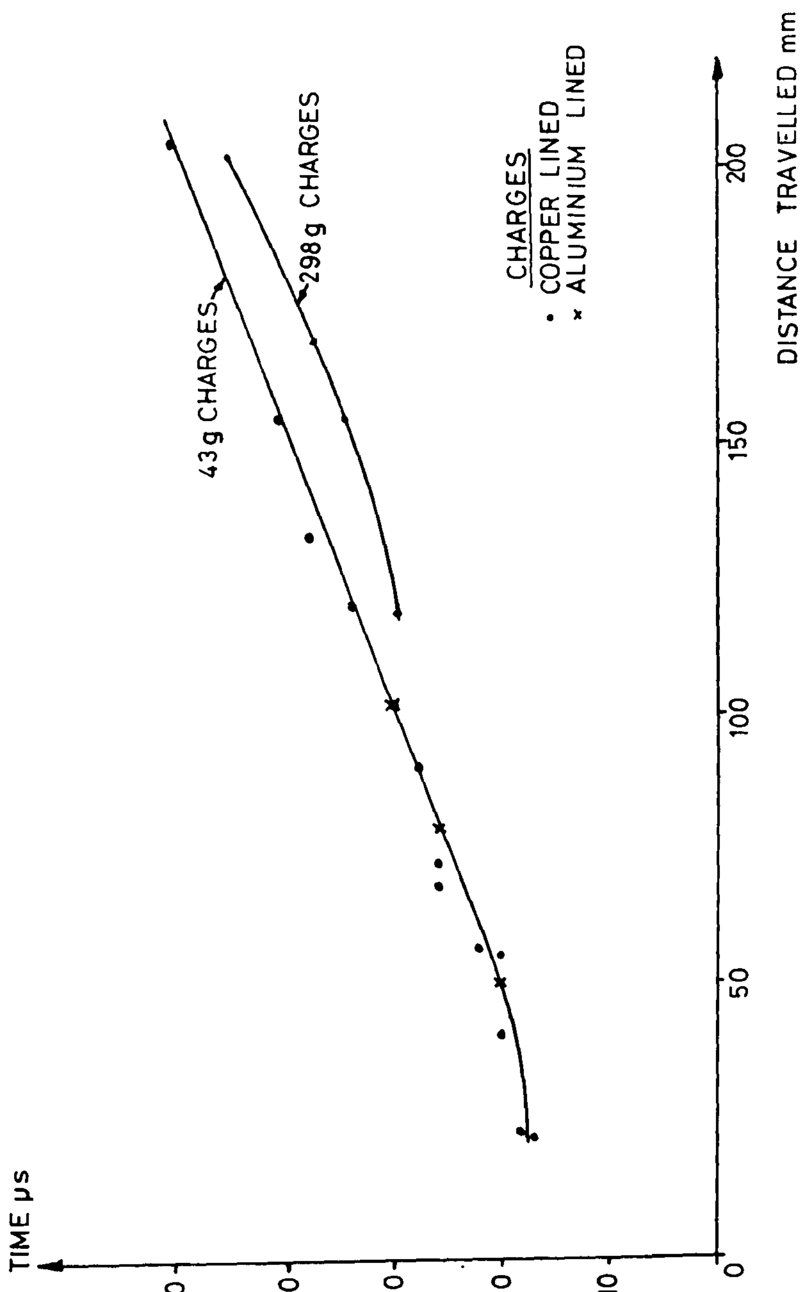

FIGURE 6.1 JET FLIGHT TIME VERSUS DISTANCE TRAVELLED FOR 43g AND 298g SHAPED CHARGES

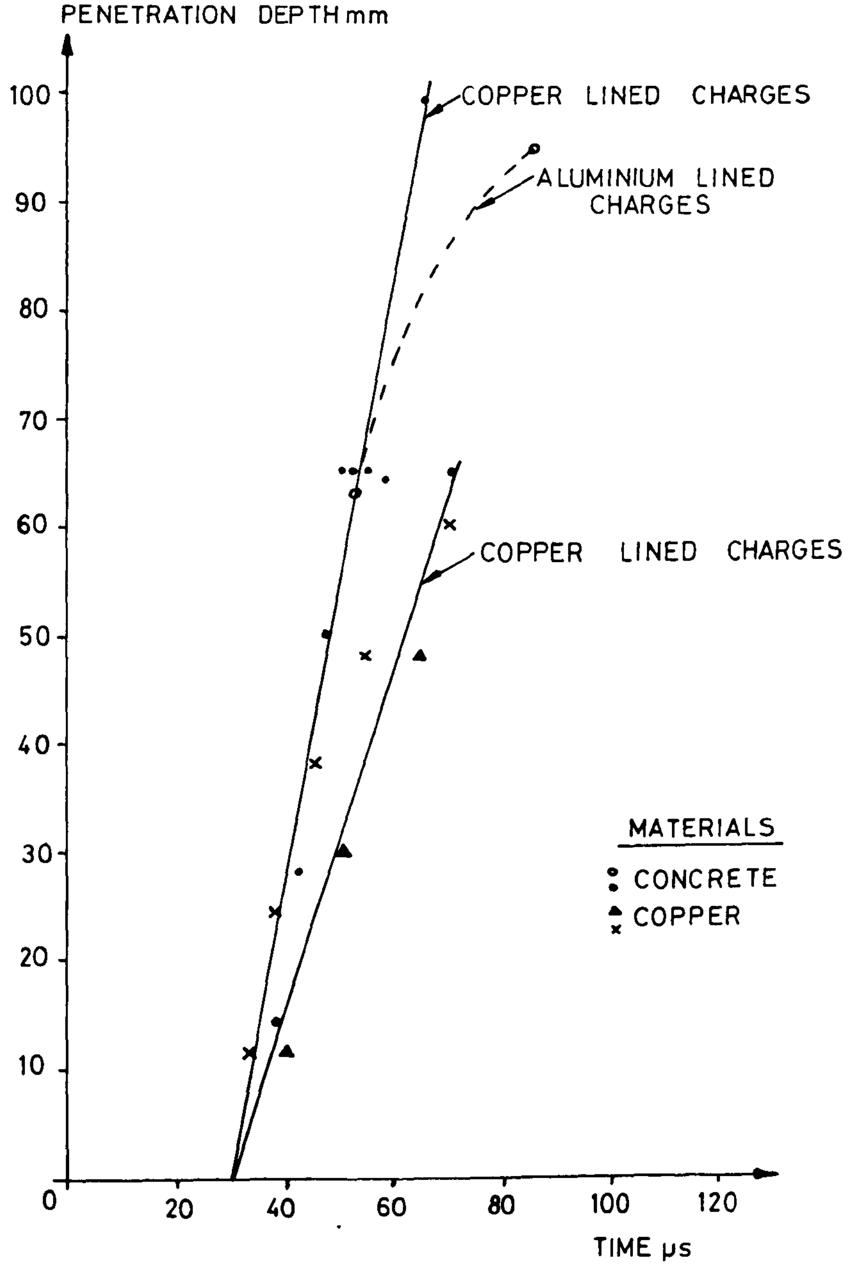

FIGURE 6.2 PENETRATION DISTANCE VERSUS TIME FOR 43g SHAPED CHARGES

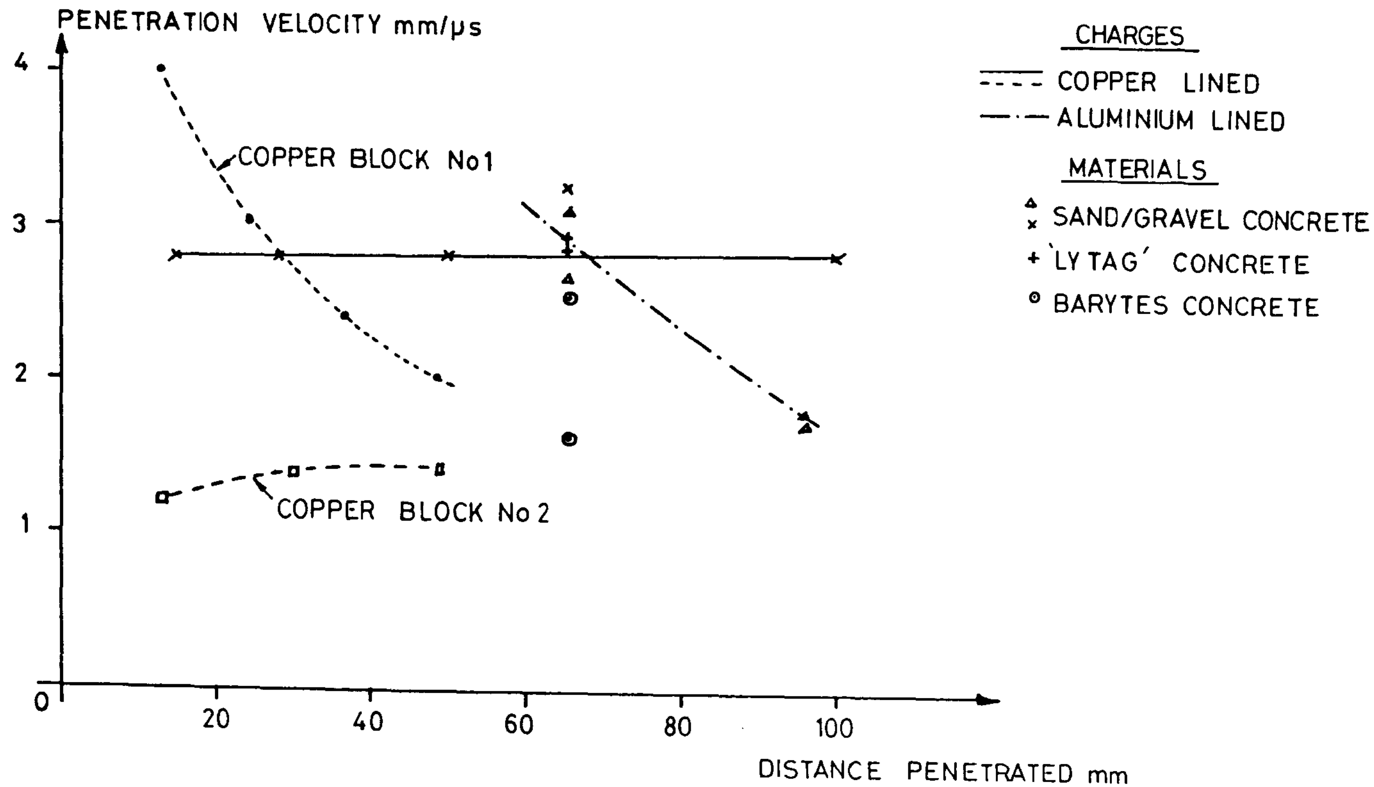

FIGURE 6.3 PENETRATION VELOCITY VERSUS DISTANCE PENETRATED FOR 43g SHAPED CHARGE JETS

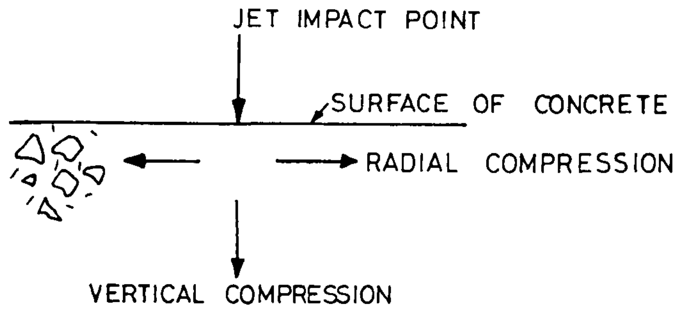

Side View

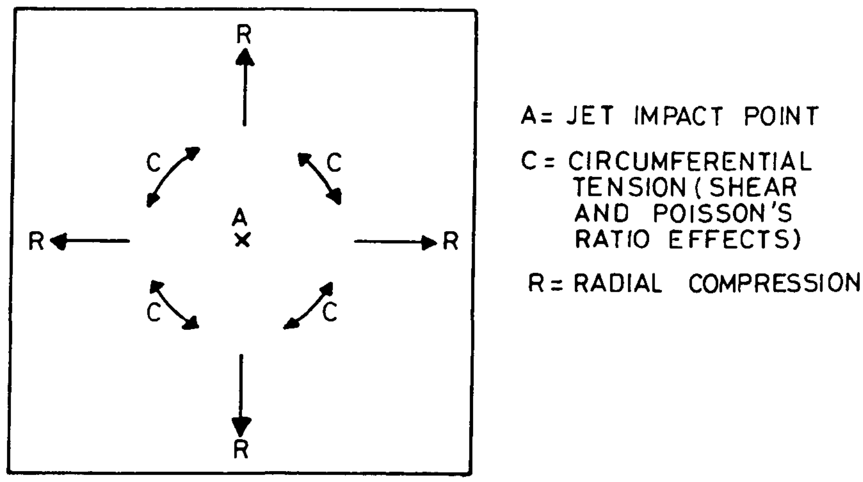

Plan View

FIGURE 6.4 DIRECTIONS OF STRESS PULSES GENERATED BY SHAPED CHARGE JET IMPACT

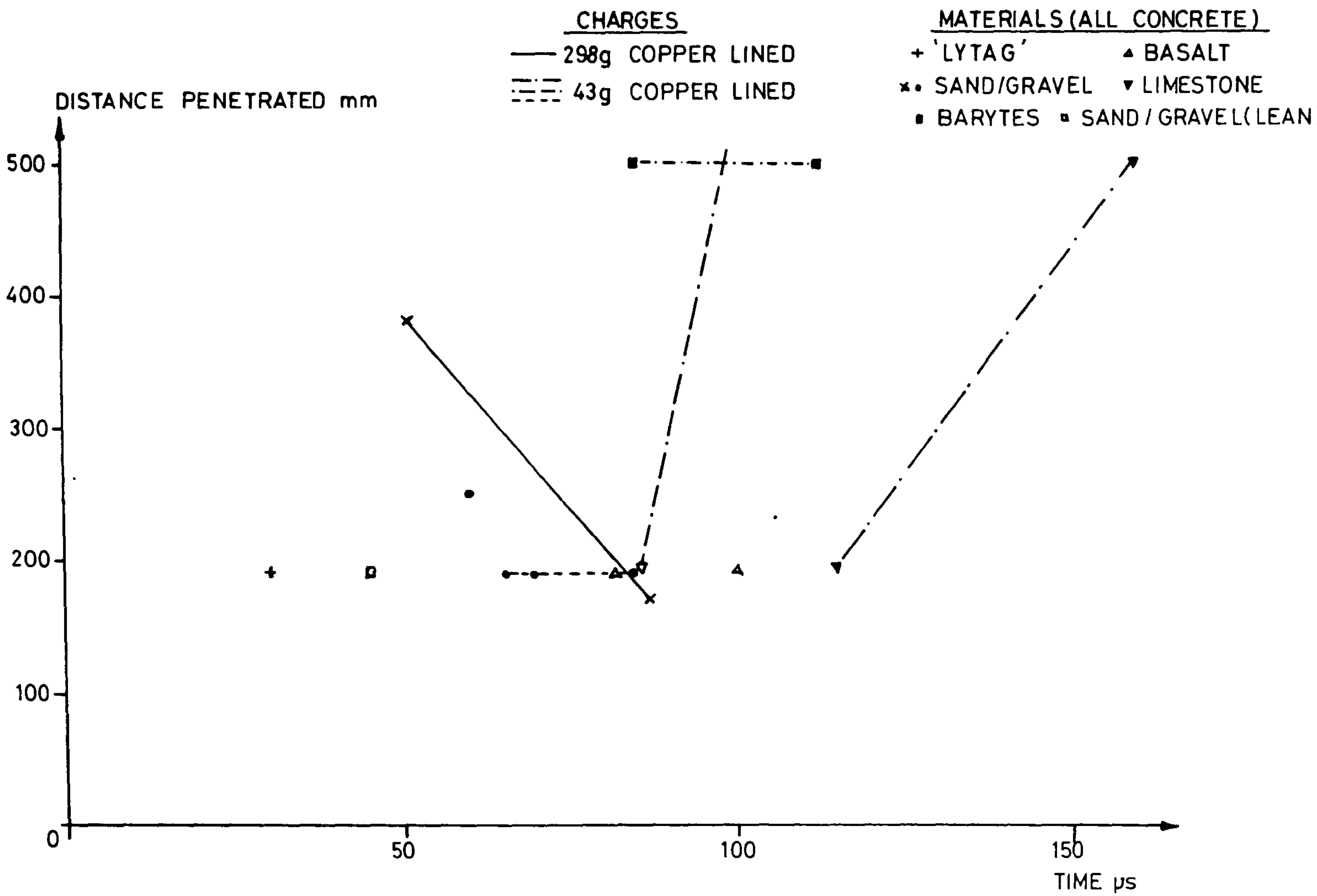

FIGURE 6.5 DISTANCE PENETRATED VERSUS TIME FOR 43g AND 298g SHAPED CHARGE JETS IN CONCRETES

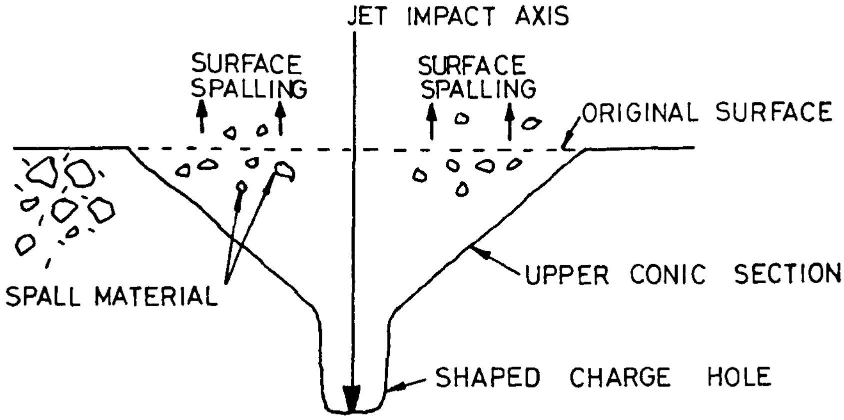

Side View Of Surface Spalling

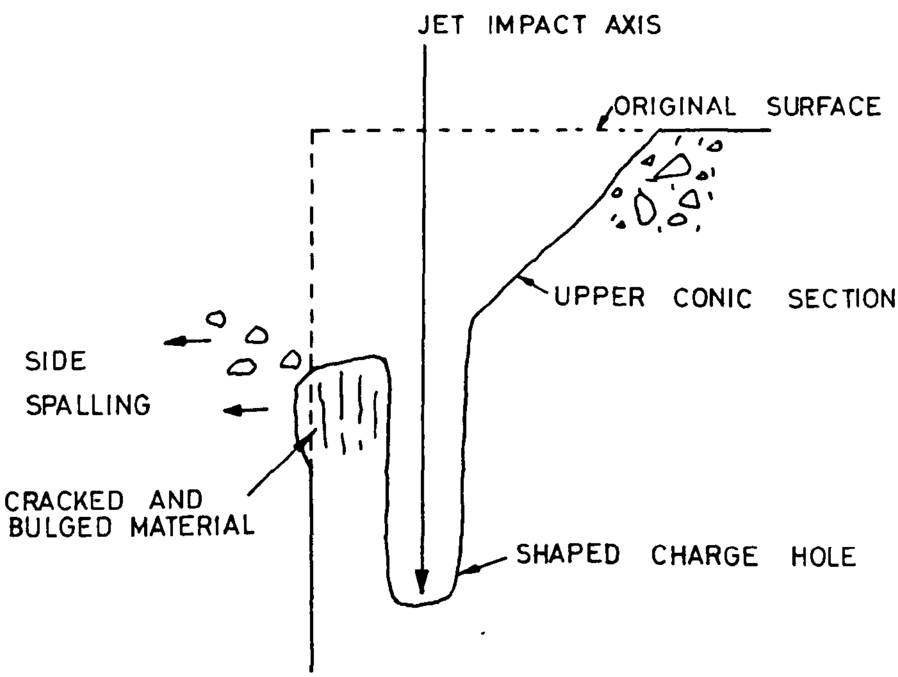

Side View Of Side Spalling

FIGURE 6.6 TYPES OF SPALLING IN CONCRETE DUE TO SHAPED CHARGE IMPACTS

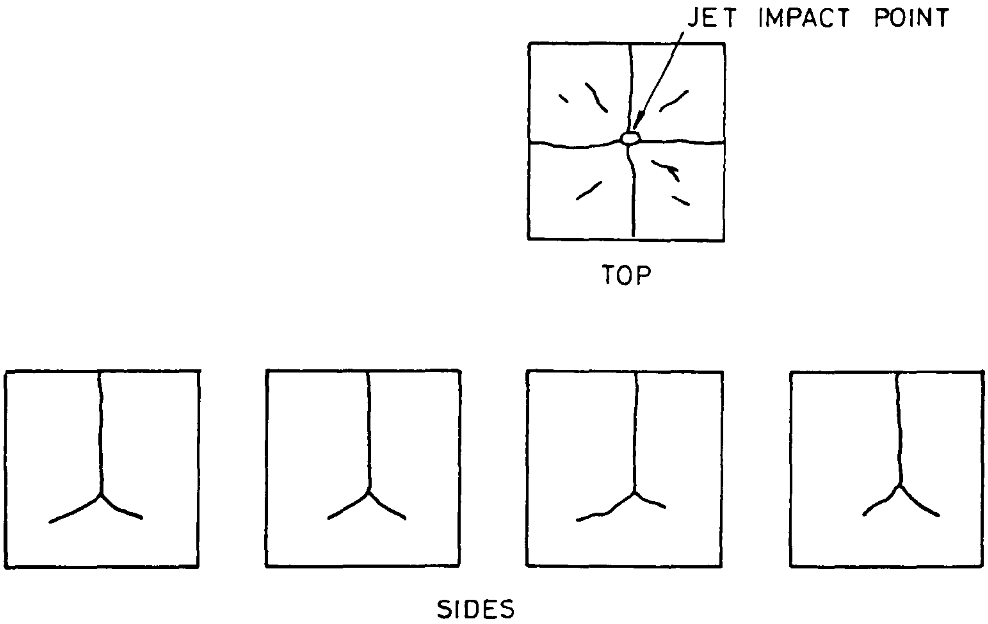

FIGURE 6.7 CRACKS IN A 380mm SAND/GRAVEL CONCRETE CUBE (43g SHAPED CHARGE JET IMPACT)

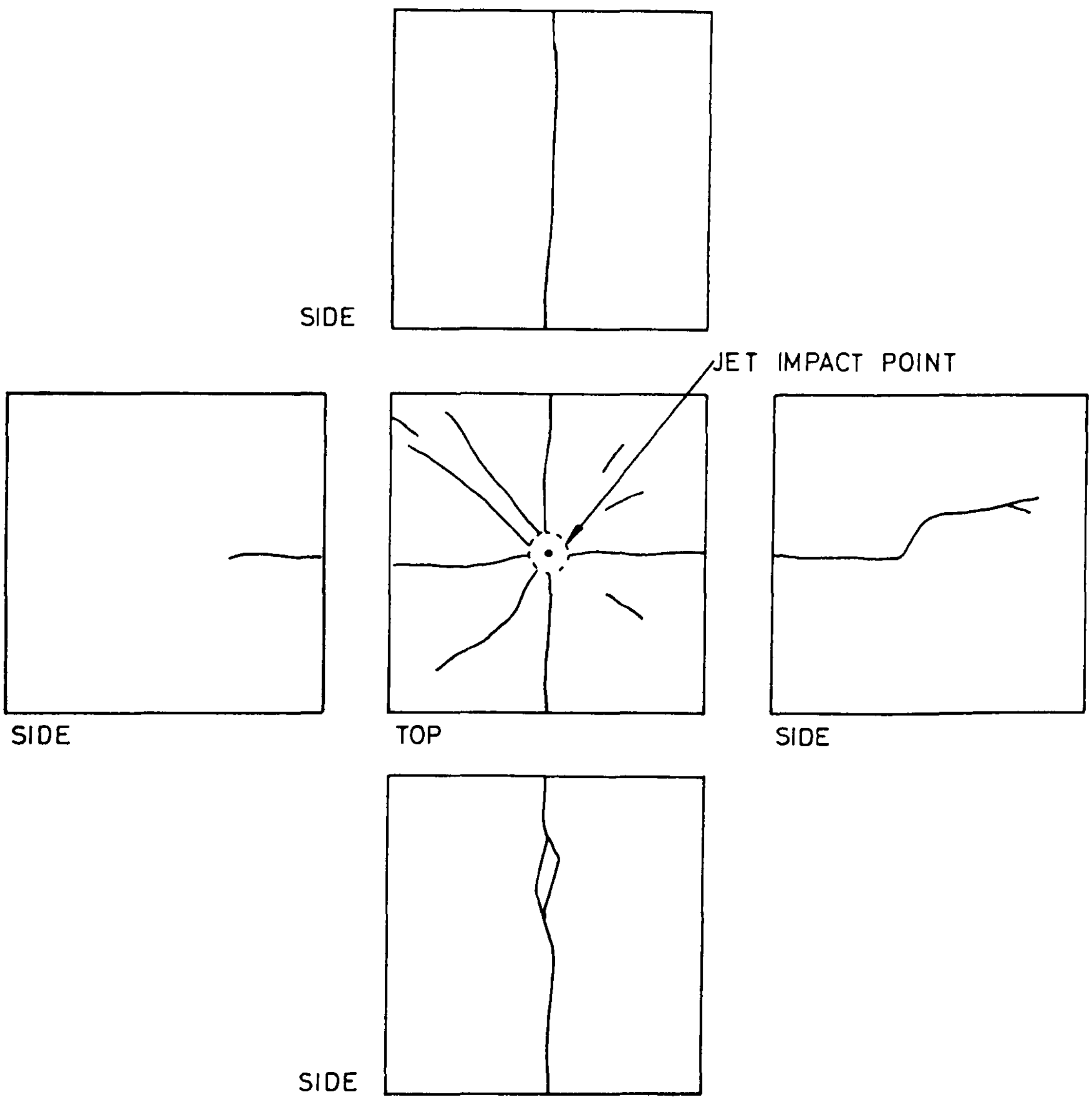

FIGURE 6.8 CRACKS IN A 760mm SAND/GRAVEL CONCRETE CUBE (298g SHAPED CHARGE JET IMPACT)

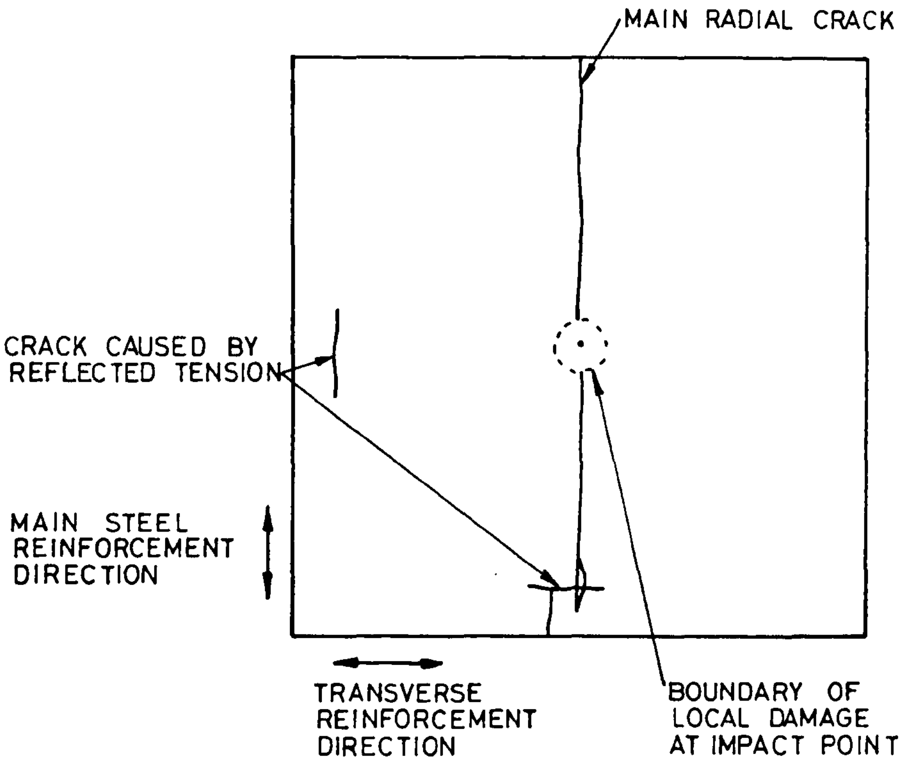

1m² Slab, Copper
Lined Charge

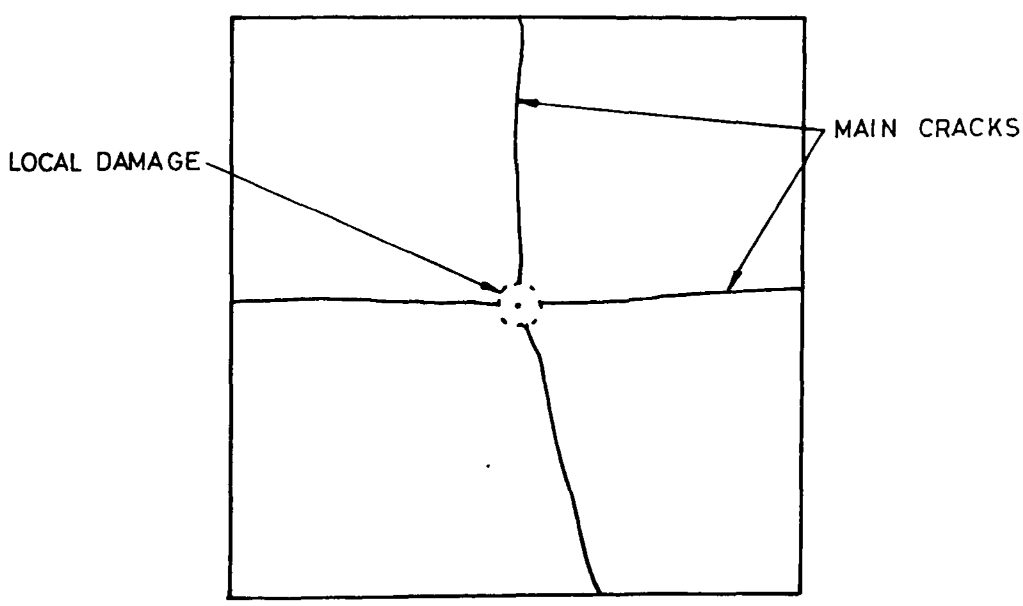

1m² Slab, Aluminium
Lined Charge

FIGURE 6.9 CRACKS IN CONCRETE SLABS
(43g SHAPED CHARGE JET IMPACTS)

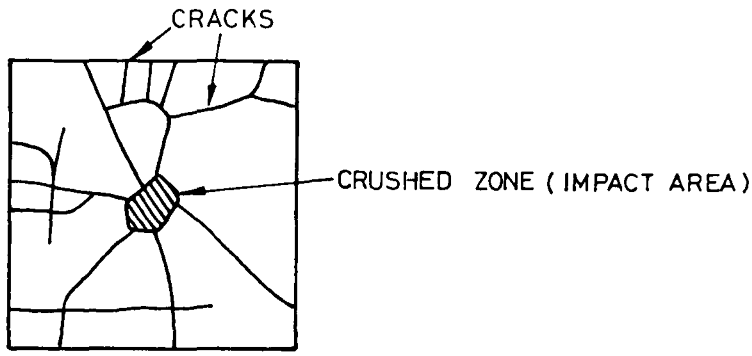

500mm x 500mm Slab, 43 g Charge

FIGURE 6.10 CRACKS IN A 500mm CONCRETE SLAB IMPACTED BY A SHAPED CHARGE JET

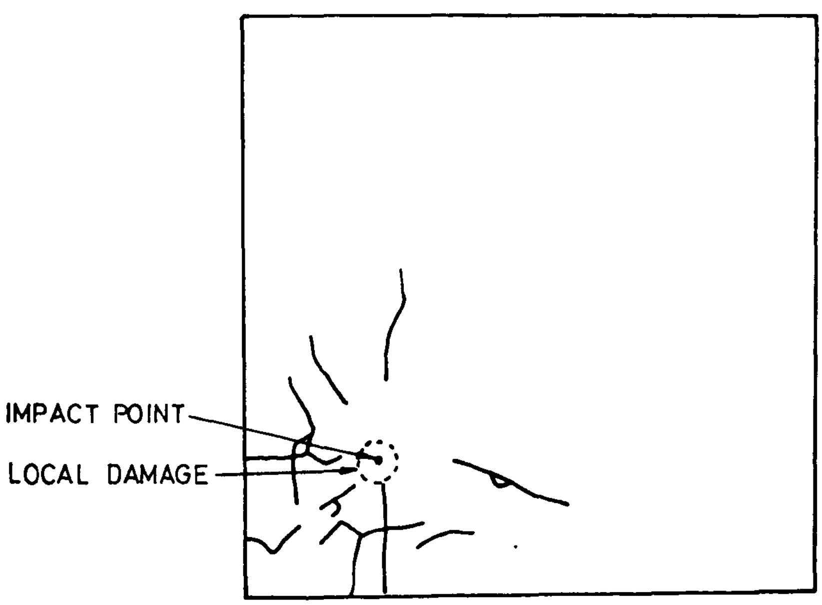

1m² Slab, 43g Charge

FIGURE 6.11 CRACKS IN A CONCRETE SLAB IMPACTED OFF-CENTRE BY A SHAPED CHARGE JET

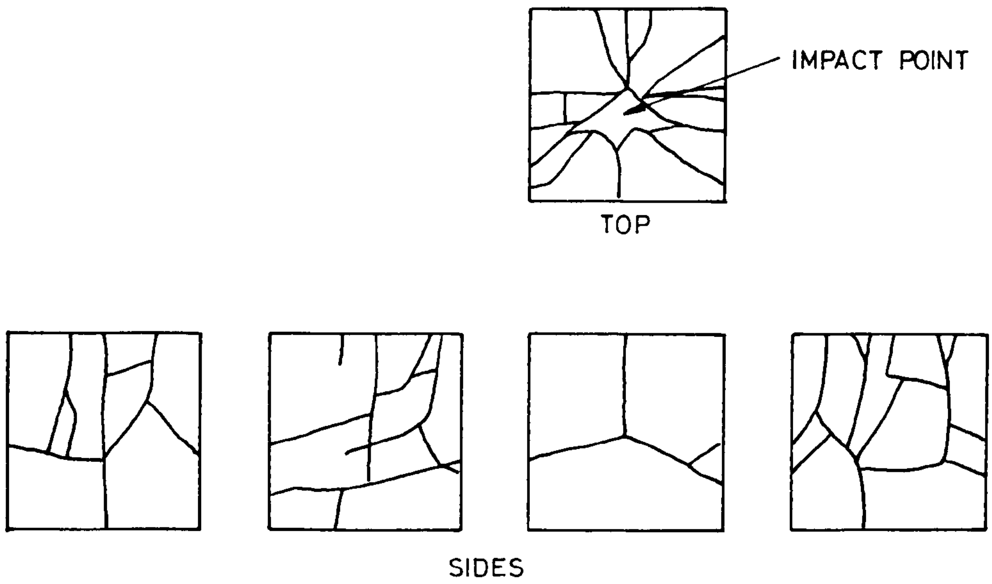

FIGURE 6.12 CRACKS IN A 380mm 'LYTAG' CONCRETE CUBE (43g SHAPED CHARGE JET IMPACT)

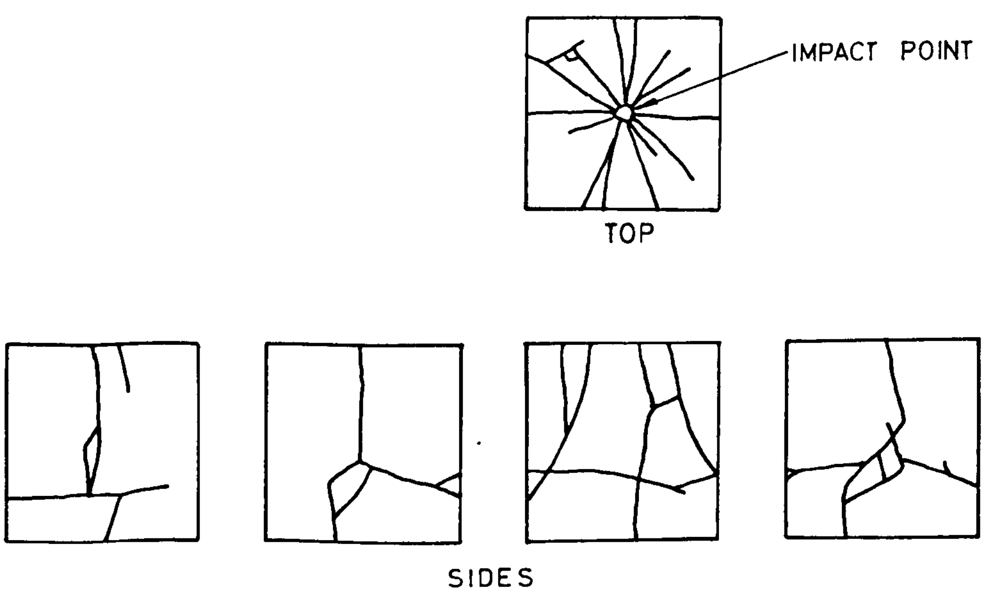

FIGURE 6.13 CRACKS IN A 380mm BARYTES CONCRETE CUBE (43g SHAPED CHARGE JET IMPACT)

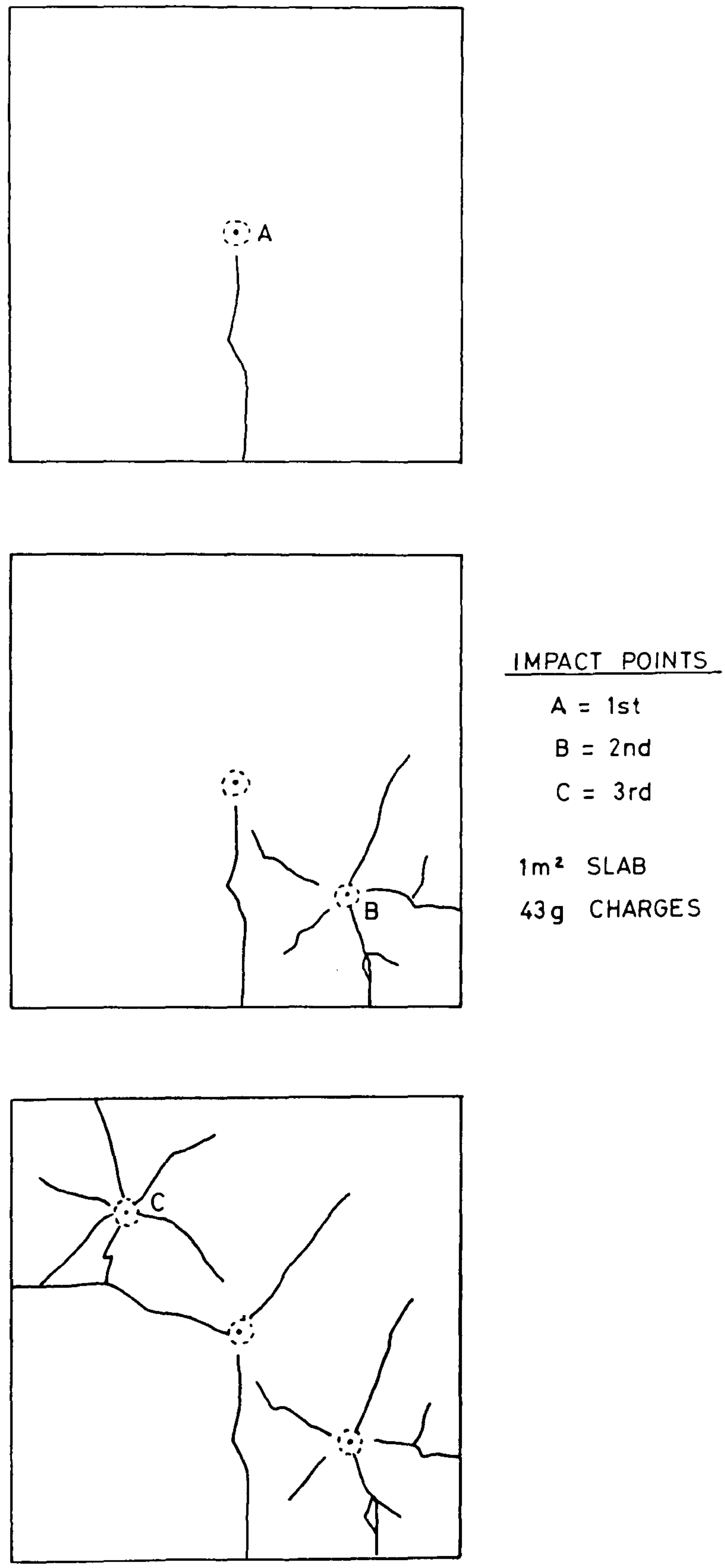

FIGURE 6.14 CRACKS IN A SAND/GRAVEL CONCRETE SLAB AFTER 3 SHAPED CHARGE JET IMPACTS

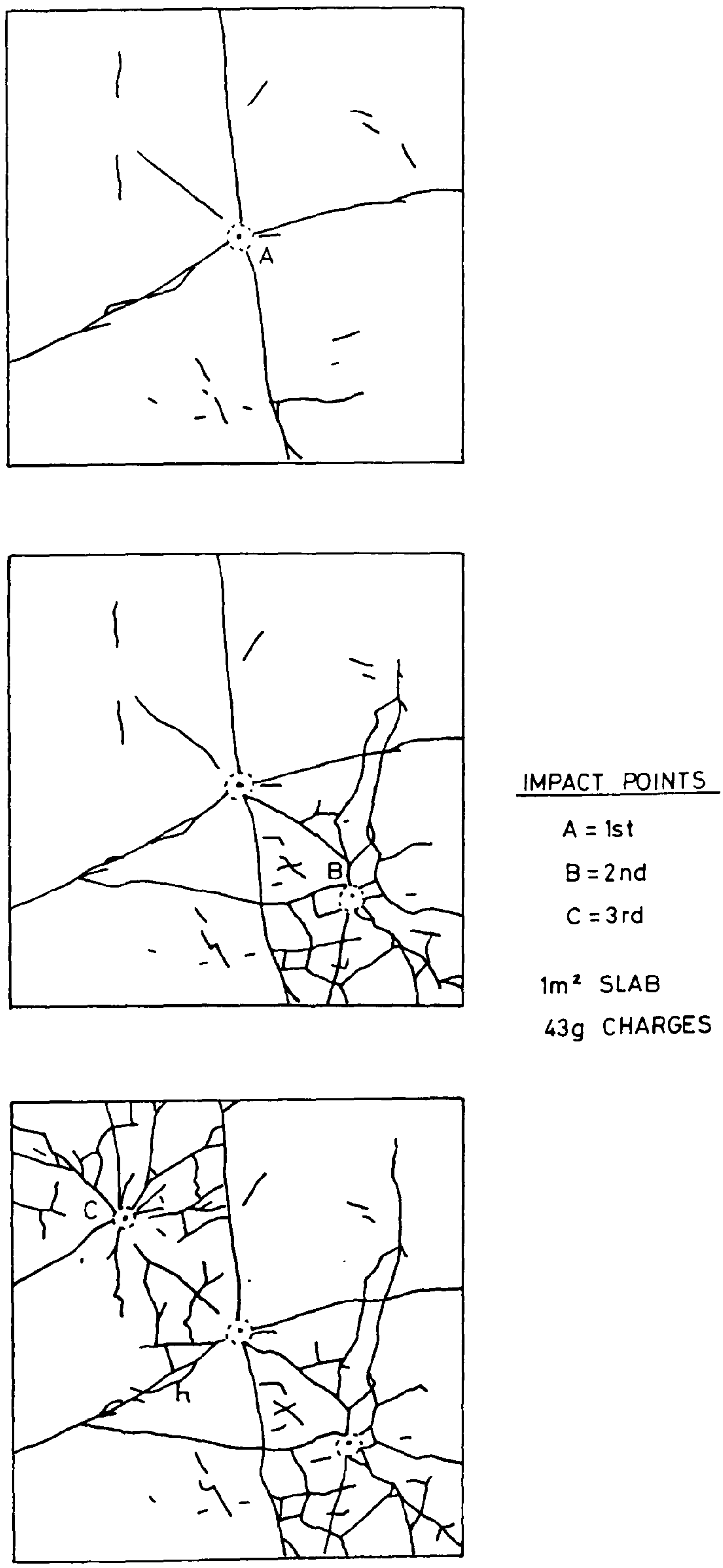

FIGURE 6.15 CRACKS IN A 'LYTAG' CONCRETE SLAB AFTER 3 SHAPED CHARGE JET IMPACTS

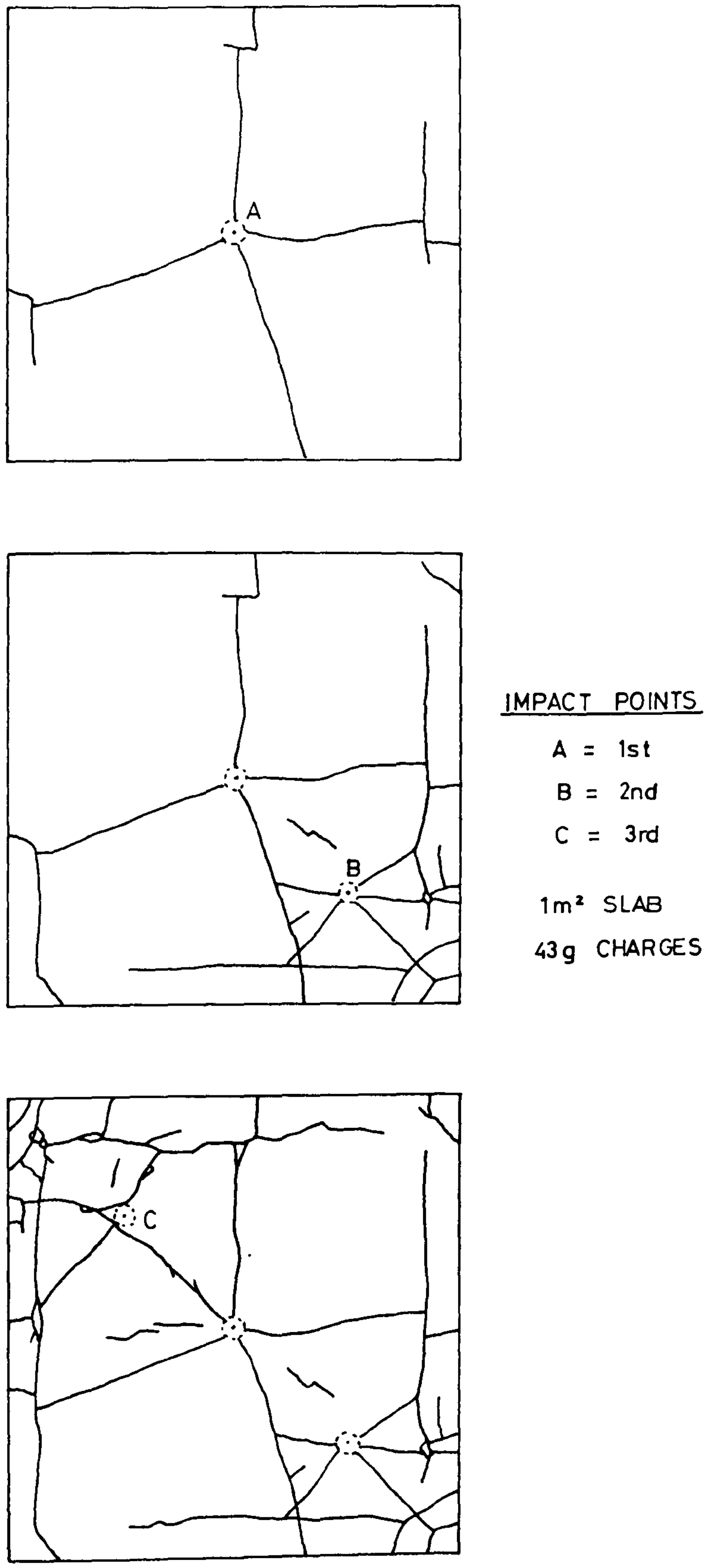

FIGURE 6.16 CRACKS IN A BARYTES CONCRETE SLAB AFTER 3 SHAPED CHARGE JET IMPACTS

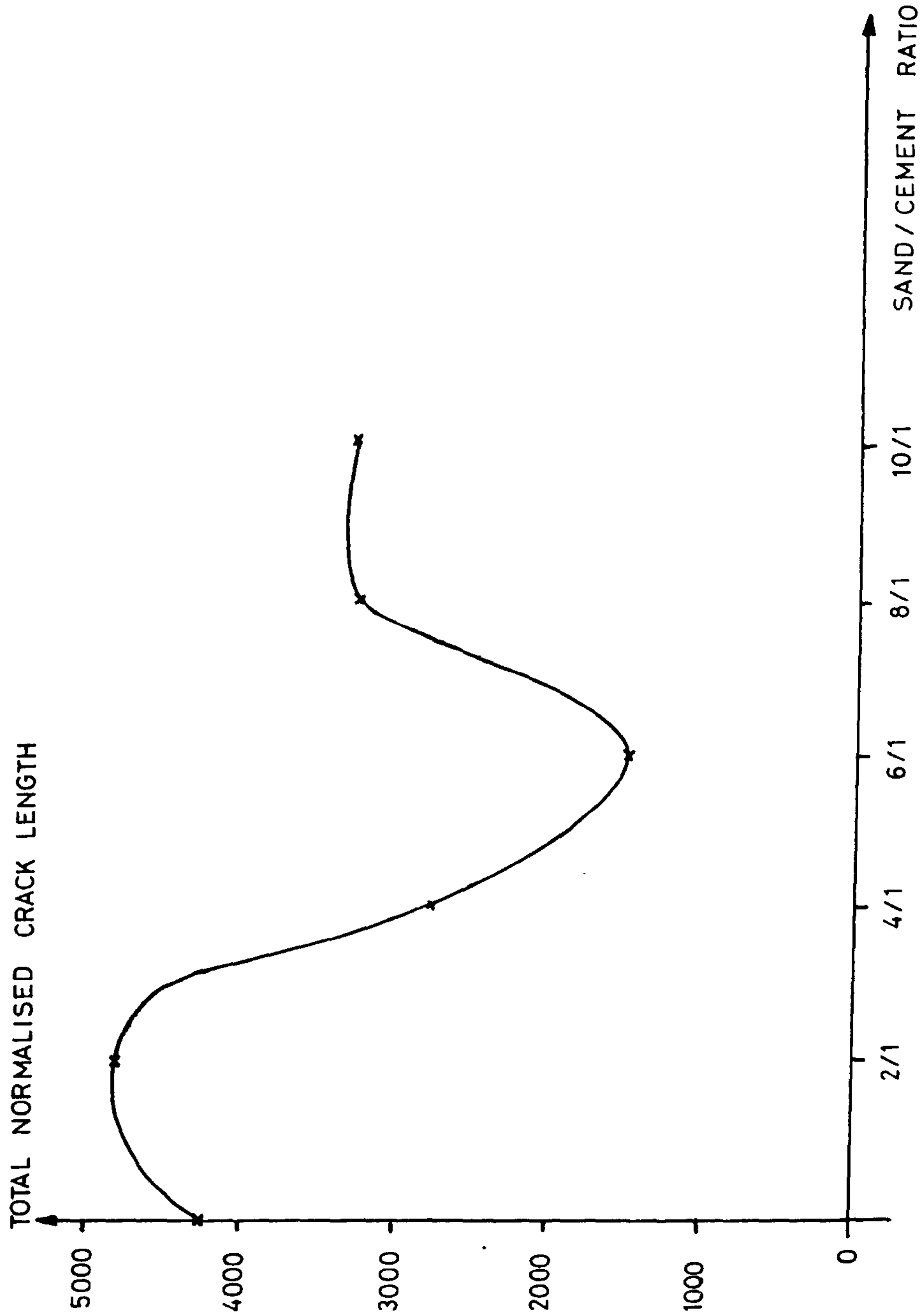

FIGURE 6.17 NORMALISED CRACK LENGTH VERSUS MIX PROPORTIONS FOR SAND/CEMENT MORTAR (380mm CUBES, 43g JET IMPACT)

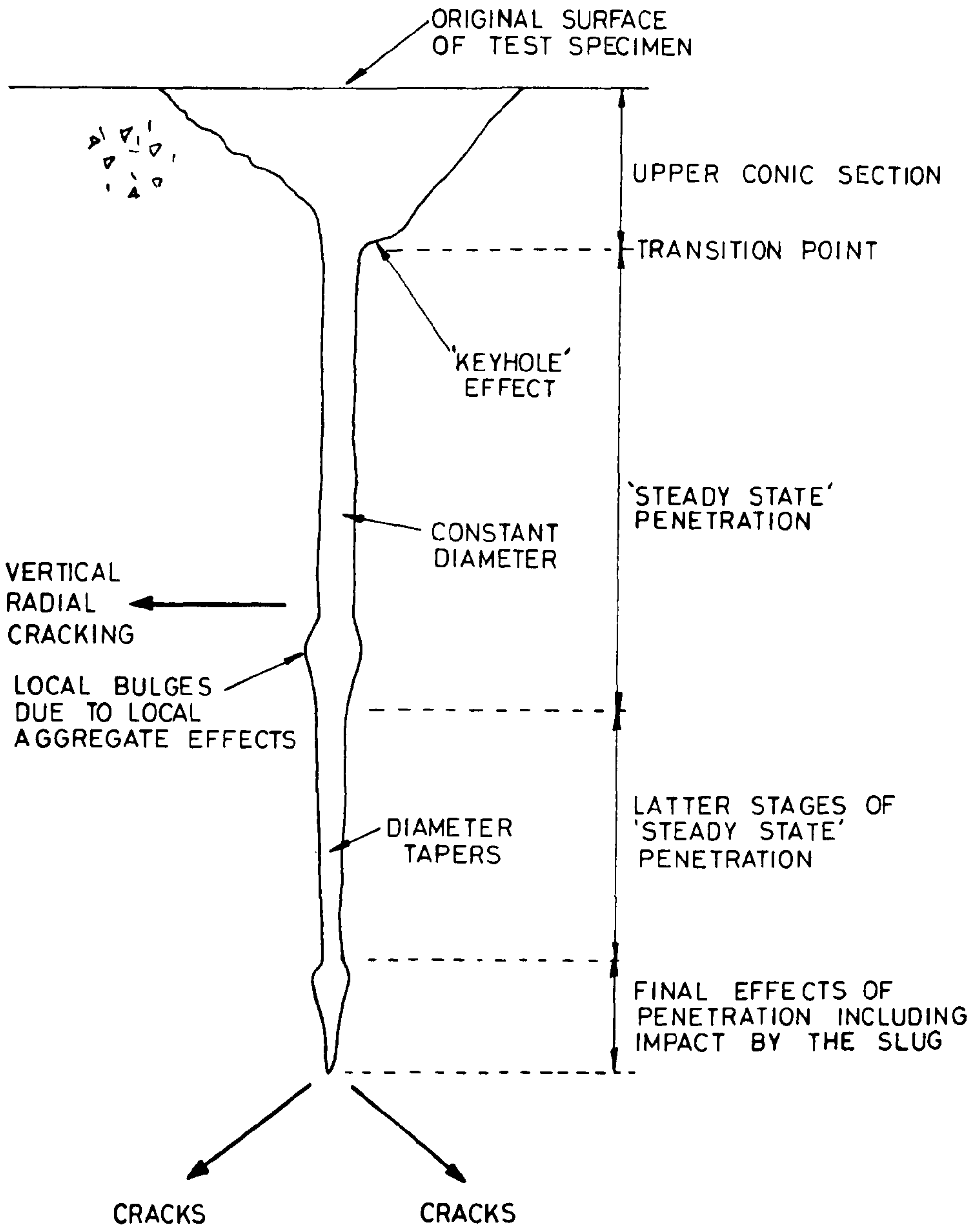

FIGURE 6.18 CROSS SECTION OF A TYPICAL HOLE FORMED IN CONCRETE BY A SHAPED CHARGE JET IMPACT

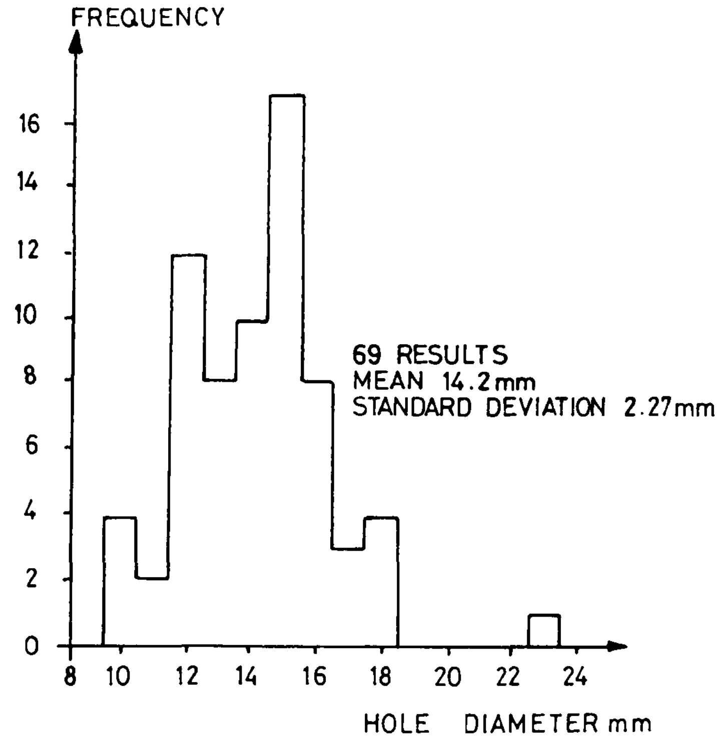

FIGURE 6.19 43g COPPER SHAPED CHARGE IMPACT HOLE DIAMETER FREQUENCY IN CONCRETE

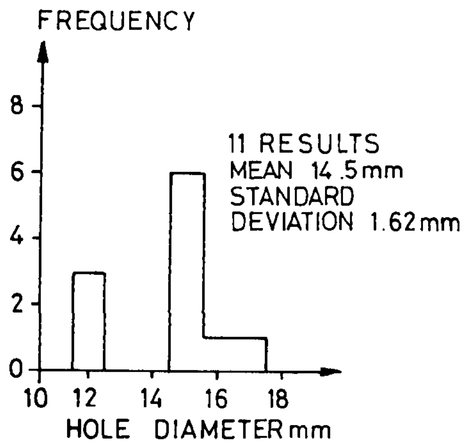

(a) Limestone Aggregate Concrete

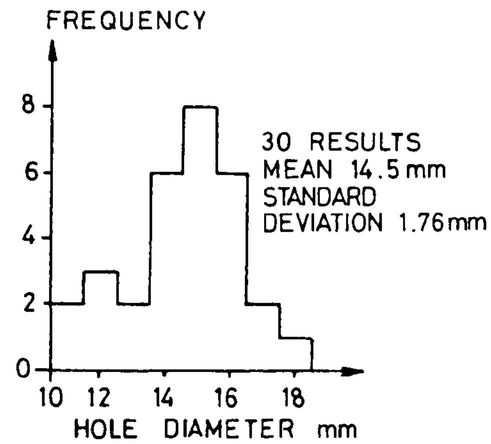

(b) Sand/Gravel Aggregate Concrete

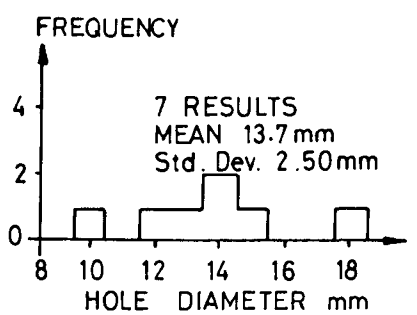

(c) 'Lytag' Aggregate Concrete

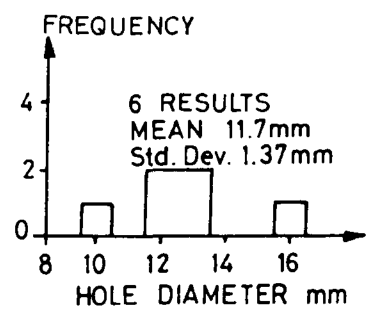

(d) Barytes Aggregate Concrete

FIGURE 6.20 43g COPPER SHAPED CHARGE IMPACT HOLE DIAMETER FREQUENCY IN VARIOUS CONCRETES

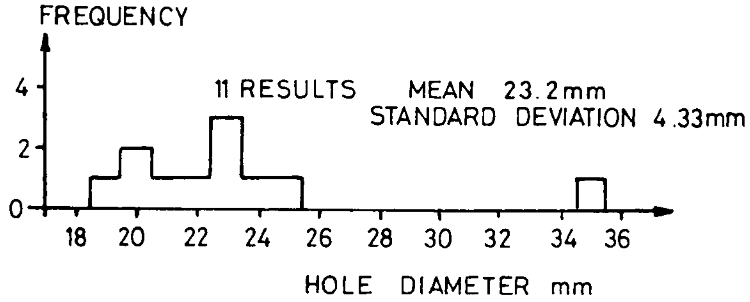

FIGURE 6.21 43g ALUMINIUM SHAPED CHARGE IMPACT HOLE DIAMETER FREQUENCY IN CONCRETE

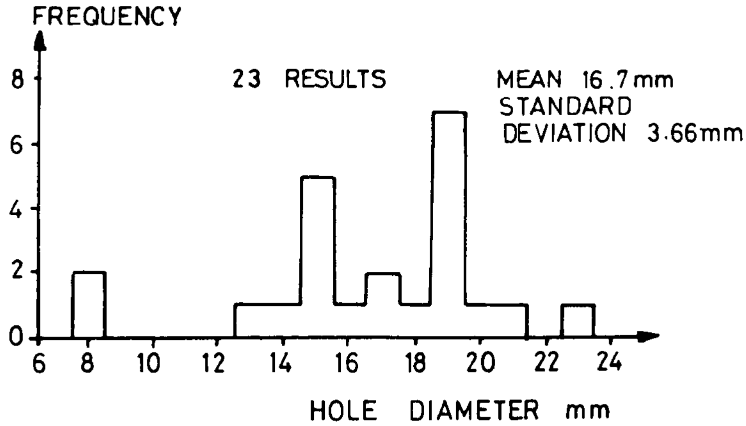

FIGURE 6.22 43g COPPER SHAPED CHARGE IMPACT HOLE DIAMETER FREQUENCY IN LEAN MIX CONCRETE

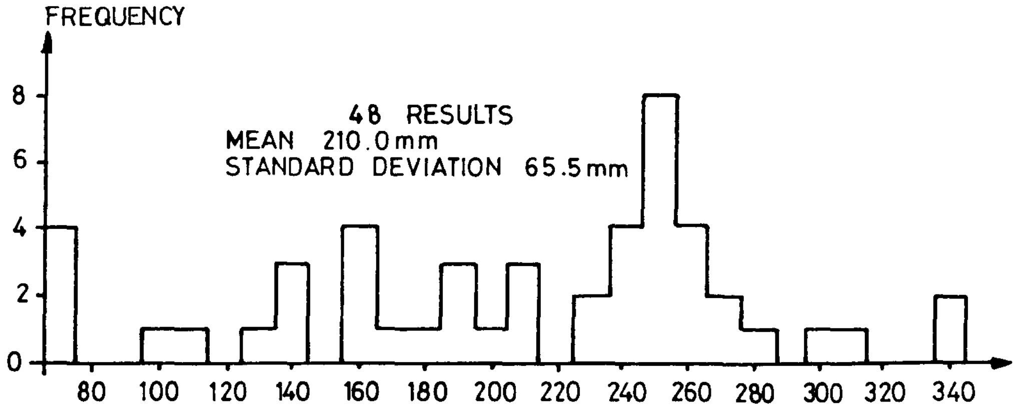

FIGURE 6.23 43g COPPER SHAPED CHARGE JET PENETRATION DEPTH FREQUENCY IN CONCRETE SLAB TESTS

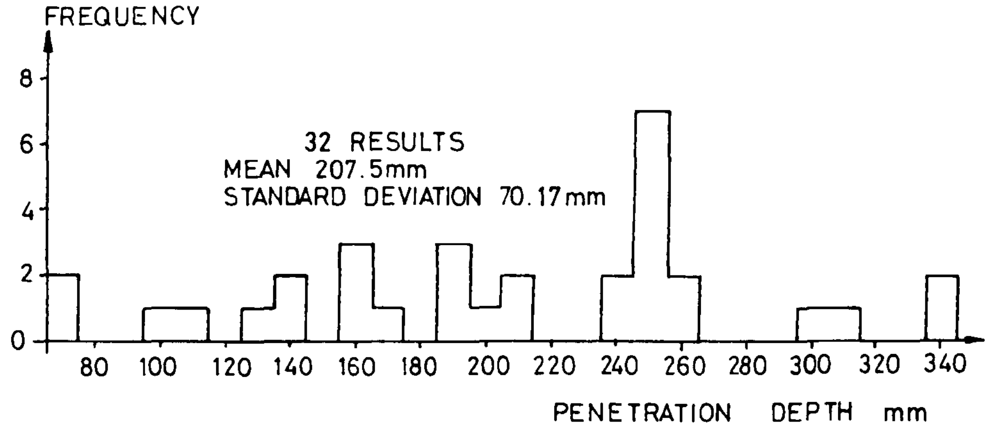

FIGURE 6.24 43g COPPER SHAPED CHARGE JET PENETRATION DEPTH FREQUENCY IN CONCRETE SLABS ON SAND

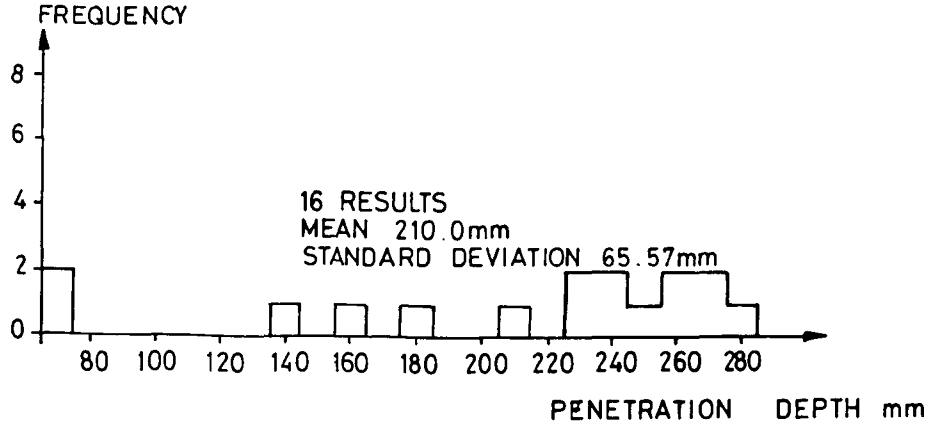

FIGURE 6.25 43g COPPER SHAPED CHARGE JET PENETRATION DEPTH FREQUENCY IN CONCRETE SLABS ON CLAY

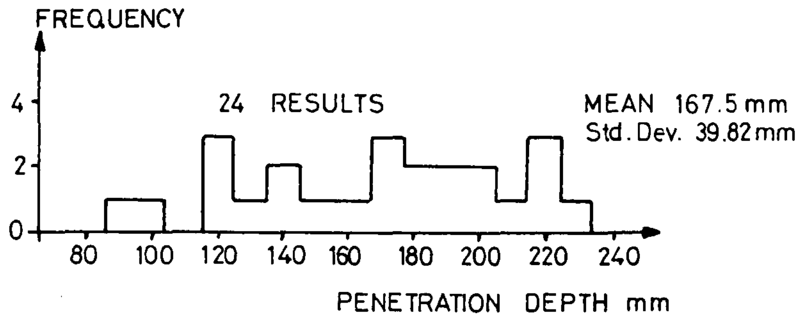

FIGURE 6.26 43g COPPER SHAPED CHARGE JET PENETRATION DEPTH FREQUENCY IN CONCRETE BLOCKS

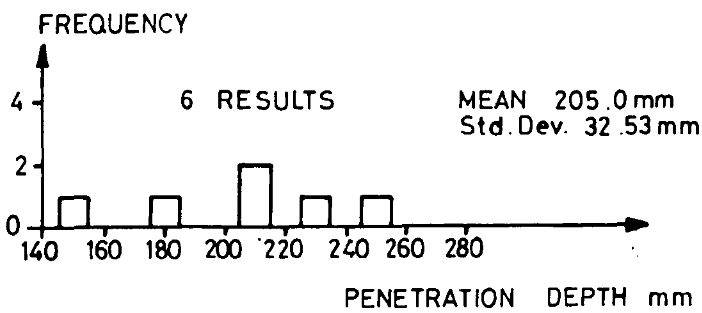

FIGURE 6.27 43g ALUMINIUM SHAPED CHARGE JET PENETRATION DEPTH FREQUENCY IN CONCRETE SLABS

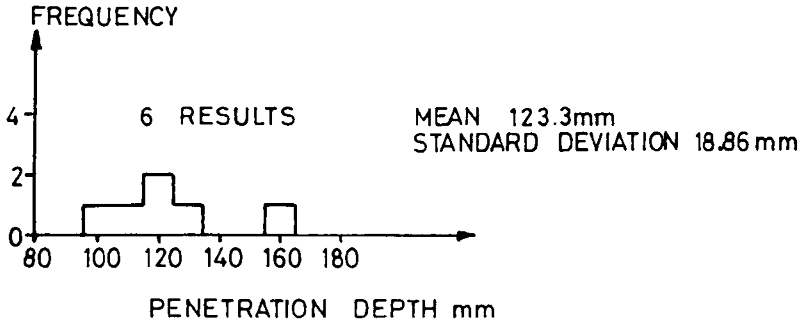

FIGURE 6.28 43g ALUMINIUM SHAPED CHARGE JET PENETRATION DEPTH FREQUENCY IN CONCRETE BLOCKS

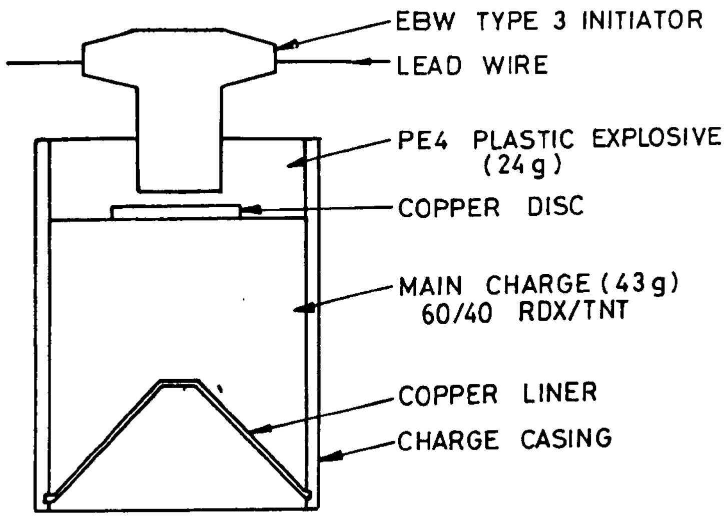

FIGURE 6.29 MODIFIED INITIATOR SYSTEM FOR A 43g COPPER LINED SHAPED CHARGE

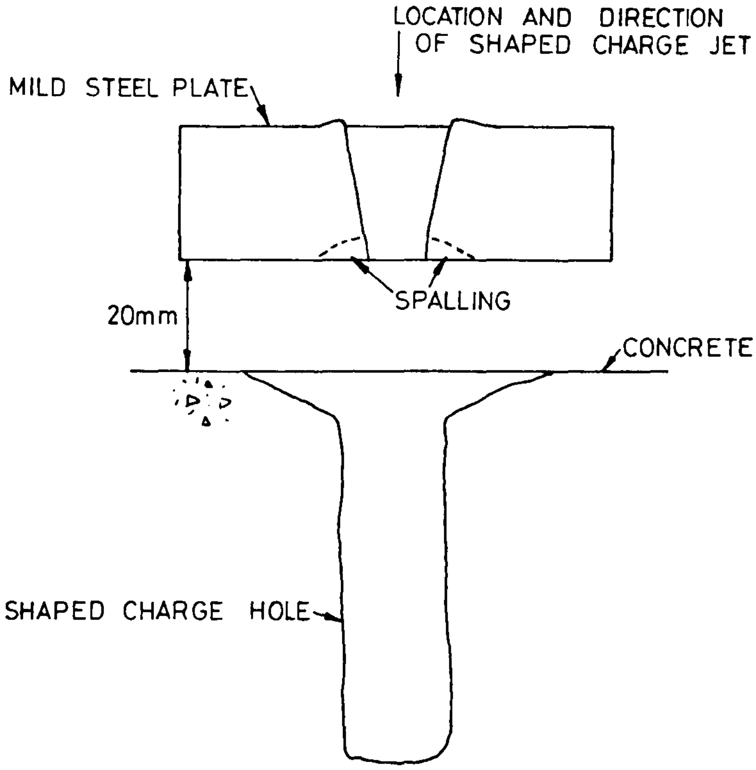

FIGURE 6.30 CROSS SECTION OF A TYPICAL HOLE FORMED IN SAND/GRAVEL CONCRETE BY A 43g COPPER SHAPED CHARGE JET AFTER PERFORATING A STEEL PLATE

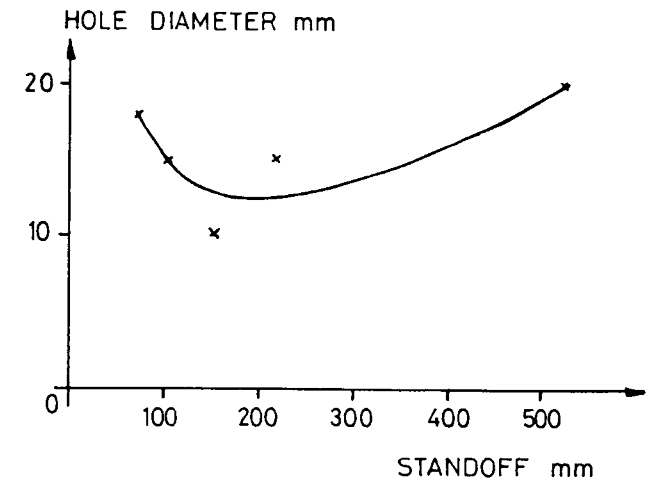

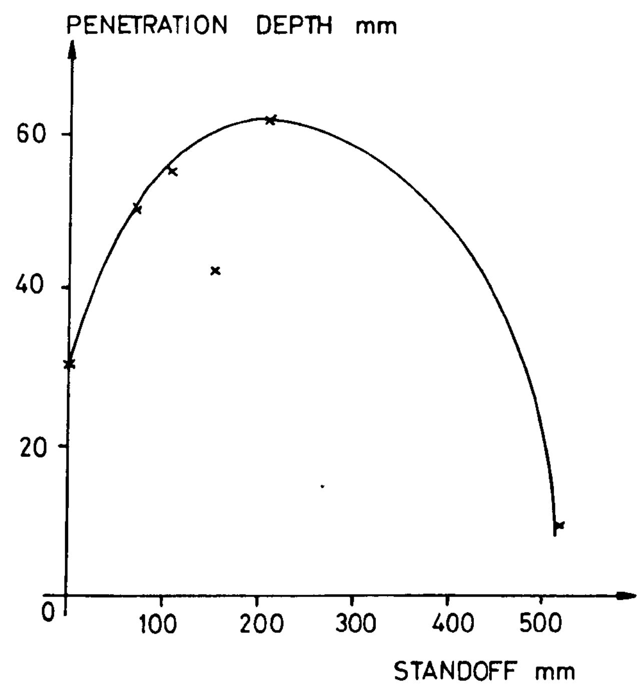

FIGURE 6.31 43g COPPER SHAPED CHARGE IMPACT HOLE DIAMETER AND PENETRATION DEPTH IN CONCRETE VERSUS STANDOFF

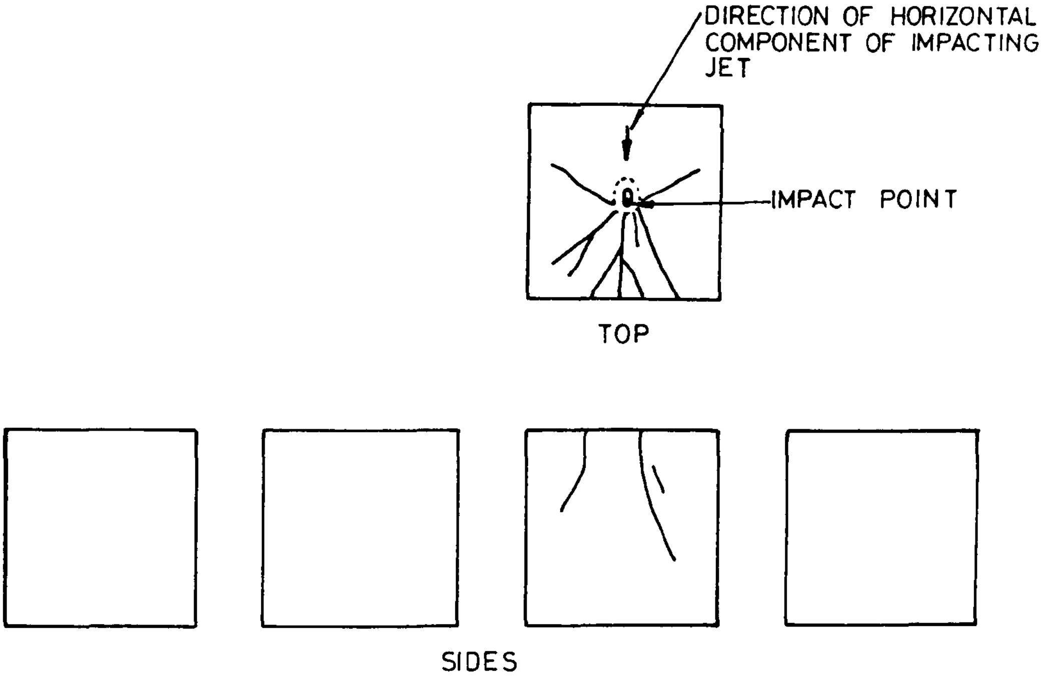

FIGURE 6.32 CRACKS IN A 380mm CONCRETE CUBE IMPACTED BY A 43g COPPER SHAPED CHARGE JET AT 60° TO THE HORIZONTAL

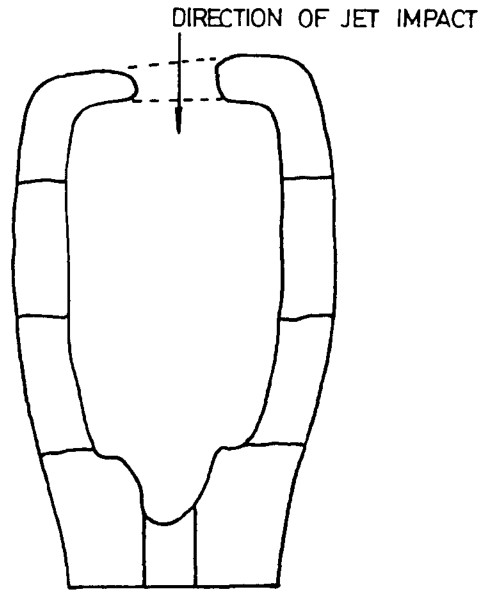

Cross Section

PLASTICINE BLOCK No.1

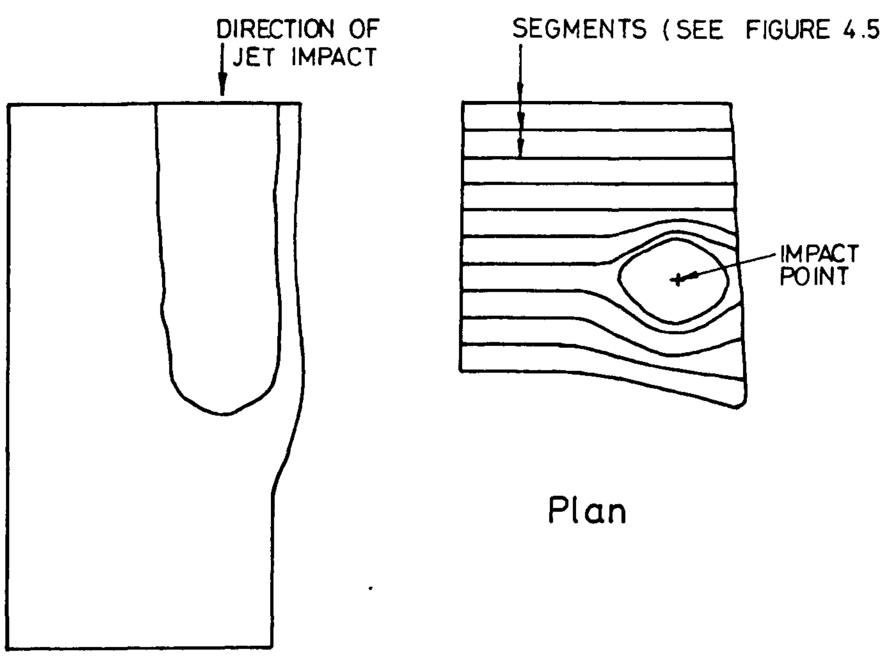

Cross Section

PLASTICINE BLOCK No.2

FIGURE 6.33 DETAILS OF 43g SHAPED CHARGE JET IMPACT HOLES IN 'PLASTICINE' BLOCKS

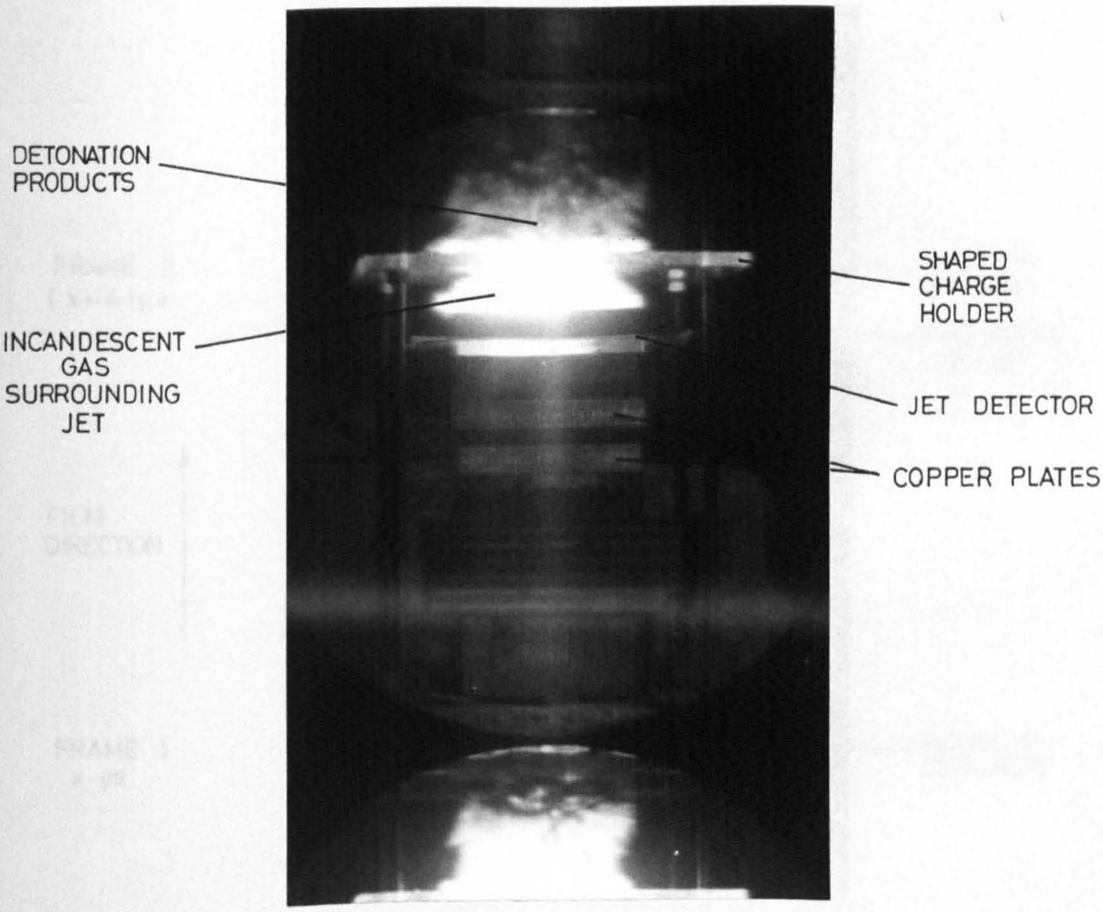

PLATE 6.1 HIGH SPEED CAMERA FRAME OF A SHAPED CHARGE JET PENETRATING COPPER

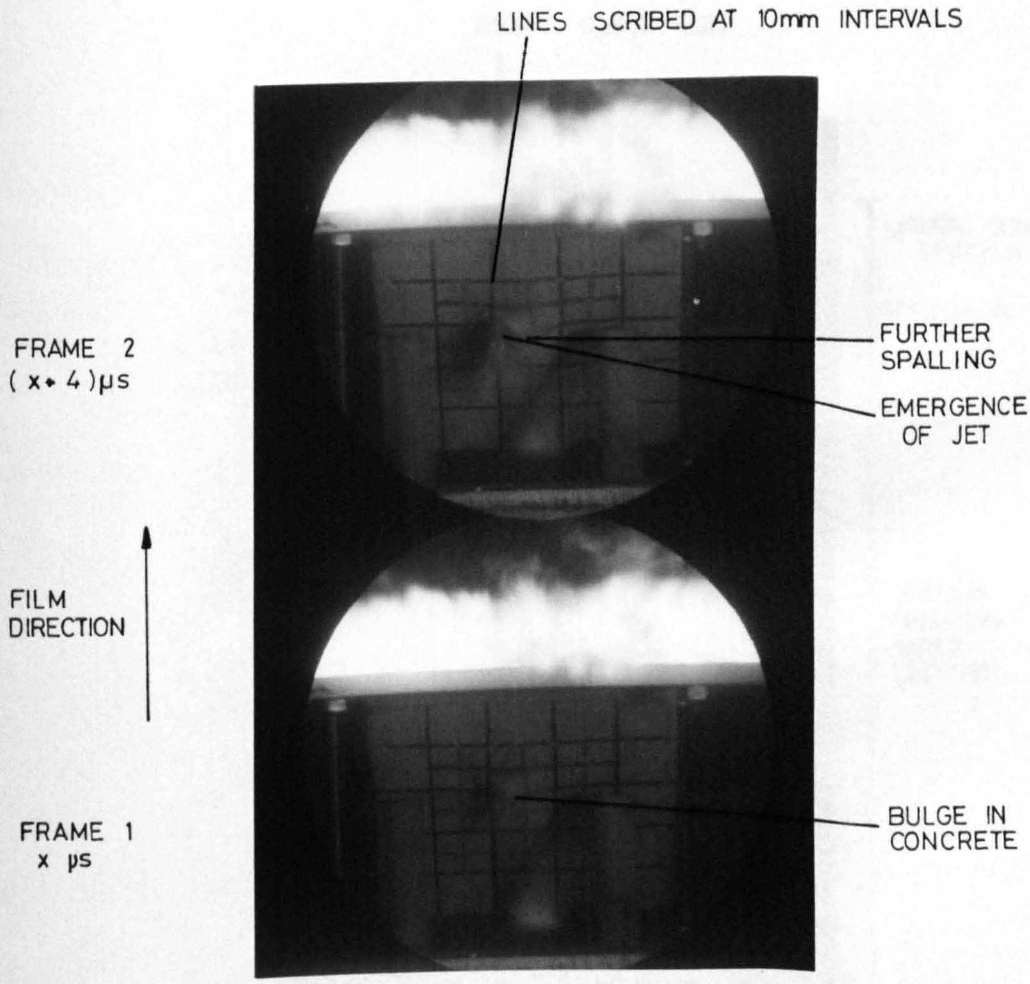

PLATE 6.2 SPALLING AND CONCRETE MOVEMENT DURING SHAPED CHARGE JET PENETRATION

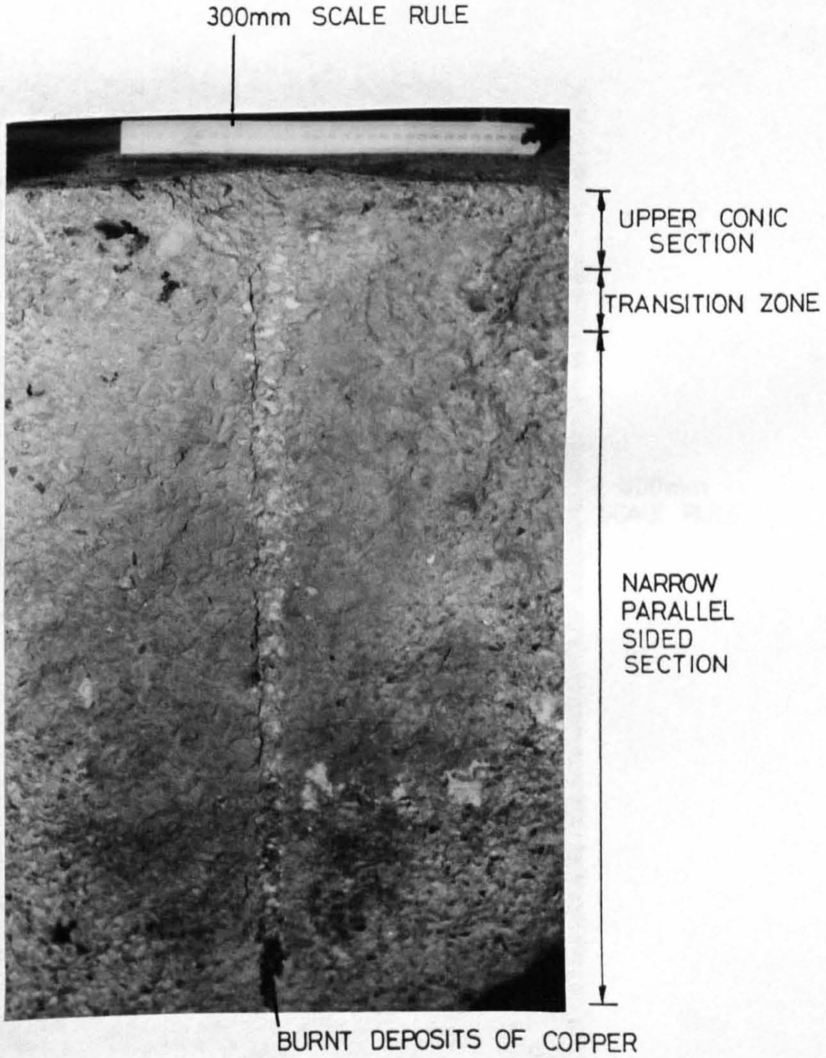

PLATE 6.3 CROSS SECTIONAL VIEW OF A 298g SHAPED CHARGE IMPACT HOLE IN A 760mm CONCRETE CUBE

PLATE 6.4 CROSS SECTIONAL VIEW OF A 43g SHAPED CHARGE IMPACT HOLE IN A 'PLASTICINE' BLOCK

CHAPTER 7

EXPERIMENTAL RESULTS FROM SUBSURFACE CHARGE EXPLOSION TESTS IN SOILS OVERLAIN BY GROUND SLABS

The subsurface explosion test programme consisted of fourteen tests and was neither as extensive nor as varied as the shaped charge test programme. The programme concentrated on eleven 1/5 scale concrete slab tests U1 to U11, one 1/3 scale concrete slab test, U12, and two tests in uncrusted soils. Tables 7.1 and 7.2 contain experimental data from the test programme and table 4.8 gives basic soil properties as determined by soil tests to British Standard 1377 (1975) and described in section 5.2.5. Slab cracking and displacement data are given in tables 5.13 and 5.14.

7.1 THE INFLUENCE ON CRATERING OF GROUND SLABS OVERLYING SOIL SUBJECTED TO SUBSURFACE EXPLOSIONS

A subsurface explosive charge in soil caused a different crater when a concrete ground slab was cast onto soil. An equivalent surcharge depth of soil equal to the mass of a concrete slab did not influence the crater in the same way as a slab. The shear strength of the concrete required energy to remove the concrete and this can be demonstrated by comparing the shapes and sizes of craters in surcharged soil and under concrete ground slabs.

Figure 7.1 shows a crater formed in surcharged sand by a 16g PE4 explosive charge. The soil surcharge equalled the mass of a 1/5 scale concrete slab and lean mix layer. Figure 7.2 shows the crater formed by a 16g PE4 explosive charge under a 1/5 scale ground slab on sand. The main features are the relative crater sizes and the shear planes as shown by the movement of coloured columns of sand formed in the sand. Part of the sand mass under the concrete slab was driven laterally away from the explosion area. The influence of the proximity of the test bay walls is unknown, but since the shear planes did not quite extend to the test bay walls, the effects of these walls may not be so important and may just have a restraining effect as an adjacent soil mass would.

Figures 7.3 and 7.4 show respectively a 16g PE4 explosive charge crater in surcharged clay and under a 1/5 scale ground slab on clay. The major difference in the case of clay soil is the size of the crater. The coloured sand columns included in the clay showed that the crater was formed by cavity expansion and the influence of this was localised. Only a limited local shear plane was found to have been formed in the soil.

7.2 INFLUENCE OF THE SOIL TYPE AND CONDITION ON CRATERING

In this study it was necessary to adopt terminology to describe the soils in various conditions. Clay was usually at a degree of saturation of about 97%. This was deemed to be fully saturated. Sand at a degree of saturation around 59% was classed as "wet" and around 36% the term chosen was 'damp'. Sand with a degree of saturation below about 30% was classed as 'dry'.

Fully saturated clay and sand at a degree of saturation of 59% influenced the details of the crater in the soil and the crack pattern in the concrete slab differently to sand at a degree of saturation of 36%. Figures 7.2, 7.4 and 7.5 show respectively the crater formed in damp sand, saturated clay and wet sand. The crater shapes were not quite the same in all the soils but in the case of clay and wet sand soils, the concrete slab was partially removed from the site. The crack patterns for the slabs on clay, wet sand and damp sand are shown in figures 7.6, 7.7 and 7.8 respectively. These figures show reconstructed slabs. The pieces of slab removed during the test by the blast are shown shaded.

The three examples above demonstrated the effect of degree of saturation of the soil in that the clay and wet sand caused more of the blast from the explosive to be directed upwards. This resulted in slabs which were more cracked than in the case of the concrete slab on dry sand. The water in the soil may have acted as an incompressible fluid in saturated and wet soils and transmitted the blast pressure better than the more compressible air found in damp soils.

The shape of craters in soils varied due to soil cohesion. In clay the crater remained as an expanded sphere with a curved roof and contained little fallback material. In wet, damp and dry sands the roof of the crater collapsed and partially filled the true crater. In some cases fallback reduced the crater to only 50% of its true size, and particularly in the case of wet sand, fallback almost filled the true crater. The true crater could always be determined during excavations by the deposit of soot from the explosive around the entire surface of the true crater.

7.3 THE INFLUENCE ON CRATERING OF REINFORCEMENT IN GROUND SLABS

The main effect of reinforcing a concrete ground slab was to prevent it from breaking into pieces in the same way as unreinforced slabs shown in figures 7.6, 7.7 and 7.8. Figures 7.9 and 7.10 show respectively reinforced concrete ground slabs subjected to subsurface explosions in clay and sand subsoil. The craters produced are shown in figures 7.11 and 7.12 for the clay and sand soils respectively. The craters did not correspond in size or shape to craters in clay and sand soils overlain by unreinforced concrete slabs as shown in figures 7.4 and 7.2 respectively. This is possibly due to the additional energy required to move the reinforced slab as a single mass rather than breaking it or punching out the central section. The slab tended to crack more when the explosion was in clay soil and this corresponded to the case of unreinforced slabs. This is again thought to be due to more blast being channelled upwards by the effect of a fully saturated soil and less blast dissipation in the pores in the soil.

7.4 THE INFLUENCE ON CRATERING OF DAMAGED CONCRETE GROUND SLABS

Concrete ground slabs subjected to a shaped charge jet impact usually cracked as shown in figure 7.13. The single radial crack shown in figure 7.13 was found to be the only major damage caused and this did not affect the subsequent crack pattern of the concrete slab under subsurface explosive blast loading. This was confirmed by a test on an uncracked slab with a pre-formed hole, as described in section 4.2.1, which was subjected to a subsurface explosion and which cracked in a similar manner to other slabs with shaped charge holes. The slabs were both on dry sand and the crack pattern in the slabs was similar to the pattern shown in figure 7.8.

7.5 MOVEMENT OF SLABS AND STRESS PULSE INVESTIGATION IN THE SOIL

The movement of concrete ground slabs was detected indirectly by electrically conducting paint crack detectors. The slabs were painted as shown in figure 7.14 and as the slab moved and cracked, the time of cracking was recorded and taken to be the start of movement. It was not possible to use potentiometric displacement transducers since the slabs moved by unpredictable amounts and also broke up in some tests. The slabs appeared to break so that the profile of the surface resembled a hemisphere. It was thus considered reasonable to expect the cracks to start at the hole in the centre of the slab and to propagate out as the slab lifted. Table 7.1 gives values for the time of cracking for three slabs, all on sand subsoils. The times vary from 534 to 950μs after detonation, which are wide limits. Their accuracy has not been checked by high speed photography since the camera's flash unit could not operate for the length of time required. The camera did show by default that slab movement did not take place in the first 300μs after initiation of the blast.

The explosive blast, as detected by a gas detector, was found to take 122μs to appear at the upper surface of a concrete ground slab. The blast wave in soil was found, by the soil pressure gauge, described in section 4.1.1, to take 770μs to travel 670mm in soil. These two values, quoted in table 7.1, tend to support the timescale for events such as cracking due to subsurface explosives. The blast wave speed in soil was 0.96mm/μs which is about one third the wave speed in concrete. However, soil is a multiphase medium and attenuation caused by reflection and refraction at soil particle interfaces would be large. At 670mm from a 74g PE4 charge, the stress registered was 5.8 N/mm^2. This is not a reliable measurement for the reasons discussed in section 4.1.1 but the value is much in excess of the value required to cause soil failure.

The wide variation in event times could also be caused by unknown factors in the coupling of the explosive to its surrounding media in the hole. Since the explosive is not compressed as in shot firing, the range of variables involved could be sufficient to mask any deliberately introduced variables in the test.

7.6 COMPARISONS BETWEEN CRATERS AT 1/5 SCALE AND AT OTHER SCALES

Table 7.2 contains soil crater dimensions for all tests in the subsurface explosion programme. This data is best assimilated from the frequency distribution for true crater diameter and true crater depth shown in figures 7.15 and 7.16 respectively. The most frequent crater diameter found was between 275mm and 325mm with an arithmetic mean value of 318mm. This was for a 16g explosive charge in a 1/5 scale test specimen. A 74g charge in a 1/3 scale test specimen, U12 in table 7.2, caused a 600mm diameter crater which differed from the predicted diameter of 509mm expected from scaling rules using 318mm as 1/5 scale diameter. Similarly from figure 7.16 the most frequent crater depth lay between 225 and 275mm with an arithmetic mean value of 227mm. The 1/3 scale crater was found to be 500mm deep which varied considerably from the 363mm predicted value using 227mm as the 1/5 scale diameter.

The frequency of the crater volumes listed in table 7.2 is shown on figure 7.17. The mean volume for 16g charges was 3.96×10^{-2} m^3 This predicts a volume of 15.36×10^{-2} m^3 for 74g charges but in the 74g charge test the volume of the crater was 35.0×10^{-2} m^3.

The 1/3 and 1/5 scale tests used explosive masses and burial depths scaled according to charge scaling laws given in section 2.8.2. Only these tests were directly compatible. Kvammen (1973) performed some full scale experiments on pavement ground slabs but explosives, burial depths and pavement thicknesses did not agree entirely with those used in this study. The closest results to this study, in terms of explosive mass, depth of burial and slab thickness have been taken from Kvammen's work and have been redrawn as figure 7.18 to the same scale as figures 7.1 to 7.5, 7.11 and 7.12. While exact comparisons are difficult due to different depths of burial, the scaled down crater dimensions from Kvammen's work are in broad terms similar to those of this study.

7.7 LIMITATIONS

Subsurface explosive charges were not constructed as shaped charges. Since they only consisted of a mass of explosive with an initiator, the detonation characteristics of each charge must have differed slightly from charge to charge. In addition the coupling between the charge and the sides of the hole into which it was introduced could not be easily controlled and so these may have varied significantly.

Instrumentation was not as reliable as in the shaped charge test series described in chapter 6, nor was it as widely used due to the small test programme. Results were not so easy to cross check or so repeatable in the subsurface tests even allowing for the limitations of the shaped charge tests. Nevertheless, as in the shaped charge test series, some trends were found.

Table 7.1

Subsurface Explosive Charge Effects

Specimen No	Arrival Time of Explosion Gases μsec	Movement of Slab μsec	Remarks
U6	112	-	-
U8 U9 U10	- - -	850 534 950	- - -
U12	-	770	74g charge 1/3 scale slab 670mm to gauge 5.8 N/mm^2 0.96 mm/μs speed

16g PE charge at 240mm burial depth except test U12

Table 7.2

Subsurface Crater Data

Specimen	Average Crater dia. mm	True Crater Maximum Depth mm	True Crater Volume $m^3 \times 10^{-2}$	Soil Type	Remarks
U1	370	240	4.0	Sand	'Damp' sand
U2	270	240	3.5	Sand	'Damp' sand Reinforced slab
U3	360	250	6.0	Clay	
U4	360	270	8.2	Clay	Reinforced slab
U5	300-330 (315)	285	5.9	Sand	'Wet' sand
U6	312-350 (331)	131	0.7	Sand	'Wet' sand
U7	410-430 (420)	205	3.0	Sand	'Dry' sand
U8	260-310 (285)	170	1.5	Sand	'Dry' sand
U9	320-400 (360)	270	5.3	Sand	'Dry' sand
U10	300-330 (315)	180	1.8	Sand	'Dry' sand
U11	220	250	3.7	Clay	
U12	600	500	35.0	Sand	74g charge 1/3 scale slab 'Wet' sand
Surcharged Sand U13	100-300 (200)	230	-	Sand	No slab 'Dry' sand
Surcharged Clay U14	370	230	-	Clay	No slab

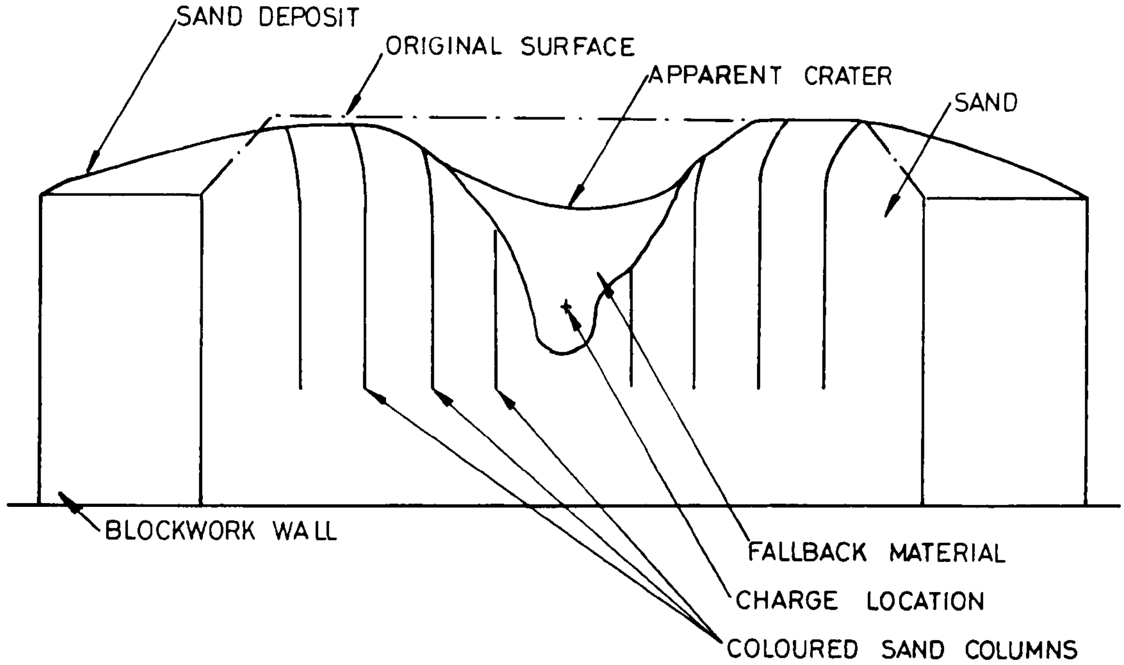

FIGURE 7.1 CRATER FORMED IN SURCHARGED SAND BY A 16g SUBSURFACE EXPLOSIVE CHARGE

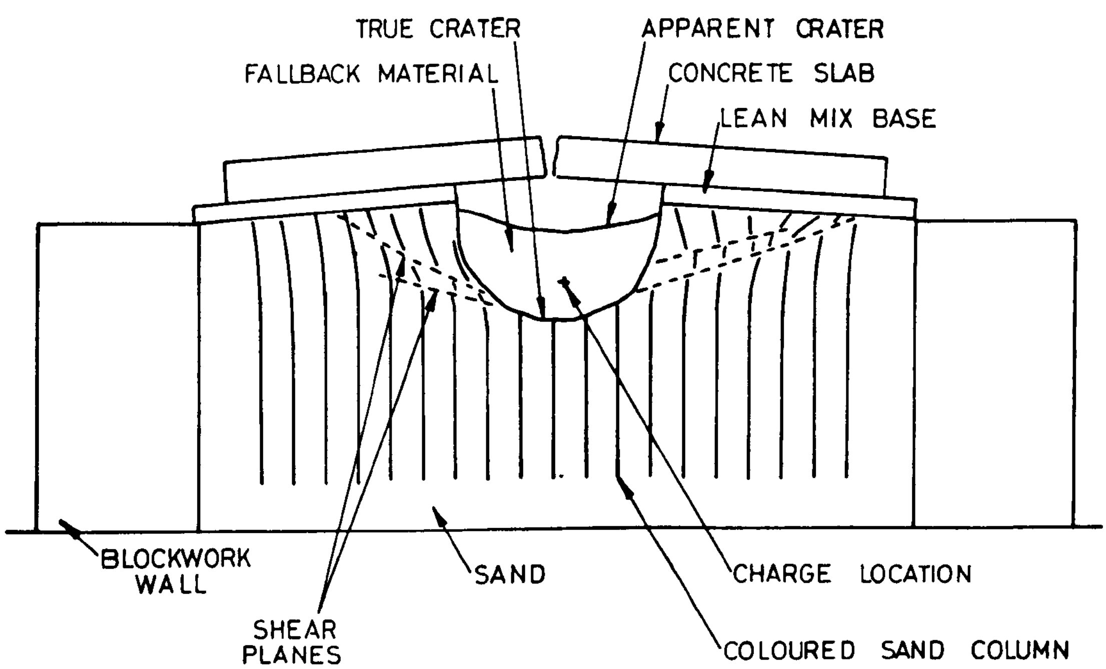

FIGURE 7.2 CRATER FORMED IN CRUSTED SAND BY A 16g SUBSURFACE EXPLOSIVE CHARGE

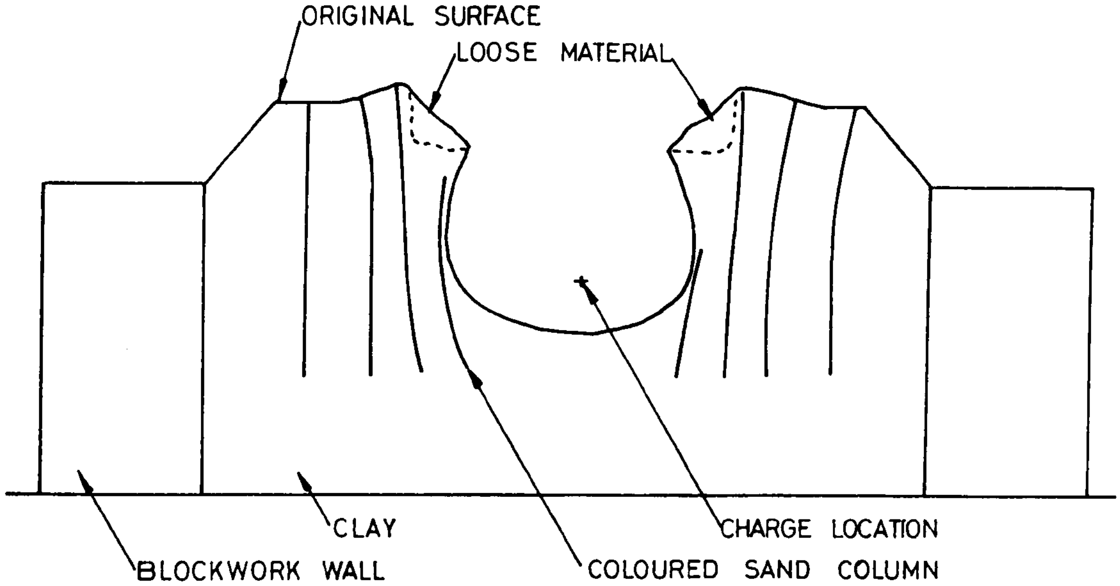

FIGURE 7.3 CRATER FORMED IN SURCHARGED CLAY BY A 16g SUBSURFACE EXPLOSIVE CHARGE

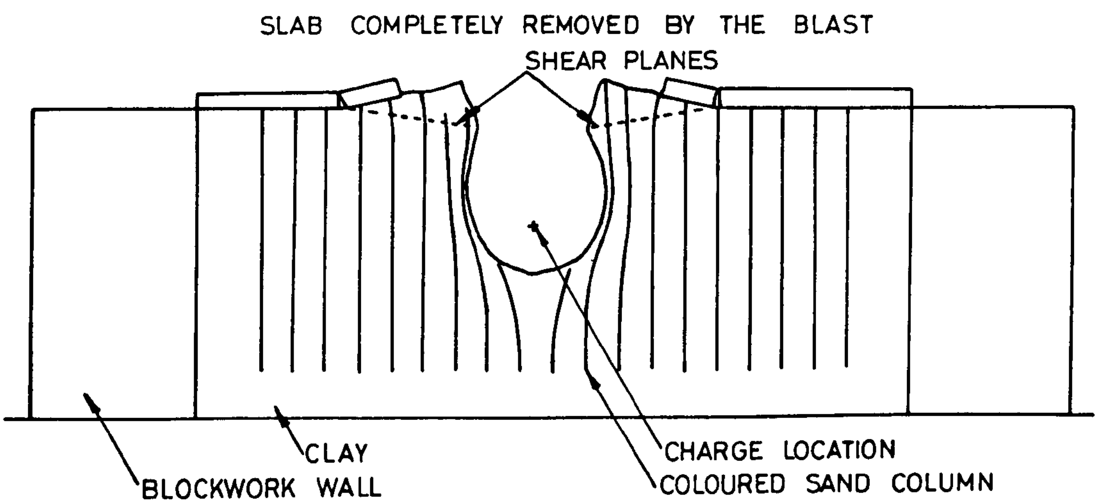

FIGURE 7.4 CRATER FORMED IN CRUSTED CLAY BY A 16g SUBSURFACE EXPLOSIVE CHARGE

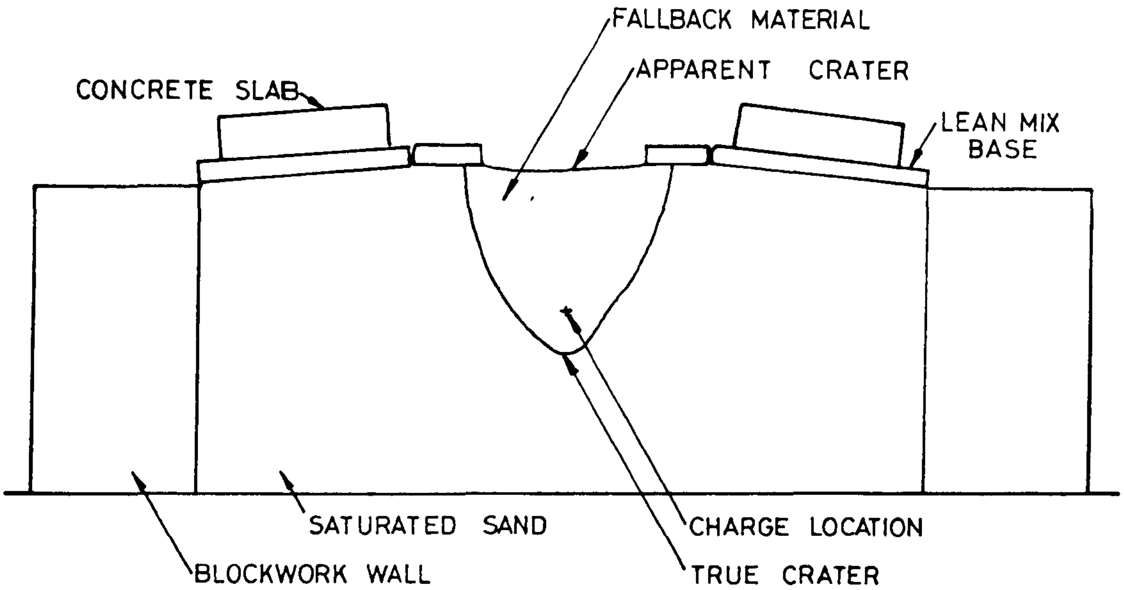

FIGURE 7.5 CRATER FORMED IN 'WET' SAND BY A 16g SUBSURFACE EXPLOSIVE CHARGE

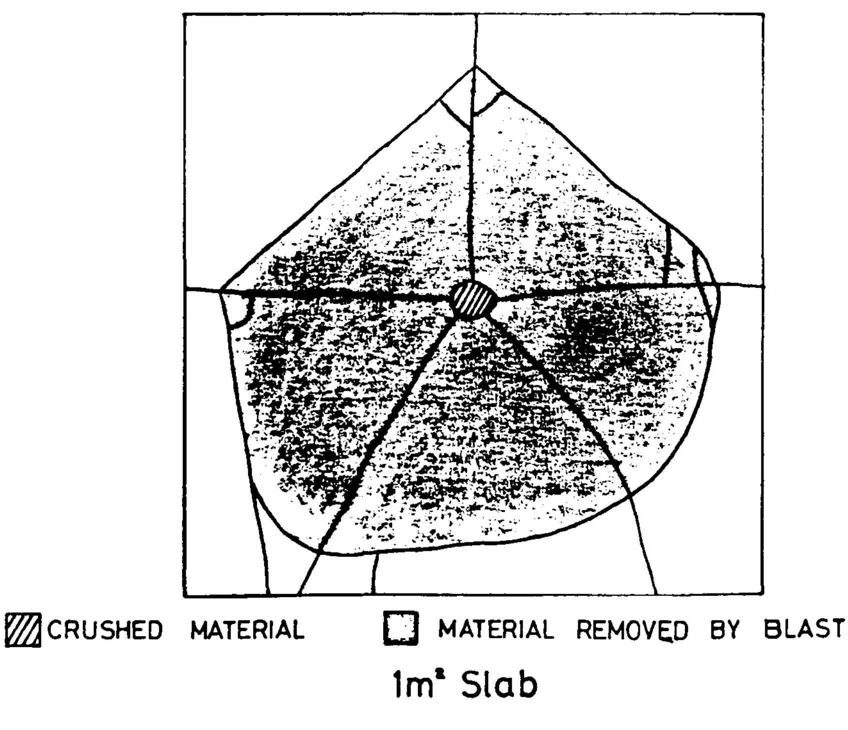

FIGURE 7.6 CRACKS FORMED IN AN UNREINFORCED SAND/GRAVEL CONCRETE SLAB BY A 16g SUBSURFACE EXPLOSIVE CHARGE IN CLAY

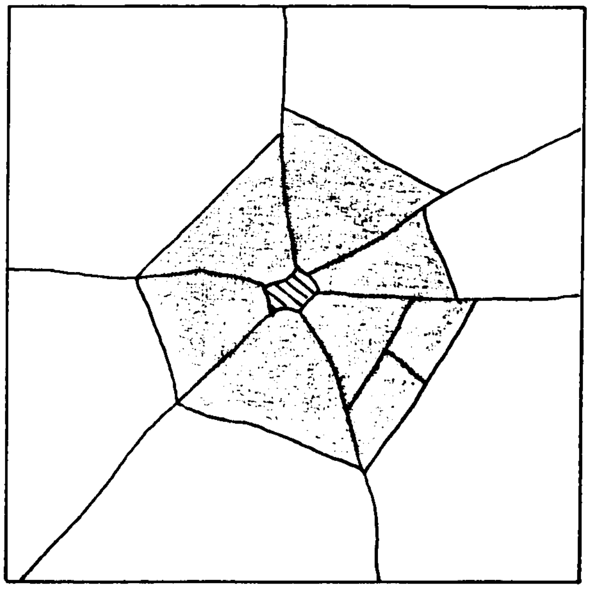

CRUSHED MATERIAL   MATERIAL REMOVED BY BLAST

$1 m^2$ Slab

FIGURE 7.7 CRACKS IN AN UNREINFORCED SAND/GRAVEL CONCRETE SLAB BY A 16g CHARGE IN 'WET' SAND

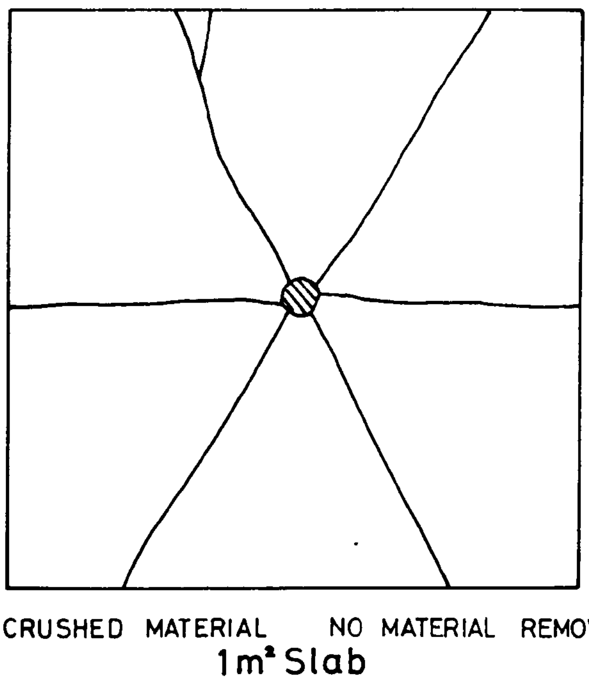

CRUSHED MATERIAL   NO MATERIAL REMOVED BY BLAST

$1 m^2$ Slab

FIGURE 7.8 CRACKS IN AN UNREINFORCED SAND/GRAVEL CONCRETE SLAB BY A 16g CHARGE IN SAND ('DAMP' OR 'DRY' SAND)

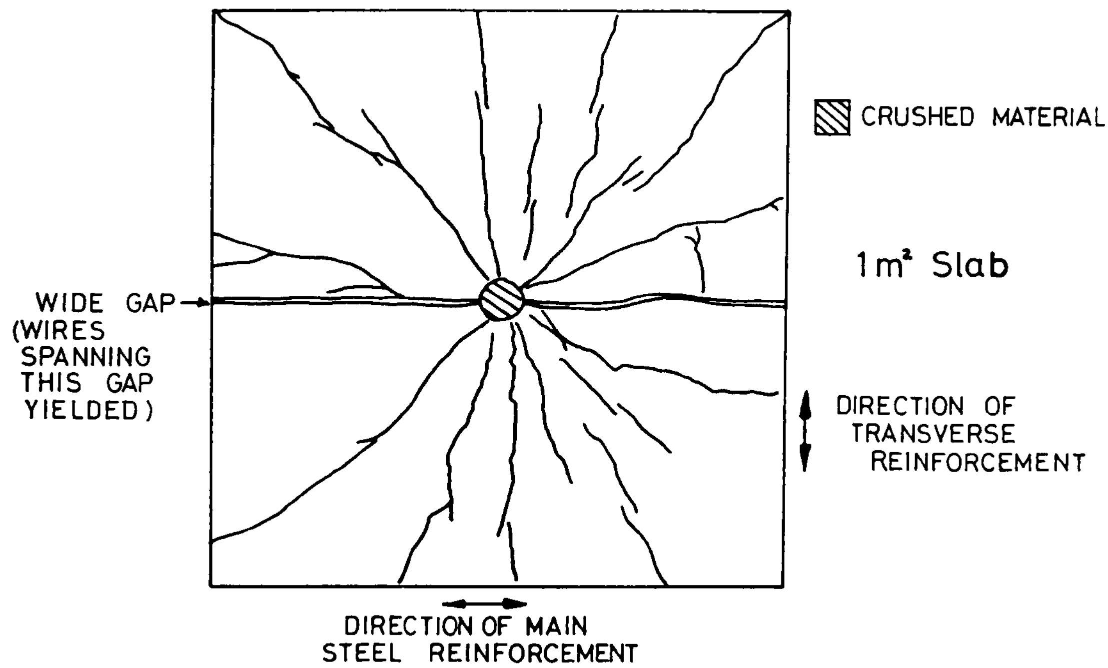

FIGURE 7.9 CRACKS IN A REINFORCED SAND/GRAVEL CONCRETE SLAB BY A 16g CHARGE IN CLAY

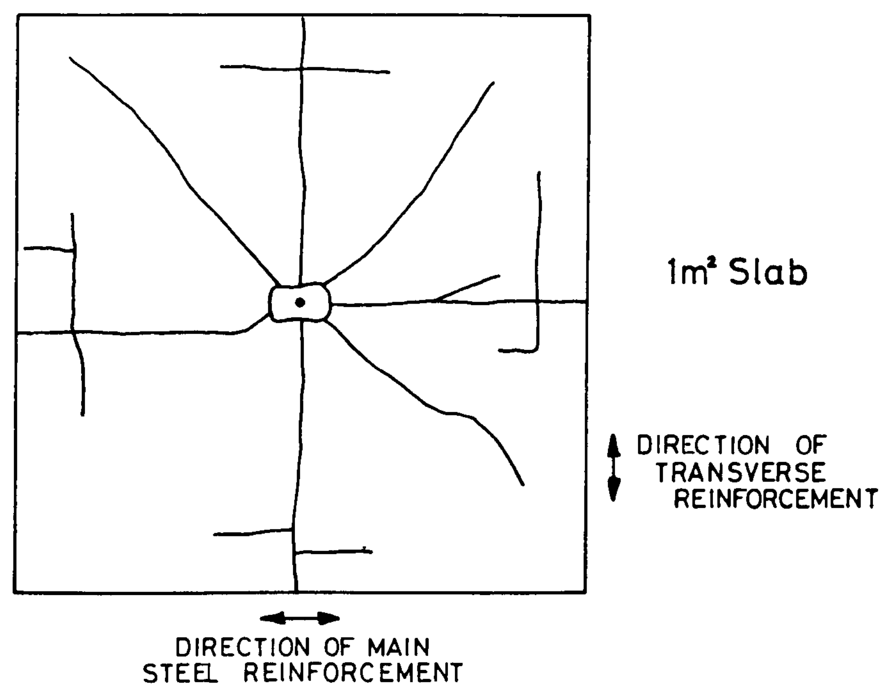

FIGURE 7.10 CRACKS IN A REINFORCED SAND/GRAVEL CONCRETE SLAB BY A 16g CHARGE IN SAND ('DAMP' OR 'DRY' SAND)

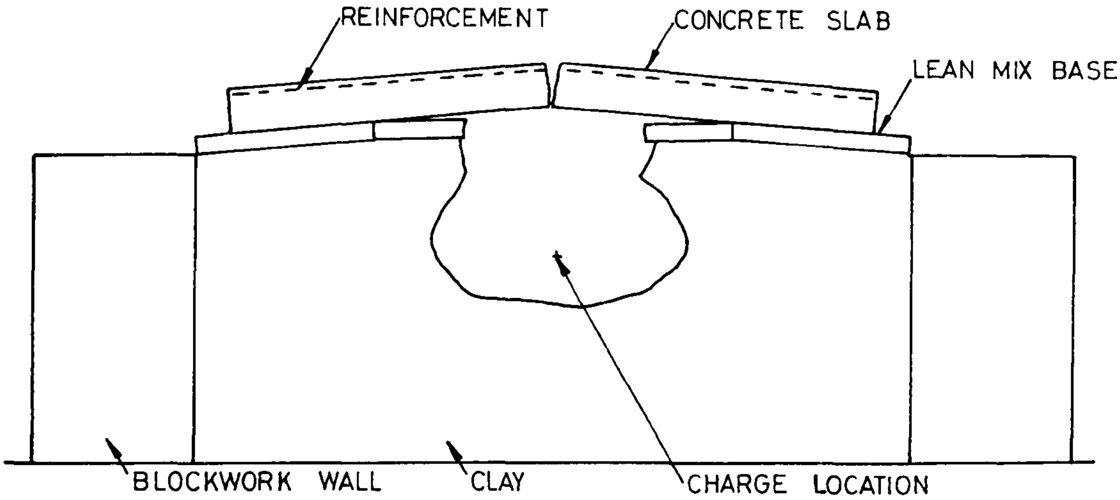

FIGURE 7.11 CRATER FORMED IN CLAY UNDER A REINFORCED CONCRETE SLAB BY A 16g EXPLOSIVE CHARGE (SUBSURFACE)

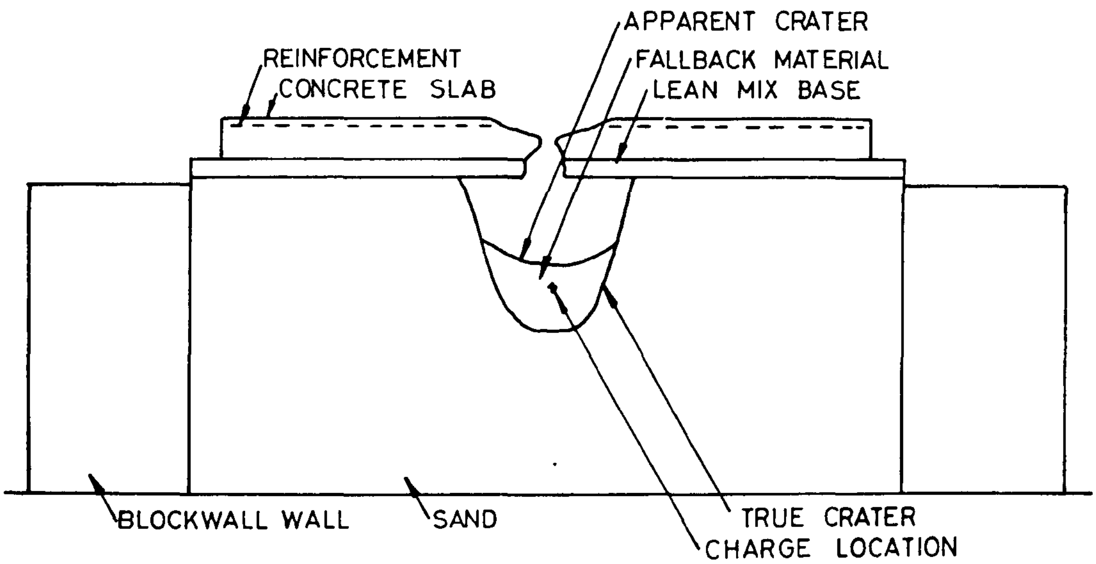

FIGURE 7.12 CRATER FORMED IN SAND UNDER A REINFORCED CONCRETE SLAB BY A 16g EXPLOSIVE CHARGE (SUBSURFACE)

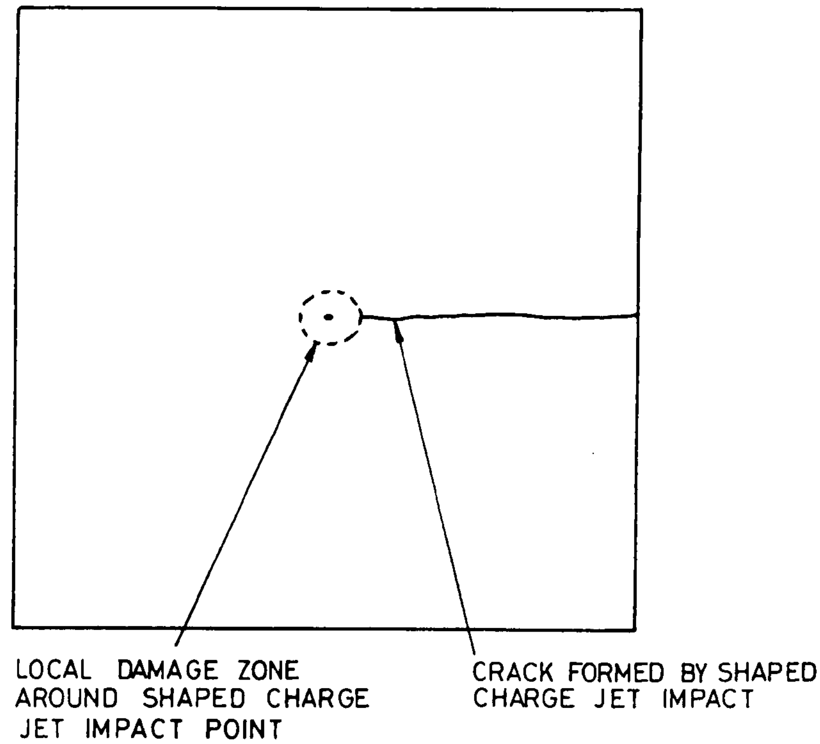

FIGURE 7.13 CRACK FORMED BY A SHAPED CHARGE JET IMPACT ON A CONCRETE SLAB

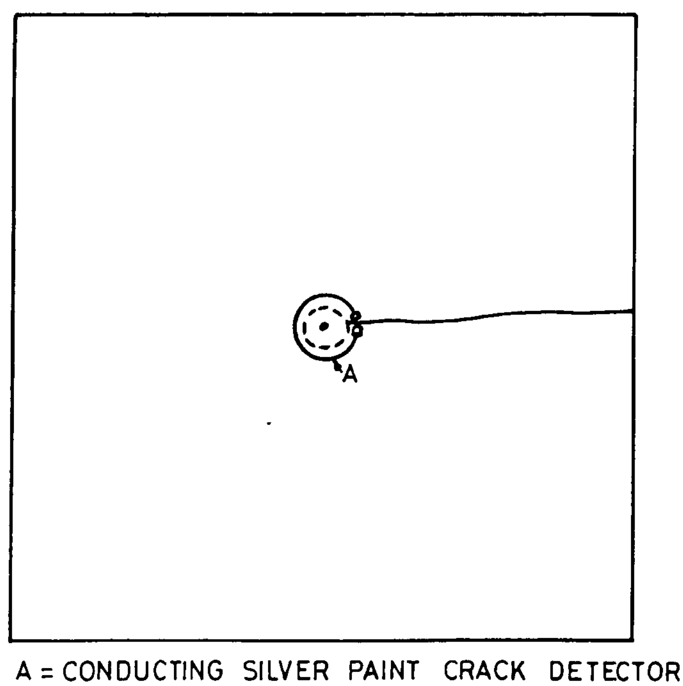

FIGURE 7.14 LOCATION OF A CRACK DETECTOR ON A CONCRETE SLAB PRIOR TO A SUBSURFACE EXPLOSION

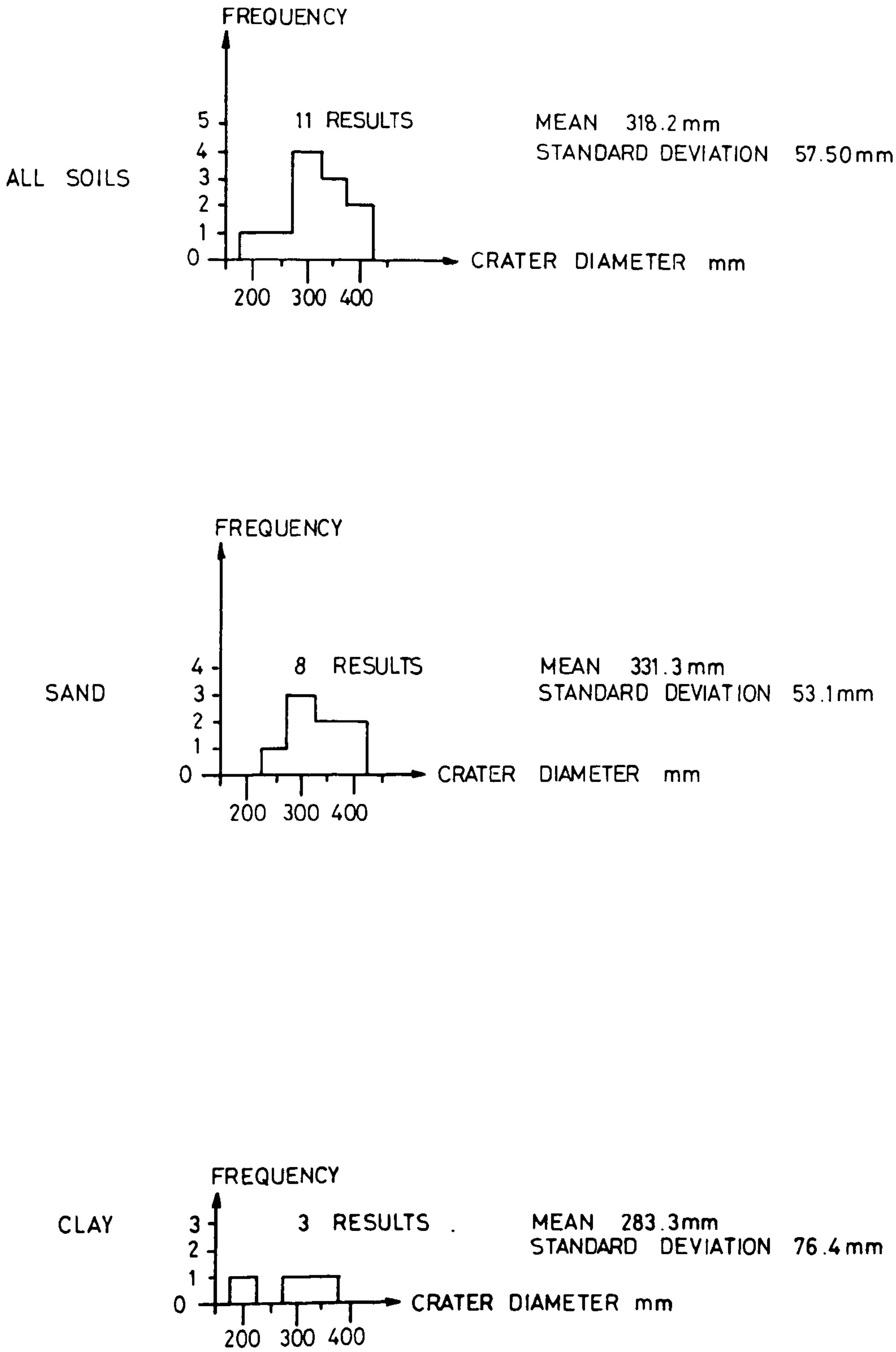

FIGURE 7.15 TRUE CRATER DIAMETER FREQUENCY IN SOILS (16g SUBSURFACE CHARGES)

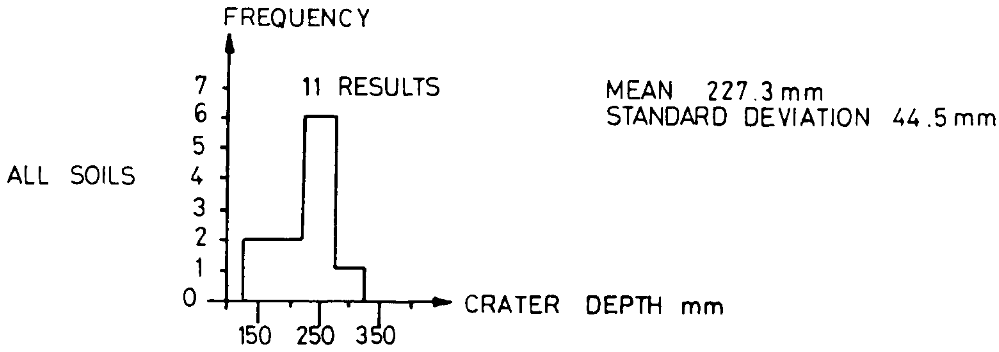

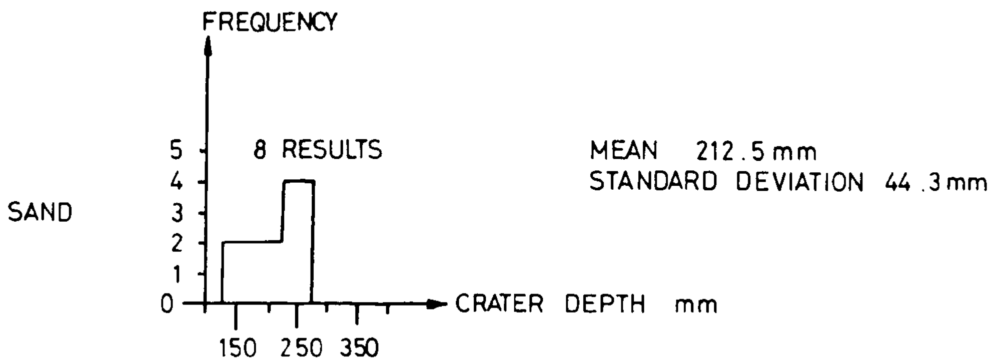

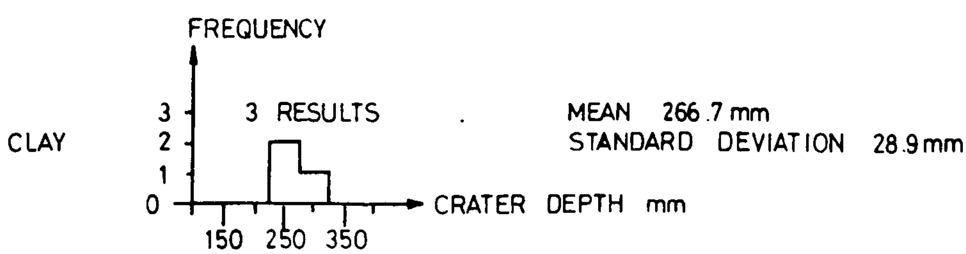

FIGURE 7.16 TRUE CRATER DEPTH FREQUENCY IN SOILS (16g SUBSURFACE CHARGES)

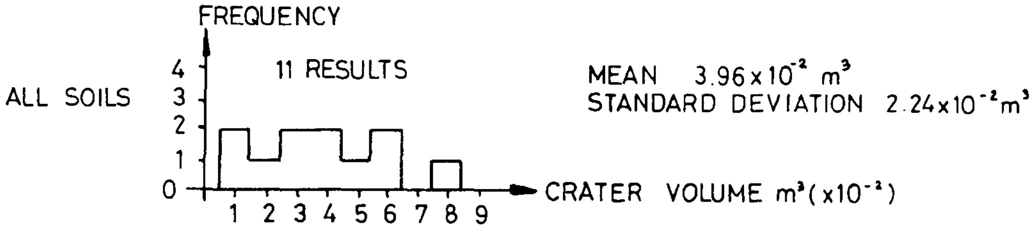

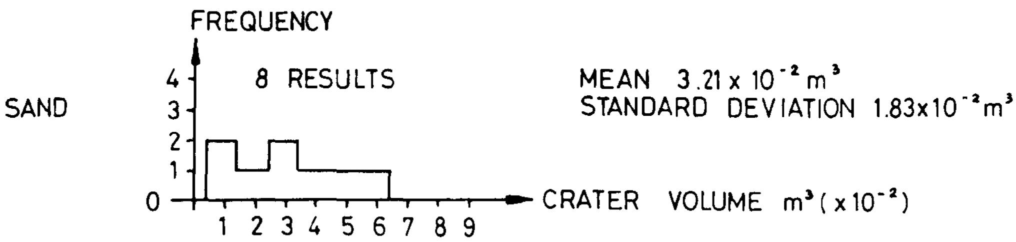

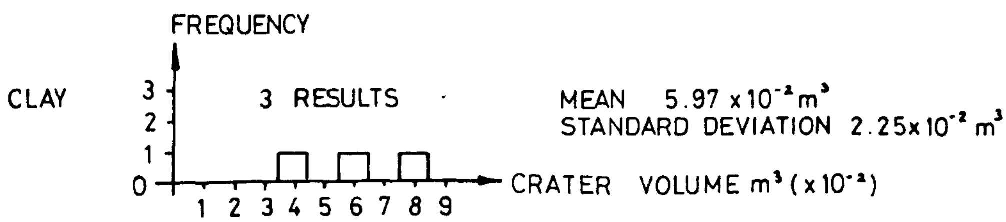

FIGURE 7.17 TRUE CRATER VOLUME FREQUENCY IN SOILS (16g SUBSURFACE CHARGES)

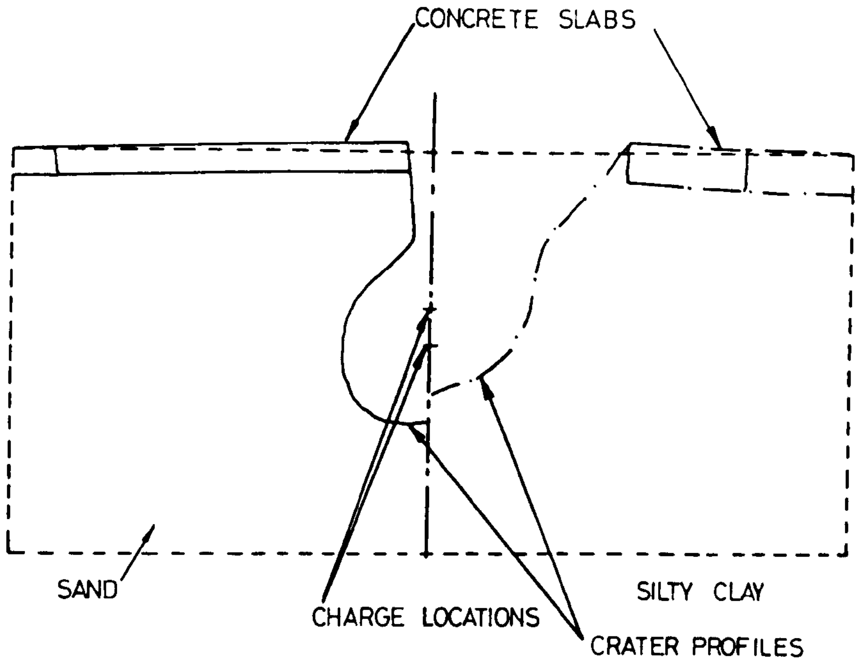

FIGURE 7.18 COMPILATION OF TYPICAL CRATERS IN SAND AND SILTY CLAY CAUSED BY SUBSURFACE EXPLOSIONS
(AFTER KVAMMEN 1973)

CHAPTER 8

CALCULATIONS

8.1 INTRODUCTION

In this chapter calculations are presented for some damage parameters, for example, the diameter of the hole produced in concrete by a high velocity metal jet. The formulae used are those developed by both the theories and the empirical wôrk reviewed in Chapter 2 and for which numerical data has been obtained.

Experimentally determined values are used in the calculations and these are compared with computed values from empirical formulae for parameters such as the diameter of a hole formed by impact of a high velocity metal jet. Values are calculated for 43g copper lined charges and equivalent data for 43g aluminium lined charges are quoted where appropriate in brackets afterwards.

8.2 SHAPED CHARGE JET PENETRTION

The hydrodynamic theory of penetration given in section 2.2.3 is tested using data obtained experimentally. Cook (1959) has provided strong experimental evidence that for ductile, mainly metallic, targets, the theory works quite well. In order to fit the theory to the penetration of concrete it was necessary to extrapolate some of the data taken from tests on metal targets to define parameters of the impact which proved physically impossible to obtain with the equipment available.

8.2.1 Assumptions

The hydrodynamic theory assumes that the target and impactor are subject to such high pressures that by comparison, their material shear strengths are negligible and thus the materials can be assumed to behave as fluids.

Penetration is assumed to continue at a uniform rate until the impactor, assumed to be a rod of uniform cross section and velocity, is worn away.

Steady state conditions are assumed to prevail throughout impact, and penetration is assumed to stop abruptly. Penetration is not assumed to be by erosion but by lateral pressure on the sides of the hole.

8.2.2 Calculation of Projectile Parameters

The jet tip speed at impact of a 43gms RDX/TNT 34mm diameter copper lined shaped charge is 5000 m/s (5000 m/s for aluminium) obtained from experiments. This has been measured by brass detector gauges described in section 4.4.2 and by high speed camera photographs, described in section 4.4.5.

The volume of a hole formed in a copper target by a high velocity copper jet was found to be 11280 mm^3.

From Johnson et al (1968) the application of Bernoulli's theorem to a projectile impact on a target can be represented by

$$\tfrac{1}{2} \lambda \rho_p \; (V_j - U)^2 \;=\; \tfrac{1}{2} \rho U^2 \qquad \ldots \; 8.1$$

where ρ_p is the projectile density

ρ is the target density

V_j is the projetile velocity

U is the speed of penetration into the target

λ is a constant which is equal to 1 for continuous projectiles and 2 for fragmented projectiles

If penetration ceases when the last part of the projectile reaches the target then the maximum penetration P' is given by

$$P' \;=\; Ut_f \;=\; \frac{Ul}{(V - U)} \;=\; l \left(\frac{\lambda \rho_p}{\rho}\right)^{\frac{1}{2}} \qquad \ldots \; 8.2$$

where l is the original length of the projectile

t_f is the time of penetration

A dimensionless factor can be introduced into the penetration equation to allow for the dynamic yield stress of the target, Y. From Johnson et al (1968) this takes the form

$$(1 - \alpha_1 (Y/ \rho_p V_j^2)) \quad \text{where } \alpha_1 \text{ is a constant}$$

In addition a factor, r, can be introduced for the residual flow of the target where this flow is taken to be the radius of the hole at the end of penetration. Total penetration P is therefore the maximum penetration of the jet plus residual flow by the impacted material. Thus

$$P = P' (1 - \alpha_1 \frac{Y}{\rho_p V_j^2}) + r \qquad \ldots 8.3$$

Substituting σ_t in equation 8.1 for $\lambda\rho_p$ and adding a factor $\gamma\rho_1$ where ρ_1 is the density of the projectile particles and where γ is a statistical factor to account for wavering of the jet, equation 8.1 becomes

$$\tfrac{1}{2} \gamma\rho_1 (V - U)^2 = \tfrac{1}{2} \rho U^2 + \sigma \qquad \ldots 8.4$$

where σ is taken to be the difference between the yield strength of the target (σ_t) and the projectile (σ_p) $= \sigma_t - \sigma_p$.

From Johnson et al (1968) a term k can be introduced to account for target strength such that

$$\tfrac{1}{2} \rho_1 (V_j - U)^2 = \tfrac{1}{2}\rho U^2 + k \qquad \ldots 8.5$$

k is defined by the pressure produced by the projectile when the penetration velocity , U = 0 and in concretes this has been calculated in section 8.4 as being 88 to 438 times the value of σ_t.

Therefore $k = \frac{1}{2} \rho_p V_j^2$

From Cook (1958).

It has been shown by Johnson et al (1968) that the cross section area, A', of a hole produced by a projectile of area A_o is given by:

$$A' = \frac{A_o}{\sigma_t} \frac{1}{2} \gamma \rho_p (V_j - U)^2 \qquad \text{... 8.6}$$

It is assumed that A' is constant but experiments show this is not the case.

From penetration P' and an assumed constant hole A' the volume of the hole V_t is

$$V_t = P'A' \qquad \text{... 8.7}$$

For a simple projectile mass m_p, $\lambda = 1$ and of the same material as the target then

$$V_t = \frac{V_p V_j^2}{8\sigma_t} = \frac{m_p V_j^2}{8\sigma_t} \qquad \text{... 8.8}$$

where V_t = hole volume

m_p = mass of projectile

V_p = volume of projectile

V_j = velocity of projectile

σ_c = target strength (static)

Substituting experimental values for V_t and V_j with copper as the jet and target gives:

$$11.28 = \frac{m_p (5 \times 10^5)^2}{8 \times 2.17 \times 10^9}$$

The copper projectile's mass, m_p = 0.76 gms (0.38g for aluminium).

m_p is the mass of the jet, not the mass of the complete liner.

From Johnson (1968) the ratio of the hole diameter D to the projectile diameter d_j is given by:

$$\frac{D}{d_j} = V_j \left(\frac{\rho_t}{8\sigma_t}\right)^{1/2} = 0.35 \sqrt{\frac{\rho_t}{\sigma_t}} \qquad \ldots 8.9$$

where V_j = velocity of projectile

ρ_t = density of target

σ_t = target strength (static)

D = hole diameter

d_j = diameter of projectile

Substituting values for copper gives:

Diameter ratio D/d_j = 11.24 (D/d_j for aluminium = 16.7)

Now D = 13mm for copper by experiment

Therefore the diameter of the projectile i.e. the jet = 1.16mm

(d_j for aluminium = 1.4mm)

Now the volume of material in the jet = $m_p \rho_p$

= $0.76 \times 8.93 \times 10^3$ mm^3

This would produce a jet of length 80.1mm assuming no elongation, no change in density and that each part of the jet had constant diameter and velocity (see section 8.2.1). (For aluminium jet length = 75mm).

Comparing this result with tests on EN28 steel and using the equations given by Cook (1959)

where D = hole diameter

σ = specimen strength (static)

ρ = density

and the subscripts c, j and s refer to concrete, the jet (copper) and steel respectively.

$$\frac{Ds}{Dc} = \left(\frac{\sigma c}{\sigma s}\right)^{\frac{1}{2}} \left[\frac{\rho_c^{\frac{1}{2}} + \rho_j^{\frac{1}{2}}}{\rho_s^{\frac{1}{2}} + \rho_j^{\frac{1}{2}}}\right] \qquad \ldots 8.10$$

$$\frac{Ds}{Dc} = \left(\frac{217}{1162}\right)^{\frac{1}{2}} \left[\frac{8.93^{\frac{1}{2}} + 8.93^{\frac{1}{2}}}{7.83^{\frac{1}{2}} + 8.93^{\frac{1}{2}}}\right]$$

$$\frac{Ds}{Dc} = 0.43$$

Hole diameter in concrete Dc = 13mm.

Therefore from the equation Ds should be 5.6mm.

Experiments show that the hole diameter in EN28 steel Ds lies between 5 and 6.5mm.

8.2.3 Comparison with Penetration of the Copper Jet into Mild Steel

Mild steel has a static yield strength of about 33% of the static yield stength of EN28 steel.

From 8.10, for mild steel the diameter ratio $\frac{D_{Ms}}{Dc} = 0.77$

where D_{Ms} and Dc are the diameters of the holes in mild steel and concrete respectively.

This gives a hole diameter for a copper jet in mild steel of 10mm which agrees with the value of 9.4mm found experimentally.

8.2.4 Comparison with Penetration of the Copper Jet into 'Plasticine'

'Plasticine' is a proprietary modelling clay of extremely low strength. Data for the material is quoted from Johnson (1968).

$$\text{From 8.10, } \frac{Dp}{Dc} = \left(\frac{217}{0.1}\right)^{\frac{1}{2}} \left(\frac{8.93^{\frac{1}{2}} + 8.93^{\frac{1}{2}}}{8.93^{\frac{1}{2}} + 1.98^{\frac{1}{2}}}\right)$$

From which the hole diameter in plasticine, Dp, is 842mm which is ten times greater than found experimentally. In order to obtain a value of 6.2 for Dp/Dc as found experimentally, the static strength of 'Plasticine' would need to be 10.4 N/mm^2 or approximately 100 times more than it is. Since static strength has been used in metallic target predictions, it is clearly inadmissible with 'Plasticine'.

8.2.5 Comparison with Penetration of the Copper Jet into Concrete

From equation 8.10, table 8.1 has been prepared comparing experimental results and calculated predictions for the diameter of holes caused by copper jet impacts on concretes of variable strength and density. An equivalent table 8.2, has been calculated for the predictions of the diameter of holes caused by aluminium jet impacts on concretes.

From table 8.1 it can be see that for the prediction of hole diameter caused by the copper jet impact to be accurate, the concrete would have to be between 6 and 12 times stronger in terms of its static cube crushing strength. For aluminium jet impacts the concrete would have to be between 5 and 13 times stronger in terms of its static cube crushing strength. Crushing strength is measured under uniaxial loading conditions whereas concrete loaded by the shaped charge jet is under triaxial compression. This may account for some of the apparent increase in the strength of the concrete in the test specimen.

8.2.6 Calculation of the Copper Jet Length from Geometry Considerations

From Johnson (1972) the velocity of the jet V_j can be computed in terms of the explosion detonation velocity $\dot{U}_D$, the initial angle of the liner apex 2α and the varying angle of the collapsing liner such that:

$$V_j = 2U_D . \frac{\sin\left(\frac{\overline{\beta-\alpha}}{2}\right)\cos\frac{\alpha}{2}}{\sin\frac{\beta}{2}\ \cos\alpha} \qquad \text{(Chapter 2, equation 2.9)}$$

From experiments V_j = 5000 m/s

From the textbook of explosives of the Procurement Executive (1970)

U_D = 7850 m/s

α = 42.5° fixed by charge design

Therefore from 2.9 β = 56.86°

From Johnson (1972) the jet length can be expressed is terms of the angles α and β, and the geometry of the cone.

If h is the distance from the top of the main charge to the base of the main charge (excluding the initiator and booster components) then using

$$L_j = h\,(1 + \tan\alpha \;.\; \tan \overline{\underline{\beta+\alpha}}\,) \quad \text{(Chapter 2, equation 2.11)}$$

the jet length L_j = 78mm (cf. 80.1mm for copper and 75mm for aluminium in section 8.2.2)

High speed photography has indicated the jet length in experiments to be of this order. The actual jet is not visible on the photographs due to the surrounding gas cloud. The length of the cloud provides the data since the cloud appears to travel at the same speed as the jet. The mass ratio of the jet to the slug, m_j/m_s does not agree with the value quoted in section 8.2.2.

From Johnson (1972) the mass ratio m_j/m_s is given by

$$\frac{m_j}{m_s} = \tan\left(\frac{\beta}{2}\right)^2 \qquad \text{... 8.11}$$

For the angle β = 56.86°

$$\frac{m_j}{m_s} = 0.293$$

and for a total liner mass of 12.79g this gives of jet mass of 2.9g (cf. section 8.2.2)

8.2.7 Calculation of the Jet Length from Target and Jet Density Considerations

From Johnson (1972) $$\frac{P}{L_j} = \sqrt{\frac{\rho_j}{\rho_t}} \qquad \text{... 8.12}$$

where P = penetration

L_j = jet length

ρ_j = jet density

ρ_t = target density

If $\rho j = \rho t$ then $P = L_j$

From experiment P = 85mm

Hence the jet length l = 85mm (cf. sections 8.2.2, 8.2.3)

8.3 PENETRATION FORMULAE APPLIED TO CONCRETE

Experiments have shown a large range of penetration depths for a given aggregate. Two formulae are often quoted for penetration predictions, equation 2.14 and 2.65 (Briggs' formula)

From equation 2.14 for jet lengths of 80mm and 85mm table 8.3 can be compiled.

Briggs (1974) empirical formula which is only stated as accurate to ± 20% is:

$$P = 0.177W_{cm}^{0.43} \qquad \text{... 8.13}$$

where P is the penetration depth in m and

W_{cm} is the charge mass in kg.

In the case of the 43g charges used in this study penetration, P, would be 123mm.

Experiments in this study have given values from 98mm to 148mm for penetration by copper jet and 104 to 160mm for aluminium jets. These lie between 20% and +33% of the value and are roughly in the right proportion to Briggs' estimate of limits.

8.4 CALCULATION OF THE PRESSURE GENERATED ON THE SPECIMEN DURING IMPACT OF A HIGH VELOCITY COPPER JET

According to Johnson (1968) the pressure generated in the target during impact can be expressed by Bernoulli's theorem. That is the pressure on both sides of a stationary interface must be equal.

Therefore pressure $p_r = \frac{1}{2}\rho j\ (V - U)^2 = \frac{1}{2}\rho t\ U^2$ ... 8.12

where ρj is the jet density

ρt is the target density

V_j = jet velocity

U = penetration velocity

For a jet and target of the same material, from 8.12

$$p_r = \rho \frac{V_j^2}{8} \qquad \text{... 8.13}$$

For a copper jet impacting a copper target

$p_r = 2.79 \times 10^4\ N/mm^2$

From 8.1 for a copper jet impact on concrete the penetration velocity U can be computed as 3345 m/s which approximates to experimentally obtained values in this study. (cf. Figure 6.2).

The pressure, p_r, generated in the hole of a concrete target at a penetration rate of 3345 m/s is given by 8.12.

$p_r = 1.315 \times 10^4\ N/mm^2$

Assuming the rear of the jet slows to a velocity of 1500 m/s at impact then the pressure in the target would still be $2.64 \times 10^3\ N/mm^2$.

Table 8.1

Predictions of Copper Lined Shaped Charge Jet

Impact Parameters from Equation 8.10

Aggregate	Concrete Density kg/m^3	Cube Crushing Strength		Hole diameter	
		Actual N/mm^2	Predicted N/mm^2 (From actual hole diameter)	Actual mm	Predicted (From actual strength) mm
'LYTAG'	1700	30	362	14	52.2
	1700	45	362	14	42.7
	1700	60	362	14	36.9
SAND/GRAVEL	2350	30	284	15	53.3
LIMESTONE	2350	45	284	15	43.5
BASALT	2350	60	284	15	37.7
BARYTES	3400	30	334	13	43.3
	3400	45	334	13	36.0
	3400	60	334	13	30.7

Table 8.2

Predictions of Aluminium Lined Shaped Charge Jet

Impact Parameters from Equation 8.10

Aggregate	Concrete Density kg/m^3	Cube Crushing Strength		Hole diameter	
		Actual N/mm^2	Predicted N/mm^2 (From actual hole diameter)	Actual mm	Predicted (From actual strength) mm
'LYTAG'	1700	30	394	22	79.8
	1700	45	394	22	65.1
	1700	60	394	22	56.4
SAND/GRAVEL	2350	30	315	23	74.5
BASALT	2350	45	315	23	60.7
LIMESTONE	2350	60	315	23	52.8

Table 8.3

Predicted Shaped Charge Jet Penetration

from Equation 2.14

Aggregate	Density of Concrete kg/m^3	Predicted penetration Distance mm
'LYTAG'	1700	184 - 195
SAND/GRAVEL LIMESTONE	2350	156 - 166
BARYTES	2300	130 - 138

CHAPTER 9

GENERAL DISCUSSION, CONCLUSIONS, LIMITATIONS AND RECOMMENDATIONS FOR FUTURE WORK

9.1 GENERAL DISCUSSION

9.1.1 Shaped Charge Jet Impact on Concrete

Impact of shaped charge jets caused two types of damage in concrete test specimens. These two types of damage were (i) local damage, that is the hole formed at the impact point and (ii) gross damage which included the cracking and sometimes the break up of the test specimen. While these two types of damage were clearly defined, the formation of each was linked by the stress pulses caused by the impact on the test specimen.

The magnitudes of stress pulses obtained show that the stresses were attenuated very quickly through the specimens. See tables 6.4, 6.5 and 6.6. Even so the values were so much in excess of the static compressive, tensile in bending and indirect tensile strengths listed in table 3.13 that the material should have failed. The rate and duration of the dynamic loading as given in tables 6.2 and 6.3 may be the reason that the material could accommodate such stresses without damage or it may be the quasi-static calibration of the strain gauges which was erroneous. Further investigation is required at a more fundamental level before this situation can be resolved.

9.1.2 Local Damage to Concrete Caused by Shaped Charge Jet Impact

In ductile materials such as metals a shaped charge jet impact produces a hole by lateral expansion of material together with a lip of material around the edge of the hole as shown in figure 9.1.

Further evidence of the mechanism of hole formation was found in tests where the shaped charge jet penetrated 'plasticine'. In this case the 'plasticine' layers exhibited no evidence of scouring action or vertical movement of material. See figure 6.33. Thus the hole in the 'plasticine' could only have been formed by lateral pressure.

The shape of the hole formed by a jet impact in concrete is shown in figure 6.18. Generally it consisted of an upper conic section, sometimes modified by the jet or slug erring off line, a roughly parallel sided section and a final portion which tapered until the limit of penetration was reached. Penetration varied but the lateral dimensions remained approximately constant over a range of concrete crushing strengths (10 - 70 N/mm^2) and densities (1700 - 3400 kg/m^3). See tables 5.2 to 5.11.

The generally held theory of jet penetration in ductile materials is that the jet scours out the hole as shown in figure 9.2, and has been described by Johnson (1972). However evidence found in this study suggested that the hole in the test specimen was largely due to crushing of the material and cavity expansion caused by the very high pressure generated in the hole by the jet. This pressure was calculated in section 8.4. Electron microscope photographs of the upper conic area, plates 9.1, 9.2 and 9.3, show no evidence of scour, only shearing and cracking. Horizontal striations shown in figure 9.3 in the conic section of the hole also indicate that some form of lateral shearing action was taking place. The spall time of 26µs for a piece of concrete 15mm from the impact and at the test block surface would be correct if shearing were the cause. Also this time, taken from table 6.9, is greater than the time taken for the whole of the shaped charge jet to impact. Thus scouring could not be the cause since this would only take approximately 10μs based on an experimentally found jet penetration rate in concrete of 3.5mm/μs taken from figure 6.2. Further evidence of shearing was found in high speed photographs, plate 6.2, showing lateral movement of material under shaped charge jet impact. Here the time lag between passage of the jet and material movement was 15μs to 25μs.

The method of formation of the upper conic section of the shaped charge hole in concrete is thought to be as shown in figures 9.4a and b,and 9.5a and b. In figure 9.4a the jet exerts a radial pressure on particles A and B. The stress condition set up is shown in figure 9.4b and the crack initiated. This pressure continues on particle C and as the jet penetrates into the block on particle B. The penetration continues with every particle cracking in the same fashion as particle A except that as penetration increases and the radius of the cracked particles widens, some particles at the extreme edges, for example, particle D in figure 9.5a, will also have some shear resistance. This is shown in figure 9.5b and is due to adjacent particles not being fully removed by the cracking. Hence the angle of cracking will be inclined and a conic shaped depression formed as shown in figure 9.5a. At some point in the penetration the resistance to shearing will be sufficient to cause no further loss of material and a parallel hole will form.

Evidence of this is crushed material found adhering to the sides of the parallel section of the hole and the intact aggregate particles protruding from the boundary surface. These particles showed no signs of scour or of being sheared vertically. Aggregate fractures were however found in the upper conic section of the hole.

The parallel sided hole was thought to be formed by either the influence of the plastic stress wave generated by the impact or the limit of crushing caused by the pressure generated in the hole by the impact. Intact aggregate particles on the boundary surface of the hole would support the pressure theory. High speed photography of the passage of a jet 15mm inside a concrete specimen showed movement of concrete material to take place 5 to 21μs after passage of the jet tip. The shock wave would have reached the point visible by the camera, 15mm from the axis of the jet, much quicker than this time, so movement due to internal pressure would appear to be indicated. This time is similar to the surface spall time of 26μs for 15mm distance.

The surfaces of test specimens remote from the jet impact but perforated by the jet showed evidence of shearing and crushing of material into the joint between the test specimen and its foundation. A cone was formed in the lower surface but it was smaller and was filled with crushed debris. Since it had no free air surface, the lower surface would have had some resistance to shear and hence a restraining effect on the lateral pressure caused by the penetrating jet. Theoretically there should have been some spalling due to tensile stresses reflected from the incident compression wave at the lower surface of a test specimen. The detection of this was extremely difficult in practice since the jet penetrated at or near the longitudinal wave velocity, usually quoted for concrete as 3.5mm/μs, and so arrived at the surface very soon after the compression wave. The local penetration effects by the jet would then have masked any tensile scabbing effects though these would contribute to the lower surface conic section by introducing tensile forces at right angles to the radial compression forces. This would have the effect of magnifying any Poisson's ratio effect.

Where shaped charge jets perforated a concrete slab and entered sand soil they crushed the sand particles. The crushed sand and a reddish brown deposit of copper or aluminium were left on the sides of the hole in the sand. In clays only the reddish deposit was found adhering to the sides of the hole since clay particles where initially much finer than sand particles and hence crushing was not detectable.

9.1.3 Gross Damage Caused to Test Specimens by Shaped Charge Jet Impact

Major damage in concrete blocks and slabs caused by a shaped charge jet impact consisted of cracking as shown in figures 9.6 and 9.7 for blocks and slabs respectively. This cracking could be considered as being of four separate types, radial cracking, secondary radial cracking, cracks due to reflected tensile pulses and corner cracking. The locations of these cracks are shown on figures 9.6 and 9.7 and the number of cracks are given in tables 5.2 to 5.6.

Main radial cracks were found to be propagated inwards from the edge of the slab. The time of initiation of the crack was longer than the combined time for the shaped charge jet to penetrate the test specimen plus the time taken for the compressive stress pulse to travel from the impact zone to the edge of the slab. These values are given in tables 6.7 and 6.8. There are several theories for the formation of this crack and the solution may be a combination of these. After the passage of the compression pulse, a tensile shear wave followed at half the compressive wave speed. In addition Poisson's ratio effects could also have occurred. When the compressive wave reached the boundary of the test specimen, it was reflected as a tensile wave into an already tensile stressed area as shown in figure 9.8. Crack velocities were found to vary and crack initiation times had a wide distribution but the general crack initiation times and velocities of propagation were consistent with the theories given above.

The secondary radial cracks were found to travel outwards from the centre of the test specimen after the main radial cracking was complete. The formation of these cracks was thought to be due to a secondary stress field set up in each of the new segments of the test specimen formed by the radial cracks. Figure 9.9 shows such a segment in which the reflected tensile waves caused by reflection of the original compressive stress pulse have themselves been reflected at crack boundaries as compression pulses. Since the original tensile stress field had only been partially relieved by cracking and the moving of segments of the test specimen as shown in figure 9.8, the resultant stress field in a segment would be as shown in figure 9.9. Furthermore, due to relative velocities of stress waves, the maximum effect would be at the corner of the segment nearer the impact point. Since the waves were being attenuated by repeated passage through the concrete their effect would diminish and hence the crack would propagate out towards a corner but might not reach it. Rhinehart (1960b) predicted that such a crack should start somewhere along the diagonal and then that it should propagate possibly in both directions along the diagonal. Unpublished high speed photography by the author and others at Sheffield University of an explosive charge detonated on a mortar block supports this prediction.

Reflected compressive waves caused the third and fourth types of cracking found. These are the reflected tensile pulse cracks and corner cracks. These are really the same crack and were caused by a compressive pulse being reflected at a boundary as a tensile pulse. When the tension was greater than the incident compression plus the tensile strength of the concrete, the concrete cracked parallel to the side of the specimen. This was clearly described by Johnson (1972) (p. 18).

Corner cracks as shown in figure 9.7, were formed in a similar fashion to reflected tensile pulse cracks but in this case interference of reflected pulses at adjacent boundaries, as shown in figure 9.8 caused the cracking. The trapped momentum in the piece of test specimen broken off at the corner by the crack caused it to move away from the test specimen. Trapped momentum is also fully described by Johnson (1972) (p. 58).

9.1.4 Other Observations of Shaped Charge Jet Impact Damage to Concrete Specimens

Tests were performed on concrete slabs with light steel mesh reinforcement in the form of a grid with 12g wires at 20mm centres one way and 16g wires at 40mm the other way at a distance of 10mm from the impact face. See table 4.1. Results given in table 5.2 showed that no measurable difference in penetration occurred, within the wide scatter of results, when compared with unreinforced slabs. The reinforcement was included near the upper surface as shown in figure 3.2 because in prototype slabs, figure 3.1, it provides resistance against non-structural cracking. However, the crack patterns produced by the jet impact were similar in location and crack width to those in unreinforced slabs. See figure 6.9. Electron microscopy of the reinforced slabs, plate 9.4, has revealed no evidence of debonding or perferential cracking along steel/concrete boundaries.

Those steel wires actually hit by the jet were cut and bent back locally. In the upper conic part of the hole the wires were debonded locally since the concrete had sheared in this region. Previous workers, for example Pack and Evans (1951), have stated that penetration is not seriously affected by reinforcement providing not too many bars are encountered by the jet and this also seems to hold true for scaled concrete according to the results given in table 5.2.

Most model tests were performed with normal incidence impacts by the shaped charge jets but several were at 60° to the horizontal. See table 4.1. These tests have shown similarity with full scale tests by Watson et al (1983) which indicates that the similarity is more than coincidental. The most noticeable feature was flaring of the upper section of the hole.

The similarities between full and scaled charge holes extended to the upper conic, the transition and the parallel hole regions. These appeared to correspond,for example the overall diameter ratio was 440 : 100 which is equivalent to 4.4 to 1 and the transition zone depth was 180 : 30 equivalent to 6 to 1 (Scale ratio was 5 : 1). Reinforcement in full and scale tests was cut in a similar fashion when encountered by a shaped charge jet.

9.2 SUBSURFACE EXPLOSIVE SHOCK TESTS

Subsurface explosive charge effects are very dependent on the charge mass and its depth of burial. For this reason it was difficult to compare results with the results of other workers since the respective tests did not usually scale either in depth of burial or charge mass. In this study comparisons have been made with the work of Kvammen (1973) but here the charge masses were not too well scaled. A true comparison test has been made at one third scale to test the scaling laws employed in this study.

Kvammen (1973) described three types of crater which could be formed by explosive charges in soils under pavements. These were the shallow type, the deep type and the camouflet, and are shown in figure 2.17.

In this study only the shallow type crater was obtained because of the influence of burial depth quoted above. Some apparent camouflet action has been found in sands but this is because the charge was not powerful enough to cause punching shear failure in the slab which remained in position, though fractured and heaved. See figure 7.2. True camouflet action was also not achieved in clays. In this case the polythene separation layer between the lean mix and pavement slabs tended to prohibit clay being removed from the crater by the blast. Instead a false roof to the crater was left, formed from clay, the slab and lean mix having been punched out locally. This can be seen in figure 7.4.

The most important feature of cratering in sands was the influence of the degree of saturation. A low degree of saturation, did not cause punching out of a section of the pavement over the crater. The likelihood of this occurring required a greater degree of saturation of around 60%. Figures 7.2 and 7.5 show respectively the influence of 'dry' and 'wet' sand.

Unreinforced slabs had extensive radial cracking and separation of pieces as shown in figure 7.8 but reinforced slabs as shown in figure 7.10 were kept in one piece by the action of the reinforcement.

There was a small vertical movement of the slab around the crater zone caused by a wedge of sand being driven by the explosion into the joint between the lean mix and the sand foundation. The wedge effect could clearly be seen in the shear planes which developed both in the one fifth scale and one third scale models. Figure 7.2 shows the shear planes in the one fifth scale test.

Fallback material in sand craters was much greater than in clay and did not depend directly on the moisture content. It consisted of loose material from the collapsed roof of the expanded crater and generally filled about 80% of the true crater.

Craters in clay were roughly spherical cavities caused by expansion of the explosion gases. See figures 7.4 and 7.11. Local material movement in the soil was not as great as for sands but the blast wave substantially cracked the concrete pavement and, in the case of unreinforced concrete slabs caused large separation of the pieces. The clay roof of the crater did not usually collapse nor was it projected out of the crater with the slab and lean mix layers. Wedge action by soil material under the pavement did occur locally to a limited extent and resulted in a well defined shear plane as shown in Figure 7.4.

The subsurface charge was generally located down a hole formed explosively or pre-formed during construction of the test slab. See figure 4.14. There appeared to be no difference in subsequent cracking or separation of material between identical pavements whether the hole had been drilled or explosively formed.

Tests were performed on two uncrusted subsoils, that is without a concrete pavement, but with an equivalent surcharge weight of soil equal to the weight of a pavement construction. The charges were buried at a depth calculated to take into account the equivalent surcharge density and thickness so that direct comparisons could be made with crusted subsoil tests, that is those with a concrete pavement.

The results showed that the concrete slab was much more than just a surcharge load and, depending on soil moisture conditions, there was a fundamental difference in crater shape formed by shallow explosions in crusted and uncrusted soils. Figures 7.1 and 7.2 show the craters in uncrusted and crusted sand while figures 7.3 and 7.4 show respectively the craters in uncrusted and crusted clay.

Reports of similar cratering experiments at larger scales are few and the explosive details are not compatible. However, the results do in general agree qualitatively which tends to suggest that full scale results would also agree quantitatively as far as crater dimensions are concerned.

Undoubtedly certain scaling effects did have a large influence on the final damage characteristics of the subsurface explosive attack. Gravity cannot be scaled and nor can time in the scale model experiments. Gravity dependent features such as heave and debris flight paths in the one third and one fifth scale tests could therefore not scale with full scale results.

9.3 LIMITATIONS

Scaling down explosive devices to the size used in this study could have lead to experimental errors simply because of machining tolerances and detonation limitations. Quality control of the construction of the cased shaped charges by X-rays and flash radiography of a sample of two shaped charge jets in operation, confirmed results obtained by other means.

Equipment specifications created problems of accurate measurement at very high rates of loading when events lasted only a few microseconds. Rise times, sampling rates and camera interframe times lead to cumulative errors of up to 20% when timing the duration of some short events in unfavourable conditions. Electronic components had significant response times in the microsecond measuring range, especially in circuits requiring voltage discharge or signal splitting.

The hazardous testing environment resulted in the need for remote control of charge firing. This tended to complicate instrumentation in particular since once the firing circuit was armed,personnel were not allowed to approach the test specimen to reset or adjust nearby equipment. For example, if capacitor circuits discharged too quickly due to dampness any delay in conducting the test could result in the circuits losing too much charge to be of use. Similar problems occurred from time to time with strain gauge circuits heating up and drifting out of balance when kept energised for too long before the test. If such problems occurred with the instrumentation it was necessary to render the firing system safe,that is electrically dead, before resetting the instrumentation. For this reason tests had to be conducted as quickly as possible between setting instrumentation and firing the charge to minimise instrumentation drift and the need to repeatedly arm the firing system.

This problem was aggravated by another major limitation in this study which was the problem of reproducing exactly all features of a test specimen. The relatively large test specimens, constructed from a variety of inhomogeneous materials were susceptible to curing conditions, especially the influence of the temperature-time relation on material strength. This is not uncommon in research into concrete and soils but it created problems in this study when extensive instrumentation failures in a test required a repeat of the test to obtain information. Instrumentation in this study had an approximately 50% chance of surviving the test long enough to yield results. This rate is reported to be about the normal rate for instrumentation in dynamic explosive testing and for non-dynamic testing in the field.

9.4 CONCLUSIONS

9.4.1 Shaped Charge Jet Impact on Concrete

1. Concrete impacted by a high velocity metal jet exhibited two kinds of damage, local as shown in figure 6.18 and overall cracking as shown in figures 6.7 to 6.16. These two types of damage can be treated in isolation since local damage usually extends only a short distance from the axis of the impact of the shaped charge jet. The two types of damage are linked by stress wave effects.
2. Provided scaling rules are observed, similarity in the types of damage identified in 1 will be found in all sizes of concrete specimens impacted by jets from scaled shaped charges.
3. Local damage and overall cracking were found to be similar in concrete blocks and slabs of similar mass subjected to approximately central impact by identical shaped charge jets.
4. Two limits of concrete mass appear to exist where for a given charge the test specimen would shatter or not crack at all under impact from a given shaped charge jet. These limits are proportional to the scale of the experiment and conform to scaling rules mentioned in 2. Thus for each charge the limits would need to be determined experimentally until sufficient reported data was available to predict them.

5. Reinforcement in concrete has been found to have no significant influence on either local damage, providing not too many bars are cut by the shaped charge jet, or on overall cracking. The steel bars did not act as crack inducers even though stress pulse velocity in the steel is greater than in concrete.

6. Age and concrete strength measured by cube crushing, indirect cylinder splitting or beam modulus of rupture were found to have no detectable effect on local damage or on overall cracking under shaped charge jet impact loading.

7. Local damage, particularly penetration depth, was found to conform to Briggs' (1974) empirical formula for 43g charges but not for 298g charges. Even so the ± 20% limits set by Briggs were exceeded by 43g aluminium lined charges. Non-empirical formulae used for metal specimen impacts were found to be inadequate for use with concrete specimens. The predicted diameter of holes were more than three times the actual values and for a correct prediction from the formulae, concrete should be 5 to 13 times stronger than its cube crushing strength would indicate.

8. Local damage parameters for oblique angles of impact by shaped charge jets were not altered, except at the test specimen surface. There the crater became oval, instead of round, due to the change in the angle of incidence of the impacting jet.

9. Shaped charges were mainly used at a single standoff distance. In experiments in which standoff was deliberately varied up to three times the normal standoff no influence was detected on the hole diameter or penetration distance.

10. For a given normal rock or gravel aggregate concrete, modifications to the impacting shaped charge jet caused larger variations in

the response of the concrete than major changes in the concrete constituents. Substitution of the 43g copper shaped charge jet by an aluminium jet resulted in a greater hole diameter, less penetration and greater overall cracking. A different initiation system for a 43g copper jet also altered local damage but not overall cracking. In this case the hole diameter and penetration depth were similar to those obtained with an aluminium jet.

11. Overall cracking of test specimens has been found to be in agreement with stress wave theories and theoretical modes of failure proposed by Johnson (1972).

12. Overall cracking has been shown to be dependent on aggregate type and cement content of the concrete mix. These factors are related since barytes (dense aggregate) and 'Lytag' (light-weight aggregate) both need more cement in the mix than other natural rock aggregates and gravels. Similarly sand/cement mortars of various mix proportions have shown this trend even though water/cement ratios kept the strength of the mortars high enough to prevent conflict with 6 above. Similarly there is no conflict with 10 since the additional cracking due to the modified charge would be added to cracking due to the change in aggregate.

9.4.2 Subsurface Blast Loading of Concrete

1. The type of soil and its degree of saturation under a concrete slab influenced the damage caused to a slab by a subsurface explosion. Explosives in clay or saturated sand caused more punching of the slab near the explosion in addition to other radial cracking than in unsaturated sand.

2. Shear planes were created in sands due to a wedge action under the slab caused by the explosion. In clays a cylindrical or

a spherical cavity was formed with little shearing except in the immediate area of the crater.

3. In sands, fallback material filled the crater but in clays, the roof of the crater remained intact even though the overlying concrete slab was punched out and thrown clear of the site by momentum effects.

4. Reinforcement in the concrete slab can prevent punching out of pieces of slab when the explosion is in clay or saturated sand. The cracking in the slab would be increased and the reinforcing wires may yield.

5. Empirical scaling rules for crusted substrates were found to be of little use. The most important factors were charge mass scaling, concrete slab thickness and the depth of burst of the explosive. If all three were satisfied results were qualitatively similar but not quantitatively exact. However any gross out of scale depth of burst of the explosive would cause lack of fit of results. Comparisons with other related and partially similar work has shown only qualitative agreement.

6. The use of scaling laws for uncrusted substrates was not possible because of 5 above and the influence of the concrete slab. Since the concrete slab possessed much more shear strength than an equivalent soil mass, it acted as a structural element and not as separate soil particles. This indicates that a different cratering mechanism is in operation in crusted substrates.

9.5 SUGGESTIONS FOR FUTURE WORK

It has been shown that, at high rates of strain, concrete variables such as mix design, type of aggregate and cube crushing strength, were relatively unimportant to the overall and local damage caused by both shaped charge jet impacts and subsurface blast loading. This means that any future work on high strain rates in concrete should concentrate on consolidating knowledge on stress wave propagation, cracking and spalling on a single standardised concrete mix. This would aid accuracy but yet still be valid for other concrete mixes.

Present theories of energy partition and dissipation have not been confirmed by practical work. Hence the lack of numerical information renders them of little use in the prediction of brittle material behaviour under high energy impacts. Fundamental information is therefore required before the analysis of complicated brittle materials can be attempted. The study of homogeneous brittle materials such as 'Perspex' (methyl methacrylate) which cracks in a similar manner to concrete could be a suitable starting point.

The instrumentation developed in this study for investigating the properties of concrete under high rates of strain has been shown to be reliable and accurate providing the limitations of section 9.3 are observed. Much more use should now be made of these techniques in concrete testing both in the laboratory and in the field to provide data for theoretical analyses. All the techniques could be operated safely and with no loss of accuracy in the field, some have already been used for the Ministry of Defence (Watson, A.J. et al, 1983).

With the recent growth in computer and finite element analysis techniques it should now be more straightforward to simulate mathematically the interaction, reflection and refraction of stress waves. This should proceed in tandem with research into basic cracking and damage investigations in order that one may contribute to the other. Already the information obtained on crack direction and speed, stress pulse passage times and projectile penetration rates could be used in a computer mathematical model.

The recent advances in fibre optics could be used to advantage in the study of internal cracking of concrete under impact loading. The tamping procedure used in the construction of test specimens in this study would have damaged any buried fibre optic tubes, but if more workable mixes were vibrated rather than tamped, then this system could be practical. Costs of the systems available have recently reduced especially the cost of the connections to the glass tubes. This was another factor in the rejection of fibre optics for use in this study.

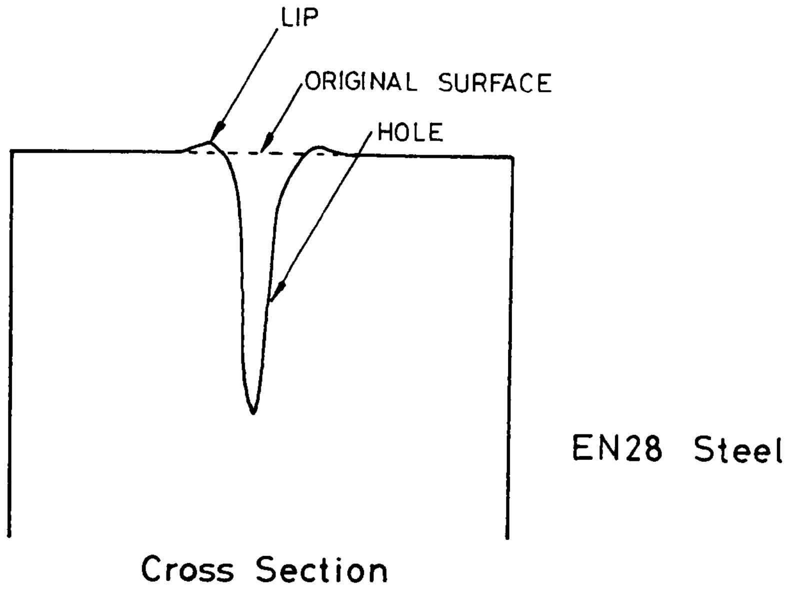

FIGURE 9.1 HOLE FORMED BY A 43g COPPER SHAPED CHARGE IN A DUCTILE MATERIAL (EN 28 STEEL)

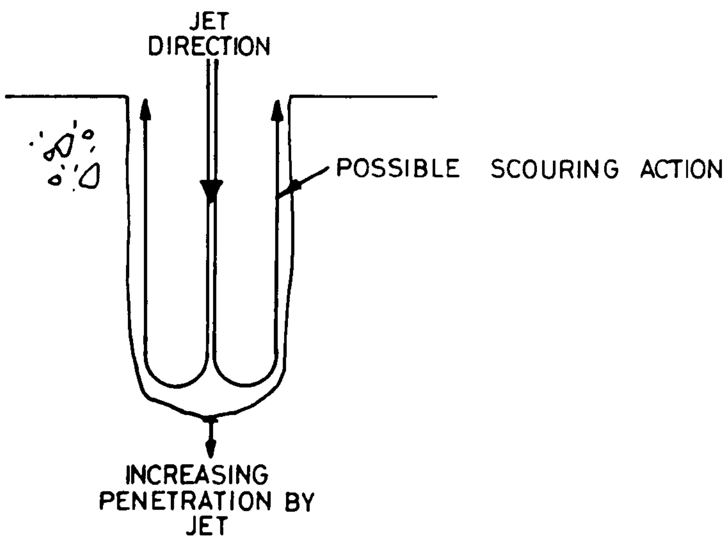

FIGURE 9.2 INFLUENCE OF POSSIBLE SCOURING ACTION BY A SHAPED CHARGE JET
(AFTER JOHNSON (1972))

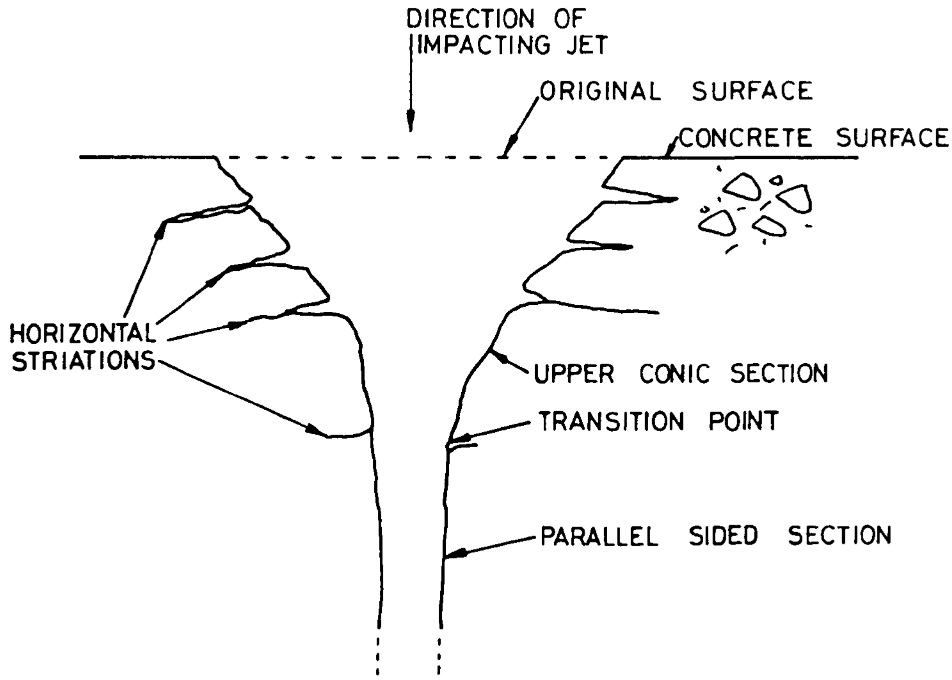

FIGURE 9.3 HORIZONTAL STRIATIONS IN THE UPPER CONIC SECTION OF A TYPICAL SHAPED CHARGE HOLE IN CONCRETE

(a)

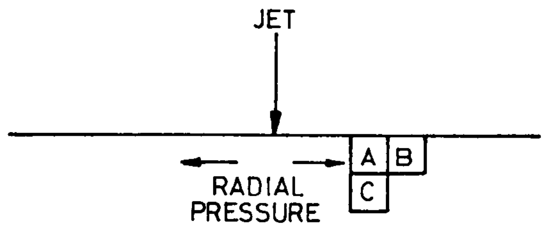

(b)

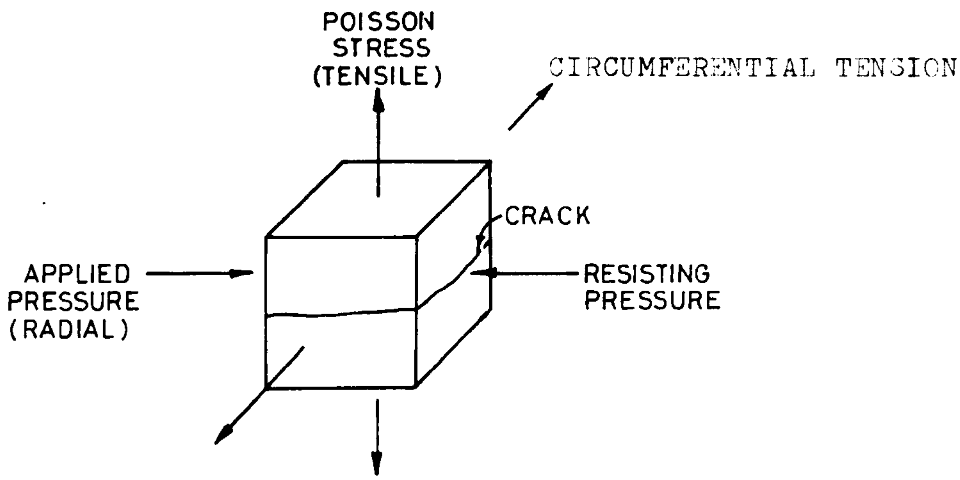

FIGURE 9.4 RADIAL PRESSURE EXPLANATION FOR THE FORMATION OF THE UPPER CONIC SECTION OF A SHAPED JET HOLE IN CONCRETE

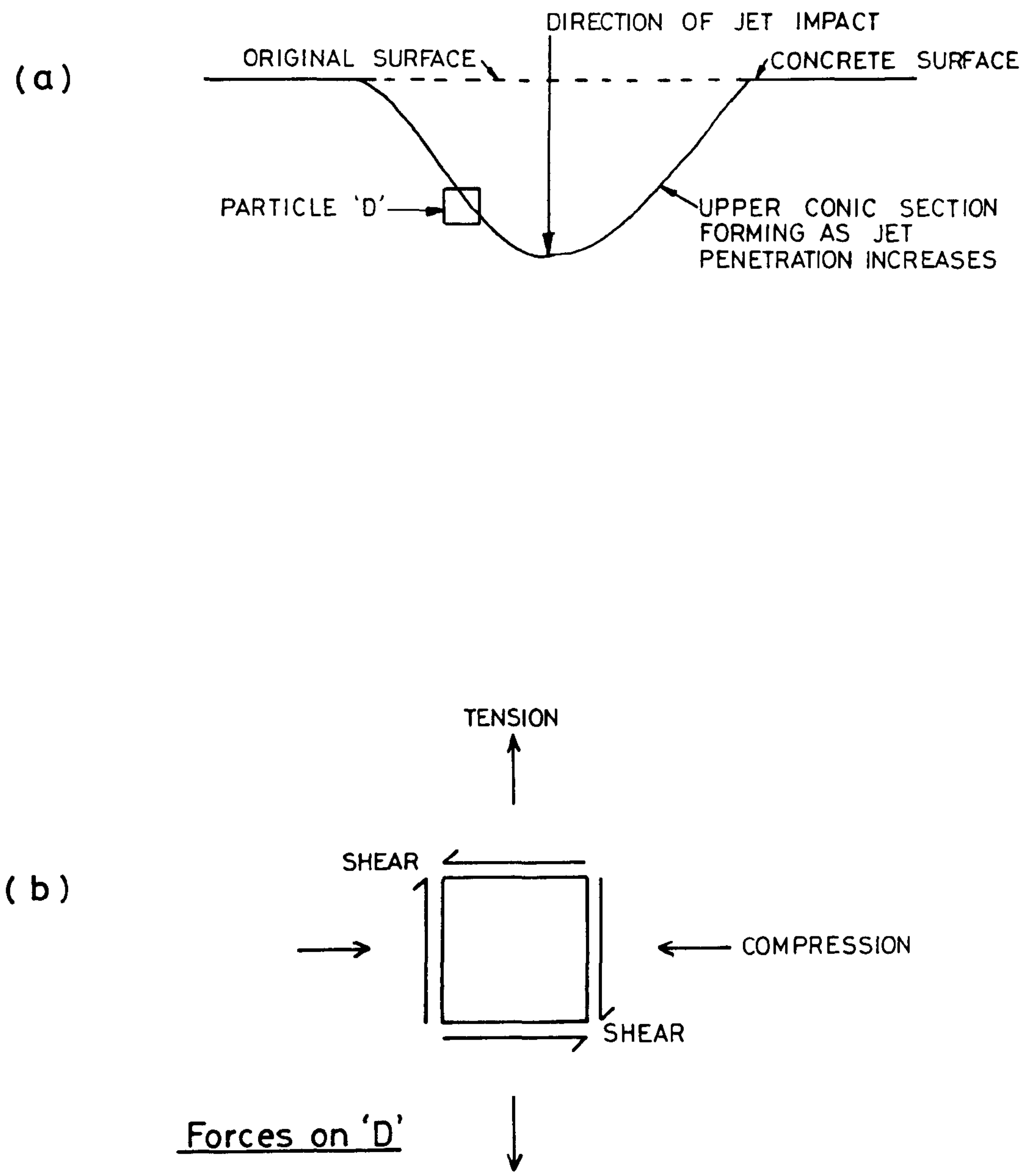

FIGURE 9.5 FORCES ON A PARTICLE ON THE UPPER CONIC BOUNDARY OF A SHAPED CHARGE JET HOLE IN CONCRETE

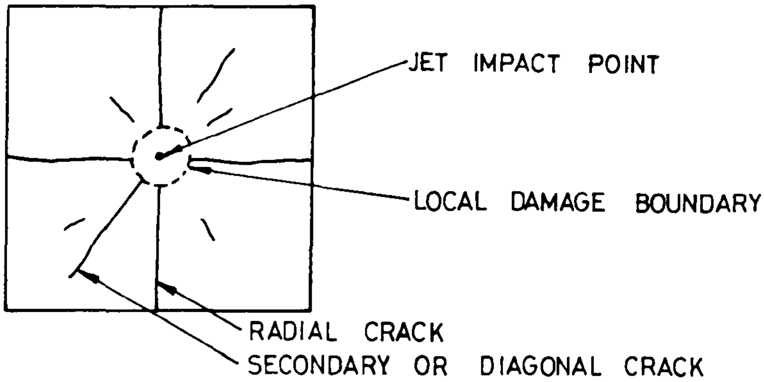

FIGURE 9.6 DEFINITION OF CRACKS FORMED IN CONCRETE BLOCKS BY SHAPED CHARGE JET IMPACTS

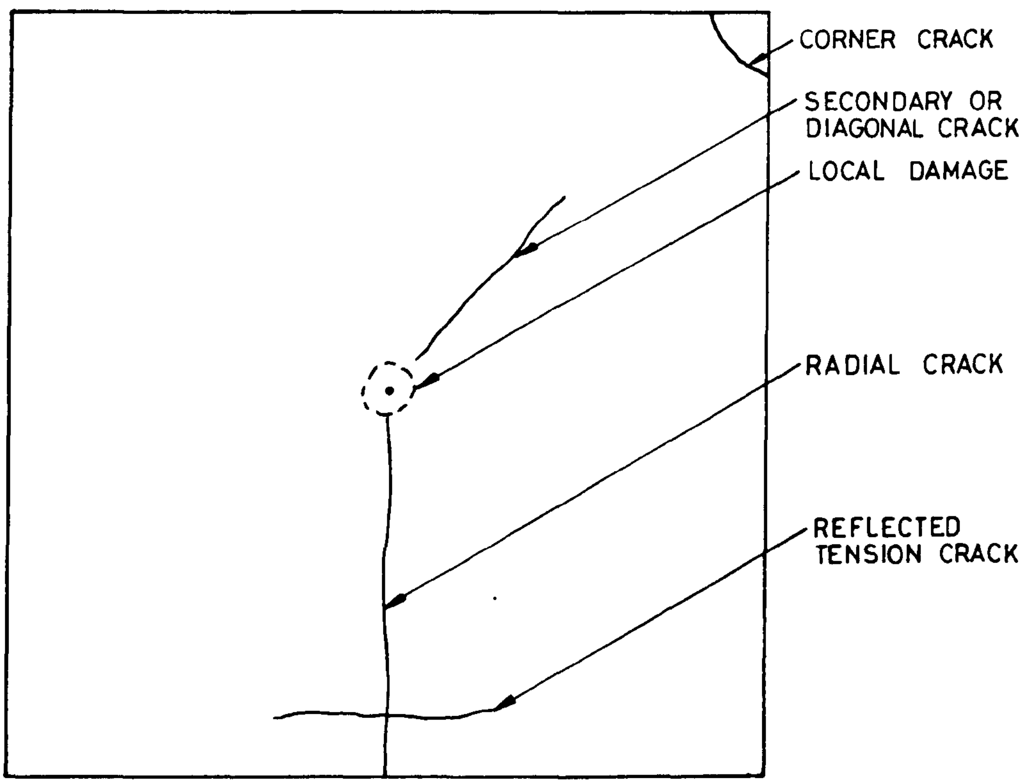

FIGURE 9.7 DEFINITION OF CRACKS FORMED IN CONCRETE SLABS BY SHAPED CHARGE JET IMPACTS

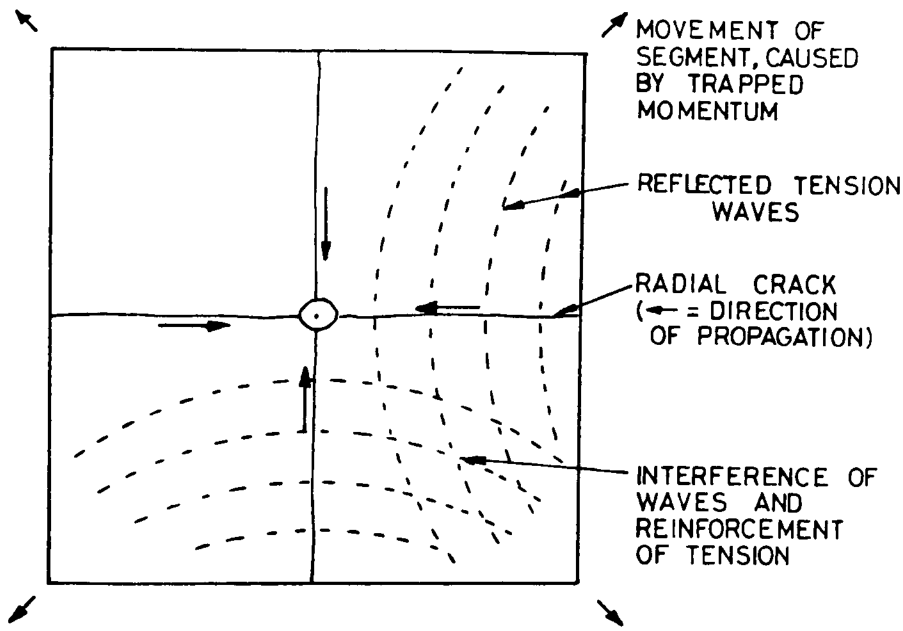

FIGURE 9.8 CRACKING OF SLABS INTO SEGMENTS UNDER THE ACTION OF SHAPED CHARGE JET IMPACTS

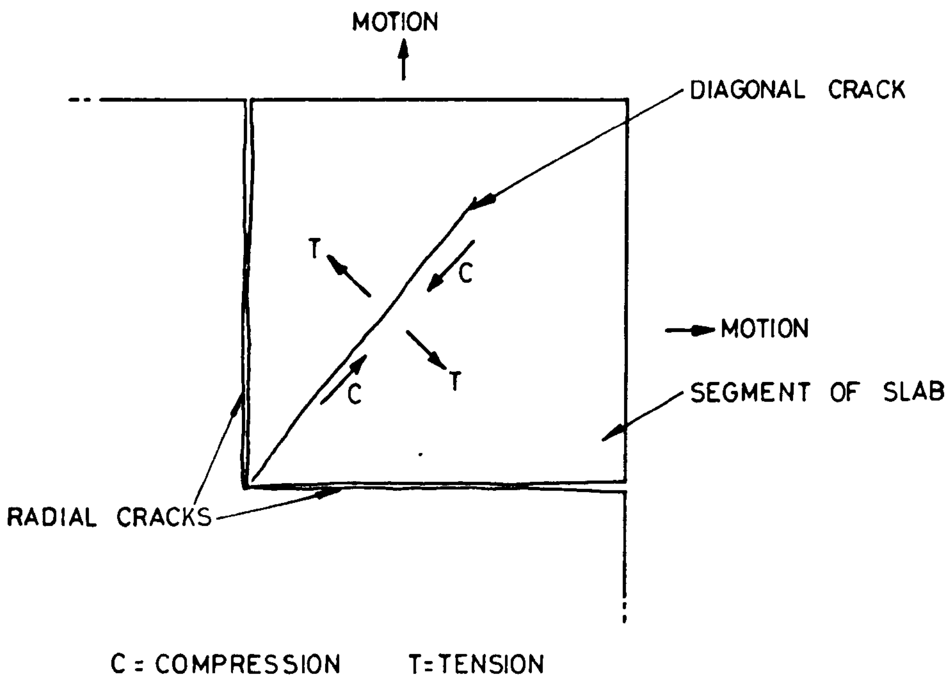

FIGURE 9.9 FORCES ACTING ON A SEGMENT OF A SLAB UNDER THE ACTION OF A SHAPED CHARGE IMPACT

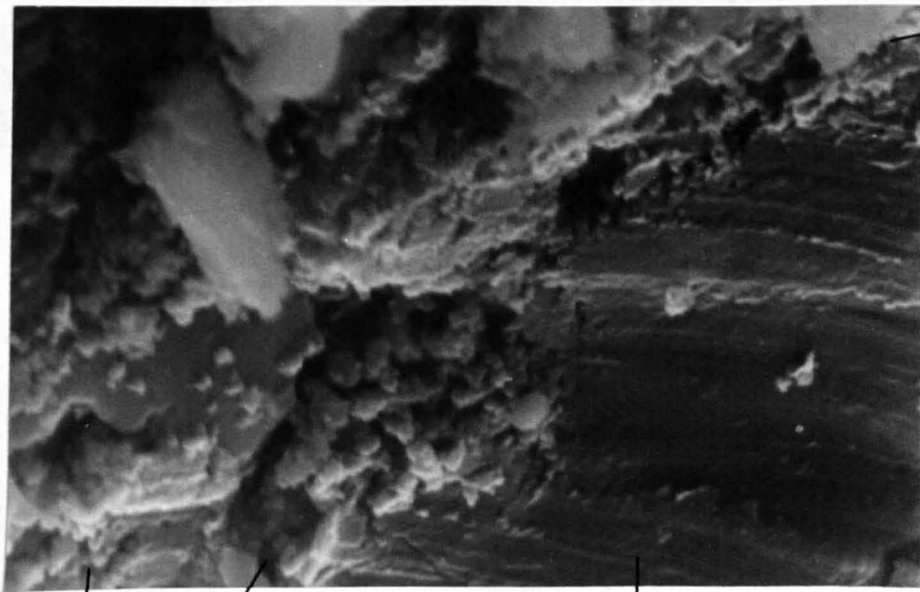

MAGNIFICATION 5000 TIMES

PLATE 9.1 SCANNING ELECTRON MICROSCOPE PICTURE OF A SUSPECTED AGGREGATE/CEMENT BOND FAILURE

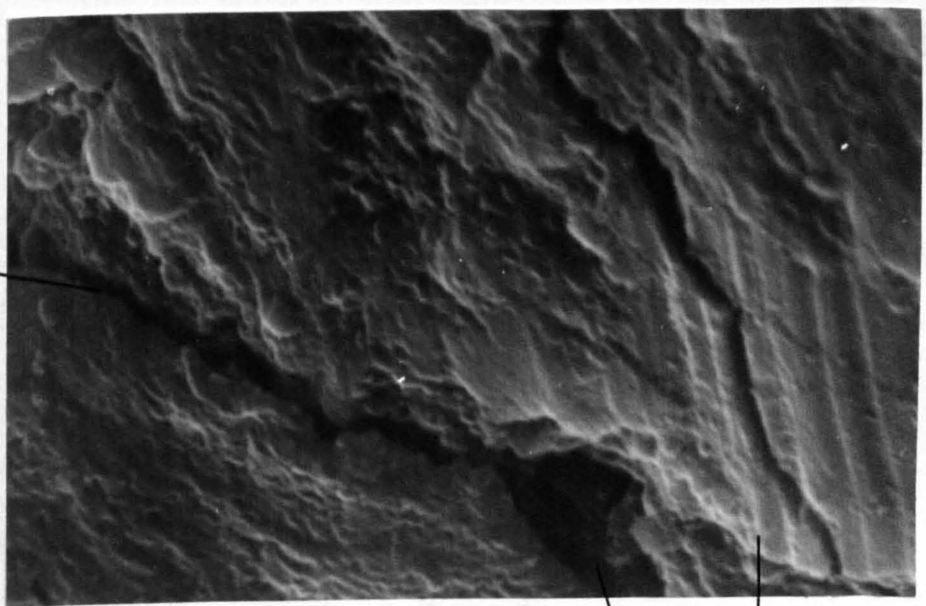

MAGNIFICATION 5000 TIMES

PLATE 9.2 SCANNING ELECTRON MICROSCOPE PICTURE OF A CRACK IN AN AGGREGATE PARTICLE

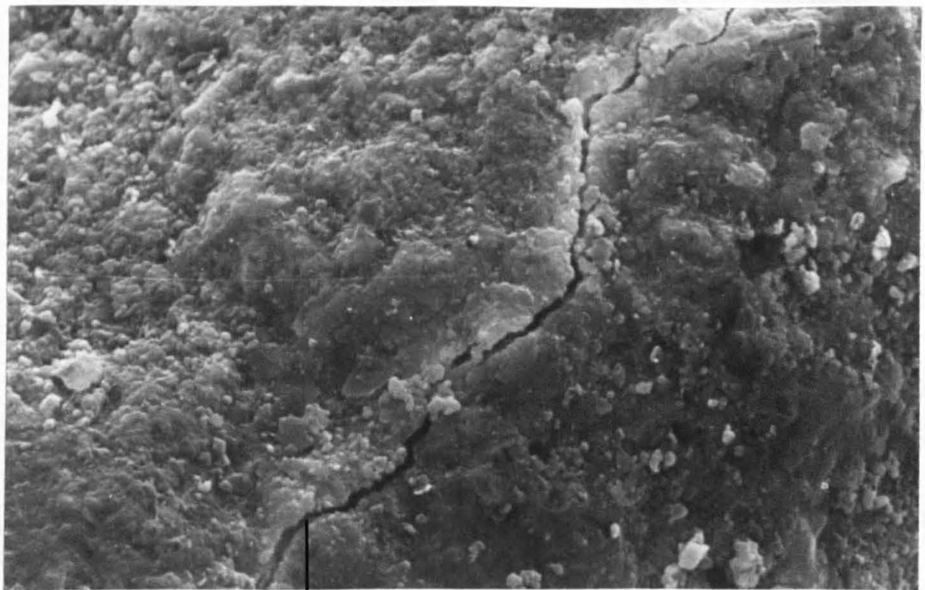

PLATE 9.3 SCANNING ELECTRON MICROSCOPE PICTURE OF A STRUCTURAL CRACK IN CONCRETE

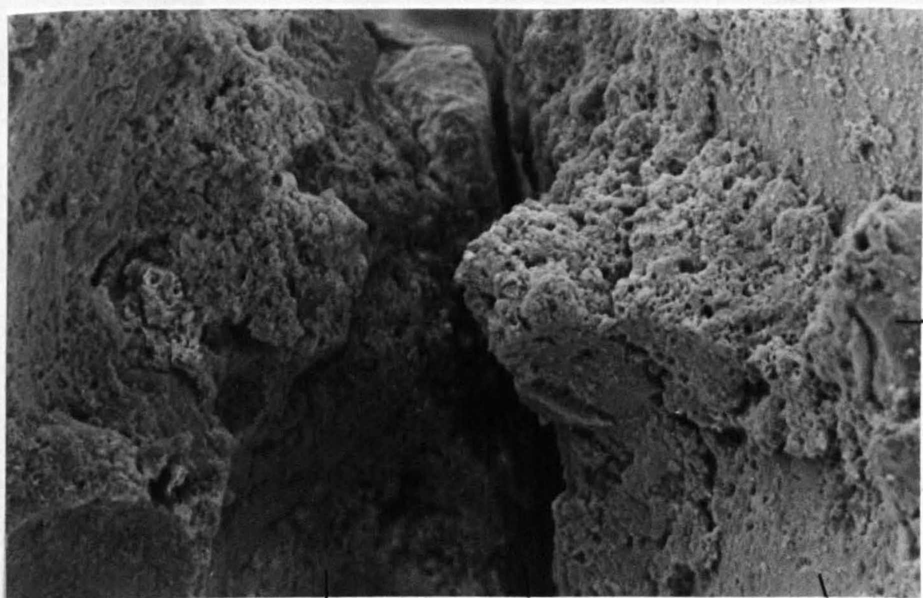

PLATE 9.4 SCANNING ELECTRON MICROSCOPE PICTURE OF A CONCRETE/STEEL REINFORCEMENT INTERFACE

REFERENCES

Abrahamson, G.R. and Goodier, J.N. (1963) Penetration by shaped charge jets of non-uniform velocity. J. App. Phys., Vol. 34, pp. 195-199.

Adridge, W.W. and Breen, J.E.(1970) Useful techniques in direct modelling of reinforced concrete structures. Paper SP24-5, ACI publication SP24, Detroit, pp. 125-135.

Armour Research Foundation (1958) Proceedings of the 3rd symposium on hypervelocity impact. Illinois Institute of Technology, Chicago.

Anonymous (1973) Variables of concrete and their effect on penetration by projectiles. Confidential report R73/471 (Restricted).

Austin, C.F. and Pringle, J.K. (1971) Variables of concrete and their effect on penetration by projectiles. Naval Weapons Centre (Restricted).

Backmann, E.B. and Goldsmith, W. (1975) The mechanics of penetration of projectiles into targets. Int. J. Eng. Sci., Vol. 16, pp. 1-99.

Baker, W.E., Westine, P.S and Dodge, F.T. (1973) Similarity methods in engineering dynamics. Hayden Book Co., New Jersey.

Barkan, D.D. (1962) Dynamics of bases and foundations. McGraw-Hill.

Birkhoff, G., MacDougall, D.P., Pugh, E.M. and Taylor, G. (1948) Explosives with lined cavities. J. App. Phys., Vol. 19, pp. 563-582.

Borges, J.F. and Lima, J.A.E. (1960) Crack and deformation similitude in reinforced concrete. RILEM bulletin New Series number 7, Paris.

Brace, W.F. (1960) An extension of the Griffith's theory of fracture of rocks. J.Geo. Res. Vol. 65, No. 10, pp. 3477-3480.

Brace, W.F. and Bombolakis, E.G. (1963) A note on brittle crack growth in compression. J.Geo. Res. Vol. 68, No. 2, pp. 3709-3713.

Briggs, J. (1974) Shaped charge attack on concrete. Australian Defence Scientific Service. Tech. note 332 (Restricted).

British Standards Institution (1964) Lightweight aggregates for concrete. BS3797.

British Standards Institution (1965) Aggregates from natural sources for concrete (including granolithic). BS882/1201.

British Standards Institution (1967) Methods for sampling and testing of mineral aggregates, sands and fillers. BS812.

British Standards Institution (1970) Methods of testing concrete. BS1881 parts 1-6.

British Standards Institution (1972) Portland cement (ordinary and rapid hardening). BS12 Part 2.

British Standards Institution (1975) Methods of test for soil for civil engineering purposes. BS1377.

British Standards Institution (1976) Specification for test sieves. BS410.

British Standards Institution (1978) Methods of testing concrete. BS4500 Parts 3.1 to 3.8.

Brock, G. (1959) Direct models - an aid to reinforced concrete design. Engineering.

Bryan, G.M. and Eichelberger, R.J. (1957) Application of radioactive tracers to the study of shaped charge phenomena. J. App. Phys. Vol. 28, No. 10, pp. 1152-1155.

Canadian Armament Res. and Dev. Est. (1961) Shaped charge jet impacts on non-homogeneous plastics. Private communication.

Carlson, R.H. (1963) High explosive ditching from linear charges. J. Geophysical Res., Vol. 68, no. 12, pp. 3693-3707.

Carpenter, J.E., Roll, F. and Zelman, M.I. (1970) Techniques and materials for structural models. ACI Symposium SP24, Detroit.

CDA Publications Ltd. (1935) Copper Data.

Chabai, J. (1965) Scaling dimensions of craters produced by buried explosives. J. Geo. Res. Vol. 70, p. 5075.

Chavez, D.J. and Cassino, V. (1975) Effect of pavement design on cratering damage from penetrating weapons. New Mexico University report AFWL-TR-74-197, Albuquerque.

Chen, W.F. and Drucker, D.C. (1969) Bearing capacity of concrete or rock. Proc. ASCE, EM4, Vol. 95, No. 2, pp. 955-979.

Chou, P.C., Carleone, J. and Karpp, R.R. (1976) Criteria for jet formation from impinging shells and plates. J. App. Phys. Vol. 47, no. 7, pp. 2975-2981.

Chou, P.C. and Carleone, J. (1977) The stability of shaped charge jets. J. App. Phys. Vol. 48, pp. 4187-4199.

Christmann, D.R. and Gehring, J.W. (1966) Analysis of high velocity projectile penetration mechanics. J. App. Phys. Vol. 37, pp. 1579-1587.

Clarke, L.A. (1971) Crack similitude in 1:3.7 scale models of slabs spanning one way. Cement and Concrete Association Tech. Report, London.

Clarke, L.A. (1974) Flexural crack similitude in slabs spanning one way. Cement and Concrete Association Tech. Report 42.496.

Clarke, L.A. (1978) Crack similitude in reinforced microconcrete. I.Struct.E./B.R.E. joint seminar, Garston, Watford, pp. 1-8.

Cole, J.E. (1979) Effect of explosive asymmetry on pressed explosive shaped charge jets. Proc. 10th Symp. on explosives and pyrotechnics, pp. 35-1 to 35-12.

Cook, M.A. (1958) The science of high explosives. Reinhold, New York.

Cook, M.A. (1959) Mechanism of cratering in ultra-high velocity impact. J. App. Phys. Vol. 30, No. 5, pp. 725-735.

Cook, M.A., Keyes, R.T. and Ursenbach, W.O (1962) Measurements of detonation pressure. J. App. Phys. Vol. 33, no. 12, pp. 3413-3421.

Cousins, J.E. (1969) Penetration by high velocity metallic jets. Bull. Mech. Eng. Educ., Vol. 8, Pergamon, pp. 45-54.

Cristescu, N. (1968) Dynamic plasticity. App. Mech. Rev., Vol.21, No. 7.

Davids, N. and Haung, Y.K. (1962) Shock waves in solid craters. J. Aero. Sci., Vol. 29.

Davies, I. Ll. (1978) The use of models in studying response to dynamic loading. I.Struct.E./B.R.E. Symposium, Garston, Watford, pp. 1-8.

Davis, R.M. (1956) Stress waves in solids. Br. Jnl. App. Phys., pp. 203-209.

Davison, D.K. (1983) Interaction of high-velocity aluminium shaped charge jets with finite steel and concrete targets. International Symposium on the Interaction of Non-nuclear Munitions with Structures, Colorado Springs, 9-13 May, 1983, pp. 43-47.

Dobbs, N. and Cohen, E. (1970) Model techniques and response tests of reinforced concrete structures subjected to blast loads. ACI publication SP24, Paper SP24-17, Detroit, pp. 407-430.

Eichelberger, R.J. (1955) Re-examination of the non-steady theory of jet formation by lined cavity charges. J. App. Phys., Vol. 26, No. 4, pp. 398-402.

Eichelberger, R.J. (1956) Experimental test of the theory of penetration by metallic jets. J. App. Phys., Vol. 27, No. 1, pp. 63-68.

Eichelberger, R.J. and Pugh, E.M. (1952) Experimental verification of the theory of jet formation by charges with lined conical cavities. J. App. Phys., Vol. 23, No. 5, pp. 537-542.

Evans, D.J., Clark, L.A. and Beeby, A.W. (1972) Some size effects in reinforced microconcrete models. Cement and Concrete Association, London.

Evans, W.M. and Pack, D.C. (1951) Penetration by high velocity ("Munroe") jets : 2. Proc. Phys. Soc. B64, pp. 303-310.

Ewing, W.M., Jarderzky, W.S. and Press, F. (1957) Elastic waves in layered media. McGraw-Hill.

Fairhurst, C. (1963) Rock mechanics. Pergamon.

Feldman, J.B. (1958) Volume-energy relation for shaped charge jet penetrations. Proc. 3rd Symp. on Hypervelocity Impact, Chicago, pp. 215-231.

Fordham, S. (1966) High explosives and propellants. Pergamon.

Glanville, W.H., Collins, A.R. and Matthews, D.D. (1954) The grading of aggregates and workability of concrete. Road Research Tech. Paper No. 5, H.M.S.O., London.

Gluchlich, J. (1963) Fracture of plain concrete. Proc. ASCE, Vol. 89, EM6, pp. 127-139.

Golding, J. (1971) Measuring oscilloscopes. Iliffe, London.

Goldsmith, W. (1960) Impact. Edward Arnold, London.

Goldsmith, W., Kenner, V.H. and Ricketts, T.E. (1968) Dynamic loading of several concrete like mixtures. ASCE, No. 94, ST7, pp. 1803-1831.

Goldsmith, W., Polivka, M. and Yang, T. (1966) Dynamic behaviour of concrete. Exp. Mech., Vol. 6, pp. 65-79.

Guerand, R. (1977) Study of perforation of reinforced concrete slabs by rigid missiles. Nuc. Eng. and Design, Vol. 41.1, pp. 91-102.

Haas, C.J. and Rinehart, J.S. (1965) Coupling between unconfined cylindrical explosive charges and rock. Int. J. Rock. Mech. Min. Sci., Vol. 2, Pergamon, pp. 181-203.

Hampton, D., Much, P.J. and Selig, E.T. (1970) Wave propagation in confined clay. J. Soil. Mech and Fdn. Div., ASCE, Vol. 96, SM4, pp. 1391-1411.

Hannant, D.J. and Frederick, C.O. (1967) Failure criteria for concrete in compression. Mag. Conc. Res., Vol. 19-20, pp. 137-144.

Harris, H.G., Gajanan, M.S. and White, R.N. (1970) Reinforcement for small scale direct models of concrete structures. ACI publication SP24, Paper Sp24-6, Detroit.

Harris, H.G., Sabnis, G.M. and White, R.N. (1966) Small scale direct models of reinforced and prestressed concrete structures. Cornell University School of Civil Engineering, Report 326.

Harris, H.G., Sabnis, G.M. and White, R.N. (1970) Reinforcement for small scale models of concrete structures. ACI Symposium SP24, Detroit, pp. 141-149.

Hartley-Jones, M. (1977) A practical introduction to electronic circuits. Cambridge University Press.

Hawkyard, J.B., Johnson, W. and Utoh, I.O. (1970) Simple analysis for the non-symmetic dynamic expansion of cylindrical cavities. J. Mech. Eng. Sci., Vol. 12, No. 5.

Heierli, W. (1962) Inelastic wave propagation in soil columns. J. ASCE, Vol. 88, SM6, pp. 33-65.

Hillier, K. (1982) Application of fracture mechanics. Concrete, pp. 43-44.

Holman, J.P. (1978) Experimental methods for engineers. McGraw-Hill.

Hondros, G. (1957) The protection and manipulation of electrical resistance strain gauges of the bonded wire type for use in concrete, particularly for internal strain measurements. Mag. Con. Res., Vol G.

Hopkins, H.G. and Kolsky, H. (1960) The mechanics of hypervelocity impact. RARDE Report B12/60 (Restricted).

Hughes, B.P. and Gregory, R. (1972) Concrete subjected to high rates of loading in compression. Mag. Con. Res., Vol. 24, No. 78.

Hughes, B.P. and Watson, A.J. (1978) Compressive strength and ultimate strain of concrete under impact loading. Mag. Conc. Res., Vol. 30, No. 105.

IABSE (1970) Plasticity in reinforced concrete. IABSE Colloquium, Kopenhagen.

Inkester, J.E. (1980) Dynamic loading of a reinforced concrete model. Ph.D. Thesis, University of Sheffield.

Institution of Civil Engineers (1971) Aircraft pavement design. Proc. Symp., London.

International symposium on wave propagation and dynamics.(1967) Wave propagation tests in layered granular media. Properties of earth materials, New Mexico.

Ito, I. and Sassa, K. (1961) On the detonation pressure produced at the inner surface of a charge hole. Mem. Fac. Eng., Kyoto University 23, pp. 103-124.

Jackson, J.G. Jnr. and Hadala, P.F. (1964) Dynamic bearing capacity of soils. U.S. Army Engineer Waterways Exp. Station, Vicksburg, Mississippi, pp. 1-76.

James, H.J. and Buchanan, J.S. (1958) Experimental studies of penetration by shaped charge jets. Proc. 3rd. Symp. on Hypervelocity Impact, Chicago, pp. 317-345.

Joachim, C.E. (1983) Rapid runway cutting with shaped charges. International Symposium on the Interaction of Non-nuclear Munitions with Structures, Colorado Springs, 9-13 May, 1983.

Johansson, C.H. and Persson,P.A. (1970) Detonics of high explosives. Academic Press, London.

Johnson, R.P. (1962) Strength tests on scaled down concretes suitable for models, with a note on mix design. Mag. Conc. Res., Vol. 14, No. 40, pp. 47-53.

Johnson, W. (1972) Impact strength of materials. Arnold, London.

Johnson, W., Travis, F.W. and Loh, S.Y. (1968) High speed cratering in wax and plasticine. Int. J. Mech. Sci., Vol. 10, Pergamon, pp. 593-605.

Jonas, G.H. (1954) Penetration of shaped charges into concrete targets. A summary of data. Aberdeen Proving Ground Tech. Note 939, Maryland.

Jones, R. (1962) Non destructive testing of concrete. Cambridge Press.

Karman, T. and Duwez, P. (1950) The propagation of plastic deformation in solids. J. App. Phys., Vol. 21.

Keast, D.N. (1967) Measurements in mechanical dynamics. McGraw-Hill, New York.

Kesler, C.E., Naus, D.J. and Lott, J.L. (1971) Fracture mechanics - its applicability to concrete. Mech. behaviour of materials, Kyoto.

Kinslow, R. (1970) High velocity impact phenomena. Academic Press.

Kline, S.J. (1965) Similitude and approximation theory. McGraw-Hill, New York.

Kluge. R.W. (1943) Impact resistance of reinforced concrete. Proc. ACI, Vol. 39, pp. 397-412.

Kolsky, H. (1953) Stress waves in solids. Clarendon Press, Oxford.

Koski, W.S., Lucy, F.A., Shreffler, R.G. and Willig, F.J. (1952) Fast jets from collapsing cylinders. J. App. Phys., Vol. 23, No. 12, pp. 1300-1305.

Kornhanser, M. (1964) Structural effects of impact. Cleaver-Hume, London.

Kuman, S. and Dupach, G.W. (1978) BRS tests on microconcrete models - a review of the scaling aspects.3. I.Struct.E./B.R.E. Seminar, Garston, Watford, pp. 1-12.

Kutter, H.K. and Fairhurst, C. (1971) On the fracture process in blasting. Inst. J. Rock Mech. Min. Sci., Vol. 8, Pergamon.

Kvammen, A. (1973) A full scale pavement cratering study. Ph.D. Thesis, University of New Mexico.

Langhaar, H.L. (1951) Dimensional analysis and the theory of models. Wiley, New York.

Lawn, J. (1975) Fracture of brittle solids. Cambridge University Press.

Lee, F.M. (1970) The chemistry of cement and concrete. Edward Arnold, London.

Livingston, C.W. (1960) Application of the Livingston crater theory to blasts in loess and clay. U.S. Army Engineer Waterway Exp. Stn., Vicksburg, Mississippi.

Long, B.G. and Kurtz, H.J. (1943) Effect of curing methods upon the durability of concrete as measured by changes in the dynamic modulus of elasticity. Proc. ASTM, Vol. 43.

Lynch, J., Hawkyard, J.B. and Johnson, W. (1970) Lab. scale experiments into cavity and crater formation by high explosives. J. Mech. Eng. Sci., Vol. 12, No. 5.

Mandl, P. and Givens, G. (1964) Dynamics of high velocity penetration into clay. N.R.C. of Canada, No. 8145.

Martin, F.R. (1956) Concrete runways. Proc. Paving Dev. Group. Cement and Concrete Association, London.

McIntosh, J.D. (1964) Concrete mix design. Cement and Concrete Association, London.

McIntosh, J.D. and Erntroy, H.C. (1955) The workability of concrete mixes with ¾in. aggregates. Cement and Concrete Association Report No. 2, London, pp. 1-7.

McNeill, G.M. (1981) An experiment in crater scaling. MVEE Draft Report. Private Communication.

Ministry of Defence and Hunting Eng. Ltd. (1982) Private Communication. (Restricted).

Montague, P. and Kormi, K. (1982) Constitutive relationships and a failure criterion for concrete based on fundamental material properties. Mag. Conc. Res., Vol. 34, No. 188, pp. 35-43.

Neville, A.M. (1973) The properties of concrete. Pitman, London.

Newman, K. and Newman, J.B. (1969) Failure theories and design criteria for plain concrete. Civ. Eng. Mat. Conf., Southampton, pp. 963-995.

Noor, F.A. and Khalid, M. (1978) Deformed wire reinforcement for microconcrete models. I.Struct.E./B.R.E. Seminar, Garston, Watford, pp. 1-7.

Norton, H.N. (1969) Handbook of transducers for electronic measuring systems. Englewood Cliffs, Prentice-Hall.

Ottosen, N.S. (1979) Constitutive model for short time loading of concrete. J.Eng. Mec. Div. ASCE, EM1.

Owens, P.L. (1973) Basic mix method. Cement and Concrete Association.

Pack, D.C. and Evans, W.M. (1951) Penetration by high velocity ("Munroe") jets : 1. Proc. Phys. Soc., B64, pp. 298-302.

Parry, R.H.G.(Ed)(1971) Stress-strain behaviour of soils. Proceedings of the Roscoe Memorial Symposium, Cambridge University.

Pichumani, R. and Dick, D.L. Jnr. (1970) Effects of small cratering charges on airfield pavements. AWFL TR-70-66. Kirtland AFB, New Mexico.

Preece, B.W. and Davis, J.D. (1964) Models for structural concrete. CR Books Ltd.

Proc. 7th International Symposium on Hypervelocity Impacts (1964), Tampa, Florida.

Proc. 6th International Conference on Soil Mechanics and Foundation Engineering (1965), Vol. 2, Montreal.

Proc. Symposium on Soil-structure Interaction (1964), University of Arizona.

Proc. International Symposium on Wave Propagation and Dynamic Properties of Earth Materials (1967) University of New Mexico Press, Albuquerque.

Procurement Executive (1970) Services textbook of explosives. Ministry of Defence (Restricted).

Property Services Agency (1978) Airfield pavements construction and maintenance works. Series 500. Private communication.

Property Services Agency (1971) Design and evaluation of aircraft pavements. D.O.E., H.M.S.O., London.

Property Services Agency (1978) Standard specification clauses for airfield works. D.O.E. (Draft). Private communication,.

Pugh, E.M., Eichelberger, R.J. and Rostoken, N. (1952) Theory of jet formation by charges with lined conical cavities. J. App. Phys., Vol. 23, No. 5, pp. 532-536.

Raouf, Z.A., Al-Hassain, S.T. and Simpson, J.W. (1976) Explosive testing of fibre-reinforced composites, Concrete, pp. 28-30.

Rayleigh, Lord (1900) Collected papers. Cambridge University Press.

Redwood, M. (1966) Mechanical waveguides, Pergamon, London.

Rees, W.W. and Evans, W.M. (1946) Penetration of cement-mortar targets by Munroe jets. ARD report 412/46, Fort Halstead.

Richards, A. (1983) Private communication.

Richart, F.E.(1970) Vibrations of soils and foundations. Englewood Cliffs, Prentice-Hall.

Rinehart, J.S. (1959) The role of stress waves in the comminution of brittle, rocklike materials. Int. Symp. on Stress Wave Propagation.

Rinehart, J.S. (1960a) Mechanics of fracture due to stress waves in brittle materials. Int. Symp. on Stress Wave Propagation in Materials, Pennsylvania State University.

Rinehart, J.S. (1960b) Stress wave propagation in materials. Interscience, New York.

Rinehart, J.S. (1960c) On fractures caused by explosives and impacts. Quarterly of the Colorado School of Mines, Vol. 55, No. 4.

Rixon, M.R. (1977) Concrete admixtures. Use and applications. C and C A. Construction Press, Lancaster.

Roney, P.L. (1961) Review of hypervelocity impact theories. CARDE Tech. Memo. 623/61 (Restricted).

Sand and Gravel Association (1964) Sands for concrete symposium. Imp. Coll., London.

Sassa, J., Coates, D.F. and Ho, I., (1967) Coupling and stress waves in close proximity to surface explosions. Int. J. Roch. Mech. Min. Sci. Vol. 4, Pergamon.

Saxe, H.C. (1963) Explosion crater prediction utilising characteristic parameters. Rock Mechanics, Proc. 5th Int. Symp. University of Minnesota, Pergamon.

Saxe, H.C. and Del Manzo, D.D. (1970) A study of underground explosion cratering phenomena. Proc. Symp. on Engineering with Nuclear Explosives, Las Vegas, Nevada.

Sedov, L.I. (1959) Similarity and dimensional methods in mechanics. Academic Press, New York.

Shacklock, B.W. (1960) Air entrained concrete-properties, mix design and quality control. The Surveyor, Vol. 119, No. 3560.

Shacklock, B.W. (1974) Concrete constituents and mix proportions. Cement and Concrete Association, London.

Shirayama, K. (1961) The estimation of the strength of concrete made with lightweight aggregates, Mag. Conc. Res., Vol. 13.

Singh, S. (1957) Possible explanation of 'after-jet' by the detonation of shaped charges. J. App. Phys., Vol. 28, pp. 1365-1366.

Singleton-Green, J. (1945) Limestone concrete. Chapman and Hall, London.

Sparks, F.N. and Hayes, J. (1966) The development of hollow coned charges for the attack of concrete. RARDE RRL/96/FNS.JH. No. R6338, Fort Halstead (Restricted).

Subedi, N.K. and Garas, F.K. (1978) Bond characteristics of small diameter bars used in microconcrete models. I.Struct.E./B.RE. seminar.

Swamy, R.N. (1979) Fracture mechanics applied to concrete. Developments in concrete technology - 1. Applied Science Publishers.

Taylor, E.S. (1974) Dimensional analysis for engineers. Clarendon Press, Oxford.

Townsend, W.H., Langseth, M. and Perkins, B. Jnr. (1961) Mechanics of crater formation in sand and clay produced by underground explosives. Terminal Ballistics Lab. Report 1381, Aberdeen Proving Ground, Maryland.

University of Sheffield (1970) Departmental code of practice for health and safety. Civil Engineering.

Urbanski, T. (1967) Chemistry and technology of explosives. Pergamon.

U.S. Army Engineer Waterways Experimental Station (1961) Cratering for high explosive charges. Analysis of crater data. Report 2-547, Vicksburg, Mississippi.

Van Valkenburg, M.E., Clay, W.G. and Huth, J.H. (1956) Impact phenomenon at high speeds. J. App. Phys., Vol. 27, No. 10, pp. 1123-1129.

Vesic, A.S. (1965) Cratering by explosives as an earth pressure problem. 6th Int. Conf. on Soil Mechanics and Foundation Engineering, Vol. II, Montreal.

Vesic, A.S. (1972) Expansion of cavities in infinite soil mass. J. Soil Mech. and Fdn. Div., A.S.C.E., SM3, pp. 265-291.

Walsh, J.B. (1965) The effect of cracks on the compressibility of rock. J. Geo. Res., Vol. 70, No. 2.

Walsh, J.M., Shreffler, R.G. and Willig, F.J. (1953) Limiting conditions for jet formation in high velocity conditions.J.App.Phys.,Vol. 24, No. 3, pp. 349-359.

Walton, W.H. (1958) Mechanical properties of non-metallic brittle materials.

Watson, A.J., Anderson, W.F. and Archer, B. (1978 to 1984) Properties of concrete when subjected to high rates of strain. M.O.D. Agreement AT/2031/087/RAR, Report 4195/00/01 to /18 and the final report (In confidence).

Watson, A.J., Anderson, W.F. and Archer, B. (1982) Hypervelocity impact of concrete. R.I.L.E.M, C.E.B., I.A.B.S.E., I.A.S.S. Symposium, West Berlin, pp. 188-201.

Watson, J.M. (1958) The design and construction of airfield pavements. I.Struct.E., London.

Watstein, D. (1953) Effect of strain rate on the compressive stress and the elastic properties of concrete. Proc. Am. Conc. Inst., Vol. 49.

Wenzel, A.B. and Espavza, E.D. (1972) Measurements of pressures and impulses at close distances from explosive charges buried and in air. U.S. Army Development Centre, Fort Belvoir, Virginia.

Westine, P.S. (1966) Replica modelling in soil dynamics. J. Soil Mech. and Fdn. Div., Proc. A.S.C.E., SM6, pp. 169-187.

Westine, P.S. (1970) Explosive cratering. J. Terramechanics, Vol. 7, No. 2, Pergamon, pp. 9-19.

White, I.G. and Clark, L.A. (1978) Bond similitude in reinforced microconcrete. I.Struct.E./B.R.E. Seminar, Garston, Watford, pp. 1-9.

Whitehurst, E.A. (1966) Evaluation of concrete properties from sonic tests. Detroit.

Whittle, l.P. and Backstrom, J.E. (1954) Properties of heavy concrete made with barytes aggregates. Journal of A.C.I.

Wood, D.S. (1952) On longitudinal plane waves of plastic strain in solids. J.App. Mech., Vol. 19, p. 521.

Young, D.F. and Murphy, G. (1964) Dynamic similitude of underground structures. J.Eng. Mech. Div., A.S.C.E., Proc. 3938.

Zia, P., White,R.N. and Vanhorn, D.A. (1970) Principles of model analysis. A.C.I. Publication SP24, Paper 24-2, Detroit, pp. 19-37.

APPENDIX 1

EQUIPMENT & MATERIALS SUPPLIERS

Barr and Stroud Rotating Mirror High Speed Camera

J Hadland P.I. Ltd
Bovingdon
Hemel Hempstead

Gould OS 4000 Digital Storage Oscilloscope

Gould Instruments Division
Roebuck Road
Hainault
Essex IG6 3UE

RACAL Universal Counter Timer

Racal Dana Instruments Ltd
Duke Street
Windsor
Berkshire

Scanning Electron Microscope. Philips PSEM500 with Link Energy **Dispersive** Analysis System

Philips Ltd
Eindhoven
Holland

PUNDIT Ultrasonic Testing Equipment

CNS Instruments Ltd
61-63 Holmes Road
London W5

Fylde FE 359 TA Bridge Amplifier

Fylde Electrical Laboratories
49-51 Fylde Road
Preston PR1 2XQ

Linear Variable Displacement Transducer R102, 50mm

Novatech Ltd
Croydon

Concrete Saw and Blades

Clipper Manufacturing Co
Thurmaston Boulevard
Barkby Road
Leicester

Concrete Mixer. Model ME Multiflow 4cu.ft. capacity

Edward Benton & Co ltd
Cretangle Works
Brook Lane
Ferring
Worthing
Sussex

Test Sieves

Endecotts Ltd
Lombard Road
London SW19

Concrete Cube Moulds
Concrete Beam Moulds
Air Entraining Apparatus
Concrete Density Can

Caplin Engineering Co Ltd
Elton Park Works
Hadleigh Road
Ipswich

Sand Cone Apparatus
Wax and Wax Pot

Engineering Laboratory Equipment Ltd
Eastman Way
Hemel Hempstead, HP2 7HB

Reynolds FS10 EBW Firing System

Aviquipo of Britain Ltd
St Peters Road
Maidenhead
Berkshire S16 7QU

Electrical Plugs, Cables and Fittings
Conducting Silver paint
Conducting Glue
Firing Cables Type UR43

R S Components Ltd
P O Box 427
13-17 Epworth Street
London EC2P 2HA

'Lytag' Lightweight Aggregate

Lytag Ltd
Rugeley Power Station
Rugeley
Staffordshire

'Barytes' Dense Aggregate

Athole G Allen Ltd
Closehouse Mine
Lunedale
Middleton in Teesdale
Barnard Castle
Co Durham

Basalt Aggregate

Tarmac Roadstone Northern Ltd
Waterswallows Quarry
Fairfield
Buxton
Derbyshire

Limestone Aggregate

Tarmac Roadstone Northern Ltd
Tunstead Quarry
Fairfield
Buxton
Derbyshire

Zone 2 Sand Aggregate
Crushed Gravel Aggregate

BCA Ltd
Rugeley Road
Hednesford
Cannoch
Staffordshire WS12 5QZ

Fireclay

Naylor Bros (Clayware) Ltd
Denby Dale
Huddersfield
HD8 8QE

Cement 'Ferrocrete' Rapid Hardening

Blue Circle Ltd
Hope Cement Works
Hope
Derbyshire

Reinforcement

Rigby (Wireworks) Ltd
New Office
Cross Smithfields
Sheffield 3

Brass Strips
Copper Plates
Aluminium Block

IMI Righton Ltd
Tyler Street
Sheffield 9

Steel Block (EN28)

Department of Metallurgy
University of Sheffield
Mappin Street
Sheffield S1 3JD

Perspex

Tuckers Ltd
Shoreham Street
Sheffield S1

Electrical Resistance Strain Gauges

TML Ltd
Dell House
Eastern Dene
Hazlemere
High Wycombe
Buckinghamshire

Explosives

R.A.R.D.E. (ET2)
M.O.D.
Fort Halstead
Sevenoaks
Kent

Air Entraining Agent 'Conplast AEA'

Chemical Building Products Ltd
Cleveland Road
Hemel Hempstead HP2 7DL

Wide Angle Sterescopic Cameras. Wild C40
Plates AGFA CEVAERT AVIPHOT PAN 100

Wild Heerbrugg (UK) Ltd
Revenge Road
Lordswood
Chatham
Kent ME5 8TE

Steko 1818 Sterocomparator

Carl Zeiss Jena
93-97 New Cavendish Street
London S1A 2AR

Motronic Data Collector for Steko 1818

Surveying and Scientific Instruments Ltd
Wootton Rivers
Marlborough
Wiltshire SN8 4NQ

Powder Paint, Rowney Fixed Power Colour

George Rowney and Co Ltd
Bracknell
Berkshire

Graphite Rods (Pentel 6H, 60mm long by 0.5mm diameter)

Andrews Ltd
West Street
Sheffield

APPENDIX 2

RULES FOR USING SHAPED CHARGES AND OTHER EXPLOSIVES

General

Shaped charges consist of a 43 or 298g 60/40 RDX/TNT charge together with an ARDE type 3 exploding bridgewire (EBW). The FS10 firing system must be used with these initiators.

Other charges consist of PE4 or CE* explosive with an L2A1 initiator. The FS10 firing system must NOT be used with these initiators.

Shaped Charge Tests

A. Preparation

A.1 Clear all personnel from the building and adjacent land. No unauthorised personnel to enter from now on.

A.2 Switch off all electrical appliances including lights.

A.3 Position the FIRING MODULE behind the nearest convenient block wall and surround it with concrete blocks.

A.4 Position the CONTROL MODULE outside the building on the embankment behind the wingwall.

A.5 Lay out but do not plug in the three cables linking the control module to the firing module. Check control module plugs are visible from firing module.

A.6 Check cables for damage and plugs for bad connections.

B. Pre-Fire Setting up Procedure

B.1 Select charge and EBW initiator. EBW initiator may be already fitted to the charge. Transport in a leather bag.

B.2 Take the two leads with YELLOW plugs and short the two plugs.

---

* Not used in experiments. Only used for demolition or air blast charges.

B.3 Strip about 25mm of insulation from each initiator lead and connect the two leads to the two yellow plug cables. Bind connections with tape.

Note: a) The EBW initiator cannot be connected in a leather bag since the leads are too short.

b) It is not necessary to remove the EBW initiator from the charge for connection purposes.

B.4 Locate the charge into its perspex holder.

B.5 Retire behind the blast wall to the firing module.

B.6 Place the shorting plug into its sockets.

B.7 Connect both YELLOW plugs to the YELLOW sockets on the firing module.

B.8 Connect the BLACK plug to the BLACK socket.

Connect the RED plug to the RED socket.

Connect the WHITE plug to the WHITE socket.

B.9 Check building for personnel.

B.10 Remove shorting plug.

B.11 Leave building taking three control module cables.

B.12 Close main doors and lock.

B.13 Proceed to control module.

B.14 Connect BLACK plug to BLACK socket

Connect RED plug to RED socket

Connect WHITE plug to WHITE socket.

C. Firing Sequence*

C.1 Check adjacent area for personnel.

C.2 Sould siren. 3 short blasts.

---

* Direct firing by the operator.
(For firing from external sources refer to camera and firing box manuals for connection details).

C.3 Place the shorting plug in its socket.

C.4 Check battery (press switch). Light indicates condition.

C.5 Sound siren. Long blast

C.6 Arm the circuit (hold switch for 4-6 seconds). Do not release switch.

C.7 On obtaining armed indication (light) keep switch held and press firing button.

D. <u>Post-Fire Procedure (Successful detonation)</u>

D.1 Withdraw shorting plug.

D.2 Withdraw BLACK, WHITE and RED plugs.

D.3 Open main doors.

Open rear door. Allow time for ventilation.

D.4 Place shorting plug in firing module.

D.5 Disconnect YELLOW, BLACK, WHITE and RED plugs.

E. <u>Post-Fire Procedure (Unsuccessful detonation)(See also Section F)</u>

IF NO SOUND IS HEARD. IF BATTERY AND ARM LIGHTS FUNCTION AND IT IS SUSPECTED THAT THE CABLING AND CONNECTIONS COULD BE FAULTY.

E.1 If item C.7 of firing sequence has failed to detonate the charge repeat items C.6 and C.7.

E.2 If no further sound is heard remove shorting plug.

E.3 Remove RED, BLACK and WHITE plugs. Check plugs.

E.4 Wait 30 minutes.

E.5 Enter building, proceed to firing module.

E.6 Place shorting plug into its socket.

E.7 Withdraw YELLOW, BLACK and WHITE plugs.

E.8 Short the two YELLOW plugs.

E.9 Check charge, connections and cables.

E.10 Proceed from item B.3 Pre-Fire Setting up Procedure

F. <u>Post-Fire Procedure (unsuccessful detonation)</u>

IF PARTIAL DETONATION HAS OCCURRED OR IT IS WISHED TO DISPOSE OF A CHARGE WHICH HAS COMPLETELY FAILED TO EXPLODE.

F.1 After item C.7 of firing sequence has failed to detonate the charge wait 30 minutes.

F.2 Follow procedure E.3 to E.8 inclusive. Lock main doors.

F.3 Follow disposal procedure L.1 to L.15.

<u>Other Charge Tests</u>

G. <u>Preparation of Testing Building</u>

G.1 Clear all personnel from the building and adjacent land.

G.2 Switch off all electric appliances including lights.

G.3 Lay out the two core YELLOW firing cable and short each end.

H. <u>Pre-Fire Setting up Procedure</u>

H.1 Select charge and initiator.

H.2 Introduce charge and initiator into the building in separate leather bags.

H.3 Ensure that both ends of the firing cable are visible.

H.4 Connect the initiator using the leather bag as protection. (It is possible to retreat behind a blast wall for further protection). (EBW initiators follow sequence B.1 to D.5).

H.5 Locate charge.

H.6 Locate initiator on charge.

H.7 Check the building is clear of personnel.

H.8 Leave the building, taking the free end of the firing cable.

H.9 Lock the main doors.

I. <u>Firing Procedure*</u>

I.1 Check adjacent area is clear of personnel.

I.2 Check resistance of circuit using ohm-meter (Refer to data).

---

* Direct firing by the operator.
(For firing from external sources refer to camera and firing box manuals for connection details).

I.3 Sound siren. 3 short blasts.

I.4 Couple firing line to generator.

I.5 Sound siren. Long blast.

I.6 Activate generator.

J. Post-Fire Procedure (Successful detonation)

J.1 Disconnect firing line from generator. Short the cable.

J.2 Open main and rear doors.

K. Post-Fire Procedure (Unsuccessful detonation)

For partial detonation wait 30 minutes and then proceed to L.1 to L.15 inclusive.

K.1 Repeat item I.6.

K.2 If still no detonation disconnect generator.

K.3 Short firing line cables.

K.4 Wait 30 minutes.

K.5 Enter building taking firing line free ends.

K.6 Disconnect firing line from initiator.

K.7 Leave building. Lock main doors.

K.8 Follow disposal procedure L.1 to L.15 inclusive.

L. Disposal Procedure

L.1 Prepare a suitable charge of PE4* and obtain a new L2A1 initiator.

L.2 Take charge and new initiator into testing building.

L.3 Short firing cable.

L.4 Connect new initiator to firing cable.

L.5 Place disposal charge on undetonated charge and then install new initiator.

L.6 Check building clear of personnel.

L.7 Retire outside building and lock main doors.

---

* Usually equal to the mass of the original charge.

L.8 Check circuit using ohm-meter. (Refer to data).

L.9 Sound siren. 3 blasts.

L.10 Connect generator.

L.11 Sound siren. Long blast.

L.12 Activate generator.

L.13 If successful short out firing cable.

L.14 Open main and rear doors. Ventilate.

L.15 Examine site of detonation and short firing cables.

L.16 It is extremely unlikely that a disposal charge will misfire Should this occur proceed to K and prepare a second disposal charge. All undetonated products should be gathered together and disposed of by a charge equal to the combined masses of unexploded charges.

APPENDIX 3

COMPUTER PROGRAM AND CALCULATIONS

FOR STEREOCOMPARATOR DATA

The output tape from the stereocompartor used for the measurement of shaped charge holes contained only a string of data. The following computer program converts this data into horizontal and vertical coordinates suitable for plotting as a series of cross sections at a constant distance apart, in this case 6mm (see figure 5.8).

```
      MASTER COMPUTE
      F=64.87
      G=64.80
      DO 5 I=1,4
      READ(1,105)N,X,Y,P
  105 FORMAT(I4,3(2X,F7.0))
      ZA=400*F*G/(G*X-F*(X+P))
      ZB=ZB=ZA
      XA=ZA*X/F
      YA=ZA*Y/F
      WRITE(2,110)N,XA,YA,ZA
  110 FORMAT(1X,I4,3F15.8)
    5 CONTINUE
      AZ=ZB/4.0
      WRITE(2,115)AZ
  115 FORMAT(1X,F15.8)
      DO 10 I=1,200
      READ(1,105)N,X,Y,P
      ZA=400*F*G/(G*X-F*(X+P))
      XA=ZA*X/F
      YA=ZA*Y/F
      ZZ=(ZA-AZ)/1000
      WRITE(2,120)N,XA,YA,ZA,ZZ
  120 FORMAT(1X,I4,4F15.8)
   10 CONTINUE
      STOP
      END
      FINISH
      ****
```

Output is of the form:

460.414	-254.732	2.002	17.91370
A	B	C	D

A is the 'x' coordinate of the cross section in mm from a base line.

B is the cross section distance from a base line perpendicular to the 'x' coordinate axis in mm.

C is the vertical distance in metres of the 'x' coordinate point from the stereoscopic camera datum.

D is the depth of the 'x' coordinate point in millimetres beneath the original slab surface datum.